Synthesis of Geometric Structures from Topology Optimized Multi-Scale Designs

Stutz, Florian Cyril

Publication date:
2021

Document Version
Publisher's PDF, also known as Version of record

Synthesis of Geometric Structures from Topology Optimized Multi-Scale Designs

Florian Cyril Stutz

Kongens Lyngby 2021

Synthesis of Geometric Structures from Topology Optimized Multi-Scale Designs
April 2021

Author:
Florian Cyril Stutz

Main supervisor:
Associate Professor Andreas Bærentzen
Technical University of Denmark

Co-supervisors:
Professor Ole Sigmund
Technical University of Denmark

Associate Professor Niels Aage
Technical University of Denmark

Technical University of Denmark
Department of Applied Mathematics and Computer Science
Building 324, Richard Petersens Plads
2800 Kongens Lyngby, Denmark
Phone +45 4525 3031
compute@compute.dtu.dk
www.compute.dtu.dk

Abstract (English)

Homogenization-based topology optimization produces multi-scale designs with optimal stiffness at a significantly reduced computational cost compared to well-established topology optimization methods. However, the homogenization approach does not directly create a mechanical structure but instead outputs parameters describing the behavior of microstructures at infinitesimally small scales. For compliance minimization, these optimal multi-scale descriptions of the optimized designs consist of lamination thicknesses and lamination orientations.

The process of synthesizing high-resolution, near-optimal geometric structures from these optimal multi-scale designs is called *de-homogenization*. This thesis presents research on the de-homogenization of multi-scale designs obtained with homogenization-based topology optimization for compliance minimization. The thesis consists of an introductory background chapter followed by two parts about de-homogenization methods. The first part focuses on integration-based methods, while the second part proposes novel approaches that do not rely on integration.

The first part further contains an investigation of microstructure orientations fields and singularities arising for single loading case (single-load) problems in two dimensions. It follows a description of a de-homogenization method for two-dimensional, singularity-containing multi-scale designs. Further, the first part contains an expansion to three dimensions of existing work for singularity-free single-load problems, achieving a reduction of computational effort of three orders of magnitude compared to density-based topology optimization. The first part concludes with a discussion of research on microstructure orientation initialization and regularization during the homogenization approach to obtain optimal multi-scale designs that are easier to de-homogenize with currently available methods.

The second part contains an investigation of microstructure orientations fields and singularities arising for single-load problems in three dimensions. Then a novel approach for two- and three-dimensional de-homogenization, called the subselection method, is presented that does not rely on integration. The subselection method is the first de-homogenization method that applies to singularity-containing three-dimensional single-load case problems with no modifications of the underlying orientation fields. The new approach precomputes a set of structural members that are locally well-aligned with the microstructure orientations. Then an optimization chooses an evenly spaced subset resulting in a near-optimal single-scale structure. Finally, the subselection method is used to de-homogenize two-dimensional problems with multiple loading cases.

Resumé (Dansk)

Homogeniseringsbaseret topologioptimering producerer multiskaladesigns med optimal stivhed betydeligt hurtigere end de mest anvendte metoder til topologioptimering. Homogeniseringsmetoden skaber dog ikke direkte en mekanisk struktur. I stedet producerer den parametre, der beskriver mikrostrukturernes egenskaber på uendeligt fin skala i form af lamineringstykkelser og lamineringsretninger.

Processen at syntetisere højopløste, optimerede geometriske strukturer ud fra disse multiskala designs kaldes de-homogenisering. Denne afhandling omhandler forskning i de-homogenisering af multiskala designs, der er opnået ved hjælp af homogeniseringbaseret topologioptimering med henblik på minimering af eftergivelighed. Afhandlingen indeholder et indledende baggrundskapitel, og dette er efterfulgt af en beskrivelse af de-homogeniseringsmetoder. Denne beskrivelse er igen opdelt i to dele, der hverst rækker sig over flere kapitler. I den første del behandles metoder, der anvender integration, og i den anden del foreslås nye metoder, som ikke er afhængige af integration.

Den første del indeholder en undersøgelse af mikrostrukturers orienteringsfelter og singulariteter, der opstår for enkelt-belastningsproblemer i to dimensioner. Derefter følger en beskrivelse af en de-homogeniseringsmetode for todimensionale, singularitetsholdige flerskala konstruktioner. Endvidere indeholder den første del en udvidelse til tre dimensioner af eksisterende arbejde for singularitetsfrie enkelt-belastningsproblemer, hvorved der opnås en reduktion af den beregningsmæssige indsats på tre størrelsesordener i forhold til densitets-baseret topologioptimering. Første del afsluttes med en diskussion af forskning i mikrostrukturers retningsinitialisering og regularisering under homogeniseringsmetoden for at opnå optimale design i flere skalaer, som er lettere at de-homogenisere med de tilgængelige metoder.

Den anden del indeholder en undersøgelse af mikrostrukturers retningsfelter

og singulariteter, der opstår ved enkelt-belastningsproblemer i tre dimensioner. Derefter præsenteres en ny metode til to- og tredimensionel de-homogenisering, kaldet subselektionsmetoden, som ikke er afhængig af integration. Subselektionsmetoden er den første de-homogeniseringsmetode, der kan anvendes på tredimensionale enkelt-belastningsproblemer med singulariteter uden ændringer af de underliggende retningsfelter. Den nye metode beregner på forhånd et sæt strukturelle elementer, der lokalt er godt orienteret i forhold til mikrostrukturens retninger, hvorefter en optimering vælger en undermængde med lige store afstande, hvilket resulterer i en næsten optimal enkeltskalastruktur. Endelig anvendes subselektionsmetoden i denne afhandling til at de-homogenisere todimensionelle problemer med flere belastningstilfælde.

Preface

This thesis is submitted in partial fulfillment of the requirements for acquiring the degree of Doctor of Philosophy (Ph.D.) in engineering. The thesis presents research conducted from February 2018 to April 2021 at the Section for Visual Computing at the Department of Applied Mathematics and Computer Science at the Technical University of Denmark (DTU), Kongens Lyngby, Denmark, and partially at the Computer Graphics Group at the Computer Science & Artificial Intelligence Lab of the Massachusetts Institute of Technology (MIT), Cambridge, MA, United States of America. The Ph.D. project was funded by DTU Compute, and secondary funding has been provided by the Villum Foundation through the *InnoTop* project. The thesis includes three publications (two published in journals, one currently in preparation).

Kongens Lyngby, April 2021
Florian Cyril Stutz

List of contributions

The following publications are submitted as part of this thesis:

Paper-I

- J. P. Groen, F. C. Stutz, N. Aage, J. A. Bærentzen, and O. Sigmund. **De-homogenization of optimal multi-scale 3D topologies**. *Computer Methods in Applied Mechanics and Engineering*, vol. 364, pp. 112–979, 2020. DOI: 10/gjhccg

Paper-II

- F. C. Stutz, J. P. Groen, O. Sigmund, and J. A. Bærentzen. **Singularity Aware De-Homogenization for High-Resolution Topology Optimized Structures**. *Structural and Multidisciplinary Optimization*, vol. 62, pp. 2279–2295, 2020. DOI: 10/gjhccf

Paper-III

- F. C. Stutz, T. F. Olsen, J. P. Groen, N. Aage, O. Sigmund, J. Solomon, and J. A. Bærentzen. **Synthesis of Frame Field-Aligned Multi-Laminar Structures**. *arXiv preprint*, 2021. arXiv: 2104.05550

Acknowledgements

I would like to express my gratitude to my supervisors, Andreas Bærentzen, Ole Sigmund, and Niels Aage. Their extensive knowledge was accessible to me at all times, and their patience in answering all my questions made this Ph.D. project possible.

I would also like to thank Jeroen Groen, who supported me with advice and inputs whenever I needed it. Furthermore, I would like to thank my collaborators, Tim Olsen and Justin Solomon, for their contributions to our joint publications, which brought their quality to a new level.

My colleagues at the Department of Applied Mathematics and Computer Science deserve praise for their humor that made the last three years enjoyable, even when work was stressful.

Further, I thank my family for their support and encouragement during the past years. And finally, I would like to thank Astrid and her family for all the joy and support they have given me during my Ph.D., especially during the pandemic.

Contents

Chapter 1

Introduction

1.1 Motivation

Topology optimization is a computational method to obtain optimal material layouts for various sets of mechanical problems. An important sub-problem is structural compliance minimization. Given a design space, loads, boundary conditions, and material properties, one searches for a structure with maximal stiffness. The most often used approach to topology optimization is the so-called density-based topology optimization. On a finite element mesh, one varies the material density in each finite element during the optimization to obtain a structure with maximal stiffness. Subsequently, one interprets these results as black and white designs. To get high-resolution structures, a giga-scale amount of elements is often necessary [Aage et al., 2017; Baandrup et al., 2020]. However, the computational burden is vast and far from real-time, which limits engineers in everyday life.

Researchers have revived the homogenization-based topology optimization introduced in Bendsøe and Kikuchi [1988] to obtain high-resolution designs faster. Homogenization-based topology optimization yields not only local densities. Instead, it outputs information about the microstructure of the material, for example, the local orientations of the microstructure and the amount of material aligned with these orientations. Using the additional knowledge about microstructure allows obtaining optimal designs at a fraction of the computational cost of density-based topology optimization. Further, the homogenization approach shows no grid dependency, which means that the topology of a result

obtained on a coarse finite element mesh does not change when solving the same problem on a finer mesh.

While the possible gains from using homogenization-based topology optimization are enormous, it is essential to know that it is surprisingly hard to interpret its results. The extraction of globally consistent structures with a finite length scale is challenging since we only obtain local orientations and material distributions. Trade-offs between local alignment, global connectivity, spacing of structural members, and globally smooth members are hard to achieve predictably. The extraction of global structures is called de-homogenization and has been increasingly in the focus of researchers since its introduction in Pantz et al. [2008].

1.2 Goals of this Ph.D. thesis

The purpose of this Ph.D. project has been to investigate de-homogenization and further develop existing methods, and possibly create new approaches to extract structures from topology optimization results. At the beginning of this Ph.D. project, there was one clear vision. We knew that we wanted to extract mechanically well-performing structures from various homogenization-based topology optimization designs. Thus, in the beginning, we asked ourselves why we are not yet able to extract these structures and what the hurdles were to advance de-homogenization. We developed the following set of questions, which turned out to cover a large group of research topics considered in de-homogenization.

1. What kind of singularities arises in homogenization-based topology optimization results, and where are they located?

2. How can we de-homogenize three-dimensional, singularity-free results obtained by the homogenization approach?

3. How can we expand de-homogenization to allow the usage of more challenging, singularity-containing problems in two and three dimensions?

4. Is there a way to expand possible findings to the previous questions to examples with multiple loading cases (multi-load examples)?

1.3 Contributions and thesis overview

This thesis aims to discuss the above four topics while leaning on the following contributions contained in this thesis.

- [Groen, Stutz, et al., 2020] [Paper-I]: De-homogenization of Optimal Multi-Scale 3D Topologies
- [Stutz, Groen, et al., 2020] [Paper-II]: Singularity Aware De-Homogenization for High-Resolution Topology Optimized Structures
- [Stutz, Olsen, et al., 2021] [Paper-III]: Synthesis of Frame Field-Aligned Multi-Laminar Structures

The sections relevant to my work and contributions have been re-used and adapted to this thesis, and hence, it is sufficient for the reader only to read this thesis. However, all papers, but especially Paper-I, contain additional information and work from co-authors that might interest the reader. Therefore, all the papers are attached in the appendix.

I will first discuss the two-dimensional (2D) integrative methods [Paper-II] due to the formulations being simpler and the topic of singularities being easier to address in two dimensions. Only thereafter will I describe the three-dimensional (3D) work on integrative methods [Paper-I]. I will then propose a novel, non-integrative method [Paper-III] and lastly discuss the application of this method to the de-homogenization of multi-load designs.

This thesis aims to give the reader a basic understanding of the relevant topics and covers several different research fields. Chapter 2 will cover the basics of density-based topology optimization, homogenization-based topology optimization, and microstructures. Chapter 3 discusses directional fields, singularities, and the relation to homogenization-based results as originally published in Paper-II. Integration-based de-homogenization is considered in Chapter 4. There, I first present previous work on de-homogenization and then present an approach for singularity-containing 2D examples. I conclude the chapter by outlining our expansion of de-homogenization to 3D singularity-free cases. In Chapter 5, I propose a newly developed non-integrative approach to de-homogenization that allows for three-dimensional examples containing singularities and two-dimensional multi-load problems.

A recurring topic throughout this thesis is the strive for clean structures that perform well from a mechanical point of view. Challenges like noise, non-

uniqueness, and the lack of global connectivity are the main obstacles in achieving this. It is worth noting that the proposed methods have applications reaching beyond de-homogenization since vector and tensor fields are recurring topics throughout physics and mechanics.

Chapter 2

Topology optimization

This chapter aims to give relevant background information on topology optimization needed to follow the contributions of this Ph.D. thesis. I will start with a short introduction to topology optimization. Then I will visit density-based and homogenization-based methods for topology optimization. Finally, I will look at materials and microstructures used for homogenization-based topology optimization. The contributions of this thesis lie in the field of de-homogenization, i.e., extracting structures from results obtained through homogenization-based topology optimization. Therefore, this background chapter aims at giving the necessary overview of the homogenization approach and its underlying microstructures. As a prerequisite, a general understanding of the finite element method [Szabó et al., 2011; Zienkiewicz et al., 2013] is required to follow this thesis. Further, a basic knowledge of optimization algorithms is helpful [Jorge Nocedal, 2006]. For more information on topology optimization in general, the reader is referred to the following review papers [Deaton et al., 2014; Sigmund and Maute, 2013].

2.1 Introduction to topology optimization

Let us consider a finite element mesh and linear elastic structure, where we have a static equilibrium equation

$$\mathbf{K}\mathbf{u} = \mathbf{f}. \tag{2.1}$$

Here, $\mathbf{K}$ denotes the stiffness matrix describing the structure, $\mathbf{u}$ is the global displacement vector at the nodes of our finite element mesh, and $\mathbf{f}$ is the global

load or global force vector. We can write the global stiffness matrix $\mathbf{K}$ as

$$\mathbf{K} = \sum_{e=1}^{N} \mathbf{K}_e \left(\mathbf{E}_e \right),$$

where we define $\mathbf{K}$ as the sum over local stiffness matrices $\mathbf{K_e}$ of the elements $e = 1, \ldots, N$. Note that the local stiffness matrix K_e in element e depends on the elasticity tensor $\mathbf{E}_e$, holding the information describing the material properties in this element. Further, we should note that the sum is understood to contain a mapping from elementwise degrees of freedom to global degrees of freedom.

The element strain energy density s_e is defined as

$$s_e = \mathbf{u}_e^{\mathrm{T}} \mathbf{K}_e \mathbf{u}_e,$$

which lets us define the compliance, $\mathcal{J}$, as

$$\mathcal{J} = \sum_{e=1}^{N} s_e = \sum_{e=1}^{N} \mathbf{u}_e^{\mathrm{T}} \mathbf{K}_e \mathbf{u}_e = \mathbf{u}^{\mathrm{T}} \mathbf{K} \mathbf{u} = \mathbf{f}^{\mathrm{T}} \mathbf{u}.$$

In engineering, a fundamental task is to find the stiffest possible structure under given volume limits. Maximizing stiffness corresponds to minimizing compliance and is the most used of all topology optimization examples. There are different ways to tackle this problem. If one creates an initial design and optimizes the compliance by moving the structures' boundary, it is called shape optimization. Note that the topology of the structure does not change in shape optimization. Alternatively, one can also change the structure itself by changing the material properties (e.g., solid or void) or the size and existence of the structural members (e.g., the diameters of bars in a truss structure). This second approach is called topology optimization and was first introduced in Bendsøe and Kikuchi [1988]. There also exist combinations of topology and shape optimization using adaptive meshes [Christiansen, 2015; Misztal et al., 2012].

We can build a simple topology optimization example as follows. We want to find a final design that lies in a design domain Ω and minimize the compliance J. We discretize Ω with N finite elements with volumes V_e. Furthermore, we describe our structure by a density variable $\rho(\mathbf{x})$, where $\mathbf{x} \in \Omega$ is a point in our design domain Ω. For the discretization, we assume that the density is constant in an element e and denote it with ρ_e. Further, we have a limit V^0 to the amount of material that we can use for creating our structure, i.e., $\int_\Omega \rho(\mathbf{x}) dV \leq V^0$. Lastly, we demand that $\mathbf{u}$ fulfills the state equation $\mathbf{K}\mathbf{u} = \mathbf{f}$ at any point of the

optimization. We receive the following optimization problem:

$$\begin{aligned} \min_{\boldsymbol{\rho}} : \quad & \mathbf{u}^{\mathrm{T}}(\boldsymbol{\rho})\mathbf{K}(\boldsymbol{\rho})\mathbf{u}(\boldsymbol{\rho}) \\ \text{s.t.} : \quad & \mathbf{K}(\boldsymbol{\rho})\mathbf{u} = \mathbf{f}, \\ & \sum_{e=1}^{N} \rho_e V_e \leq V^0 \\ & \rho_e \in \{0,1\} \quad \forall e = 1, \ldots, N. \end{aligned} \tag{2.2}$$

When we optimize over the relative density variable $\rho(\mathbf{x})$, the stiffness matrix $\mathbf{K}$ changes with every iteration since the element stiffness matrices $\mathbf{K}_e$ depend on ρ_e through $\mathbf{E}_e(\rho_e)$. Therefore, the stiffness matrix changes at every design update (also called iteration), and we need to re-solve the state equation at every iteration. This is a very costly operation for complex problems with a large number of finite elements.

The challenge of Problem 2.2 lies in the binary form of the density variables. In fact the computational burden of such a problem limits us from solving examples with thousands or millions of elements, even for heuristic approaches [Sigmund, 2011]. To circumvent the binary optimization, we would like to relax the problem allowing $\rho \in [0,1]$:

$$\begin{aligned} \min_{\boldsymbol{\rho}} : \quad & \mathbf{u}^{\mathrm{T}}(\boldsymbol{\rho})\mathbf{K}(\boldsymbol{\rho})\mathbf{u}(\boldsymbol{\rho}) \\ \text{s.t.} : \quad & \mathbf{K}(\boldsymbol{\rho})\mathbf{u} = \mathbf{f}, \\ & \sum_{e=1}^{N} \rho_e V_e \leq V^0 \\ & \rho_e \in [0,1] \quad \forall e = 1, \ldots, N. \end{aligned} \tag{2.3}$$

The challenge with the above optimization problem is the definition of material properties for $\rho_e \in (0,1)$. It is not intuitively clear what an intermediate density material is or if one can exctract a mechanically well-performing solid-void design from the solution of the above optimization problem. In the next section, I will describe a method to model the mechanical properties of an element with intermediate density.

2.2 Simplified isotropic material with penalization (SIMP)

To address the challenges of intermediate densities Bendsøe [1989] proposed the simplified isotropic material with penalization approach (SIMP). The local

stiffness matrix in an element e depends on the Youngs' modulus E of that element. For solid material ($\rho = 1$) we write $E(1) = E_0$. For $0 \leq \rho \leq 1$ we then define the SIMP interpolation

$$E(\rho_e) = E_{min} + \rho_e^p (E_0 - E_{min}),$$

where the power p is called the penalization parameter and for implementation reasons, void elements are assigned a minimal stiffness E_{min}. This allows to mimick void-like behavior by a very soft material, that does not influence the structure's stiffness but keeps us from re-meshing the structure after each iteration. Note, however, that it is also possible to exclude major regions of void by on-the-go re-meshing [Bruns et al., 2003; Liu, Hu, et al., 2018].

If we choose a power $p = 1$ for our compliance optimization, we receive the so-called variable-thickness-sheet problem introduced in Rossow et al. [1973]. This problem can be interpreted as a sizing problem in two dimensions, where ρ corresponds to the elementwise thicknesses of plates. This is a simple problem that has been proven to be convex and thus has a unique solution [Petersson, 1999].

However, for everyday topology optimization one should choose $p > 1$ to converge to a black and white structure. As an initial guess, we usually use $\rho = {}^{V^0}/_N, \forall e = 1, \ldots, N$. Choosing p too big will lead the optimization to a local minimum near the initial guess. Choosing p too close to one will lead to a lot of elements with intermediate densities, thus resulting in a "grayscale" result instead of a black and white design. Sigmund and Maute [2013] name $p = 3$ as optimal value. A detailed explanation of why SIMP is mechanically sound and sensible to use is given in Bendsøe et al. [1999].

There exist other interpolation schemes than SIMP, like, e.g., the rational approximation of material properties (RAND) introduced in Stolpe et al. [2001] using an interpolation function with a non-zero gradient for $\rho_e = 0$, which can yield convergence benefits for the design update.

2.2.1 Checkerboard problems

For topology optimization, bi-linear rectangular elements are often used. These elements are known to not fulfill the discrete Ladyzhenskaya–Babuška–Brezzi (LBB) condition [Díaz and Sigmund, 1995]. This leads to the so-called checkerboard instability problem [Sigmund and Petersson, 1998]. An example of the checkerboard problem occurring is given in Figure 2.1. To prevent checkerboard results, one applies a regularization operator (also called filter) on the density

variables [Bourdin, 2001; Bruns et al., 2001]. A filter smooths the intermediate and final results of the topology optimization as follows. An element's density is averaged with its neighbors, effectively removing checkerboard patterns from the admissible design space. Another solution to the checkerboard problem would be to increase the degree of the ansatz functions of the finite elements, although, this would make the topology optimization more costly.

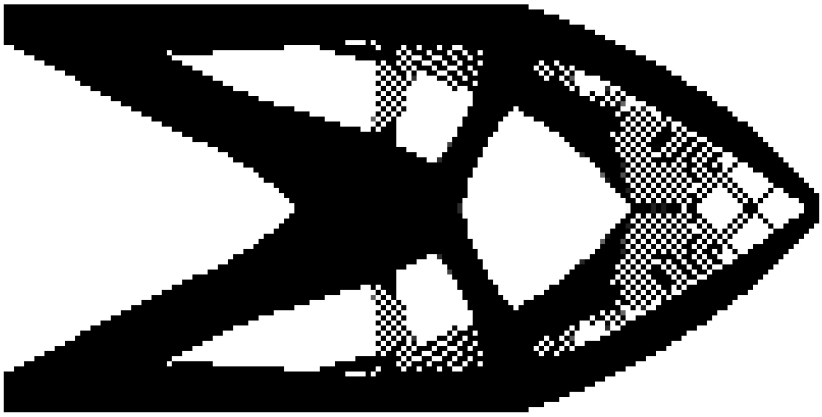

(a) Checkerboard pattern arise in this example without regularization.

(b) A filter radius of 1.5 is applied on the densities, which resolves the problem of checkerboard elements. Note how the border between solid and void regions becomes grayscale due to the regularization.

Figure 2.1: Cantilever problem solved on a 160×80 mesh. In Figure a, no regularization has been applied, and hence checkerboard patterns arise. In Figure b, regularization has been applied, which effectively gets rid of the checkerboard patterns.

2.3 Homogenization-based topology optimization

Before the proposition of SIMP, earlier work considered composite materials to ensure the existence of a solution [Bendsøe and Kikuchi, 1988]. The usage of such composite materials relaxes the design space of black and white designs allowing for a much higher number of possible designs. However, a composite material is an inhomogeneous material. It could, for example, consist of infinitesimally small, periodically tessellated microstructures that alternate between solid and void at a micro-scale. One refers to topology optimization using such composite materials as either homogenization-based topology optimization or shorter the homogenization approach.

The name homogenization approach comes from the following general idea. A composite material has oscillatory properties at a micro-scale due to its periodically tessellated microstructure. Forces acting on a composite material, however, vary at a much larger scale called macro-scale. And on the macro-scale, our composite material acts as a homogeneous material. The method to obtain a smoothly varying material description at the macro-scale based on the alternating micro-scale description is called homogenization. Such a macro-scale material description is called the effective or homogenized stiffness tensor. Once the homogenized material description has been found, we can find a displacement field of a structure consisting of such a material. It can then be shown that one can decompose the displacement field to obtain a dominating term that depends only on the macro-scale description and not on the micro-scale behavior. Note that I will only give a short description of this approach underneath, but for more details, the reader is referred to Bendsøe and Sigmund [2004]. Lastly, it should be mentioned that the topic of homogenizing material properties is related to the term homogenization as used in mathematics when studying partial differential equations with fast-changing coefficients.

It is important to note that a composite material can incorporate multiple length scales. On each microscopic level, the composite material consists of a microstructure, but on the macroscopic level, the effective properties of the composite material vary smoothly. In the following, we assume one micro-scale and that the microstructure is periodic in a neighborhood of a point $\mathbf{x}$ in a given linear elastic structure.

Let δ denote the length of the microstructures' period. We then write the elasticity tensor E^δ as

$$E^\delta = E(\mathbf{x}, \frac{\mathbf{x}}{\delta}).$$

There exist many periodic unit cells of the microstructure at the point $\mathbf{x}$ for $\delta \to 0$, which implies that the properties can be considered periodically dependent on $\mathbf{y}$ and the function

$$\mathbf{y} \to E(\mathbf{x}, \mathbf{y})$$

is called $\mathbf{Y}$-periodic. Here $\mathbf{x}$ denotes the variation of the material parameters on a macroscopic level, and $\mathbf{y}$ describes the periodic variation at the micro-scale.

If a macroscopic force is applied on a structure, the resulting displacement field $\mathbf{u}$ can be expressed as an asymptotic expansion:

$$\mathbf{u}(\mathbf{x}, \mathbf{y}) = \sum_{i=0}^{\infty} \delta^i \mathbf{u_i}(\mathbf{x}, \mathbf{y}). \tag{2.4}$$

Here, the leading term $\mathbf{u_0}(\mathbf{x}, \mathbf{y})$ is a macroscopic displacement field that can be shown to be independent of the micro-scale, i.e., $\mathbf{u_0}(\mathbf{x}, \mathbf{y}) = \mathbf{u_0}(\mathbf{x})$ [Bendsøe and Sigmund, 2004]. The effective properties (or homogenized properties) of the composite material, i.e., the elasticity tensor E^H, can be found by solving so-called cell problems for the microscopic displacement field $\mathbf{u_1}(\mathbf{x}, \mathbf{y})$. It can then be shown that $u_0(\mathbf{x})$ is the resulting macroscopic deformation field that arises under the applied forces when the elastic properties of the structure are assumed to be given by E^H. Note that E^H is normally precomputed for various parameters describing the microstructures (e.g., rotations, layer-thicknesses) [Groen and Sigmund, 2018].

The separation of scales that the homogenization approach uses allows us to solve the topology optimization problem at the macro-scale while using material that incorporates material changes at the micro-scale. Combined with the right microstructure, we can obtain optimal designs from the homogenization-based approach. The following section describes the most important composite materials considered for the topology optimization results used in this thesis.

2.4 Optimal and single-scale microstructures for homogenization-based topology optimization

Homogenization allows the computation of the effective properties of multi-phase composites. The most relevant composite is the two-phase material, where one phase is a solid material, and the other phase is void, as illustrated in Figure 2.2.

Theoretical bounds limit achievable effective properties. The first bounds provided in the context of elasticity were introduced by Reuss [1929] and Voigt

Figure 2.2: Two-phase composite with solid and void phase. This composite is also called rank-1 material.

[1966]. Later Hashin et al. [1963] improved the bounds, i.e., the possible properties that composite materials can attain were restricted further. The reader is referred to Allaire [2002], Cherkaev [2000], Milton [2002], and Bendsøe and Sigmund [2004] for more details on material bounds.

2.4.1 Rank-n materials

A composite structure with a solid-void alternating laminate structure is called rank-1 laminate.

If we replace the void in a rank-1 material with another rank-1 laminate at an infinitely smaller scale, we obtain a rank-2 composite as depicted in Figure 2.3a. We can repeat this replacement N times and subsequently obtain a rank-N microstructure that contains N layers at N different length scales.

These two-phase materials with a finite number of sequential laminates can achieve the theoretical upper bounds for maximum strain energy [Francfort and Murat, 1986; Lurie et al., 1984; Milton, 1986; Norris, 1985]. One can show the lower limit of layers needed to obtain an optimal solution for different types of problems - this was shown for 2D cases by Avellaneda [1987] and for 3D cases by Francfort, Murat, and Tartar [1995].

The optimal number of layers depends not only on the dimension but also on

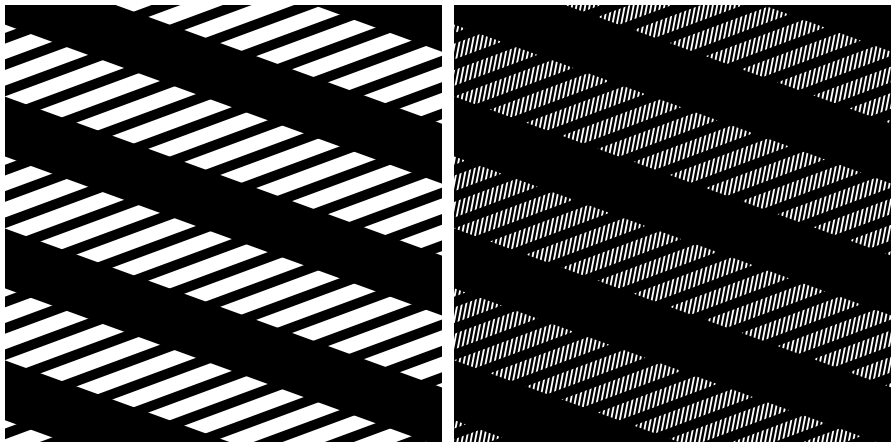

(a) Rank-2 material with two layers at two length scales.

(b) Rank-3 materials with layers at three length scales.

Figure 2.3: Ranked materials with layers at multiple lengths scales.

the number of loading cases:

- For two-dimensional problems with a single strain (2D single-load problems) a rank-2 material with orthogonal layers is optimal. Such a material is depicted in Figure 2.4a.

- Problems with a single strain in three dimensions (3D single-load problems) can be solved optimally by a rank-3 material with orthogonal layers. Such a material is depicted in Figure 2.4b.

- For two-dimensional problems with multiple strains (2D multi-load problems) a rank-3 laminate as depicted in Figure 2.3b is optimal.

- Three-dimensional problems with multiple strains (3D multi-load problems) require rank-6 laminates for optimal results. Recently Wang et al. [2021] showed that rank-4 material can reach up to 92% of the theoretically obtainable stiffness of rank-6 laminates. This is an important finding since de-homogenizing rank-4 materials promises to be more manageable than de-homogenizing rank-6 materials.

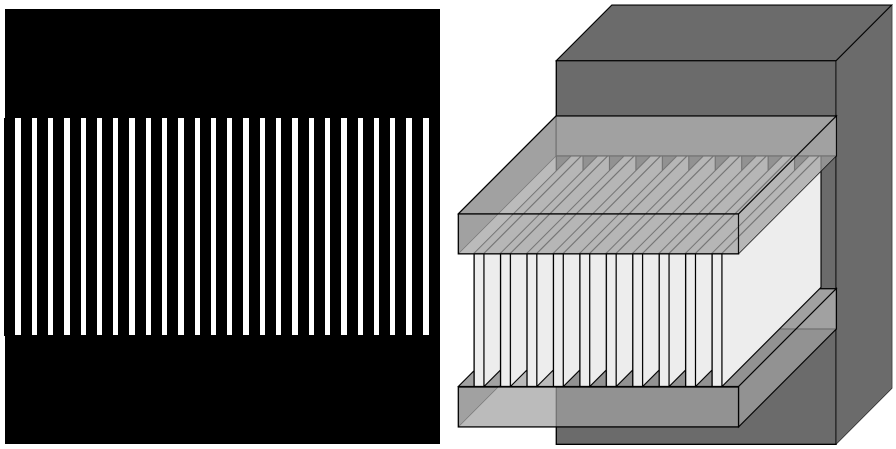

(a) Sketch of a rank-2 material with two orthogonal layers.

(b) Sketch of a rank-3 material with three orthogonal layers in dark grey, light grey and white.

Figure 2.4: Ranked materials with orthogonal layers in two and three dimensions. Note that all layers are at different length scales.

2.4.2 Optimal microstructures

Density-based topology optimization approaches depend on the number of used finite elements. Here, mesh-dependent refers to obtaining a different topology for design solved on more finite elements. Ideally, a higher resolution would result in better modeling and sharper boundaries and not in a completely different structure [Sigmund and Petersson, 1998]. An example of mesh-dependency is shown in Figure 2.5 for a cantilever example. Note how the topology differs between the resolutions, since the results contain more structural members the higher the number of element is.

On the other hand, multi-scale topology optimization does not depend on the resolution of the finite element mesh. This is due to the microstructure holding much more information per point than the solid-void description of density-based topology optimization (e.g., two layer orientations and two layer-thicknesses for a rank-2 material). Therefore, only a coarse finite element mesh is needed to sufficiently represent the proposed structures. This implies a largely reduced computational effort over the usage of mesh-dependent density-based approaches. Figure 2.6 shows the same cantilever problem as used in Figure 2.5 but solved using homogenization and de-homogenized by the approach proposed in Groen and Sigmund [2018]. We see how already for a very coarse mesh the homogenization-based optimization method can capture the topology towards

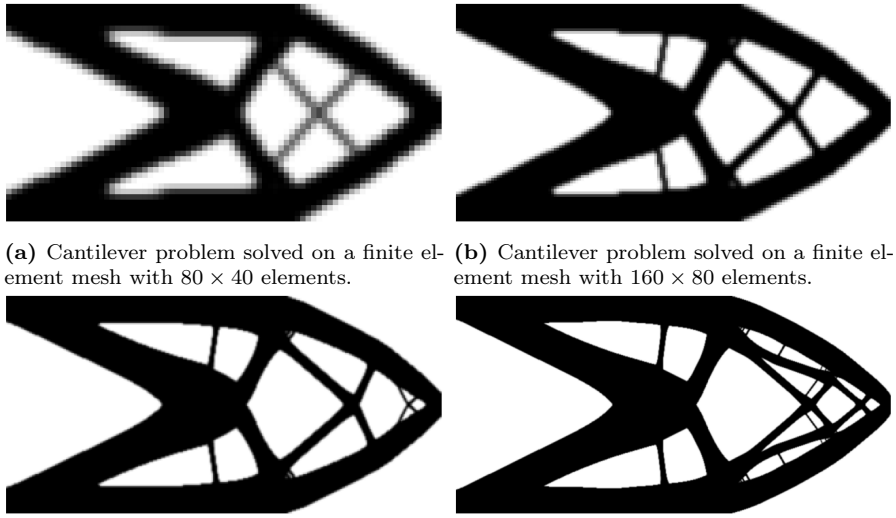

(a) Cantilever problem solved on a finite element mesh with 80×40 elements.

(b) Cantilever problem solved on a finite element mesh with 160×80 elements.

(c) Cantilever problem solved on a finite element mesh with 320×160 elements.

(d) Cantilever problem solved on a finite element mesh with 640×320 elements.

Figure 2.5: Visualization of the mesh dependency of density-based topology optimization. Note how the topology of the structure changes, when the mesh resolution is changed.

which the density-based approach seems to converge.

The first researcher to consider optimal microstructures for homogenization-based topology optimization was Bendsøe [1989] using rank-2 material for a single-load case problem in two dimensions. Allaire and Francfort [1993] and Allaire and Kohn [1993] considered the same optimal rank-2 microstructure.

Allaire, Bonnetier, et al. [1997], Cherkaev and Palais [1996], Díaz and Lipton [1997], Olhoff et al. [1998] use optimal rank-3 microstructures for a single-load 3D problem. Multi-load case problems for solving two-dimensional plane problems are considered in Allaire, Belhachmi, et al. [1996] and Cherkaev, Krog, et al. [1998]. Multi-load case problems for solving two-dimensional plate problems are considered by Díaz, Lipton, and Soto [1995], Hammer et al. [1997], Krog et al. [1997]. Finally, Díaz and Lipton [2000] use optimal rank-6 microstructures for solving problems in 3D with multiple load-cases.

It should be noted that in practice the compliance values obtained by homogenization-based topology optimization using optimal microstructures can not be outperformed by single-scale design approaches like SIMP [Bendsøe and Sigmund, 2004].

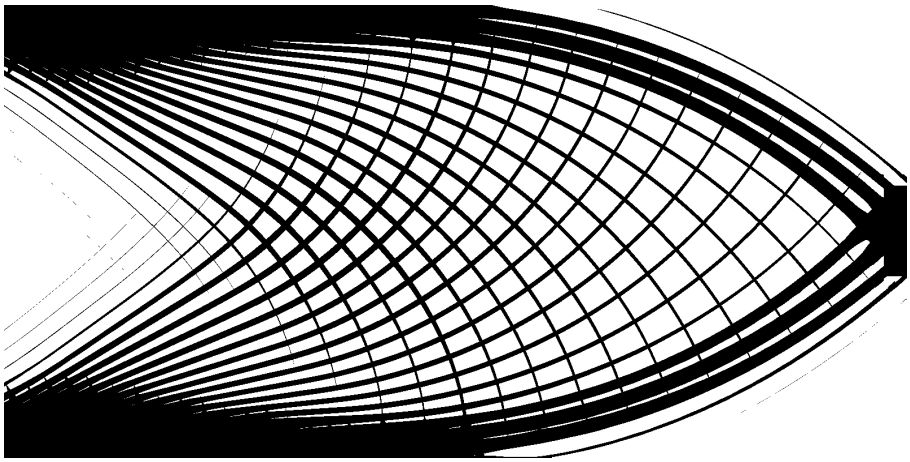

Figure 2.6: The same cantilever problem as in Figure 2.5. This example is solved on a 80×40 elements using homogenization-based topology optimization and de-homogenized using the approach proposed in Groen and Sigmund [2018].

2.4.3 Single-scale microstructure

Single-scale microstructures are microstructures that consist of only one length scale as opposed to, e.g., rank-N materials. Single-scale microstructures are of interest since the fields produced by the homogenization approach using single-scale microstructures are, in general, cleaner for multi-load problems [Träff et al., 2019]. This, in turn, makes the field easier to de-homogenize.

The best known single-scale microstructure is the unit-cell description introduced in Bendsøe and Kikuchi [1988]. They were the first to consider multi-scale topology optimization with a microstructure defined at a single scale. The unit-cell microstructure consists of a square cell with a hole in the center, parameterized by the widths $\tilde{\bar{a}}_1, \tilde{\bar{a}}_2$, and the rotation of the unit cell, as seen in Figure 2.7. Bendsøe et al. [1999] show that the unit-cell microstructure performs closely to the optimal rank-2 microstructure with orthogonal layers for 2D single-load case problems.

Recently single-scale microstructures based on optimal rank-3 laminates for multi-load case problems in 2D were analyzed in Träff et al. [2019]. Träff et al. [2019] note that, in general, simplification of optimal microstructures to single-scale microstructures results in a loss of up to eight percent performance of the compliance minimization.

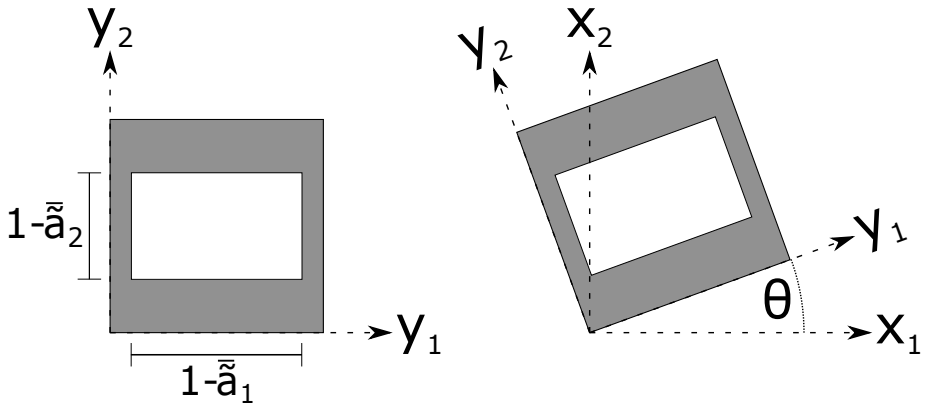

Figure 2.7: The unit-cell microstructure with a rectangular hole parameterized by a_1, a_2 in the local frame (y_1, y_2) on the left and on the right rotated in the global frame (x_1, x_2).

2.5 Homogenization-based topology optimization in the contributions

In this section, I will give an example of how homogenization-based topology optimization was performed for the work discussed in this thesis. This section was originally published in Stutz, Groen, et al. [2020] [Paper-II] and has been adapted for this background chapter. For more details, the reader is referred to Groen and Sigmund [2018], Groen, Stutz, et al. [2020], and Stutz, Groen, et al. [2020].

2.5.1 Microstructure parameterization

In Paper-II we used the square unit-cell with a rectangular hole as shown in Figure 2.7 as a microstructure parameterization for the homogenization approach. The effective properties were obtained using numerical homogenization using the young's modulus $E = 1$ and poisson's ratio $\nu = 0.3$ as described in Groen and Sigmund [2018]. We created a database of the effective properties for various hole-sizes, i.e., for different physical heights $\bar{\tilde{a}}_1$ and widths $\bar{\tilde{a}}_2$. This allows interpolating the effective properties $\boldsymbol{E}^H$ and corresponding sensitivities for arbitrary hole sizes. The elasticity tensor in the global frame of reference $\boldsymbol{E}$ can then be computed as

$$\boldsymbol{E}(\theta, \bar{\tilde{a}}_1, \bar{\tilde{a}}_2) = \boldsymbol{R}(\theta)\boldsymbol{E}^H(\bar{\tilde{a}}_1, \bar{\tilde{a}}_2)\boldsymbol{R}(\theta)^{\mathrm{T}}, \tag{2.5}$$

where $\boldsymbol{R}$ is the two-dimensional rotation matrix. To adhere to the volume limit, we need to compute the density of the microstructure ρ by

$$\rho = 1 - \bar{\bar{a}}_1 \bar{\bar{a}}_2. \tag{2.6}$$

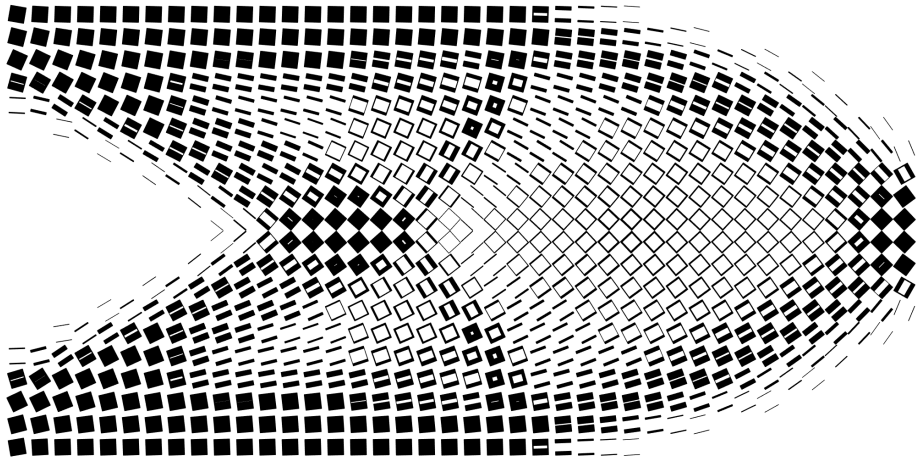

Figure 2.8: This Figure shows the result of a cantilever problem solved using the homogenization approach and a 40×20 finite element mesh. For each element one cell of the local microstructure has been enlarged to 0.8 times the size of a finite element. Layers with less than 1% thickness are not shown. Note that there is no notion of connectivity or spacing of the global structural members that we desire to find in the homogenization results.

2.5.2 Optimization and regularization of the microstructure orientation

In earlier work, the microstructure was updated based on the principal stress direction. In our work, the angles are solely obtained based on their gradients. This change allowed the introduction of a regularization energy to receive a less noisy 4-direction field. The regularization objective is defined as follows. For two adjacent elements f_1 and f_2 connected by edge e we compare the angles of the microstructure θ_{f_1} and θ_{f_2}. The penalization value $\mathcal{P}_e \in [0, 1]$ is calculated by

$$\mathcal{P}_e = \frac{1}{2} - \frac{1}{2}\cos(4\theta_{f_1} - 4\theta_{f_2}). \tag{2.7}$$

Note that P_e is zero for angle differences of $k\pi/2$ with $k \in \mathbb{Z}$. We then take the sum of the penalization values of all n_e edges and obtain the regularization

objective $\mathcal{F}_\theta$,

$$\mathcal{F}_\theta = \sum_{f=1}^{n_e} \mathcal{P}_e. \tag{2.8}$$

The regularization objective is divided by the objectives value for the starting guess of the layer-normals at every iteration.

2.5.3 Problem formulation

For the topology optimization, we minimize an objective function $\mathcal{F}$ combining compliance $\mathcal{J}$ and regularization objective $\mathcal{F}_\theta$. We use bi-linear finite elements and assume that the material properties are constant for every element. To avoid checkerboard patterns, we use a density filter on the design vectors $\boldsymbol{a}_1$ and $\boldsymbol{a}_2$, which results in the filtered hole heights $\tilde{\boldsymbol{a}}_1$ and widths $\tilde{\boldsymbol{a}}_2$ [Bourdin, 2001; Bruns et al., 2001].

We use the interpolation scheme introduced in Groen and Sigmund [2018] to limit the microstructure widths to be either void, completely solid, or in the interval $[\eta, 1-\eta]$ with $\eta = 0.05$. The scheme modifies $\tilde{\boldsymbol{a}}_1$ and $\tilde{\boldsymbol{a}}_2$ into the physical hole height $\bar{\tilde{\boldsymbol{a}}}_1$ and width $\bar{\tilde{\boldsymbol{a}}}_2$.

The optimization problem is solved in so-called nested form. For each iteration, first, the state equation is solved, and afterward, the design vectors are updated. We can write the optimization problem as follows,

$$\begin{aligned}
\min_{\boldsymbol{a}_1,\boldsymbol{a}_2,\boldsymbol{\theta}} &: \mathcal{F}(\boldsymbol{a}_1,\boldsymbol{a}_2,\boldsymbol{\theta},\mathbf{u}) = \\
&\qquad \frac{\mathcal{J}(\boldsymbol{a}_1,\boldsymbol{a}_2,\boldsymbol{\theta},\mathbf{u})}{\mathcal{J}^{(1)}} + \gamma_\theta \frac{\mathcal{F}_\theta(\boldsymbol{\theta})}{\mathcal{F}_\theta^{(1)}}, \\
\text{s.t.} &: \mathbf{K}(\boldsymbol{a}_1,\boldsymbol{a}_2,\boldsymbol{\theta})\mathbf{u} = \mathbf{f}, \\
&: \mathbf{v}^{\mathrm{T}}\boldsymbol{\rho}(\boldsymbol{a}_1,\boldsymbol{a}_2) - V^0 A \leq 0, \\
&: \mathbf{0} \leq \boldsymbol{a}_1, \boldsymbol{a}_2 \leq \mathbf{1}, \\
&: \boldsymbol{-4\pi} \leq \boldsymbol{\theta} \leq \boldsymbol{4\pi},
\end{aligned} \tag{2.9}$$

where A is the area of Ω. Here $\mathbf{v}$ holds the element areas V_e, and V^0 is the maximum allowed material fraction. The compliance of the first analysis step $\mathcal{J}^{(1)}$ is used to normalize the compliance values as done for the regularization objective. We use the MATLAB implementation of the Method of Moving Asymptotes (MMA) [Svanberg, 1987] to update the design vectors.

The starting guess of the hole size for microstructure is $\boldsymbol{a}_1 = \boldsymbol{a}_2$ such that we exactly reach the volume constraint. The initial orientation of the microstruc-

ture can be based on the principal stress directions obtained by a pre-analysis step using isotropic microstructures. However, we also use initial orientations $\boldsymbol{\theta} = \mathbf{0}$, which we call a grid-aligned start guess.

Finally, we use γ_θ to steer the influence of the regularization onto the optimization. Note that this can be a fixed value, but it is also possible to choose a variable amount of regularization and decrease regularization during the optimization.

Note that the result from the above topology optimization consists of local layer orientations and local hole sizes. An example of a design resulting from the homogenization approach is shown in Figure 2.8. The goal of this thesis was to develop de-homogenization approaches to extract a structure from results like in Figure 2.8 as done for Figure 2.6 with the method proposed in Groen and Sigmund [2018].

Chapter 3

Vector fields and singularities (related to Paper-II)

In this chapter, I present an analysis of two-dimensional vector fields and singularities important for de-homogenization. The analysis investigates singularities in the layer-normal fields arising from the homogenization approach and the following sections have been adapted for this thesis from Stutz, Groen, et al. [2020] [Paper-II]. Further, I will relate the singularity locations to the obtained layer-thicknesses and the underlying stress fields. Observations about layer-normal fields and singularities in three dimensions are discussed later in Chapter 5.

In Paper-II, I found that singularities in layer-normal fields are highly related to the underlying stress tensor fields. A major finding was the relationship between the location of singularities and the material distributed by the optimizer. In general, in two dimensions, singularities are either in void or in fully solid regions such that the structure becomes isotropic at singular points.

3.1 Vector fields and direction fields

To study the vector fields generated by the homogenization approach, it is essential to understand vector fields, direction fields, eigenvectors and eigenvalues of the stress tensors. This allows us to precisely define singularities and their indices and use this knowledge to study stress tensor and layer-normal fields.

Vaxman et al. [2016] introduced a notation that is tailored for this purpose. An alternative source of information about vector fields and singularity is the paper by Goes et al. [2015]. In the following section, I will describe relevant definitions from Vaxman et al. [2016] related to the homogenization approach and introduce their notation. We start with the definition of a directional field and N-directional fields.

Definition 3.1 (**Directional field, vector field and direction field**) A **directional field** denotes a function $\mathbf{v}$ that assigns directional information to almost every point in a given domain. If a directional field $\mathbf{v}$ provides a magnitude of importance for every point p, for which $\mathbf{v}$ is defined, then $\mathbf{v}$ is called a **vector field** (see Figure 3.1a). If the directional field does not provide any magnitude (e.g., all assigned vectors are normalized) it is called a **direction field** (see Figure 3.1b).

(a) 1-vector field **(b)** 1-direction field

Figure 3.1: Comparison of a 1-vector and a 1-direction field.

Definition 3.2 (**N-directional field**) A directional field can assign multiple directions to the same point in a domain Ω. Let us assign N vectors to almost every point in Ω. Then the use-cases of $N = 1, 2, 4$ are of importance to the application of the homogenization approach. We write **N-vector** or **N-direction** field to indicate the number of directional information given at every point.

Figure 3.2 shows direction fields and vector fields important to the homogenization approach, where we indicate a given magnitude with arrows. The 1-vector fields are what we usually refer to when talking about vector fields. If $N = 2$ the vector is invariant under a rotation of angle π and we call such a field a 2-vector field. For $N = 4$ follows the 4-vector field with a rotational symmetry of $\pi/2$.

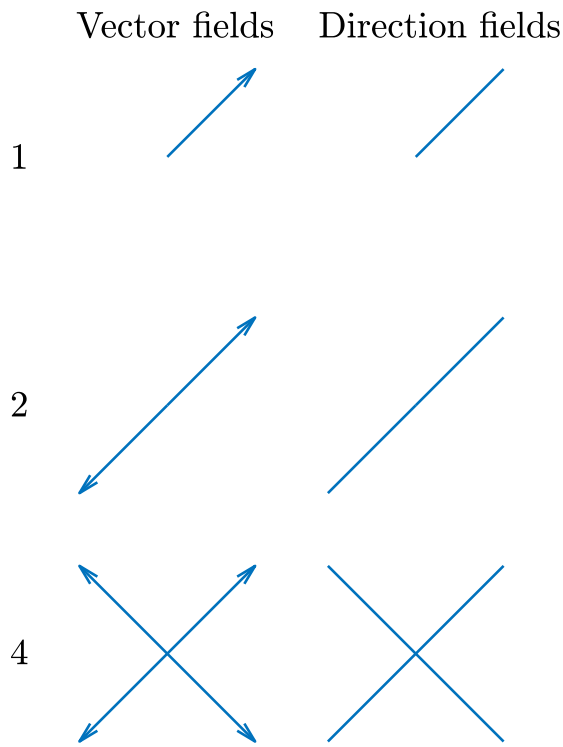

Figure 3.2: Vector and direction fields for $N \in \{1, 2, 4\}$. A given magnitude is indicated by arrows.

3.2 Singularities and their indices

Singularities often arise in the presence of internal loads, multiple loads or a designated passive domain. The following definitions describe singularities and their indices.

Definition 3.3 (**Singular point, singularity**) A point $\mathbf{p}$ in a 1-vector field $\mathbf{v}$ for which $\mathbf{v}$ is not defined or zero is called a **singular point** or **singularity** (see Figure 3.3).

Definition 3.4 (**Index of a singularity**) A singular point $\mathbf{p}$ can be assigned an **index** by the following procedure. We consider the vector field $\mathbf{v}$ on a closed, simple curve $\mathbf{c}(t)$, $t \in [0, 1]$, around $\mathbf{p}$, which does not contain a second

singular point. We obtain $\mathbf{v}$ limited to $\mathbf{c}(\mathbf{t})$, by

$$\mathbf{v}(\mathbf{c}(t)) = \|\mathbf{v}(\mathbf{c}(t))\| \begin{pmatrix} \cos(\alpha(t)) \\ \sin(\alpha(t)) \end{pmatrix}.$$

Here $\mathbf{c} : [0,1] \to \mathbb{R}^2$ denotes the counterclockwise parameterization of the curve and $\alpha : [0,1] \to \mathbb{R}$ the enclosed angle between the x-axis and $\mathbf{v}(\mathbf{c}(t))$. The index of $\mathbf{p}$ is then defined as $\text{idx}_p = \frac{1}{2\pi}(\alpha(1) - \alpha(0))$ measuring the rotation of the vector field around the singular point.

In Figure 3.3 we consider a singularity in $(0,0)$ and depict the curve c with $c(0) = c(1) = (1,0)$ as a red circle. Further, we see that the enclosed angles α, depicted as black circle arcs, grow from $\alpha(0) = 0$ to $\alpha(1) = 2\pi$. Thus we have a singularity (depicted in green) with index $\text{idx}_p = \frac{1}{2\pi}(2\pi - 0) = 1$. Note that singularities exist for all types of N-directional fields, where the index must always be a multiple of $1/N$. To identify the index of a singularity in a N-directional field, one proceeds similar to singularities in 1-directional fields. Following a closed curve around the singular point, one measures the change of the angle of the N-directional field. In a discrete example, as in Figure 3.6d for example, we choose one of the directions and follow that direction along the curve.

3.3 Singularities in smooth tensor fields

The singularities of smooth tensor fields have been studied exhaustively in order to visualize tensor fields. Delmarcelle et al. [1994] show that singularities in tensor fields can only have indices that are multiples of $\pm 1/2$. I try to present a descriptive version in the following theorem.

Theorem 3.5 *A smooth tensor field can only incorporate singularities of index $\pm 1/2$ or multiples thereof.*

Proof (Sketch) If we follow a closed, simple curve around a singularity $\mathbf{p}$, not containing a second singularity, with index $\pm 1/4$ as depicted in Figure 3.4, we see that red and blue vectors trade places. That would not be a problem for a 4-direction field where all four directions are equivalent, but if we have a tensor, we can distinguish the red and blue direction from each other by the magnitude of the eigenvalue. So, say blue is the direction of maximum eigenvalue that we follow, but coming back to the initial point it then must be red. The tensor has changed smoothly along the black curve, so there must have been a point

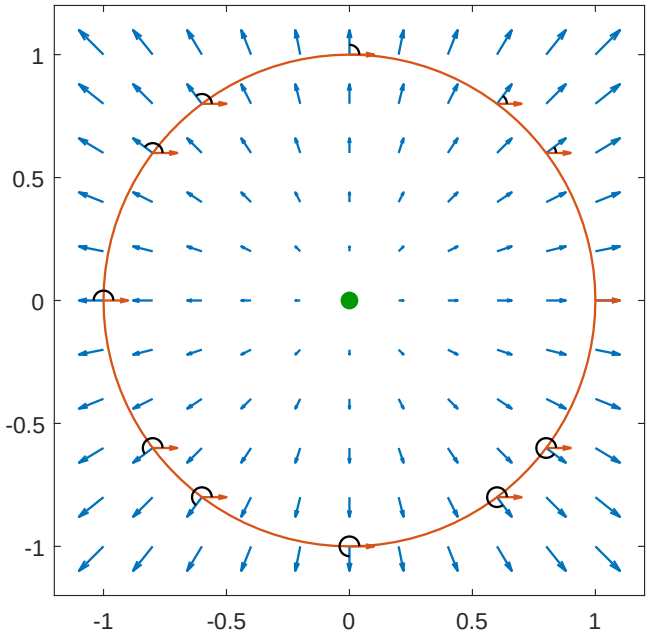

Figure 3.3: Vector field containing a singularity of index 1 (in green), showing the tracked curve (in red) and the angle arcs (in black).

along the black curve at which the eigenvalues were the same. However, if the eigenvalues are the same, any plane vector is an eigenvector, and we have a singular point. This contradicts the way the black curve was chosen and concludes the proof. □

In homogenization-based topology optimization the layer-normals are aligned with the stress tensors either by demanding it through the implementation or in a gradient descent algorithm since layers aligned to the load-path are optimal [Pedersen, 1989]. Therefore, the following singularity types are found regularly in the output fields of the homogenization approach.

An example for a singularity of index $-1/2$ is given in Figure 3.6a where all corners of a triangle are pulled apart (see Figure 3.5a). Figure 3.6b shows a singularity of index -1. This can be seen as two singularities of type $-1/2$ pushed together. This type of singularity occurs in a corner loaded square (see Figure 3.5b). Figure 3.6c shows a singularity of index $1/2$ as occurs for example in a center loaded clamped beam (see Figure 3.5c).

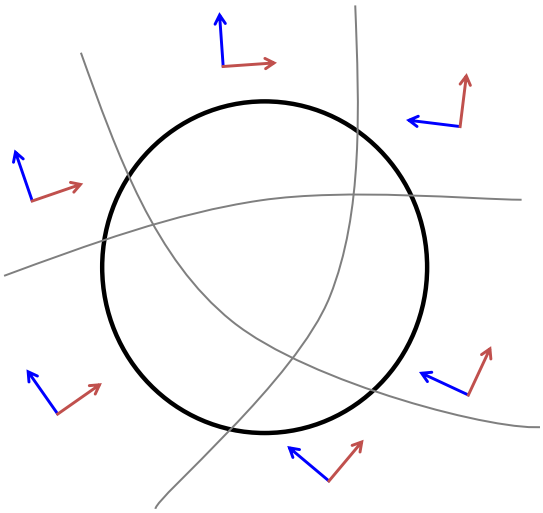

Figure 3.4: Sketch of a singularity with index $1/4$.

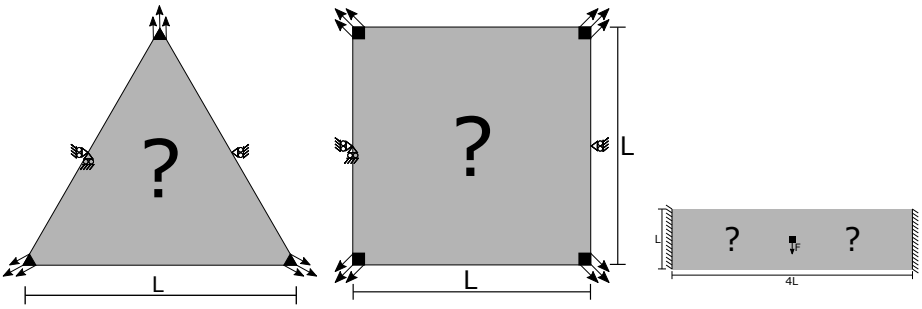

(a) Corner-loaded triangle **(b)** Corner-loaded square **(c)** Center-loaded clamped beam

Figure 3.5: Examples of load cases leading to singularities.

3.4 Singularities in 4-direction fields

It is essential to differentiate between the 4-vector field described by a stress tensor field and the 4-direction field described by the layer-normals output by the homogenization approach. The latter can also incorporate singularities of index $\pm 1/4$ due to numerical errors, regularization of the layer-normals or simply due to the optimizer being stuck in a local minimum.

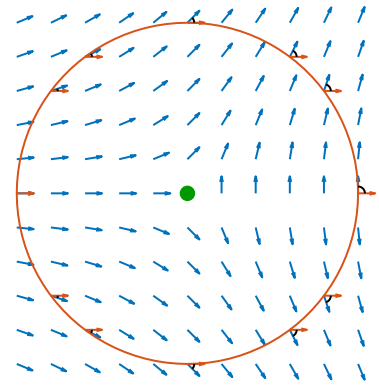

(a) 1-vector field index $-1/2$

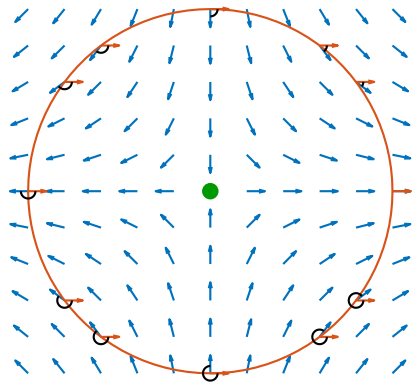

(b) 1-vector field index -1

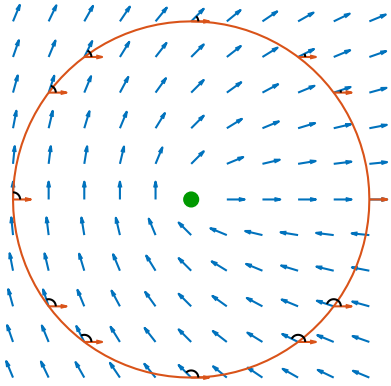

(c) 1-vector field index $1/2$

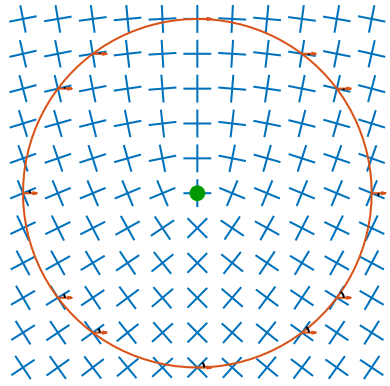

(d) 4-direction field index $1/4$

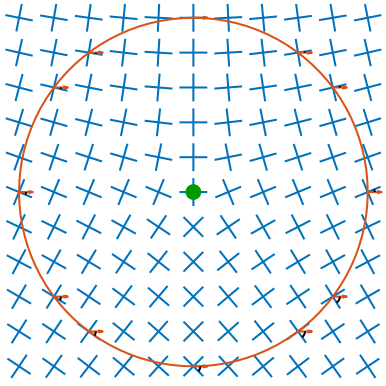

(e) 4-direction field index $-1/4$

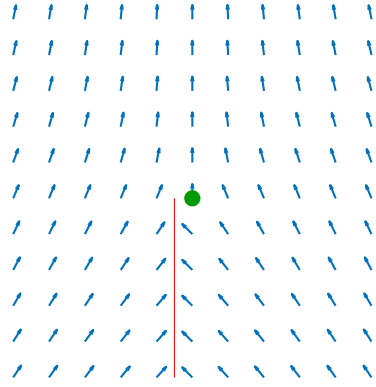

(f) 1-direction field index $-1/4$

Figure 3.6: Vector and direction fields for different singularities.

Figures 3.6d and 3.6e show 4-direction fields incorporating each a singularity of index $\pm 1/4$. It is impossible to separate these 4-direction fields into two 1-direction fields, which is shown in Figure 3.6f. Especially regularization seems to result in singularities of index $\pm 1/4$. Increasing the regularization value γ_θ limits the angular changes. Figures 3.7a - 3.7f depict how a singularity of index $\pm 1/2$ is spatially ripped apart more and more with increasing regularization. In this example the singularity of index $\pm 1/2$ is split into two singularities of index $\pm 1/4$, that are located in the center of the domain at the end of the red lines. The red lines indicate where the direction fields jump by 90 or 180 degrees.

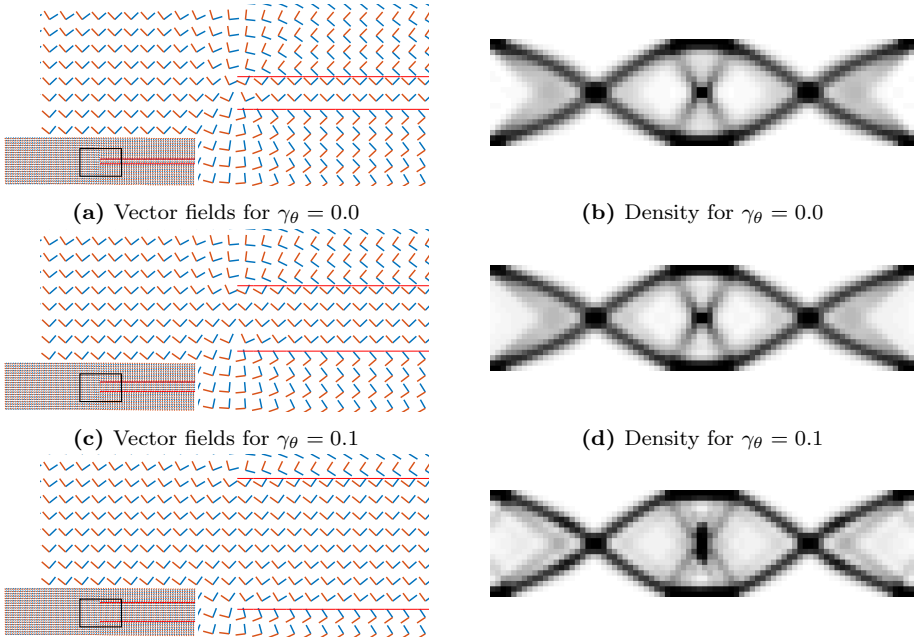

(a) Vector fields for $\gamma_\theta = 0.0$

(b) Density for $\gamma_\theta = 0.0$

(c) Vector fields for $\gamma_\theta = 0.1$

(d) Density for $\gamma_\theta = 0.1$

(e) Vector fields for $\gamma_\theta = 0.5$

(f) Density for $\gamma_\theta = 0.5$

Figure 3.7: Vector fields and densities for different degrees of regularization.

3.5 Relation between the location of singularities and the material distribution in the homogenization results

For de-homogenization, it is of importance to understand where singularities occur in the layer-fields output by the homogenization approach. I am not aware

of a theoretical solution to this, but we observe that, in general, singularities occur in regions with very high or very low density.

Let us assume that in the output of the homogenization approach, the layer-normals are well-aligned with the stress directions everywhere, such that singularities in the stress field correspond to singularities in the layer-normal fields. We investigate a singularity $\mathbf{p}$, where the stress field is non-zero. At such a singular point the stress field rotates with an index $\mathrm{idx}_p \neq 0$. Thus, in the immediate surrounding, we see all directions in the interval $I = [0, 2\pi \mathrm{idx}_p]$. Suppose we measure the angular velocity on several curves around $\mathbf{p}$. In that case, we realize that the shorter the curve, i.e., the closer to $\mathbf{p}$, the higher the angular velocity becomes, as the field always needs to rotate by $2\pi \mathrm{idx}_p$. Or in other words, at $\mathbf{p}$, the stress field turns infinitely fast. The homogenization approach outputs two layer-normals $\boldsymbol{n}^{1,2}$ and widths $w_{1,2}$ and thus a density $\rho = w_1 + w_2 - w_1 w_2$ for the element containing $\mathbf{p}$. Now, if $0 \leq \rho < 1$, only the directions $\boldsymbol{n}^{1,2}$ in I are well-aligned with the unit cell. Thus, for all other directions in I, a shearing force will arise. The optimizer can improve the compliance by making the element containing $\mathbf{p}$ isotropic, which means that we can observe a density peak $\rho \to 1$ in the vicinity of the singularity $\mathbf{p}$. The same effect can be seen in Figure 3.7, where the material is distributed differently since the layer directions differ from the stress direction due to regularization. It is important to note that singularities also may occur in void regions. Following the above thought of using material to create isotropic elements, it is intuitively understandable that the optimizer mostly tries to stay clear of regions with fast turning stress fields and hence creates singularities in elements with $\rho = 0$ as well.

The above observation does not allow a prediction of where singularities occur in the layer-normal fields. However, it does allow to reason, why regions containing singularities can often be entirely filled with material in the post-processing without an excessive amount of additional material needed as we already see a density peak. In general, one needs to be careful regarding the occurrence of singularities as the above observation assumes layer-normal fields that are well-aligned to the principal stress directions.

Chapter 4

Integration based de-homogenization

In this chapter, I will discuss approaches to de-homogenization that make use of integration. First, I visit earlier work done on de-homogenization and related work of other research fields, namely computer graphics. Second, I will discuss an approach to de-homogenization of layer-normal fields that contain singularities and was published in Stutz, Groen, et al. [2020] [Paper-II]. The full paper is provided in Appendix B. Lastly, in this chapter, I will discuss integration-based de-homogenization of three-dimensional problems in a singularity-free context. This work has been published, in parts, in Groen, Stutz, et al. [2020] [Paper-I]. The full paper is provided in Appendix A. Before we visit the related work in Section 4.1, I would like to give a short overview of the work I did on de-homogenization in Paper-I and Paper-II.

In Paper-I, we found that microstructure orientations in three dimensions can be noisy due to non-uniqueness of the optimal solution introducing singularities that are not mechanically necessary. We investigated the influence of starting orientations and regularization on the fields and were able to produce far less noisy fields. In combination with a newly developed combing strategy, we were able to de-homogenize the fields and create well-performing mechanical structures. The combing procedure has later been altered and used in Paper-II as well.

In Paper-II, we found that the starting orientations of the microstructure orientation can influence the resulting structure without a loss in performance.

We also found that starting orientations and regularization influence the location and presence of singularities. Further, in Paper-II, we used a method from computer graphics [Kälberer et al., 2007] to de-homogenize topology optimization results containing singularities. We obtained well-performing mechanical structures without restriction on the location where singularities needed to lie.

4.1 De-homogenization for smooth, continuous and singularity-free 4-direction fields (related to Paper-II)

In this section, we look at de-homogenization by discussing related work and an example in Figure 4.1. This section has originally been published in Paper-II; the full paper can be found in Appendix B.

Pantz et al. [2008] were first to propose a method to project the unit square microstructure macroscopically using an integration-based method. Their de-homogenization approach minimizes an alignment energy to find a parameterization aligned with the orientations of the microstructure. The approach assumes two separate vector fields, whose orientation is not of importance. Later, Groen and Sigmund [2018] simplified the approach by Pantz and Trabelsi, still using two separate vector fields, however, with the challenge of having consistently aligned vector fields as the approach is not invariant to angle jumps of angle π. This was solved by using a connected component analysis on the vector fields. Both approaches do not explicitly deal with angle jumps of angle $\pi/2$.

Earlier work [Allaire, Geoffroy-Donders, et al., 2018; Groen and Sigmund, 2018; Pantz et al., 2008] de-homogenize the square unit-cell with a rectangular hole using two periodic layers superimposed onto each other. We follow the same approach in Paper-II. Provided that vector fields are separable (i.e., no singularities of index $\pm 1/4$) we can use the procedure as presented in Groen, Wu, et al. [2019] for de-homogenization. I want to use the rest of this section to present that approach to de-homogenization. Note that Figure 4.1 shows the main steps of this method for a standard cantilever example.

From a 4-direction field (Figure 4.1a) two 1-direction fields are extracted (Figure 4.1b). Based on the two smooth 1-direction fields $\boldsymbol{n}^i, i \in \{1, 2\}$ one creates two mapping functions ϕ_1 and ϕ_2 that preserve the orientation of the microstructures. It should be noted that the map does not need to be strictly conformal. The values of ϕ_i are allowed to be inaccurate when there is no material in the layer (i.e., $w_i < 0.01$) or when the domain is completely solid (i.e., $\rho > 0.95$).

Hence, the problem only needs to be solved accurately in the intermediate material part of the domain of the i-th layer $\tilde{\Omega}_i$. This leads to the following spatially weighted partial differential equations (PDE),

$$\begin{aligned} \alpha_1^i(\boldsymbol{x})\nabla\phi_i(\boldsymbol{x}) &= \alpha_1^i(\boldsymbol{x})\boldsymbol{n}^i(\boldsymbol{x}), \quad \boldsymbol{x}\in\Omega \\ \text{s.t.} \qquad \alpha_2^i(\boldsymbol{x})\nabla\phi_i(\boldsymbol{x})\cdot\boldsymbol{t}^i(\boldsymbol{x}) &= 0, \quad \boldsymbol{x}\in\Omega \end{aligned} \tag{4.1}$$

where $\boldsymbol{t}^i$ denotes the orthogonal vector to $\boldsymbol{n}^i$. The domain is separated into three parts, which dictate the weights on the objective α_1^i and the weights on the constraints α_2^i,

$$\begin{aligned} \alpha_1^i(\boldsymbol{x}) &= \begin{cases} 0.01 & \text{if} \quad w_i(\boldsymbol{x}) < 0.01, \\ 0.1 & \text{if} \quad \rho(\boldsymbol{x}) > 0.95, \\ 1 & \text{if} \quad \boldsymbol{x}\in\tilde{\Omega}_i. \end{cases} \\ \alpha_2^i(\boldsymbol{x}) &= \begin{cases} 0 & \text{if} \quad w_i(\boldsymbol{x}) < 0.01, \\ 0 & \text{if} \quad \rho(\boldsymbol{x}) > 0.95, \\ 1 & \text{if} \quad \boldsymbol{x}\in\tilde{\Omega}_i. \end{cases} \end{aligned} \tag{4.2}$$

Numerically, we solve the above-mentioned problem as a linear system using the finite element approach, where the constraint is enforced in an augmented setting using penalty parameter γ_ϕ, called the alignment weight. Figure 4.1c shows one of the two parameterization ϕ_i for the cantilever example. Contour lines have been added for a better understanding. Figure 4.1d shows the cosine of the parameterization indicating all isocontours and the periodic structure.

With both parameterizations known we can create an implicit geometry description $\tilde{\rho}_i$ for each of the layers:

$$\tilde{\rho}_i(\boldsymbol{x}) = H\left(\left(\frac{1}{2} + \frac{1}{2}\mathcal{S}\left\{P_i\phi_i(\boldsymbol{x})\right\}\right) - \tilde{w}_i(\boldsymbol{x}) \right). \tag{4.3}$$

Here H is the Heaviside function and $\mathcal{S}\in[-1,1]$ corresponds to a triangle wave. Furthermore, P_i is a periodicity scaling. Hence, the design can be de-homogenized by an implicit geometry function $\tilde{\rho}$ as,

$$\tilde{\rho}(\boldsymbol{x}) = \min\left\{1, \sum_{i=1}^{2}\tilde{\rho}_i(\boldsymbol{x})\right\}. \tag{4.4}$$

Finally, we can impose an average layer spacing ε, which can be interpreted as the unit-cell size. To do so, we define the periodicity scaling parameter P_i based on the average lattice spacing in the domain of interest $\tilde{\Omega}_i$,

$$P_i = \frac{2\pi}{\varepsilon}\frac{\int_{\tilde{\Omega}_i}\mathrm{d}\tilde{\Omega}_i}{\int_{\tilde{\Omega}_i}||\nabla\phi_i(\boldsymbol{x})||\mathrm{d}\tilde{\Omega}_i}, \tag{4.5}$$

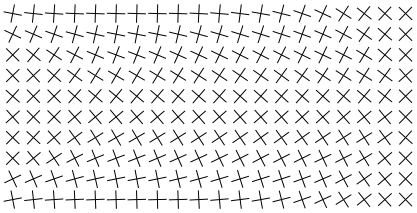

(a) 4-direction field

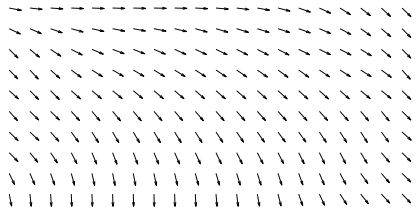

(b) 1-direction field

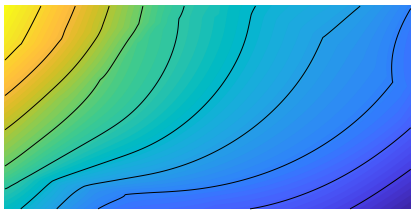

(c) parameterization with some isocurves

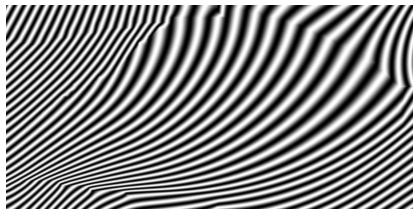

(d) Cosine wave

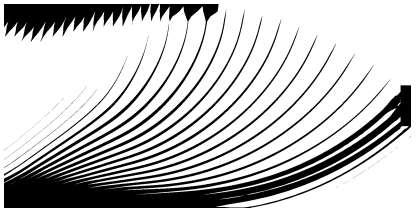

(e) Projection using ω

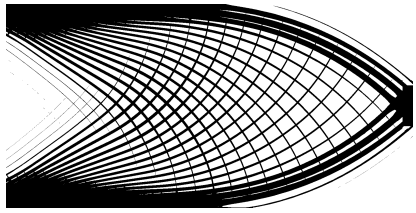

(f) Combining two layer projections

Figure 4.1: Projection pipeline for standard cantilever beam – from a 4-direction field to de-homogenized mechanical structure.

where the average layer spacing ε allows to steer the average spacing between the structural members. Figure 4.1e shows $\tilde{\rho}_i$ and ultimately $\tilde{\rho}$ is depicted in Figure 4.1f.

4.2 Singularity aware de-homogenization in two dimensions (related to Paper-II)

With the knowledge accrued about singularities in the last chapter, we are able to study examples that contain singularities. In this section, I shortly talk about earlier work on singularity containing examples. I then present how we propagate consistent labeling of the direction fields in the case of singularities (see Section 4.2.1) and show the connection to quad-meshing (see Section 4.2.2).

Pantz et al. [2010] investigated the challenge of singularities in fields arising from the homogenization approach for the first time. The singularities with indices $1/2$ are all located in void regions and are nucleated, i.e., the areas containing singularities are excluded from the parameterization step and onward. Geoffrey-Donders [2018] proposed a method of spotting singularities of index $\pm 1/2$ using a technique explained in more detail in Hotz et al. [2010]. This only allows for jumps of angle π. In order to deal with the singularities, correction functions are computed to prevent mismatches at seams.

For the following sections it is important to know about related work from computer graphics. The landmark contribution of Kälberer et al. [2007] proposed the "Quad-Cover" algorithm for field-guided quad meshing using multiple coverings. Multiple coverings in the sense that the parameterization domain is duplicated multiple times. This means, that the rotationally symmetric field simplifies to a vector field on every single covering and thus becomes integrable. In practice only a single parameterization domain is used and operators to account for the different coverings are introduced. Bommes et al. [2009] proposed a refinement of Quad-Cover, solving the resulting system in an iterative approach yielding an improvement of the obtained parameterizations.

4.2.1 De-homogenization in the presence of singularities

In the presence of singularities the above described methods for de-homogenization can fail for several reasons. Depending on the index of the singularity different issues can arise:

- If only a singularity of index -1 is contained in the 4-direction layer-normal field, the separation into two integrable 1-direction fields is still possible (see Figure 3.6b). As locally neighboring vectors need to be pointing in the same direction the extraction of vector-fields does not arise trivially. This extraction is called combing. In practice, a breadth-first search has shown to be challenged by this task as depicted in Figure 4.2b because the singular point is hit. For topology optimization fields more robust results can be reached by expanding the search through intermediate densities first, before expanding into void and solid. This algorithm has been proposed in 3D in Paper-I and a 2D version is explained in Section 4.2.1.1 and depicted in Figure 4.3. The result for the corner loaded square can be seen in 4.2c.

- In the case of a singularity of index $\pm 1/2$ the 4-direction field can still be combed, such that two separate 1-direction fields arise (see Figure 3.6a,

3.6c). However, the combing of these 1-direction fields cannot be done consistently anymore. Any combing strategy will inevitably create mismatches, i.e., some neighboring elements will contain vectors that are rotated by π (see further Section 4.2.1.2). A promising approach to extract a high-resolution structure for such fields has been proposed in Geoffrey-Donders [2018].

- In case of a singularity with index $\pm 1/4$ the whole procedure gets even more challenging. Recall that following a curve c around a singularity of index $1/4$ in a 4-direction field means that we return to the start of our curve misaligned by $\pi/2$ (see Figure 3.6d-3.6f). Therefore, we cannot find two 1-direction fields to which we can assign the directions of our 4-direction field. Instead, one needs to cut open the field in such a way, that one can integrate the 1-direction fields using multiple coverings as introduced in Kälberer et al. [2007]. I will discuss this topic in Section 4.2.2.

4.2.1.1 Combing the 4-direction field

As a first step, we have to comb our 4-direction field. This means we want to choose two orthogonal 1-directions for every element. In quad meshing, this is normally done with a breadth-first search as shown in Kälberer et al. [2007]. As the homogenization approach results are noisy and unreliable in elements with very low or very high density, it makes sense to prioritize combing in medium-density regions. In Figure 4.3 we see such a density-based approach, where the chosen directions are given as black arrows and seam edges are depicted in bright red. We color the elements according to the time where they are visited by the combing algorithm. For readability, we bundle 50 elements to one step and color them with the same color. Unlike in Paper-I we only use the direction of a single neighboring element to compute the direction to be fixed in element f. This allows for a much faster algorithm and is possible due to the angular information being more robust in 2D. The density priority is obtained by $\rho_{priority} = |\rho_{start} - \rho_f|$, where normally $\rho_{start} = 0.5$ is chosen. We therefore comb the field first in areas with a density close to 0.5 and then spread out into the remaining domain. The numerical implementation of the combing only selects one direction per element. The second direction is implicitly given as the rotation of the extracted 1-direction field by $\pi/2$.

4.2.1.2 Finding the seams

For every 4-direction field containing a singularity with index $1/4$ or $1/2$, we receive a combed 1-direction field that has jumps of angle $\pi/2$ and/or π. Such

fields are not integrable and to be able to parameterize our domain, we need to cut open our mesh as proposed in Kälberer et al. [2007].

Definition 4.1 (**Seams, mismatch, seam edge**) Two directions whose enclosed angle exceeds $\pi/4$ are said to **mismatch** by $\pi/2$. Accordingly, two directions whose enclosed angle exceeds $3\pi/4$ are said to mismatch by π. An edge e is called **seam edge** if the directions in the two adjacent elements f_1, f_2 mismatch. A **seam** is any series of connected seam edges.

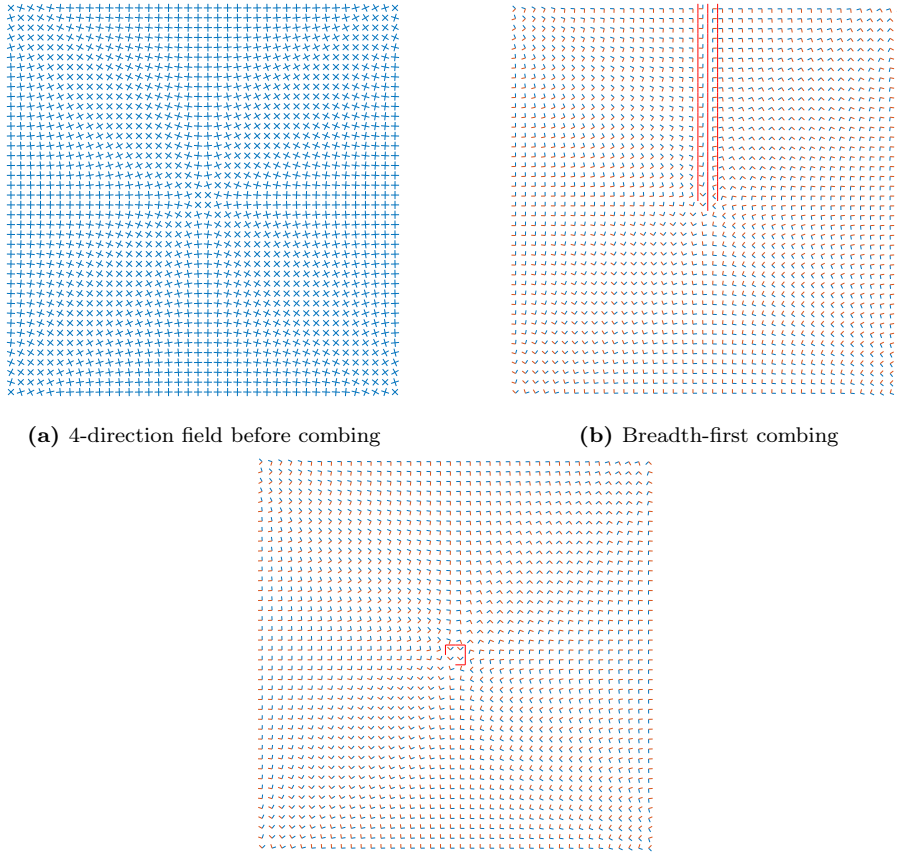

(a) 4-direction field before combing

(b) Breadth-first combing

(c) Density-based combing

Figure 4.2: Example of two different combing strategies for a given 4-direction field resulting in different seams. The breadth-first combing only uses information about the neighborhood of elements, whereas the density-based combing uses density values to prioritize the combing of elements.

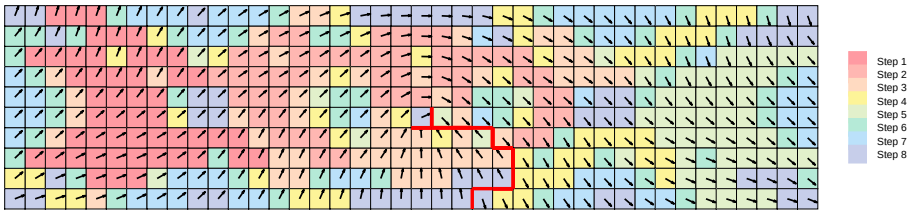

Figure 4.3: Extraction of a 1-direction field using a density-based combing strategy. The combing is started at a root element and follows intermediate densities first. The colors show steps of 50 elements at a time, whose 1-direction has been fixed. The colors show steps of 50 elements at a time, whose 1-direction has been fixed.

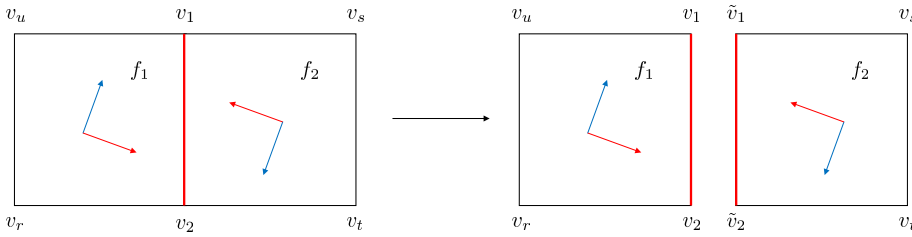

Figure 4.4: Sketch of cutting a grid open between two neighboring elements at a seam edge.

4.2.2 Constrained mixed integer solver

In Quad-meshing, multiple coverings and a method to address seams were introduced in Kälberer et al. [2007]. An expansion introducing an iterative scheme to solving for the parameterization is given in Bommes et al. [2009]. We want to exploit the underlying mechanisms to create a topology on which we can integrate the combed fields, combining them with the integration scheme introduced in Groen and Sigmund [2018]. Therefore, we give a short simplified introduction to Kälberer et al. [2007] and Bommes et al. [2009] in Sections 4.2.2.1-4.2.2.3.

4.2.2.1 Cutting the mesh open

As a first step, one cuts open the mesh along the seams created in Section 4.2.1.2. Let $e = (v_1, v_2)$ be a seam edge, connecting the vertices v_1 and v_2 as in Figure 4.4. The edge e separates the two elements f_1 and f_2. Auxiliary vertices $\tilde{v}_1$ and $\tilde{v}_2$ are introduced and the connectivity of f_2 is changed from $[v_1, v_2, v_t, v_s]$ to $[\tilde{v}_1, \tilde{v}_2, v_t, v_s]$.

4.2.2.2 Gluing the mesh together

If one would solve the resulting linear system in Equation 4.1 on this cut open mesh, disconnected structural members would arise at the seam locations, since the integer isolines on the left and the right side of the seam would not meet up. Therefore, one needs to make sure that the parameterizations ϕ_1 and ϕ_2 in vertex v differ by integers i, j from the parameterizations in $\tilde{v}$. This ensures connected bars and also the same spacing between bars on both sides of the seam. In case of a singularity of $1/4$ the parameterization ϕ_1 can corresponds to the parameterization ϕ_2 on the other side. These rotations Rot^e_{90} are given implicitly by the combed field. Kälberer et al. [2007] formulate the rotational and integer condition with the following equations

$$\begin{aligned}(\phi_1(\tilde{v_1}), \phi_2(\tilde{v_1})) &= \mathrm{Rot}^e_{90}((\phi_1(v_1), \phi_2(v_1))) + (i, j),\\ (\phi_1(\tilde{v_2}), \phi_2(\tilde{v_2})) &= \mathrm{Rot}^e_{90}((\phi_1(v_2), \phi_2(v_2))) + (i, j),\end{aligned} \tag{4.6}$$

where $i, j \in \mathbb{Z}$ enforces that the integer isolines meet up. The operator Rot^e_{90} accounts for the mismatch of the rotations on both sides of the seam. It can be seen as a multiplication with the imaginary number i in the complex plane, where we regard the parameterizations $(\phi_1(v_1), \phi_2(v_1))$ as a complex number. Maybe most intuitively is the rotation with angle π. When we look at Figure 4.4 and think of the vectors as gradients of the parameterizations ϕ_1 and ϕ_2, we see, that if the value of a parameterizations ϕ increases on one element, then it must be decreasing on the other element. Thus the signs of the parameterizations need to change, which corresponds to a multiplication with i^2. For rotations of angle $\pi/2$ or $3\pi/2$ the two parameterizations ϕ_1 and ϕ_2 need to switch position, since the "blue" field becomes the "red" field. This corresponds to a multiplication with i or i^3 in the complex plane. If we define the angle as the rotation in counterclockwise direction, we get:

$$\mathrm{Rot}^e_{90}((\phi_1(v_1), \phi_2(v_1))) = i^{l(e)}(\phi_1(v_1), \phi_2(v_1)),$$

where $l(e) \in \{1, 2, 3\}$ is given by the mismatch of the angles at edge e.

Further details about the operator Rot^e_{90} and this procedure can be found in Bommes et al. [2009] and Kälberer et al. [2007]. We make use of the constraint mixed integer solver provided in Bommes et al. [2012] to solve for the parameterizations.

4.2.2.3 Solving for the parameterization

Once the system is assembled, it is solved in the continuous case, i.e., no integer restrictions are applied at first. This yields an approximation to the desired solution solving the problem up to disconnected bars at the seams. The mismatch

variables (i, j) can now be seen as slack variables $j \in J$, where J is the set of all slack variables. For every iteration the slack variable closest to an integer

$$k = \arg\min_{j \in J} \mid j - \text{round}(j) \mid,$$

is enforced to round(k) and the new system is solved. In an iterative fashion, this procedure is continued until no more slack variables are left.

4.2.3 Parameter choice for homogenization and de-homogenization

The homogenization and the de-homogenization are both influenced by some key parameters. The pipeline discussed above allows us to study different examples of start orientations for the layer-normals and regularization values (see Section 4.2.3.1). Further we also outline the important de-homogenization parameters (see Section 4.2.3.2).

4.2.3.1 Influence of the start point choice and the regularization of the homogenization approach

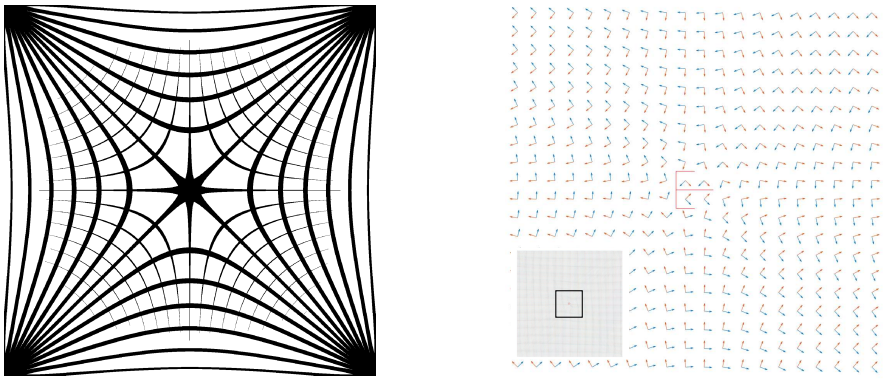

(a) Structure

(b) Enlargement of the centre of the combed vector fields

Figure 4.5: Example of a corner loaded square using principal stresses as a start guess for the layer-orientation, no regularization applied.

It is known for the corner loaded square (see Figures 3.5b, 4.5 - 4.8) that there does not exist a unique optimal solution. The shown examples were all achieved

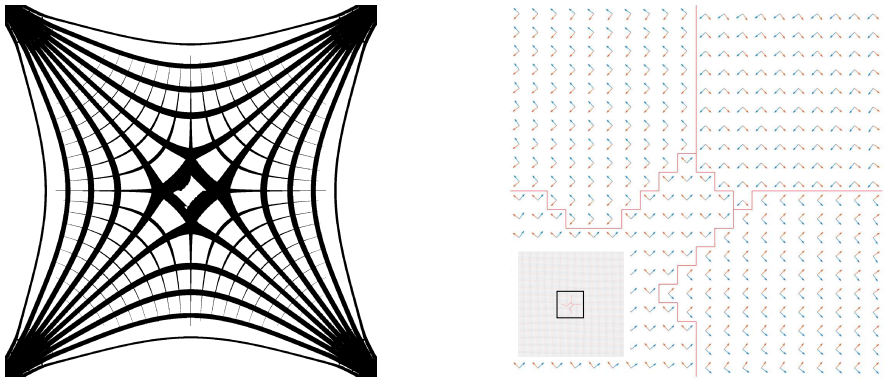

(a) Structure

(b) Enlargement of the centre of the combed vector fields

Figure 4.6: Example of a corner loaded square using principal stresses as a start guess for the layer-orientation, regularization $\gamma_\theta = \frac{1}{5}$ applied.

using a resolution of 120 x 120 elements for the topology optimization as well as for the parameterization step. To visualize the resulting structures, we choose for the de-homogenization an average layer spacing $\varepsilon = 5h_f$, where $h_f = 15$ is the number of fine scale elements used, and an alignment weight $\gamma_\phi = 50$. For the examples in Figures 4.6 and 4.8 the value $\gamma_\theta = \frac{1}{5}$ is applied. In this example we see that the start guess dictates the resulting structure. If the start point for the homogenization approach consists of a grid-aligned 4-direction field we receive the structures depicted in Figures 4.7 and 4.8 that are fairly grid-aligned. However, if we solve one finite element step, assuming that in all elements we have a density $\rho = 1$, we receive a stress tensor field, whose eigenvectors can be used as a start guess for the homogenization approach, as shown in [Paper-I]. The results differ from the grid-aligned start guess and are shown in Figures 4.5 and 4.6. Note that even if we impose regularization, the start guess still dictates the outcoming structure as shown in the Figures 4.6 and 4.8. With the principal stress directions as starting guess we receive spatially ripped apart singularities, when imposing regularization. With the uniform grid as starting guess we stay completely clear of getting a singularity in the center of the domain. Instead we receive singularites of index $-1/4$ near the corners for the example shown in Figure 4.7 and no singularities at all for the example shown in Figure 4.8. Note that despite the large geometric variations in these solutions, compliance values C_h for obtained homogenization results are extremely close demonstrating the non-uniqueness of this problem.

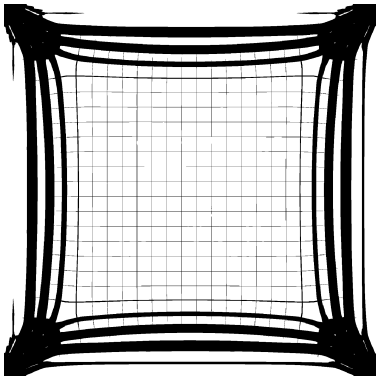

(a) Structure

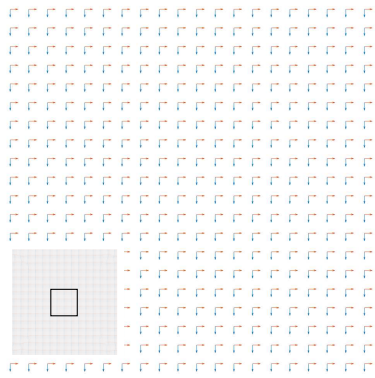

(b) Enlargement of the centre of the combed vector fields

Figure 4.7: Example of a corner loaded square using grid-aligned directions as a start guess for the layer-orientation, no regularization applied.

4.2.3.2 Alignment weight γ_ϕ and structural member thickness ε

There are two main parameter choices influencing the result during the de-homogenization: The alignment weight γ_ϕ and the average layer spacing ε. We refer to Groen and Sigmund [2018] for the choice of the layer spacing ε. For comparison reasons, we use in this subsection an $\varepsilon = {}^{10}/_{L}$, where L is the resolution in vertical direction. Further, topology optimization and de-homogenization are done on the same resolution. If no singularity is present, then the alignment weight γ_ϕ should be chosen in a range of 100-1000 as shown in Groen, Wu, et al. [2019]. It holds, that the lower the maximal absolute divergence of a vector field, the bigger ε can be chosen, as it simply enforces a very strict alignment to the second vector field. However, in case of a singular point, the field spins with a certain index around that point. If we now enforce a big alignment weight on a low-resolution (80 x 20 elements) example we receive stretched isocontours as shown in Figure 4.9a. The gradient of the parameterization becomes almost zero in a large region. The constraint of Equation 4.1 is implemented as a penalization term multiplied with the alignment weight γ_ϕ. Note that this term can be minimized by the gradient becoming zero due to the usage of the dot product. However, this leads to an increase in the first term of Equation 4.1 and an unwanted stretching of the isocontours. For a low-resolution example, the space of bi-linear basis-functions is limited and thus the parameterization is limited in adapting to the rotation around a singularity. This leads to smearing out of the rotational influence from the singularity to neighboring elements. If the element size is large, this influences a higher relative area of the optimization

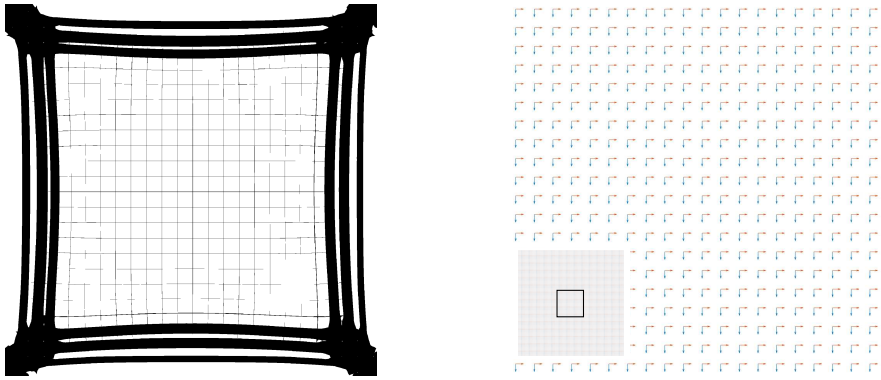

(a) Structure

(b) Enlargement of the centre of the combed vector fields

Figure 4.8: Example of a corner loaded square using grid-aligned directions as a start guess for the layer-orientation, regularization $\gamma_\theta = \frac{1}{5}$ applied.

domain. Thus if the alignment weight is chosen very high the gradient becomes zero in these elements due to the first term of Equation 4.1 being suboptimal already. This often results in a violation of the volume constraint as can be extracted from Table 4.1. In order to allow for a better comparison we provide the value $V_s C_s$, which should however not be considered as a sole objective, since the compliance does not depend linearly on the volume. By using a higher resolution (160 x 40, 320 x 80, 640 x 160) (see Figures 4.9b, 4.9c and Table 4.1) most of this problem is resolved. We can see that a trade off in the alignment weight is still desirable for these high-resolutions. On the one hand, a low alignment weight can lead to non-load bearing bars, as isocurves might lead into an area with zero layer width due to bad alignment. On the other hand, a too large alignment weight can lead to an overvaluing of the constraint and thus to stretched isocontours. For the examples in Table 4.1, we observe that the optimal alignment weight can depend on the resolution γ_ϕ between 50 and 5000 dependent on the de-homogenization grid.

4.2.3.3 Island removal via connected component

To get rid of elements that are neither connected to the boundary condition nor to the load, we do a simple connected component analysis, where we only retain the largest component. This immediately leads to the desired removal of islands. However this still leaves some unloaded bars, these can be removed by a couple of FE analysis and removal of unloaded elements as proposed in Groen

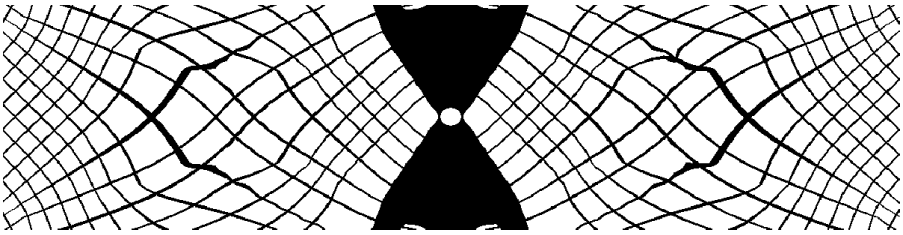

(a) Isocontours with resolution 80×20 and alignment weight $\gamma_\phi = 500$

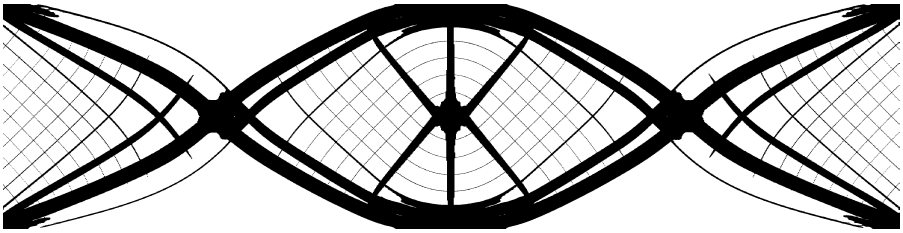

(b) Structure with resolution 320×80 and alignment weight $\gamma_\phi = 5000$

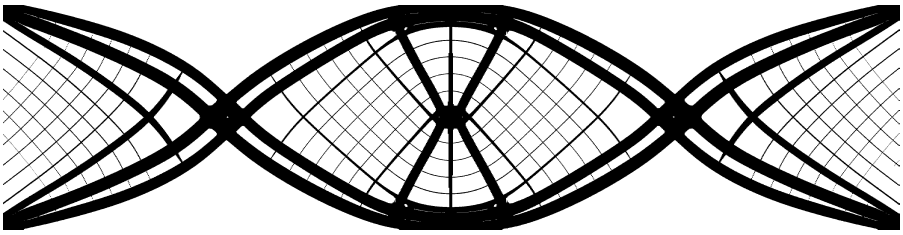

(c) Structure with resolution 640×160 and alignment weight $\gamma_\phi = 5000$

Figure 4.9: Examples of center loaded clamped beam for different resolutions and alignment weights.

and Sigmund [2018].

4.2.4 Conclusion of Paper-II and future work

In Paper-II, we identified the singularities occurring most often in 4-direction fields arising from homogenization-based topology optimization. Further, we investigated the location and reasons for singularities to occur. We also showed the influence of the start guesses of layer-orientations on the outcome of the optimization. The proposed parameterization approach using an approach very similar to Quad-Cover allows parameterizing fields containing singularities of

Table 4.1: Performance for different alignment weights γ_ϕ and resolutions res. We use the following abbreviations: C_h = compliance of homogenization approach, V_s, C_s = volume and compliance of de-homogenized structure, t_h, t_s, t = time for homogenization-based topology optimization, the de-homogenization and the overall time in seconds. Since the compliance does not depend linearly on the volume $V_s C_s$ should not be considered as the sole objective.

res	γ_ϕ	C_h	V_s	C_s	$V_s C_s$	t_h	t_s	t
80 x 20	0	21.89	0.298	61.79	18.42	44.8	5.4	50.2
	50	21.89	0.316	32.60	10.30	44.8	6.2	51.0
	500	21.89	0.349	24.26	8.45	44.8	5.2	50.0
	5000	21.89	0.351	24.50	8.60	44.8	4.0	48.7
160 x 40	0	21.82	0.295	337.74	99.52	135.4	11.2	146.6
	50	21.82	0.334	24.69	8.25	135.4	10.2	145.6
	500	21.82	0.343	22.76	7.81	135.4	10.2	145.7
	5000	21.82	0.338	23.46	7.93	135.4	10.8	146.2
320 x 80	0	21.84	0.297	71.95	21.39	402.9	34.3	437.2
	50	21.84	0.313	22.52	7.05	402.9	30.8	433.8
	500	21.84	0.300	24.89	7.48	402.9	30.7	433.7
	5000	21.84	0.285	26.75	7.63	402.9	30.8	433.7
640 x 160	0	22.02	0.298	73.51	21.90	1824.5	112.8	1937.3
	50	22.02	0.293	25.57	7.48	1824.5	109.9	1934.3
	500	22.02	0.288	25.91	7.46	1824.5	147.1	1971.6
	5000	22.02	0.313	22.07	6.91	1824.5	111.5	1936.0

index $\pm 1/4$. The proposed parametrization approach also allows us to cut out areas completely filled with void or solid material from the parametrization step. These contributions increase the number of designs for which the de-homogenization method can generate high-resolution near-optimal structures at a low computational cost.

We also identified several areas for future research. Most importantly we think that adapting the parameterization to a layer-based mesh would be desirable. With the proposed method one can exclude elements that have a very low density for example, but we think it would beneficial to be able to exclude only one of the two layers when computing the parameterization. Finally, we also identified the expansion of the presented approach to 3D as future research. However, as I will get back to in Chapter 5 we decided to go down a completely different route using no integration to de-homogenize three-dimensional singularity-containing examples.

4.3 De-homogenization of singularity-free structures in three dimensions (related to Paper-I)

In this section, I will discuss the work I did on the de-homogenization of singularity-free layer-normal fields in three dimensions. This work has been published as a part of Groen, Stutz, et al. [2020] [Paper-I]; the paper can be found in Appendix A. Here, I want to shortly discuss the overall contributions of the paper and then go a bit more into detail on the challenges arising in three dimensions compared to two-dimensional problems. I will then explain how we tried to tackle these challenges with a combing algorithm that takes into account either the layer-thickness or the densities obtained from the homogenization-based topology optimization.

4.3.1 Introduction and discussion of paper

Groen, Stutz, et al. [2020] [Paper-I] is an expansion of previous work proposed in Groen and Sigmund [2018] to three dimensions. We use rank-3 microstructures with orthogonal layers, which are optimal for the considered single-loading case problems. As with the work in two dimensions [Groen and Sigmund, 2018; Stutz, Groen, et al., 2020], the proposed method consists of a homogenization-based topology optimization step and a subsequent de-homogenization step that uses integration to find a parameterization and ultimately extracts a mechanical structure.

Going from two to three dimensions introduces a difficult challenge of non-uniquely orientated but still optimally orientated layer-normals. This means that the layer-normals obtained from the homogenization approach may look incredibly noisy but indeed be orientated optimally. This problem arises due to planar structures like sheets or walls being able to carry loads in many directions. I will refer to this problem as the wall problem and describe it in more detail in Section 4.3.2.

One of my contributions to Paper-I is a combing strategy that considers the underlying layer-thicknesses to circumvent the arising wall problem. Further, I investigated the fields arising from three-dimensional homogenization-based topology optimization. I discovered the influence of the wall problem on de-homogenization and looked into the occurrence of it. Further, I investigated the effect of different start guesses on the microstructure orientation. I concluded that orientations based on the stress tensors obtained from an initial

finite element step yield the best layer-normal fields for our de-homogenization pipeline. Further, such an initial step also yielded the best performing layer-normal fields in terms of compliance (see Paper-I) and was able to improve the solving time. Note, however, that this does not necessarily mean that grid-aligned start guesses cannot yield well-performing results as shown in Section 4.2.3.1 for the two-dimensional square problem.

In Paper-I, we de-homogenized the multi-scale designs received from the homogenization-based topology optimization on a fine mesh containing more than 200 million voxels. However, in this section, I will also show that one can easily use marching cubes [Lorensen et al., 1987] to obtain a smoother surface. In the paper, we show that the de-homogenized fine-scale structures achieve outstanding compliance values and reduce the computational cost by order of three magnitudes compared to density-based topology optimization. Therefore, our approach is applicable to efficiently obtain ultra-high-resolution large-scale designs without a high-performance computing system allowing topology optimization to become more valuable to engineers in everyday life.

Of course, we also identified challenges for future research in the paper. Mainly the expansion of de-homogenization to examples containing singularities, which we addressed for 2D in Paper-II and 3D in Paper-III. Further, we identified more robustness for the de-homogenization as desirable. To do so, an understanding of where and why singularities arise in layer-normal fields must be established. The last big research area identified is the expansion of de-homogenization to multi-loading problems with rank-3 structures in two dimensions and rank-6 structures in three dimensions. All of these problems lead to the development of a new approach presented in Chapter 5 where I investigate singularities in 3D and propose a method that works without all layers needing to be well-defined everywhere (i.e., circumventing the wall problem). There is an increase in robustness since one does not depend on a single combing sweep anymore. Further, the approach in Chapter 5 is usable for multi-load structures and can treat singularities explicitly.

4.3.2 A new challenge in three dimensions: the wall problem

Going from the two-dimensional problems discussed in Section 4.2 to three dimensions yields a problem with the layer-normal fields. In two dimensions, the topology optimization results can produce three cases for an element:

1. Both layer-thicknesses w_1 and w_2 are zero. The element lies in the void.

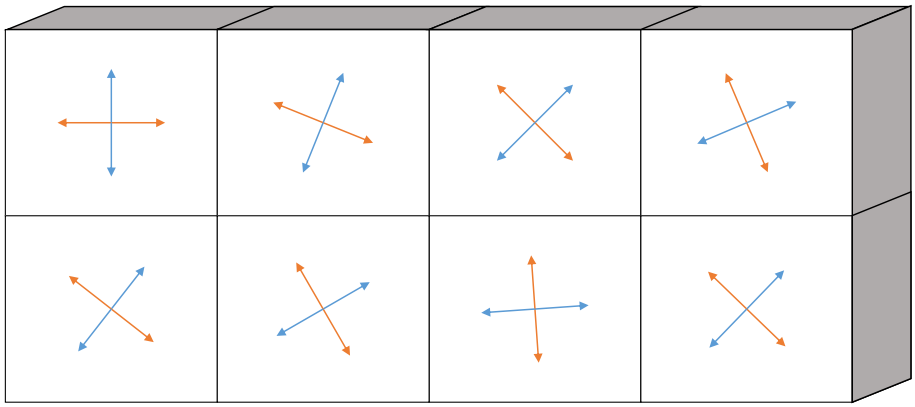

Figure 4.10: Visualization of the wall problem. The normal of the wall is constant. However, the two other layer-normals (in red and blue) can be orientated randomly since a wall can bear loading in any in-plane direction.

2. One or both layer-thicknesses are above 95%. The element is interpreted as fully solid.

3. One of the layer-thicknesses is zero, e.g., w_1, the other layer-thickness, e.g., w_2, is between 1% and 95%.

In case 1, the optimizer does not know how to align the microstructure since there is no material. We can not extract meaningful microstructure orientations. In case 2, the microstructure orientation can be very noisy. Due to the high amount of materials, the microstructure becomes isotropic, and all layer-normal orientations are optimal. Therefore the optimizer cannot differ between smooth fields and noise. Regularization could help to smooth the fields. However, this is not necessary since in case one and case two, de-homogenization is very easy. An element whose layer-thicknesses are zero can be omitted from de-homogenization, and we can completely fill an element with material when one of the layer-thicknesses is above 95%.

The important case in two dimensions is case 3. In this case, one of the layers is non-zero and not fully solid. This layer will be well-aligned to the load path by the optimizer. The fields obtained from the topology optimization are smooth in case 3 since the load paths do not randomly change in a not fully solid structure, i.e., singularities should not occur outside of solid and void in two dimensions, see Section 3.5. The well-aligned layer-normal will now lead to the corresponding field to be continuous. Note that the second field will also be continuous as the second layer-normal is orthogonal to the first layer-normal.

Going to three dimensions, we receive the following possible cases for the layer-thicknesses.

1. All three layer-thicknesses w_1, w_2 and w_3 are zero. The element lies in the void.

2. One, two or all layer-thicknesses are above 95%. The element is fully solid.

3. Two layer-thicknesses are between 1% and 95% (e.g., w_2 and w_3) and one layer-thickness (e.g., w_1) is zero.

4. Two of the layer-thicknesses are zero (e.g., w_2 and w_3) and the third layer-thickness (e.g., w_1) is between 1% and 95%.

Here, cases 1 and 2 follow the same logic as above in the two-dimensional case. In case 3, we have a similar situation as in case 3 of the two-dimensional problem. Since two layers are well-aligned with the load path, the third, orthogonal layer-normal will also be continuous. Note here that elasticity has no randomness, which implies a very low noise level in intermediate-density regions.

However, case number 4 is problematic and needs special attention. The orientation of the microstructure becomes non-unique in this case since two layer-thicknesses are zero. This is what I call the wall problem and is depicted in Figure 4.10. Let us assume the layer with intermediate density has a constant normal field; we receive a wall. A wall can bear loading in any direction orthogonal to the wall's surface normal. When doing homogenization-based topology optimization, the microstructure is, in general, aligning with the principal stresses. However, the optimizer cannot differentiate between all in-plane orientations for the wall problem if only gradients are used to determine the microstructure orientations. We, therefore, receive fields from the topology optimization that seem noisy but indeed are optimally aligned. For example, in Figure 4.10, the red and blue layer-normal can be orientated entirely independently of the stress tensors while not affecting the mechanical performance of the structure.

However, these random orientations due to the wall problem are highly problematic for de-homogenization since they influence the combing of the fields and subsequently the parameterization. The two-dimensional approach proposed in Groen and Sigmund [2018] relaxes integration for the parameterization in solid and void regions and for layers with zero layer-thickness. Further, heavy regularization is used on these layer-normals. Those two steps circumvent the integration problem partially for singularity-free problems. Another approach

would be to re-mesh the finite elements used for integration. However, one challenge is that the cut from zero layer width to non-zero layer width is not a hard cut. In fact, we can see that a layer jumps back and forth from existence to non-existence. Another challenge is, as we found out, that these regions where a layer changes from solid to void can influence a mere breadth-first combing negatively due to noise. Noisy orientations that influence the combing are called spurious singularities.

4.3.3 Examples used in Paper-I

In this section, I will introduce the examples that we worked with for Paper-I. We will revisit these examples in Chapter 5. Note that Figure 4.11 shows sketches of the boundary conditions of all examples.

The most common and best understood example is the Michell cantilever. Figure 4.12 shows a de-homogenized cantilever design. As shown in Figure 4.11 the load is distributed over an area of size $L/6 \times L/6$ and not just applied at a single node. Here L corresponds to the shortest edge length of the design domain. Further, the elements containing the load area are set to be filled with material. We do the same for the first $L/24$ elements from the load area inwards. These

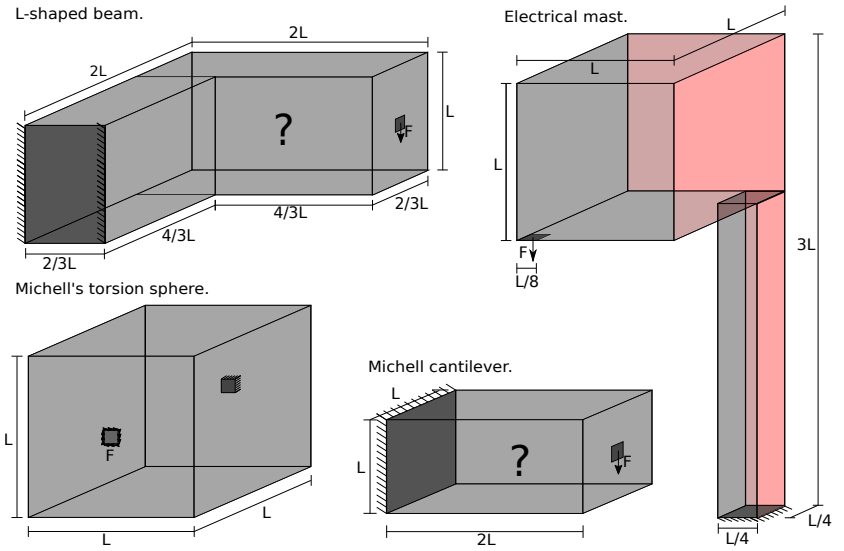

Figure 4.11: Dimensions and boundary conditions for the four examples used in Paper-I.

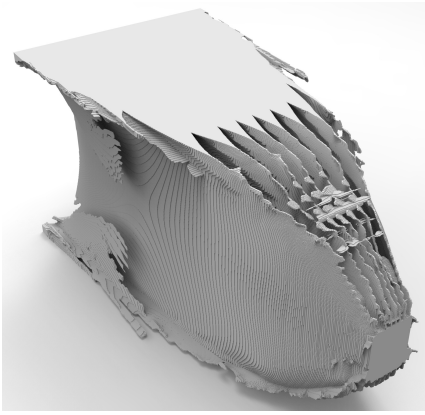

(a) De-homogenized design using our approach.

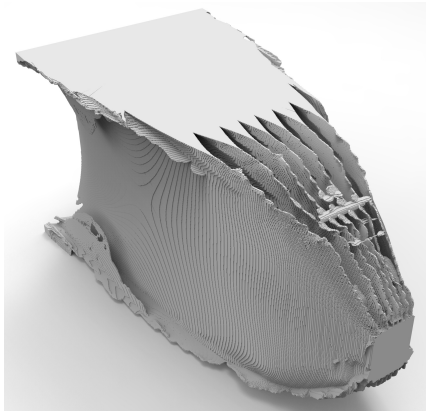

(b) De-homogenized design after excess material has been removed in post-processing.

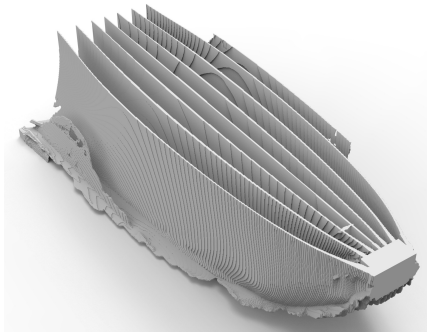

(c) Cut open cantilever after post-processing.

Figure 4.12: A Michell cantilever optimized on $96 \times 48 \times 48$ elements and de-homogenized on a fine mesh of $960 \times 480 \times 480$ voxels.

fully solid elements are added similarly for all other examples as well.

The next example is called the electrical mast and has been proposed in Geoffroy-Donders et al. [2020]. Here, we only model a fourth of the domain with some symmetry conditions depicted in red in Figure 4.11. De-homogenized structures can be seen in Figure 4.13. Figure 4.14 also shows the electrical mast example, once obtained using de-homogenization and once obtained using density-based topology optimization. Note that there will arise a singularity at the center of the electrical mast (in the complete domain) for most results from the homogenization approach. This would correspond to a singularity at the edge of the domain space where the two symmetry planes meet in our modeling. A hori-

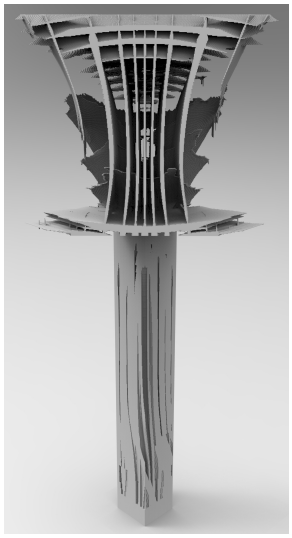

(a) De-homogenized structure obtained from the homogenization approach using $24 \times 24 \times 72$ finite elements.

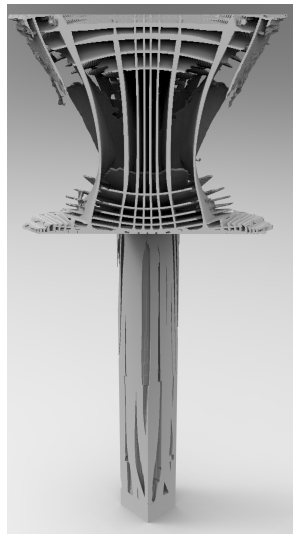

(b) De-homogenized structure obtained from the homogenization approach using $48 \times 48 \times 144$ finite elements. Here the structure is shown before post-processing.

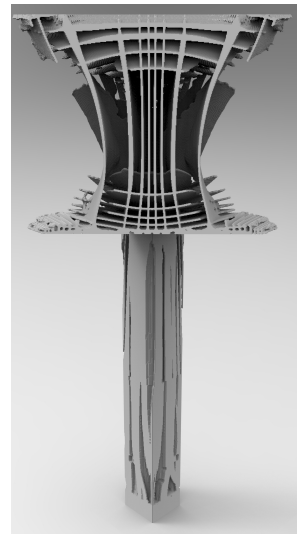

(c) The same structure as in Figure b but here post-processing has been applied to removed voxels which did not contribute to the stiffness of the stucture significantly.

Figure 4.13: Electrical mast examples cut open to reveal the interior. A voxel mesh of $1152 \times 384 \times 384$ is used to depict the examples.

zontal cut through the problem will often show a singularity with index -1 at this location and will have strong similarities with the two-dimensional problem depicted in Figure 4.5. Note that strong regularization can split up that singularity and move it into the modeled quarter of the domain for certain start guesses for the microstructure orientations.

The third example is called the Michell torsion sphere and shown in Figure 4.15. The load is applied as a line load around a square with dimensions $L/12 \times L/12$. Figuratively speaking, it has similarities to a towel being wrung out, where one end is held still while the other end is turned. This also led to the name torsion sphere. In this example, solid elements are used at both boundary conditions to obtain symmetry. Note that the holes seen in the outermost shell in Figure 4.15 are due to the structure reaching the boundary of the design domain. With integrative methods, there is no straightforward way to control that the integer levels of the parameterization, which produces the structure, do not reach the domain's boundary. More control over the structure can be achieved by the approach I will discuss a bit later in Chapter 5.

The last example is called L-shaped beam. Passive elements are used to create the design shown in Figure 4.11. The distributed load is applied to a square patch of solid materials of size $L/6 \times L/6$. The L-shaped beam example, as depicted in Figure 4.16, shows some torsion bending coupling, where the cylindrical part connects to the cantilever-like structural part closer to the load.

For all examples, a maximal volume limit of 10% has been set for the optimizer. For more details, please refer to Paper-I. Note that the above results are computed using a heavy-side function to decide if a voxel should be filled or not with material. Of course, we can also easily employ the marching cubes algorithm [Lorensen et al., 1987] to obtain a smoother visualization, as depicted in Figure 4.17. However, the structure received from the marching cubes algorithm needs to be converted to a tetrahedral mesh to do post-processing. This, in turn, allows though to do additional shape optimization steps to possibly increase the performance of the de-homogenized design.

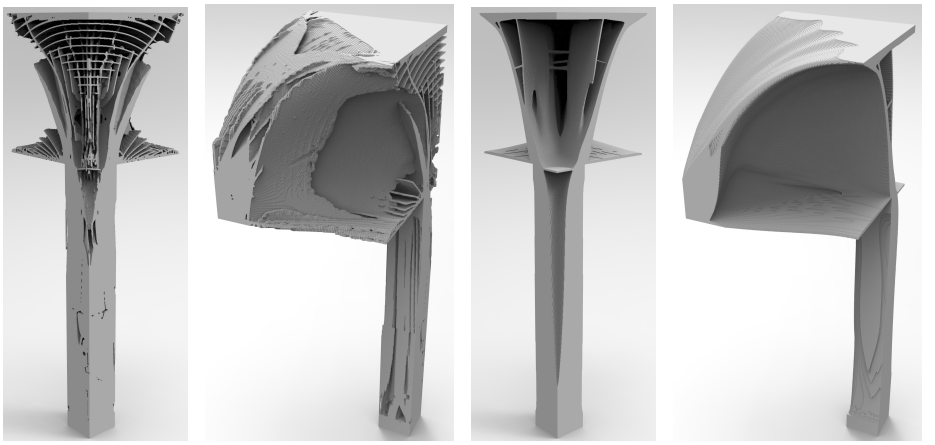

(a) View from the back onto the de-homogenized and post-processed electrical mast from Figure 4.13c.

(b) Side view of the structure shown in Figure a

(c) Back view onto an electrical mast obtained from density-based topology optimization.

(d) Side view onto the electrical mast shown in Figure c.

Figure 4.14: In Figures a and b we see a de-homogenized design of the electrical mast after post-processing as also depicted in Figure 4.13c. In Figures c and d we see a reference design obtained from density-based topology optimization.

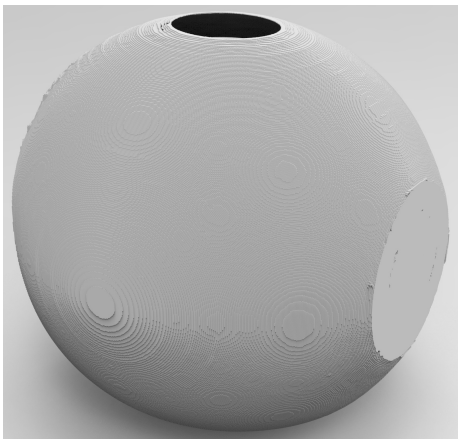

(a) Full view.

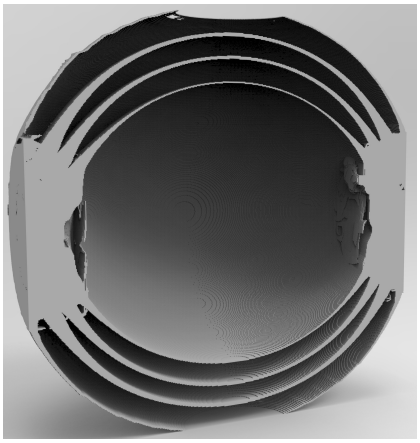

(b) Sectional view on the level of the loads to reveal the boundary conditions and the shell structure.

Figure 4.15: Michell's torsion sphere optimized on $48 \times 48 \times 48$ elements and de-homogenized on a fine mesh of $576 \times 576 \times 576$ voxels.

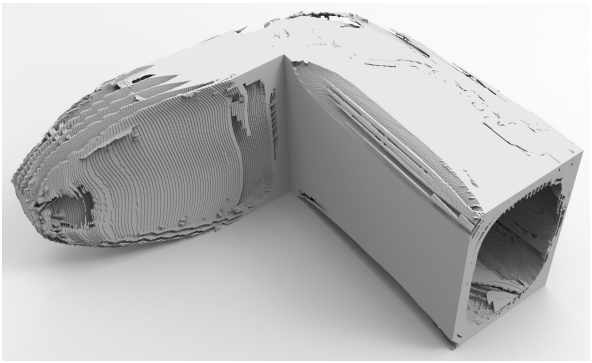

(a) Angled view of the L-shaped beam.

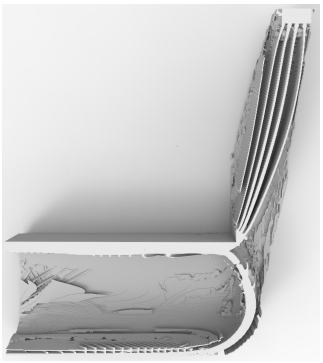

(b) Sectional view on the level of load. Note the clearly visible elements that were set to solid near the load.

Figure 4.16: The L-shaped beam example optimized on $96 \times 96 \times 48$ finite elements and de-homogenized on a fine mesh of $768 \times 768 \times 384$ voxels.

4.3.4 Initialization of the microstructure orientation

To obtain better layer-normal fields for de-homogenization, I compared different orientations used to initialize the microstructure. I found that using an initial fi-

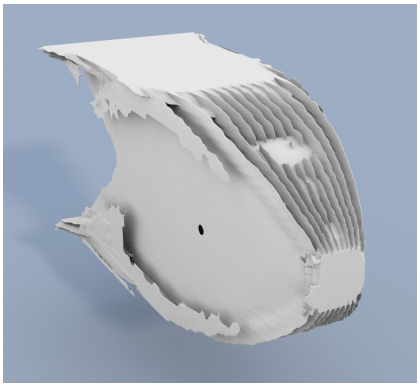

(a) Cantilever example with surface exctracted using the marching cubes algorithm.

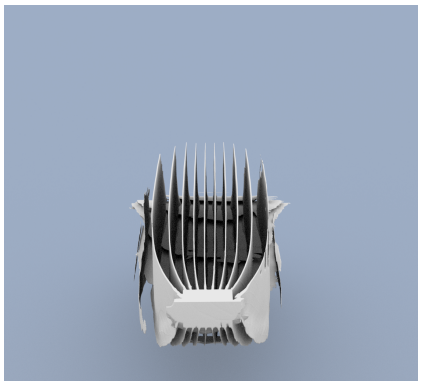

(b) Sectional view on the level of load. Note the clearly visible elements that were set to solid near the load.

Figure 4.17: Using marching cubes on the results from the de-homogenization yields smoother surfaces. However, compared to using a voxel-based mesh, post-processing the above structure would need a conversion to a tetrahedral-mesh first.

nite element analysis to determine the principal stress-directions and using them as a start guess for our optimization yielded the best results. In Figure 4.18, we see a comparison of different start guesses used for initializing the microstructures' orientation. Note that the start guess can influence the obtained solution, i.e., the resulting solution to the homogenization-based topology optimization problem depends on the start guess. This finding has already been discussed a bit earlier in Section 4.2.3.1. The fields in Figure 4.18 show the layer-normal of the diagonal elements, where the load is on the left side, and the edge bordering the other three-quarters of the electrical mast is on the right side. In the diagonal cross-sections through the fields in Figure 4.18, we see how a stress tensor-based starting orientation of the microstructures (Figure 4.18c) yields smoother fields compared to random (Figure 4.18a) or grid-aligned starting orientations (Figure 4.18b). We found in the paper that using starting guesses based on stress tensors also led to better compliance values than grid-aligned starting guesses. In Figure 4.18d, we see that when we increase the lower cut-off of the density values, we start to cut out elements with noisier orientations. This finding motivated the investigation of new, density-based combing strategies.

4.3.5 Influence of regularization

To obtain less noisy layer-normal fields, some regularization during the topology optimization can be helpful. Here it is though important to note that regular-

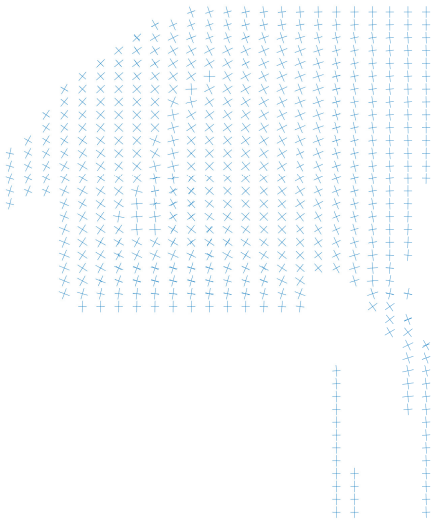

(a) Random vectors as starting orientations. Fully solid (>95% density) and void (<1% density) elements have been removed.

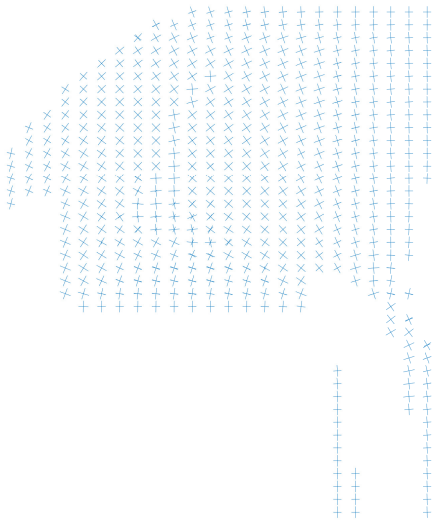

(b) Grid-aligned vectors as starting orientations. Fully solid (>95% density) and void (<1% density) elements have been removed.

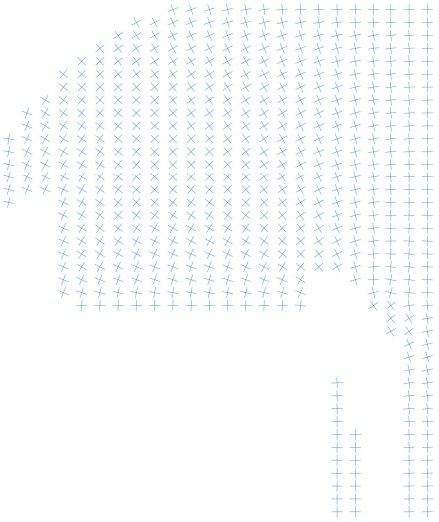

(c) Stress tensor-aligned vectors as starting orientations. Fully solid (>95% density) and void (<1% density) elements have been removed.

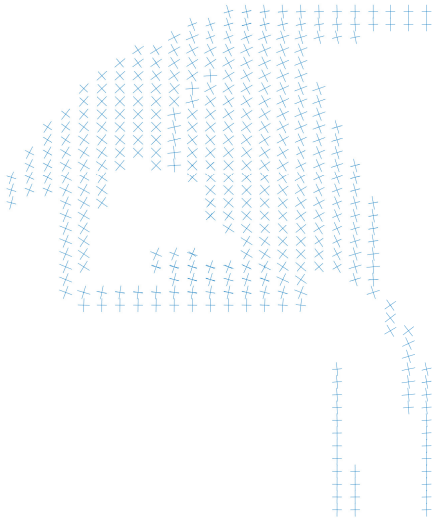

(d) Grid-aligned vectors as starting orientations. Additionaly to the removed fully solid (>95% density) and void (<1% density) elements, low-density elements (1-8% density) have been removed.

Figure 4.18: Diagonal cuts through different electrical mast fields obtained through different initial microstructure orientations depicting the wall problem. No regularization has been used. Note that the whole frames are printed, but since the de-homogenized structure consists of diagonal walls we only really see the two fields that do not contribute significantly to the de-homogenized structure.

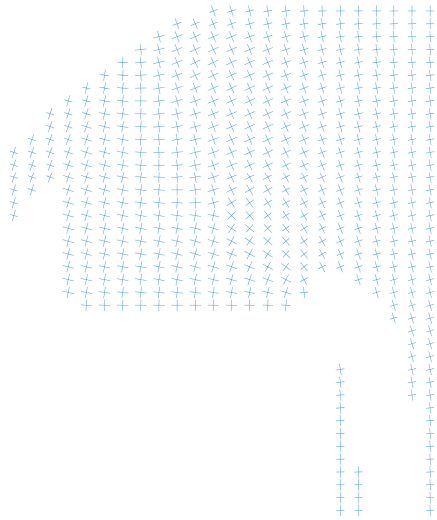

(a) Grid-aligned vectors have been used as a start guess. An intermediate amount of regularization has been used ($\gamma_\theta = 0.01$).

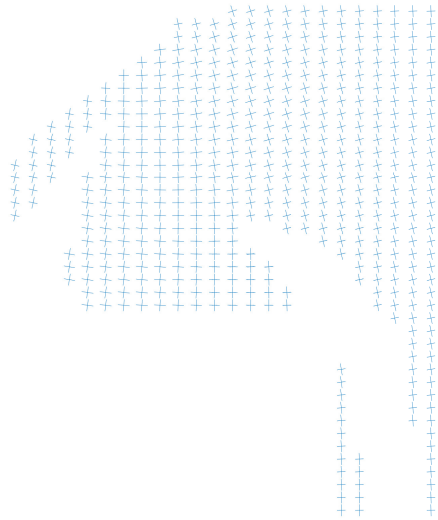

(b) Grid-aligned vectors have been used as a start guess. An intermediate amount of regularization has been used ($\gamma_\theta = 0.10$).

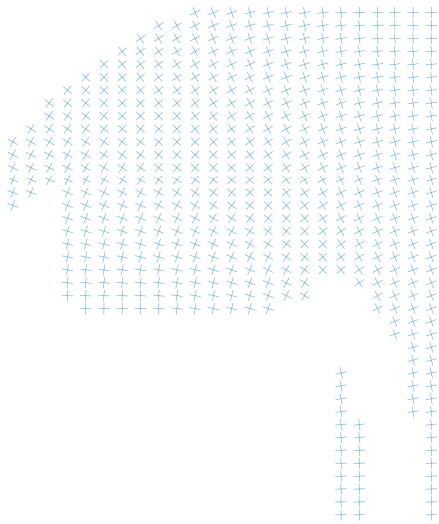

(c) Stress vectors have been used as a start guess. An intermediate amount of regularization has been used ($\gamma_\theta = 0.01$).

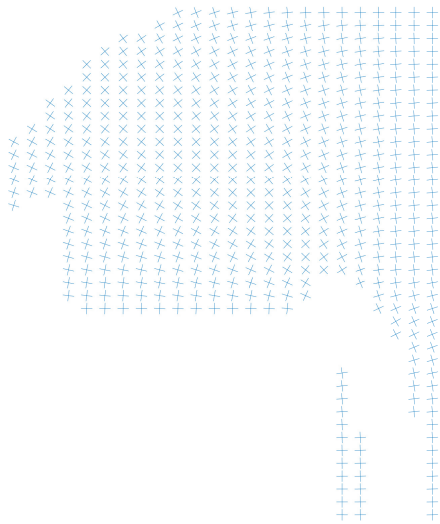

(d) Stress vectors have been used as a start guess. An intermediate amount of regularization has been used ($\gamma_\theta = 0.10$).

Figure 4.19: Diagonal cuts through different electrical mast fields depicting the wall problem. Different amounts of regularization have been applied. In all Figures a-d fully solid (>95% density) and void (<1% density) elements have been removed.

ization is applied globally. This means that also layer-normals of active, i.e., non-zero layers, are affected. However, since non-active layers do not influence the compliance, regularization leads to dramatically improved layer orientations while only increasing compliance by around 2%. In Figure 4.19b, we see that an intermediate amount of regularization can clean up the normals quite significantly. However, the orientation of the layer-normals now differs significantly from the principal stress directions. This can inflict problems by introducing singularities into the layer-normal fields that do not exist in the underlying stress tensor fields. For example, in Figure 4.19a, we see that the small amount of regularization has introduced a singular curve with a negative index into the fields. We can also see from Figures 4.19c and 4.19d that using a stress tensor-based start guess leads to much cleaner fields that align better with the underlying final stress tensors. In general, it might make sense to update the orientations of the microstructure periodically after a certain amount of iterations to align with the stress tensors of the homogenization-based structure. This would yield a good balance between the capability to use regularization and obtaining clean layer-normal fields.

4.3.6 Layer-thickness and density-based combing strategies

We decided to use the knowledge that layer orientations are best aligned in intermediate-density regions to our benefit and introduced a combing strategy that prioritizes combing based on layer-thickness or element material density. I will focus the discussion here on treating whole frames based on density as used in Paper-I since we did not see any significant difference between density-based and layer-thickness-based field label extraction for our examples. I suspect that the introduction of regularization cleaned up the fields enough to make the frame-based combing robust enough to not see a difference to vector-based combing.

4.3.6.1 Combing for singularity-free problems

We can comb layer-normal fields that do not contain any singular curves such that we can integrate the separated fields without the introduction of seams. Let us consider a continuous frame field consisting of layer-normals $\pm\boldsymbol{n}^1, \pm\boldsymbol{n}^2, \pm\boldsymbol{n}^3$, and layer widths w_1, w_2, w_3. We want to extract three smooth and continuous 1-direction fields $\tilde{\boldsymbol{n}}^1, \tilde{\boldsymbol{n}}^2, \tilde{\boldsymbol{n}}^3$, and their corresponding widths $\tilde{w}_1$, $\tilde{w}_2$, and $\tilde{w}_3$.

In Paper-I, we observe that singularities appear to occur in the void outside the

mechanical structure or in fully solid regions. We later discovered that singular curves can also exist in intermediate-density areas but that the singular curve then aligns to one of the layer-normals. I will discuss this finding and those so-called traversal singular curves in Chapter 5. Note that for our examples, we were still able to compute the 1-direction fields in a manner that traversal singular curves did not affect our results since traversal singular curves align with a layer-normal and frame extraction is reasonably robust. However, I believe the approach in Chapter 5 to be better suited at handling traversal singular curves.

As mentioned, in the absence of singularities, we can propagate a consistent choice of vectors to obtain 1-direction fields starting from an initial element. To deal with spurious singularities (arising due to the wall problem, for example), we propagate field labels through the domain by visiting elements critical to the mechanical structure first (i.e., elements with intermediate densities). This approach does not work when singularities occur inside the mechanical structure (regardless of density). However, these singularities occur only for specific boundary conditions. In fact, we were aware that there is a singular curve in the torsion sphere example. However, the singular curve passes from one boundary condition to the other entirely contained within the void or fully solid regions. Therefore, we were still able to achieve good compliance values with our de-homogenized structures.

The observations above inspired the use of a priority queue for combing. Instead of a mere first-in-first-out prioritization, we create a queue based on the densities obtained from the homogenization approach. For each element, we can compute the density as $\rho = 1 - (1 - w_1)(1 - w_2)(1 - w_3)$. As the initial point for the combing, we can either set an explicit start point or chose the element whose density is closest to a given starting density $\rho_{\mathbf{start}}$. We can also demand that for the starting element, all layers widths w_i be in the interval $[0.05, 0.95]$, for example. We set $\tilde{\boldsymbol{n}}^1 = \boldsymbol{n}^1, \tilde{\boldsymbol{n}}^2 = \boldsymbol{n}^2, \tilde{\boldsymbol{n}}^3 = \boldsymbol{n}^3$, and hence the widths follow as $\tilde{w}_1 = w_1$, $\tilde{w}_2 = w_2$, and $\tilde{w}_3 = w_3$. For the neighboring elements, we then compute the density priority $\rho_{\mathbf{priority}} = |\rho_{\mathbf{start}} - \rho|$. Here we prioritize smaller values when sorting the neighbors into the queue $\boldsymbol{Q}$. Subsequently, the element in the queue with the lowest $\rho_{\mathbf{priority}}$ is taken out, and we fix its 1-direction fields as discussed below. Lastly, we add its non-visited neighbors to $\boldsymbol{Q}$. Finally, we mark the element as visited in a vector $\boldsymbol{V}$.

If we take an element e out of $\boldsymbol{Q}$, we want to find the right-handed frame $\tilde{\boldsymbol{F}}_e$ that describes the layer-normals $\tilde{\boldsymbol{n}}^1, \tilde{\boldsymbol{n}}^2, \tilde{\boldsymbol{n}}^3$,

$$\tilde{\boldsymbol{F}}_e = \begin{bmatrix} \tilde{\boldsymbol{n}}^1(\boldsymbol{x}_e) & \tilde{\boldsymbol{n}}^2(\boldsymbol{x}_e) & \tilde{\boldsymbol{n}}^3(\boldsymbol{x}_e) \end{bmatrix}. \tag{4.7}$$

There are $j = 24$ possible frame orientations $\boldsymbol{F}_e^j$ that have to be tested to

find the best $\tilde{\boldsymbol{F}}_e$. Note that working with frames prevents us from choosing a vector $\boldsymbol{n}$ twice for two different fields or simultaneously choosing $\boldsymbol{n}$ and $-\boldsymbol{n}$ for one element. Further, working with right-handed frames ensures a consistent orientation for all chosen frames. To select the best frame $\tilde{\boldsymbol{F}}_e$, we identify the set of neighboring elements $\mathcal{N}_e$ of element e that already have been visited. For each neighbor element $i \in \mathcal{N}_e$, we identify the rotation matrix $\boldsymbol{R}^j_{e,i}$ between the possible orientations $\boldsymbol{F}^j_e$ and the frame $\tilde{\boldsymbol{F}}_i$,

$$\boldsymbol{R}^j_{e,i} = \tilde{\boldsymbol{F}}_i^T \boldsymbol{F}^j_e. \tag{4.8}$$

The corresponding orientation angle $\psi_{e,i,j}$ that defines the frame orientation can be calculated as,

$$|\psi_{e,i,j}| = \arccos\left(\frac{\mathrm{trace}(\boldsymbol{R}^j_{e,i}) - 1}{2}\right), \tag{4.9}$$

Hence, $\psi_{e,i,j} = 0$ would mean that the frame in e coincides with the frame in i for a given possibility j. The best orientation follows as,

$$\tilde{\boldsymbol{F}}_e = \boldsymbol{F}^k_e, \quad \text{for} \quad k = \arg\min_{j=1,\dots,24} \sum_i |\psi_{e,i,j}|. \tag{4.10}$$

Once we found frame $\tilde{\boldsymbol{F}}_e$, we store the widths $\tilde{w}_i$ according to the vectors $\tilde{\boldsymbol{n}}^1, \tilde{\boldsymbol{n}}^2, \tilde{\boldsymbol{n}}^3$. Subsequently, we remove element e from the queue and mark it as visited, and add the non-visited neighbors of element e to the queue. We repeat this process until we have extracted three smooth 1-direction fields.

4.3.6.2 Different choices of combing and further research

We chose to use right-handed frames since they provided us with robust results. The above-described method leads to a traversal of all elements in order of density closest to ρ_{start}, but in a spatially contiguous fashion. Note that it might be necessary to visit a void or fully solid element to connect two intermediate density regions. This could be bypassed by allowing only increasing $\rho_{\mathbf{priority}}$ values when visiting elements and instead have multiple combing processes and combining them after termination. For our single-load problems, we have not seen any need to implement this. Still, it might be a worthwhile topic to investigate for an expansion to multi-load problems. Multi-load fields have a non-constant number of vectors and are a lot less consistently orientated in general. An expansion to multi-load fields would also mean that we would need to treat the fields separately since we cannot extract frames. We have implemented such an approach for our fields but found it not majorly advantageous. However, I would like to share it since it might prove helpful in the future.

We can easily change the approach from above to extract fields instead of frames. One extracts a first field prioritized by its layer-thicknesses and subsequently extracts a second field from the remaining directions. This process is repeated until all fields have been extracted. Note that this approach is less robust since the layer-normals are treated separately and not at once, as we do with frames. To improve the robustness, we can account for the layer-thickness by weighing the vectors with the layer width. For an element e removed from $\boldsymbol{Q}$, we multiply the normal vectors $\pm\mathbf{n}^k$ with their assigned widths w_k where $k = 1, 2, 3$. We then calculate the cross products $\langle \pm w_k \mathbf{n}^k, \tilde{w}_i \tilde{\mathbf{n}}^i \rangle$ for all neighbor elements $i \in \mathcal{N}_e$. We then choose the direction in element e that maximizes the sum over all its corresponding cross-products. This approach does not only account for the rotations but also accounts for layer-widths, which might be particularly useful for multi-load problems, where orientations can be much more similar, but layer-widths might still differ more. We did not see any additional benefit over the frame-based approach for our examples, which is most likely due to the simplicity of our examples.

It could also be of interest to extract multiple combings to achieve a higher trust in the resulting field labels. Note that using a density-based combing method is also highly useful for singularity-containing fields. Of course, introducing seams can deal with singularities, however as shown in Figure 4.2, a breadth-first search will expand all seams throughout the domain. The combings can then end up containing many seams due to spurious singularities or noisy fields in high-density regions. One can profit from using layer-thickness-based combing the most, if void elements, non-active layers, and fully solid layers are ignored when creating the parameterization and not just recomputed by regularization as in our case.

4.3.7 Singularities and areas with highly rotational frame fields in our examples

After the submission of Paper-I, we became aware of how and where singularities occur in three-dimensional fields. And we realized that our examples and fields often were not completely singularity-free, especially not free of spurious singularities, i.e., noisy frame orientations that prevent consistent combing results. In Chapter 5, I will discuss the research into singularities in three-dimensional homogenization-based frame fields I did subsequently to Paper-I. For now, I would like to discuss the findings regarding spurious singularities and singular curves in the examples mentioned above. It is important to know that all examples were obtained with a high regularization value ($\gamma_\theta = 0.50$). Further, Figures 4.20, 4.21, and 4.22 show outlier frames with a very high rotational energy in red (around top 0.01%). Note that only non-void elements were considered for

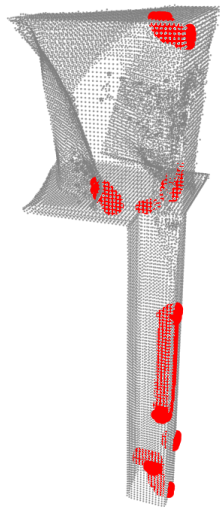

(a) Back view of the electical mast.

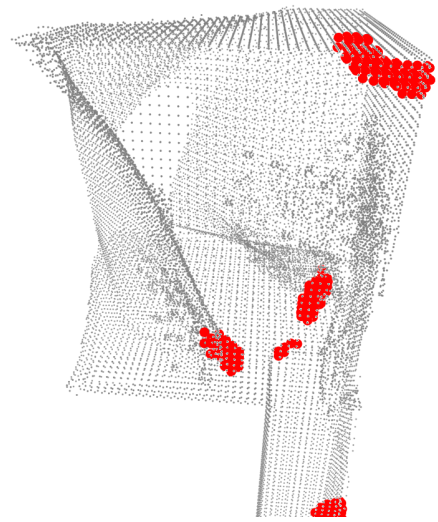

(b) Close up view of the head of the electrical mast example.

Figure 4.20: The electrical mast example. We see some highly rotational frames (in red) at the foot, where the mast is fully solid. We also see a long singular curve in the foot, which I would expect from the fields. Note that the upper end is cut short since there is no material above (see also Figure 4.14). We see some highly rotational fields where the head and the mast meet. This is not a singular curve, but due to fastly changing principal stress directions paired with a mostly solid region. Lastly, we see highly rotational frames near the top plate, either due to the singular curve or due to the solid elements found in that area.

these figures.

In Figure 4.20, we see the electrical mast example. The expected singular curve along the boundary of the electrical mast towards the other three non-modeled quarters can only be seen in the foot of the mast since further up, the elements lie in the void (see also Figure 4.14). Additionally, we see some areas with high rotational energy at the bottom of the foot, where the mast is completely solid. We also see high rotations, where the foot and the head meet. In these elements, the principal stress directions change rapidly, and the elements become nearly fully solid; in combination, we obtain these spurious singularities. Finally, we see some marked elements at the top plate. It is unclear if this is part of the expected singular curve (possibly moved due to the high amount of regularization) or solely due to the elements being very high in density in that area. I would expect a combination of both. Note that all of these highly rotational field locations are in near fully solid areas, which is part of the reason why our de-

homogenized examples still perform quite well.

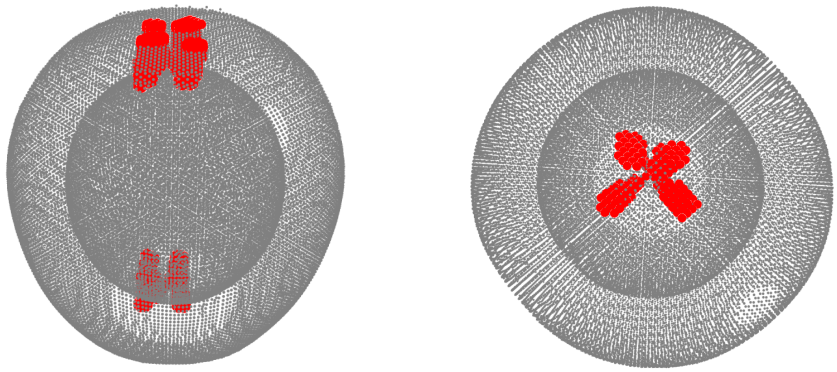

(a) Side view showing the singular curves within the solid structure.

(b) View onto the boundary condition showing the four singular curves.

Figure 4.21: This figure shows the torsion ball example. We can see how regularization splits up a higher index singular curve into four lower index singular curves that are spatially very close and run from one boundary condition to the other.

In Figure 4.21 we see the torsion ball example. Four singular curves are going from one boundary condition to the other. In a two-dimensional cross-section through a torsion ball example obtained without regularization, we would see a singularity of index 1. However, due to regularization, the singular curve was split into four singular curves with a lower index. Note that this singularity traverses from solid to void without passing through intermediate areas, which is why our de-homogenization still performs so well.

The highly rotational frames of the L-shaped beam in Figure 4.22 are more challenging to understand. We see highly rotational areas near the load (at the border to the void) in Figure 4.22a. These are solely spurious angle changes. In Figure 4.22b, we see highly rotational areas traverse through the domain, most likely singular curves. We would assume a single singularity from the stress field, very similar to the torsion ball. I think that the singular curve has been split again due to regularization, although it is not straightforward visible in this case. This singular curve is traversing through the active layer (hence also called traversal singular curve) and does not necessarily need to lie in a fully solid region. Note that the active layer changes smoothly, and we can still integrate the field with almost constant layer-normal near the traversal singular curves. Therefore, the de-homogenized structure still performs well. However, combing strategies based on frames can be influenced negatively by these traversal singularities.

Finally, I would like to note that there exist no singular curves in the cantilever examples. Sometimes spurious singularities close to the load at the solid-void boundary can occur, which will look the same as for the cantilever part of the L-shaped beam in Figure 4.22a.

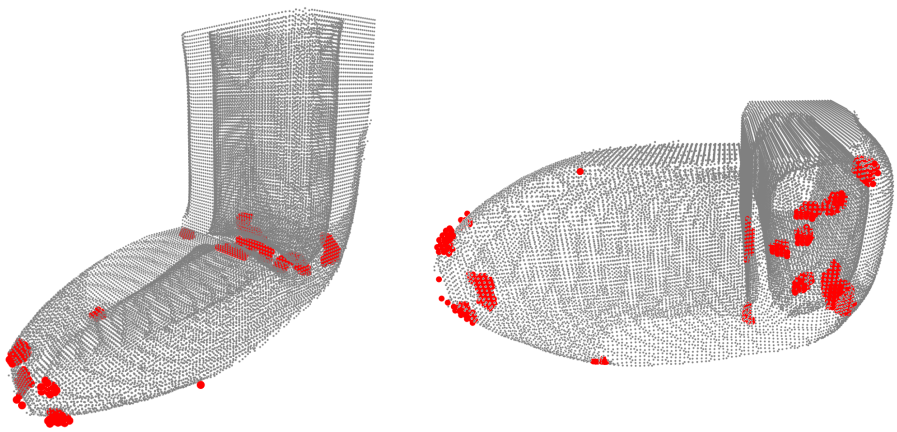

(a) Angled view depicting highly rotational frames near the load at solid-void boundary.

(b) View from the bottom onto traversal singularities that were split up due to regularization.

Figure 4.22: The L-shaped beam example. Figure 4.22a shows highly rotational frames close to the load at the solid-void boundary. Figure 4.22b shows singular curves passing through the solid domain.

Chapter 5

Non-integrative de-homogenization

This chapter will introduce a novel, non-integrative method for de-homogenization. The chapter consists of two parts. In the first part, I present the novel approach and show its application to single-load examples [Paper-III]. In the second part, I will then expand the method to two-dimensional multi-load designs.

5.1 Synthesis of frame field-aligned multi-laminar structures (related to Paper-III)

Previous work on de-homogenization and the work discussed in Chapter 4 is using integrative methods for de-homogenization. We there construct a parameterization from the direction fields and then extract a structure from it. In general, any de-homogenization method needs to address the following three challenges:

1. We want to synthesize structures with globally connected structural members.

2. The global structural members need to align well locally with the layer-normals.
3. The structural members should be evenly spaced.

We saw in Paper-II that we can extract globally connected structural members (challenge 1) for singularity-containing fields using seems to enforce integer jumps at seams. We can address challenge 2 by finding a large enough alignment weight to obtain structural members well-aligned with the layer-normals. However, a large alignment weight also means that the global structural members become less evenly spaced for integrative methods, leading to missing structural members (i.e., spread out isocontours) (see Section 4.2.3.2). It is important to note that for methods using integration, the second and the third challenge are opponents and that we must tune the alignment weight for optimal solutions.

We realized that we need to address these opposing objectives, local alignment, and globally evenly spaced structural members. We were also interested in obtaining a better understanding of where singularities occur in three dimensions and how we could handle them more explicitly. And finally, we saw that it would be tricky to expand integrative methods to multi-load case problems where not all directions are well-defined.

These reasons motivated the development of a novel approach to de-homogenization that does not use integration. Instead, the new method is a two-stage approach that separates the problem of finding globally connected structural members from the problem of finding evenly spaced structural members. We present this new approach in Stutz, Olsen, et al. [2021] [Paper-III], which can be found in the Appendix C. Our work is focusing on orthogonal fields (also called frame fields), where all three layer orientations are orthogonal. Note, however, that there is no explicit need for the fields to be orthogonal for topology optimization examples, as discussed a bit later in Section 5.2.

For the three-dimensional case, we can rephrase the three challenges above as follows. Given microstructure or lamination orientations, we seek a set of surfaces such that each surface aligns everywhere with one of the lamination normals. The surfaces should be evenly spaced with a prescribed average spacing. In detail, we first seek a set of surfaces whose local surface normals are aligned with the frame field. Such a *superset* of surfaces can be seen in Figures 5.1a and d. We find these surfaces individually using a stream surface tracing approach. A novel optimization energy then allows finding an evenly spaced subset of stream surfaces given a large superset. A set of selected stream surfaces can be seen in Figure 5.1b and e.

The main contribution in this chapter is a method that solves the selection prob-

lem mentioned above fully automated only depending on the local orientations and not on any global notion. In Paper-III, we further provided two methods for the synthesis of output shapes. For fields arising from topology optimization, we create a volumetric solid by compositing samples of each stream surface onto a voxel grid. See Figure 5.1e for an example. This *splatting* procedure is described in Section 5.1.4.2. The second method for synthesizing output shapes produces an-isotropic hexahedral meshes. Paper-I and Paper-II suggest a strong relationship of de-homogenization to quad-dominant meshing in 2D and hex-dominant meshing in 3D. However, depending on the examples, a deterioration of the hexahedra is desirable, as is the anisotropy resulting thereof. For specific frame fields, we can compute a graph of the intersection points of the stream surfaces and output a combinatorial structure from which we can obtain a hexahedral mesh. This is discussed in Section 5.1.4.4 and depicted in Figure 5.1f.

Here, in this thesis, I will focus on my contributions to Paper-III and therefore only summarize the tracing of stream surfaces and the hex-mesh extraction.

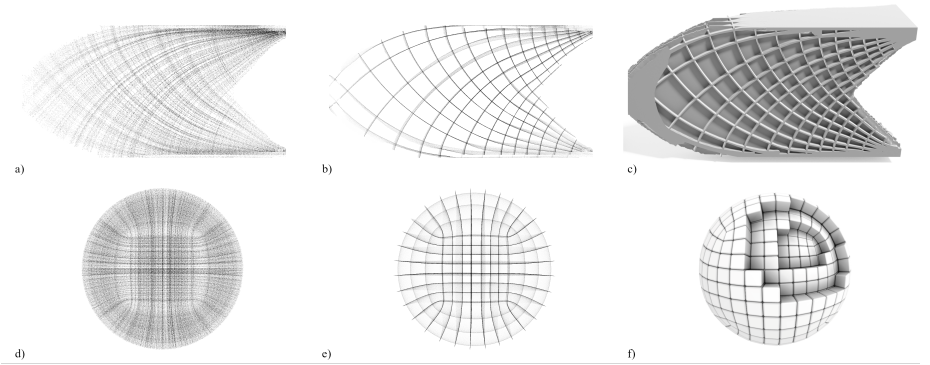

Figure 5.1: Given field directions as an input, we can generate a set of optimal laminations aligning exactly with the field orientations (Figures a and d). Using a novel optimization energy that only needs local orientation awareness, we can create a well-spaced subset of these laminations (Figures b and e). We then proceed to create near-optimal, highly stiff multi-laminar structures as a volumetric solid (Figure c) or, in some cases, output a hexahedral mesh (Figure f).

5.1.1 Related work

Frame fields arising from topology optimization impose particular requirements on hexahedral mesh generation schemes. For example, the frame fields might exhibit anisotropy to an extent where one edge length deteriorates. Moreover, the rotation of the frame fields might be higher than usual in the case of fields designed for hexahedral meshing, which could make the fields nonintegrable. These challenges suggest that existing hex-meshing or hex-dominant meshing algorithms are not suitable for such problems.

In recent years, density-based topology optimization has been used to find optimal mechanical structures in various fields. In the area of compliance minimization, giga-scale finite element models have been applied [Aage et al., 2017; Baandrup et al., 2020]. While such large-scale topology optimization makes the benefits of topology optimized structures very apparent, it also relies on supercomputing hardware and is not applicable in real time, which is one of the key steps towards the goal of incorporating topology optimization in the everyday engineering design process. It should be noted that approaches to address the high number of finite element needed have been proposed [Liu, Hu, et al., 2018; Wu, Dick, et al., 2016]. However, the mesh-dependency of density-based methods sets a very high lower limit on the amount of finite elements needed.

Paper-I and Paper-II indicate a strong relationship of de-homogenization to quad-dominant meshing in 2D and hex-dominant meshing in 3D. However, depending on the examples, a deterioration of the hexahedra is desirable as is the anisotropy resulting thereof. As shown in [Groen and Sigmund, 2018] and Paper-II, spurious singularities can occur. In 3D, orientations of the microstructures are not unique, a problem for the de-homogenization that can to a certain degree be circumvented by regularization [Paper-I].

Approaches for truss-structures have been presented for singularity-free fields in Arora et al. [2019] and Larsen et al. [2018] and in Wu, Wang, et al. [2019] for fields containing singularities.

Field-based quad-meshing and hex-meshing is most often done by combing fields and integrating to find scalar functions with integer-jump conditions, where the combed field are differently labelled [Bommes et al., 2009; Kälberer et al., 2007; Nieser et al., 2011]. A lot of research for field-based hex-meshing focuses on achieving pure-hex meshes [Huang et al., 2011; Palmer et al., 2019; Ray et al., 2016; Solomon et al., 2017]. These methods focus on the field design part of the hex-meshing pipeline with the main goal to achieve as many hexahedral elements as possible. Thus, these methods minimize a smoothness energy while ensuring that at the surface one direction of the octahedral frame is well-aligned

with the surface normal [Huang et al., 2011]. As a natural effect, hex-meshes extracted from such a model tend to have minimized anisotropy and minimized deterioration of the hexahedral elements.

For de-homogenization and hex-dominant meshing of homogenization-based topology optimization results, it is of importance to note that the fields are typically *prescribed* (rather than optimized during the meshing procedure) and cannot be changed to obtain more smoothness without reducing the mechanical performance of the obtained structure [Paper-II]. Approaches like Kälberer et al. [2007] and Nieser et al. [2011] are promising for de-homogenization but contain a pitfall since fields arising from the homogenization approach often have singularities of higher indices ($\pm 1/2$ in 2D) or have significant divergence at mechanical boundary conditions. Such higher indices imply a greater rotational speed and typically integration based methods for de-homogenization must enforce alignment to the fields with a penalization approach [Groen and Sigmund [2018]; Paper-I; Paper-II]. This penalization weight trades off structural alignment with spacing of the structural members and implicitly introduces anisotropy. If the alignment weight is chosen too small, the resulting parameterization will not align well with the underlying field as it tries to create unit-length gradients. If the alignment weight is chosen too large, the gradient of the parameterization will become zero and result in stretched out iso-contours and missing structural members [Paper-II]. These problems might be mitigated by introduction of additional optimization terms, which has so far not been deeply investigated. It is important to note that anisotropy is desired and of the utmost importance for the mechanical performance.

In field-based hex-dominant meshing as done by Gao et al. [2017], the isotropy of the desired hexahedra is a key ingredient of the algorithm. This is due to the optimization, which trades off the regularity of the hexahedra and their alignment to the underlying field. An expansion to anisotropic hex-dominant meshing might be achieved, if the desired hex-edge length was known beforehand and not only given implicitly.

Ni et al. [2018] have a promising approach to solve for vertex position of a tetrahedral mesh, which is similar to Gao et al. [2017]. The nature of the approach is aimed at producing vertices of a hex-mesh with a prescribed isotropic edge-length. Note that Gao et al. [2017] and Ni et al. [2018] create tetrahedra where the hexahedra do not align with the field, which could cost dearly in terms of mechanical performance, when used for de-homogenization, since the resulting structure would not align with the load path at all in these regions. Recently, polycube methods have advanced the hex-meshing field, but since methods like Guo et al. [2020] and Livesu et al. [2020] do not rely on fields they are not applicable to de-homogenization.

The work of Takayama [2019] expanding the 2D work of Campen, Bommes, et al. [2012] and Campen and Kobbelt [2014] relies on user-defined (as opposed to frame field aligned) implicit surfaces as an input to guide the creation of hex-meshes. Moreover, several authors, including us, draw inspiration from the notion of the spatial twist continuum which is, essentially, the dual of a hexahedralization and was introduced by Murdoch et al. [1997].

Campen, Silva, et al. [2016] create a foliation as a means of finding a bijective parameterization of a 3D shape. While there is a clear similarity between the notion of a stream surface and a transversal section of a leaf of a foliation of a 3-manifold [Milnor, 1970], their aim is to create a bijective map entailing strong conditions on the direction field whereas we take the frame field as is.

It should be mentioned that stream surfaces are often used as a visualization tool seen in fluid dynamics [Hultquist, 1992; Machado et al., 2014].

We strive for global surfaces or layers, which are locally well-aligned with the results from the homogenization-based topology optimization, while incorporating implicitly the anisotropy dictated by these fields and circumventing the issue of missing structural parts due to enforcing field alignment and resulting zero-gradient regions.

5.1.2 Frame fields and singularities in three dimensions

We are mainly motivated by fields arising from topology optimization, but one can also think of fields that would not permit generating laminations or even hexahedral meshes obtained from an integration-based method. In the following, we will shortly discuss these fields and their origins. In Section 5.1.2 we will give a discussion of singularities in three dimensions. As we will demonstrate in Section 5.1.5, our selection algorithm can take fields from *any* of these sources as input; it is designed to extract field-aligned structures while being agnostic to the source of the field.

5.1.2.1 Singularities in three-dimensional topology optimization fields

A crucial part of the homogenization-based topology optimization is to find the optimal rotations of the microstructures, since microstructures have a high stiffness in their principal directions but low shear. Thus regularization of the

orientations during the topology optimization will influence the resulting performance of the mechanical structure since more material needs to be allocated to strongly regularized regions [Paper-II]. If regularization of the orientation fields is done after the topology optimization, either actively as discussed in Arora et al. [2019] or by not enforcing high enough penalization weights for an integrative method as discussed in Groen and Sigmund [2018] and Paper-II, the resulting structure will not align well to the optimal microstructure orientation. Such non-optimally aligned regions may cause a dramatic loss of performance of the structure [Groen and Sigmund [2018], Paper-II]. Therefore, the motivation of this paper is to find structures that adhere to the local orientation of the microstructure as closely as possible outside of void or fully solid regions. This in turn introduces anisotropy between the global members of the structures. Note, that this anisotropy is not negatively influencing the structure from a mechanical point of view.

Singularities arise in two-dimensional homogenization-based topology optimization for three reasons [Paper-II];

- Singularities in the underlying stress field will lead to singularities in the layer-normal fields since the microstructure aligns to the principal stress directions.
- Regularization inflicted on the layer-normal fields during the topology optimization will break up singularities with a higher index in the stress fields into multiple singularities of lower index in the layer-normal fields.
- In regions where the microstructure is completely solid or void, singularities can be introduced by noise. In solid regions the microstructure becomes isotropic and the optimal orientation of it becomes non-unique. In void regions the microstructure is not present and an optimal orientation of the microstructure is therefore non-existing.

In Paper-II, we showed that in two dimensions, singularities in topology optimized layer-normal fields must occur in completely solid or void regions. Unfortunately, this observation does not hold in three dimensions. Firstly, microstructure orientations in three dimensions are non-unique due to in-plane stress; this can cause spurious singularities to appear, which can be tackled with a low amount of regularization, as shown by Paper-I. Secondly, as seen in Figure 5.2, singularities in stress fields can occur even when the microstructures are not completely solid. If we consider Figure 5.2a we see a field describing a singularity with index 1. In Paper-II we observed that because the rotational velocity of the field increases towards infinity at the singularity, the topology optimization process fills the region around the singularity with material to account for the

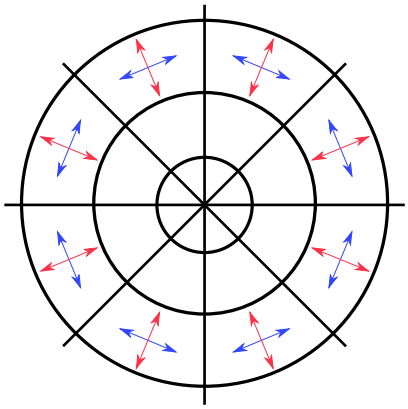

(a) two-dimensional example of a singularity with index 1.

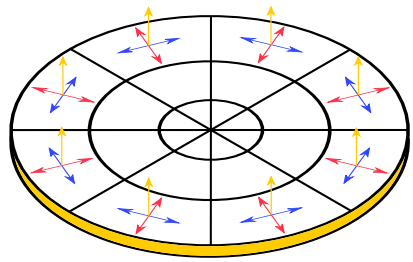

(b) The same singularity as in Figure 5.2a but now embedded in an orthogonal layer (in yellow) in three dimensions.

Figure 5.2: On the left we see an example of a singularity with index 1 in two dimensions. It is clear that the rotational speed increases the closer we get to the singular point. Paper-II have shown, that the optimizer has an incentive to put such singularities in an either fully void or fully solid region, since there would always be shear forces acting on any non-solid microstructure at the singular point. On the right we see the same field and singularity embedded into an orthogonal layer (in yellow) in three dimensions. Note how the optimizer now can choose to fill the yellow layer with material and completely ignore the red and blue field, while still creating a stiff structure. Moreover, this singularity does not have to be in a completely solid region since the relative layer-thickness of the yellow layer can be lower than 100 percent. In this case we refer to the microstructure as *transversely isotropic* since the the microstructure is isotropic in one plane (the yellow one) but anisotropic perpendicular to this plane.

spinning stress-field at the singularity. On the other hand, when we embed the fields from Figure 5.2a in three dimensions, as shown in Figure 5.2b, the optimizer can choose to fill the newly introduced orthogonal layer with material and not assign any material to the two existing layers. Furthermore, we observe that this third layer does not have to be completely solid but can have any arbitrary layer-thickness, e.g., 50%. In this case we refer to the microstructure as being *transversely isotropic* since the the microstructure is isotropic in one plane (the yellow one) but anisotropic perpendicular to this plane. The option to cut out singularities and later on fill them with material, will inevitably lead to excessive use of material in three dimensions. The example described in Figure 5.2 is, to the best of the author's knowledge, the only singularity in three dimensions that occurs outside of fully solid or entirely void regions.

The following thoughts can explain this. First, if all layer-normals change direc-

tion at a location outside the void, for example, around a source, then the region would need to be filled with material by the optimizer to be made isotropic. Second, non-zero stress directions will always be perpendicular to a layer-normal, with non-zero layer-thickness, meaning that stresses must always be transferred within a solid slab or plate. This will always align a stress field's singular curve with a layer-normal outside of fully solid or entirely void regions. This leaves us only with fields as shown in Figure 5.2b, where of course, the indices of the singularities can be different. Third, consider for a moment that in Figure 5.2b, the red or blue layer would be non-zero. Then their layer-normal would rotate infinitely fast at the singular curve, and thus the optimizer would fill the region completely with material to make the microstructure isotropic at the singular curve. Hence, we conclude that the only singular curve not embedded into complete solid or the void can be seen in Figure 5.2b, where the red and blue layer-thicknesses are zero.

Our stream surfaces generation method can differentiate the expansion of stream surfaces near a singular curve. Note how in Figure 5.2b, the field with the yellow normal is aligned with the singular curve while having a constant normal. We could use this observation to identify which layer is traversing the singular region orthogonal to the singular curve in a computationally cheap manner and expand the corresponding stream surface through the singular region. However, we do not need to do this for fields arising from the homogenization approach since we stop the expansion of stream surfaces in zero-material layers (like the red and blue labeled layers in Figure 5.2b). This means that only the stream surface following the traversing layer will be created.

5.1.2.2 Boundary-aligned frame fields

Topology optimization yields frame fields as a by-product of a mechanical problem; the fields are not designed with meshability or integrability in mind. In contrast, a number of techniques in geometry processing optimize for frame fields with the specific goal of extracting a quadrilateral or hexahedral mesh. Since our work focuses primarily on the volumetric case, we refer the reader to Vaxman et al. [2016] for discussion of the many methods available for two-dimensional field computation, and briefly highlight representative three-dimensional methods below.

The basic goal of volumetric frame field computation is to optimize for a field of three orthogonal directions at each point in a region enclosed by a surface, with the constraint that one of the three directions aligns to the surface normal along the boundary. This field is then used as input to methods like Nieser et al. [2011] and Lyon et al. [2016] to extract a mesh through parameterization.

Huang et al. [2011] originally propose a representation of orthogonal frames—later dubbed "octahedral" frames by Solomon et al. [2017]—that is agnostic to their labeling. Their work extracts smooth fields by optimizing Euler angle variables, with additional constraints at the boundary; their approach was refined by Ray et al. [2016] with improved boundary constraints and optimization. Solomon et al. [2017] propose a relaxation of [Ray et al., 2016], allowing for use of the boundary element method (BEM). Palmer et al. [2019] provide a more complete description of the space of octahedral frames, leveraging the structure they identify to propose manifold-based optimization schemes; they also propose a related orthogonally decomposable ("odeco") frame representation in which the directions remain orthogonal but can scale independently.

Many open questions remain regarding the singular topology of octahedral / odeco fields and its relationship to hexahedral meshing; see Liu, Zhang, et al. [2018] for initial results and some relevant discussion. Corman et al. [2019] and Liu, Zhang, et al. [2018] propose algorithms that compute frame fields with prescribed singular structures.

5.1.2.3 Closed-form frame fields

A closed-form frame field is a field where the orientations of the frames can be found using a closed-form mathematical expression instead of being found using optimization or by solving a system of equations. In this paper, we consider a field describing a cylinder, much like the field illustrated in Figure 5.2, where there is a single singular curve in the center of the cylinder. Suppose one tries to extract well-aligned hexahedra from such a field using integrative methods. In that case, one will be challenged due to the high anisotropy of the hexahedral elements, which can not be treated by methods, that were designed to create isotropic hexahedra [Paper-II]. Note that the edge length of hexahedra will ultimately deteriorate towards the singular curve with such a cylinder field. A stream surface based approach can be designed to expand through singular curves for the cylinder's near-constant field (as discussed earlier in Section 5.1.2.1), while creating highly anisotropic hexahedra in the remaining domain. Extending this example, we also run our algorithm on a non-integrable field describing a helicoid. Again, this produces highly anisotropic hexahedra matching the spiral shape of the input field.

5.1.3 Computing collections of stream surfaces

The overarching idea of our method is to compute a large set of surfaces, $\mathcal{S}$, which align with the frame field, and then find a well-spaced selection of these, $\mathcal{S}_{opt}$, representing the multi-laminar structure that we seek. In this section, I discuss how we find and select these aligned surfaces using stream surface tracing. Section 5.1.4 will discuss how the final output is computed from this representation.

In engineering, a *streamline* is a curve that is everywhere tangential to a vector field [Hultquist, 1992]. A stream surface is merely the generalization to 3D, i.e., a surface whose normal is everywhere aligned with one of the vectors of the input fields.

We do not rely on the frame field being combed, and hence, we do not have consistent labeling of the vectors in the frame. Instead, we find the frame vector best aligned with the estimated normal of the next point that we compute when expanding a stream surface. It is also worth noting that we generally wish to stop stream surface tracing when the stream surface would otherwise exit a given bounding shape. Thus, we assume a known mask or layer-thickness in the following.

5.1.3.1 Tracing stream surfaces

I will here only give a summarized description of how we trace stream surfaces and treat singularities. A more detailed description can be found in Paper-III. We start by independently creating stream surfaces to obtain the set $\mathcal{S}$. Instead of computing a surface with connectivity, only a point cloud is computed for each stream surface. We initialize each surface at a single randomly generated seed point $\mathbf{p}_0$. The surface's normal direction is chosen randomly from the frame field directions. The surface is then grown from the seed point by adding points in the vicinity and computing their location based on the normal-field. A candidate for a new surface point is obtained by a method similar to Poisson Disk Sampling (PDS) sampling introduced by Bridson [2007]. The candidate's location is then updated using a fourth-order Runge-Kutta method [Chapra, 2012] to mitigate drift in the surface expansion.

Once obtained, we add the newly generated point to a first-in-first-out queue. Here it might be worthwhile in the future to investigate if layer-thickness priority yields a benefit to the expansion of stream surfaces. We do not add the newly generated point to the queue if it is too close to any previously generated point

of the stream surface, lays outside the design domain. We also do not add points to the queue that lie in fully solid regions or if the corresponding layer-thickness is zero at the new point. Note that the last two cases are why our approach does not need to handle singular curves actively for topology optimization examples. Only traversal singular curves could be problematic but, since we only trace stream surfaces in active layers we can expect the layer-normal to be nearly constant.

There can arise a problem with drift when computing the stream surfaces. This can be problematic if a stream surface meets itself, having traced around a sphere, for example, since we obtain a sort of crack. This can be seen in Figure 5.3 for the torsion ball. To mitigate the problem, we recompute all point locations based on the neighboring points of the surfaces in a post-processing step.

We now have a method that allows us to trace stream surfaces in our input fields.

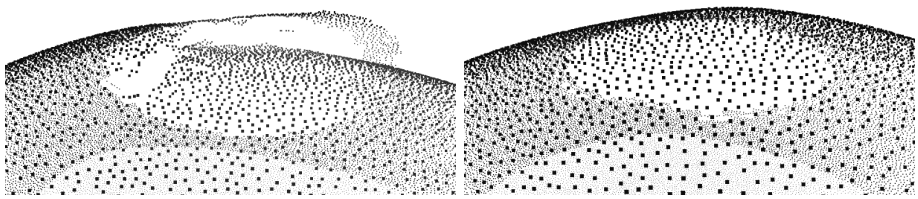

Figure 5.3: On the left, we see the effect of drifting. Minor deviations in point position and interpolation of the field over long distances lead to a crack in the surface. On the right, we show the resulting surface after the surface points have been recomputed.

5.1.3.2 Singularities

In three dimensions, singularities are curves along which the frame field is not defined. When creating stream surfaces in octahedral fields that do not arise from the homogenization approach, we often need to deal with the singular curves explicitly. If we do not actively prevent stream surfaces from getting close to a singular curve, we risk that the stream surfaces split into two or more parts (referred to as "forking"). The reason for forking surfaces is that the rotation of the frame fields is very high near singular curves. These high rotations lead to a considerable amount of local variations between the orientations computed during the surface tracing and finally to forking surfaces. Figure 5.4 depicts an

example of a forking stream surface. For an in-depth discussion of singularities in octahedral fields can be found in [Liu, Zhang, et al., 2018].

The subselection approach does not choose forking stream surfaces if they only represent a tiny portion in $\mathcal{S}$. The reason is that a forking stream surface always creates a worse energy response than two separate stream surfaces covering the same region. However, multiple forking surfaces can be detrimental to the results of our selection approach presented in Section 5.1.3.6. Therefore, we choose to exclude singular regions from the design domain during the stream surface creation for other examples than the topology optimization structures. This will introduce holes in our model (see, for example, Figure 5.16) but will preserve the overall quality of the output. We mark regions as singular by computing a rotational energy based on the approach of Paper-I and then excluding the outliers of that energy. A more detailed description of how we treat singular regions can be found in Paper-III. With this method to prevent forking surfaces in place, we now have everything to create the set of stream surfaces $\mathcal{S}$.

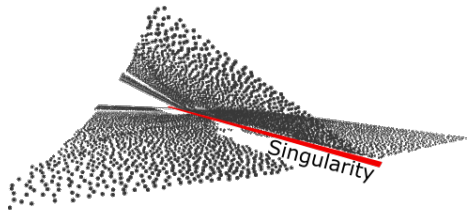

Figure 5.4: A stream surface that has expanded to close to a singular curve and, as a result, has forked into multiple sheets. Such surfaces are undesirable and are caused by rapid changes in the normal fields.

5.1.3.3 Energy for an optimization-based subselection approach

We will now take the set of surfaces $\mathcal{S}$ that we have created in the previous sections and continue with finding a well-spaced subset $\mathcal{S}_{opt}$. We will compute $\mathcal{S}_{opt}$ by optimizing over binary variables w that will be assigned to the stream surfaces. However, before we can define our optimization problem, we need to define the contribution of each stream surfaces to the optimization energy. For simplicity and consistency with the figures, we will describe this procedure in two dimensions. The algorithm works the same in three dimensions, and we will explain essential details for the implementation inline on an ongoing basis.

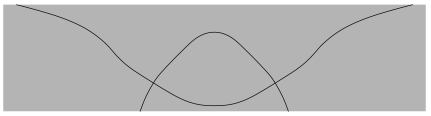

(a) Two streamlines following two different orthogonal fields.

(b) Sum of energies $\bar{E}_S$ for the streamlines in Figure 5.5a. Green and blue elements have an energy value of one, orange elements have a value of two.

Figure 5.5: On the left, we see two streamlines following orthogonal field directions. On the right, we see the sum of the energies $\bar{E}_S$ from Equation 5.1 for the two streamlines. Here the contributions of the streamlines are colored in blue and green in regions with value one. The orange highlighted regions are elements where both streamlines create an energy response and subsequently the summed value equals two. An optimizer would try to minimize the amount of these orange elements since it tries to minimize overlapping streamline-energies. This version of the energy is blind for the fact that the two streamlines follow different fields. In order to be able to space out both family of streamlines correctly, we need to split the energy as shown in Equations 5.2 and Figures 5.6 and 5.7.

First let γ denote the desired average spacing in the set $\mathcal{S}_{opt}$. As an aid, we define the projection of a point $\mathbf{x} \in \mathbb{R}^2$ onto a streamline $S \in \mathbb{R}^2$ as $\mathbf{x}_p = \arg\min_{x_s \in S} ||\mathbf{x} - \mathbf{x_s}||$. We can then define an energy for the streamline S by

$$\begin{aligned} &\bar{E}_S : \mathbb{R}^2 \to \{0,1\} \ , \\ &\bar{E}_S(\mathbf{x}) = \begin{cases} 1, & \text{if } ||\mathbf{x} - \mathbf{x_p}|| \leq \gamma, \\ 0, & \text{else.} \end{cases} \end{aligned} \tag{5.1}$$

This energy is shown in Figure 5.5b for the two streamlines following orthogonal field directions in Figure 5.5a. For our application to 4-direction fields, we need to distinguish between the two orthogonal field directions locally. Therefore, we choose for every $\mathbf{x} \in \Omega$, two orthogonal directions from the 4-direction field at random and assign them to 2-direction fields f_1 and f_2. This assignment of the orthogonal directions to f_1 and f_2 allows us to define a function $S_{dir}(\mathbf{x}_s) = \{1,2\}$ that indicates for every point $\mathbf{x}_s \in S$ if the streamline follows the local label of field f_1 or field f_2. In three dimensions, we use the normal of the stream surface as a field identifier. We now split the energy for every streamline into two parts:

$$\begin{aligned} &E_S : \mathbb{R}^2 \to \{0,1\} \times \{0,1\} \ , \\ &E_S = (E_{S_1}, E_{S_2}) \ , \end{aligned} \tag{5.2}$$

where the split energies E_{S_1} and E_{S_2} are defined as,

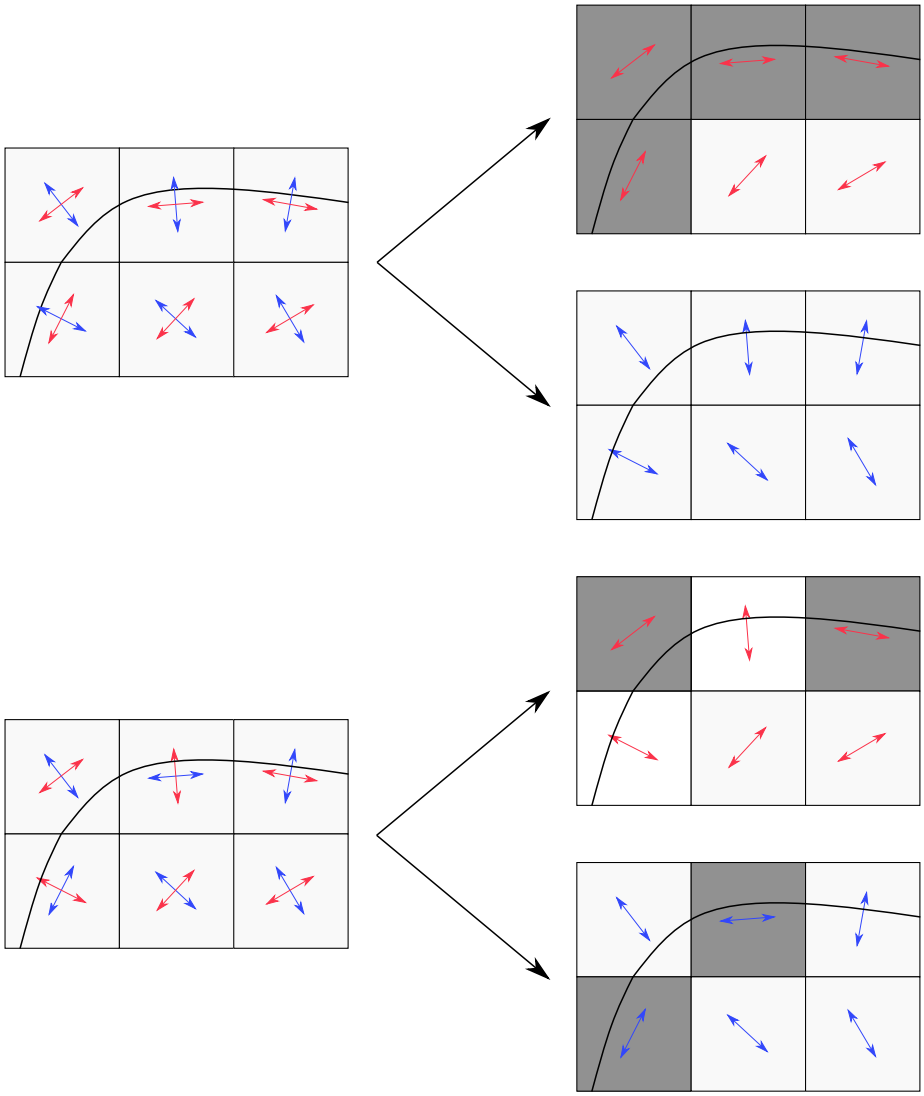

Figure 5.6: Example of the energies created from a streamline traced in the same field but differently labeled. On the left, we see a streamline traced in a combed (above) and uncombed (below) version of a 4-direction field. On the right, we see the corresponding energies for label "red" and label "blue", which are local labels. Note how the streamline activates only one of the two energies for each element, as indicated by the gray coloring.

$$
\begin{aligned}
E_{S_1}(\mathbf{x}) &= \begin{cases} 1, & \text{if } S_{dir}(\mathbf{x}_p) = 1 \wedge ||\mathbf{x} - \mathbf{x}_p|| \leq \gamma \ , \\ 0, & \text{else,} \end{cases} \\
E_{S_2}(\mathbf{x}) &= \begin{cases} 1, & \text{if } S_{dir}(\mathbf{x}_p) = 2 \wedge ||\mathbf{x} - \mathbf{x}_p|| \leq \gamma \ , \\ 0, & \text{else.} \end{cases}
\end{aligned} \tag{5.3}
$$

(a) Sum of energies E_{S_1} for a combed field.

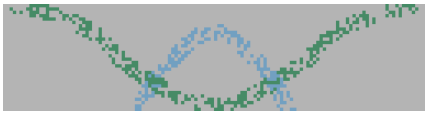

(b) Sum of energies E_{S_1} for an uncombed field.

(c) Sum of energies E_{S_2} for a combed field.

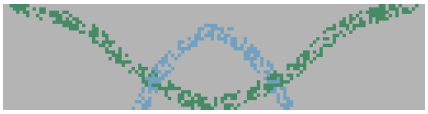

(d) Sum of energies E_{S_2} for an uncombed field.

Figure 5.7: Sum of split energies from Equation 5.2 for the streamlines depicted in Figure 5.5a. The sums of the energies are shown once when a combed version of the underlying field is used and once when an uncombed version is used. Note how in a combed field the streamlines are separated into the energy that follows the same field label as the streamlines. In an uncombed field, the contributions of the streamlines split to both energies. However, it is clear that the contributions of a streamline to the two energies form a disjoint union. Regions with value two (highlighted in orange in Figure 5.5) do no longer exist.

Note that there is no need for consistency of the field labels f_1 or f_2 in a neighborhood, i.e., no combing is needed, as shown in Figure 5.6. This makes the energies very simple to implement and the approach very robust. The split energies from Equation 5.3 can be seen in Figure 5.7. Having defined the energy we can now formulate a binary optimization problem,

$$\underset{\mathbf{w}\in\{0,1\}^{n_S}}{\text{minimize}} \int_\Omega \left| \sum_{i=1}^{n_S} w(i) E_S(\mathbf{x}) - (1,1) \right| \quad \mathrm{d}\Omega \ , \tag{5.4}$$

where we refer to the optimization variables w_i as weights and $n_S = |\mathcal{S}|$. If we use the energies from Equation 5.1 the selected streamlines would all follow the same lamination direction since the optimizer would penalize crossing streamlines. Figure 5.8 shows an example of such an optimization. If we instead use the same set of streamlines but use the energies defined in Equation 5.2 for the optimization, we obtain both laminations, as can be seen in Figure 5.9.

Note that defining the problem in Equation 5.4 as a least-squares problem instead of a least absolute deviations problem would overly punish multiple covered regions of the energy and lead to missing streamlines. The L^1 norm in Equation 5.4, on the other hand, penalizes double-covered probe points equally as hard as non-covered probe points. The difference between using an L1-norm or an L2-norm can be seen in Figures 5.10. Details on the solution of the minimization problem in Equation 5.4 are discussed in Section 5.1.3.6. We now

continue to find the variable $n_{\mathcal{S}}$.

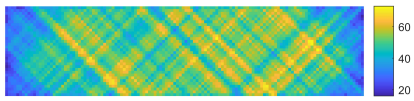

(a) This Figure shows the sum of the energies E_S of all streamlines provided to the optimizer.

(b) This Figure shows the sum of the energies E_S of the streamlines selected by the optimizer.

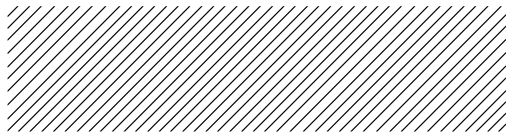

(c) This Figure shows the curves selected by the optimizer.

Figure 5.8: This Figure shows the selection result using the energies defined in Equation 5.1.

5.1.3.4 Number of streamlines $n_{\mathcal{S}}$ in the covering set of streamlines $\mathcal{S}$

To solve the minimization problem in Equation 5.4 we need to know how large the number of streamlines $n_S = |\mathcal{S}|$ provided to the optimizer needs to be.

First, we need to define the desired average spacing γ of the streamlines in $\mathcal{S}_{opt}$. Then the cardinality of $\mathcal{S}_{opt}$ can be approximated by,

$$|\mathcal{S}_{opt}| = \frac{n_x}{\gamma} + \frac{n_y}{\gamma} \ , \tag{5.5}$$

where n_x and n_y are the dimensions of the design space in $\mathbf{x}$, respectively y direction. Note that the cardinality of $\mathcal{S}_{opt}$ grows in linear dependence to the dimensions of the design space, since streamlines are one dimensional objects. This means that doubling all dimensions of the design space will only lead to a doubling of the cardinality of $\mathcal{S}_{opt}$. This also holds true in three dimensions, here due to the two-dimensionality of stream surfaces. We further need to define the error ε by which a streamline should deviate on average from its optimal position. We denote this in fraction of the optimal average spacing γ, e.g. $\varepsilon = 0.1$ would allow a streamline to be placed in a band of 0.2γ width around its optimal location. We can then derive the cardinality of $\mathcal{S}$ by:

$$n_{\mathcal{S}} = |\mathcal{S}| = \frac{1}{\varepsilon}|\mathcal{S}_{opt}| = \frac{1}{\varepsilon}\left(\frac{n_x}{\gamma} + \frac{n_y}{\gamma}\right) \ . \tag{5.6}$$

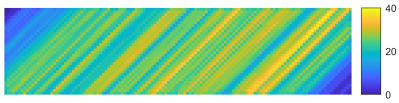

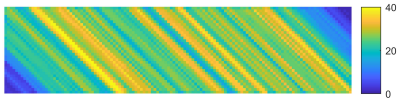

(a) This Figure shows the sum of the energies E_{S_1} and E_{S_2} of all streamlines provided to the optimizer.

(b) This Figure shows the sum of the energies E_{S_1} and E_{S_2} of the streamlines selected by the optimizer.

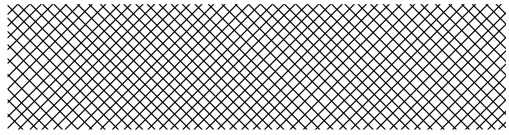

(c) This Figure shows the curves selected by the optimizer.

Figure 5.9: This Figure shows the selection result using the energies defined in Equation 5.2.

As with $\mathcal{S}_{opt}$, we note that the cardinality of $\mathcal{S}$ grows linear with the dimensions of the design space. We also note that the cardinality of $\mathcal{S}$ grows linear in dependence to the desired error ε, meaning that reducing ε by a factor k will increase the cardinality of $\mathcal{S}$ only by a factor k. Both these observations are again valid in two dimensions as well as in three dimensions.

We have now computed how many stream surfaces we need to provide to the minimization problem in Equation 5.4 to obtain good results.

5.1.3.5 Resolution of the energy

To solve the minimization problem in Equation 5.4 the only thing that remains is to discretize the energy E_S on a pixel grid, where we refer to a single pixel as a probe point. To efficiently subselect streamlines, we need to know the resolutions of the discretized energies, i.e., the number of probe points needed to differentiate streamlines in the set $\mathcal{S}$. This number depends on the desired error ε and the desired average spacing γ. Each streamline should activate the probe points lying in a band of width γ around the streamline. Two streamlines that are more than $\varepsilon \cdot \gamma$ apart should activate a different set of probe points.

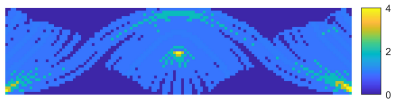

(a) This figure shows the sum of the energies E_{S_1} and E_{S_2} of the streamlines selected by the optimizer when using an L1 norm.

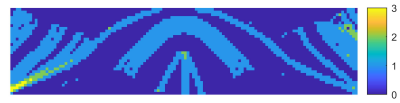

(b) This figure shows the sum of the energies E_{S_1} and E_{S_2} of the streamlines selected by the optimizer when using an L2 norm.

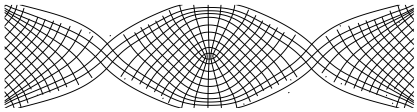

(c) This figure shows the curves selected by the optimizer when using an L1 norm.

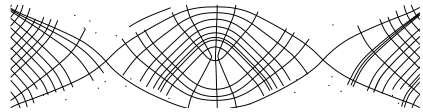

(d) This figure shows the curves selected by the optimizer when using an L2 norm.

Figure 5.10: This Figure shows the streamline selection results obtained when using an L1 norm or an L2 norm during the optimization. Note the missing streamlines in the L2 norm result due to multiply covered regions being penalized too harshly.

This implies that the number of probe points needed can be computed by,

$$n_p = \frac{n_x}{\varepsilon \cdot \gamma} \cdot \frac{n_y}{\varepsilon \cdot \gamma} = \frac{1}{\varepsilon^2} \left(\frac{n_x}{\gamma} \cdot \frac{n_y}{\gamma} \right) \quad . \tag{5.7}$$

Here we note that the number of probe points grows quadratically in two dimensions, meaning doubling both dimensions of the design space will increase the number of probe points needed by a factor of four. Respectively, the number of probe points grows cubically in three dimensions. Note, however, that the subselection is only a fraction of the time spent on the whole approach as can be extracted from Table 5.1.

We have now discretized the energy E_S in the minimization problem in Equation 5.4 and are now ready to solve it.

5.1.3.6 Subselection using a relaxed approach to binary programming

Solving the minimization problem in Equation 5.4 can be done by using integer linear programming. However, the underlying problem is likely NP-hard due to

the binary constraints. This makes a direct solve of the problem formulated in Equation 5.4 infeasible. To solve the least absolute deviations problem, we relax the optimization variables w_i to be in the interval $[0, 1]$ instead of $\{0, 1\}$. This leads to the following convex linear program, which can be solved in polynomial time:

$$\underset{\mathbf{w}\in[0,1]^{n_\mathcal{S}}}{\text{minimize}} \int_\Omega \left| \sum_{i=1}^{n_S} w(i) E_S(\mathbf{x}) - (1,1) \right| \quad \mathrm{d}\Omega \ . \tag{5.8}$$

We solve the relaxed problem in Equation 5.8 with an interior point method and then fix weights that have been set to either 0 or 1. Subsequently, we solve a binary program with the remaining weights (typically $< 5\%$ of the original weights) using a branch and cut algorithm. A branch and cut algorithm splits the original problem into sub-problems and uses cutting planes to cut away parts of the possible solution space until an optimal integer solution is found for a sub-problem. If that solution is better than a relaxed solution of a second sub-problem, the second sub-problem does not need to be solved. This is done iteratively until the algorithm converges. For details, we refer to Padberg et al. [1991]. We use the implementation provided in CVX [Grant et al., 2014].

Note that the high number of binary weights chosen in the relaxed problem is due to the energy having binary values. If we were to base the energy on a signed distance function instead, we would almost exclusively receive non-binary weights as a result from the relaxed problem in Equation 5.8 since the optimizer would try to trade off contributions of different streamlines.

The observation in Section 5.1.3.4 that the computational burden of the problem in Equation 5.4 grows linear in the amount of stream surfaces has an important practical use. Forking stream surfaces, which can occur due to heavy noise in the topology optimized fields and are described in Section 5.1.3.2, will cover more space than non-splitting surfaces. They are therefore chosen less by the optimizer when the number of surfaces in $\mathcal{S}$ increases.

We have now found a well-spaced set of laminar surfaces $\mathcal{S}_{opt}$ and can now continue with the generation of output structures.

5.1.4 Output generation

The stream surface tracing and selection procedure described above produces a set of stream surfaces, $\mathcal{S}_{opt}$, where each surface is represented as a point cloud. In itself, this representation is helpful for visualization. However, our end goal is to provide methods for synthesizing output structures. In this thesis, I will shortly present two methods that can be used for a stream surfaces set $\mathcal{S}_{opt}$.

Detailed descriptions of these methods can be found in Paper-III. The first method produces a volumetric structure using the layer-thicknesses obtained from topology optimization. The second method generates hexahedral meshes from the selected stream surfaces.

5.1.4.1 Post-processing the surfaces

Before we extract a volumetric solid or a hexahedral mesh, we employ a post-processing step on the stream surfaces in $\mathcal{S}_{opt}$. We do not need high-resolution stream surfaces to create the energies for the selection algorithm. However, higher resolved surfaces generate smoother and more precise structural members of the volumetric structure. To obtain a high-resolution surface from a stream surfaces in $\mathcal{S}_{opt}$ we proceed as follows. First, we add all surface points of a selected stream surface, to a first-in-first-out queue. We then use the same algorithm as for the original surface creation but with a lower minimal distance requirement between surface points. This will generate new points between the locations of the original surface points and thus we obtain a higher resolution.

5.1.4.2 Volumetric solids

For topology optimization results, we want to obtain a geometric structure from our stream surfaces. To do so, we synthesize a structure from the selected surfaces and the layer-thicknesses obtained from the topology optimization. Extracting a volumetric solid from a point cloud in three dimensions is very similar to the volumetric reconstruction of surfaces from point clouds [Fuhrmann et al., 2014]. We create a distance field for each stream surface that attains value one for stream surface points and value zero for points that are one layer-thickness or more away from the stream surface. We then compute a voxel-based maximum of the distance fields of all stream surfaces and compute the boundary of the volumetric solid as a triangle mesh using dual contouring with the iso-value 0.5 [Ju et al., 2002]. Note that the iso-value 0.5 is chosen since the resulting structural lamination should be centered at the stream surface. A more detailed description can be found in Paper-III

5.1.4.3 Tapering structural members

Computing the distance field in the above-stated manner yields one problem. We will see tapering structural members of the volumetric solid depending on the divergence of the layer-normal field.Figure 5.11 depicts this problem. The

tapering structural members occur since the homogenization approach only describes local layer-thicknesses. Integration-based de-homogenization approaches account for this by the use of parameterizations. If a voxel is inside the final structure or not depends on the parameterization value and not on the distance to the closest iso-contour. Since the parameterization will always change by one integer from one iso-contour to the neighboring one, integration-based methods do not create tapering structural members. Our approach creates tapering structural members since we do not account for the variation of spacing between stream surfaces and only assign the local widths.

To obtain non-tapering structural members, we compute, in two dimensions, the distance to the neighboring streamlines for each line segment. First, we mark all points of a given streamline close to crossing streamlines and combine them into clusters. Figure 5.11b depicts these clusters. We then use the distance between the clusters on a streamline to measure the spacing between crossing streamlines. Now we can compute a correction factor to account for the deviation of the actual spacing from the desired spacing γ. We assign the correction values to the near segments of the crossing streamlines. When we compute the volumetric solid we can multiply the layer-thicknesses with these correction values to get rid of tapering structural members as shown in Figure 5.11c. We obtain a decrease in compliance of around 2.7% by removing tapering structural members from the example in Figure 5.11.

In three dimensions, this approach would need a hexahedralization of the surface results. This is hard to achieve with our current hexahedralization explained in Section 5.1.4.4. The hexahedralization cannot handle stream surfaces converging towards the boundary conditions, i.e., a minimal distance is needed between stream surfaces. Further particular examples do not consist of a hexahedral structure, e.g., the torsion ball or the cantilever with only one active layer. Therefore, I believe that another approach is more promising than using hexahedra to compute correction values. From the surface of describing our volumetric solid, we can create a tetrahedral mesh describing the structure. We could then use such a tetrahedral description to do shape optimization as proposed in Christiansen [2015]. This would correct tapering structural members and could improve compliance values by correcting possibly miss-aligned or forking stream surfaces. It should also be noted that for multi-load problems, an approach using shape optimization seems far more promising.

5.1.4.4 Hexahedral meshes

Extracting a hexahedral mesh from the stream surfaces $\mathcal{S}_{opt}$ can be of interest since the an-isotropy of the frame fields is preserved by our approach. However,

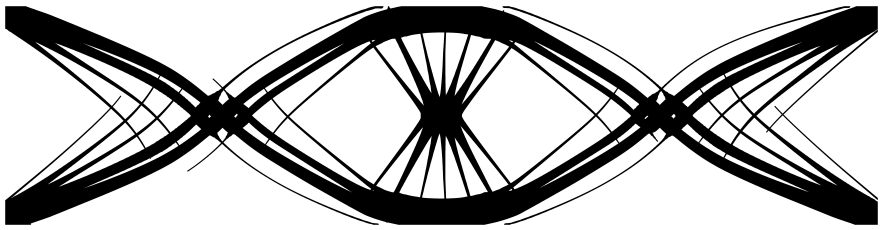

(a) De-homogenization using no correction values for the layer-thicknesses. The shown Figure has a compliance-volume value of $C \cdot V = 7.90$.

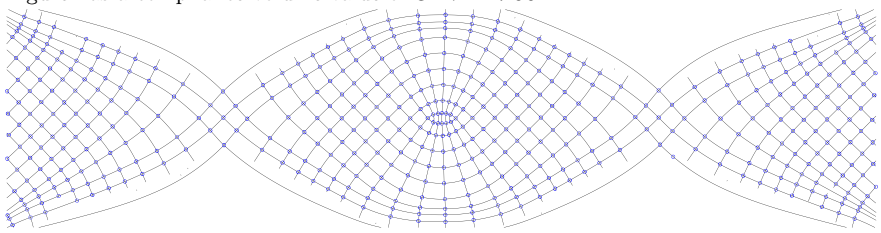

(b) Mesh used for the computation of the correction values. The blue circles indicate the clusters of intersection points found. If not both orthogonal segments exist a one-sided correction value is computed.

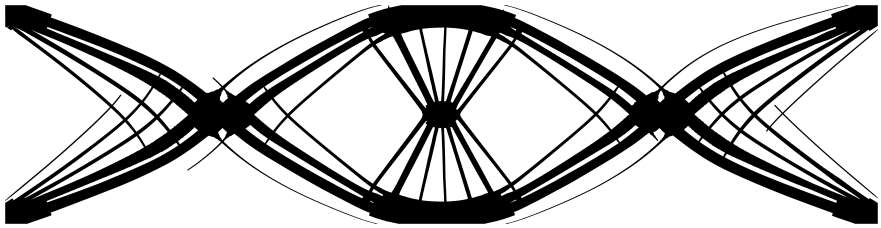

(c) De-homogenization using correction values for the layer-thickness. Note how the tapering bars problem is resolved. The shown Figure has a compliance-volume value of $C \cdot V = 7.69$.

Figure 5.11: Comparison between using and not using correction values on the layer-widths. The usage of the local distance between the layer-thicknesses decreases the compliance by around 2.7%.

the hexahedralization can not be used for topology optimization fields since a minimal distance between stream surfaces is needed. But fields arising from the homogenization approach have often laminations converging towards the boundary conditions. A detailed description of the hexahedralization can be found in Paper-III. I will give here a summary of the approach.

The hexahedra extraction is split into two parts. First, a graph is constructed containing all stream surface crossings, and then a hexahedralization is obtained by computing the dual thereof. As a first step, one creates an initial graph, where all stream surface points are denoted as vertices, and closeby vertices are

connected up by edges. Note that all graph vertices fall in one of the following classes

- *surface vertices* are vertices whose neighbors belong to the same stream surface,
- *intersection vertices* are vertices whose neighbors belong to two stream surface, and finally,
- *triple intersection vertices* have neighbors belonging to three stream surfaces.

Surface vertices are discarded, and the clusters of triple intersection vertices are collapse to a single cluster center. At each of these cluster center an instance of Dijkstra's algorithm is started assigning to each intersection vertex the minimal distance from a cluster center. When all intersection vertices have been assigned a minimal distance to a cluster, one can find the connection between two clusters by simply looking at neighboring intersection vertices that have been reached from different clusters. In a separate graph containing only the cluster centers, one can then connect up the corresponding two clusters. This second graph is called the *spatial twist continuum* (STC) graph. As Murdoch et al. [1997] observed the dual of the STC graph is a hexahedral mesh, which is computed in the final step.

5.1.5 Implementation and results

Our implementations are in C++ and Matlab. Codes related to the creation and manipulation of surfaces are primarily written in C++. Codes for selecting surfaces are running in Matlab by use of the CVX package [Grant et al., 2008, 2014] and the Mosek solvers [ApS, 2021].

Note that the generation of the stream surfaces and the synthesis of volumetric are easy to parallelize. However, the subselection cannot be parallelized but contributes only a fraction of the total runtime, as indicated in Table 5.1.

5.1.5.1 Missing structural members and field alignment – a comparison

As discussed in subsection 5.1.1 our method aims to circumvent the problem of missing structural members due to enforcement of alignment to the input field

Table 5.1: In this table, we show the statistics for the different steps in our pipeline. The first three blocks of rows offer relevant statistics for the initial point sampling of stream surfaces, the selection of optimal stream surfaces, and the super-sampling of the selected stream surfaces. The fourth block reports statistics for generating the volumetric solids, and the fifth block shows the time to run the hexahedralization algorithm. We then report in the sixth block the overall runtime of our approach. We include the times for the homogenization-based topology optimization and document them in the last block for completeness. Note how our algorithm is only a fraction of the topology optimization runtime.

	Cantilever (3 layers)	Cantilever (1 layer)	Electrical Mast	Torsion Sphere	Sphere	Helix	Cylinder
$\lvert\mathcal{S}\rvert$ (Number of stream surfaces)	480	478	450	374	480	170	400
Generating $\mathcal{S}$ (runtime)	20 min	28 min	17 min	1h 51 min	49 min	1 h 4 min	1 h 1 min
Average points per surface	961	1 351	667	5 043	2 019	5 082	1 906
Subselection (runtime)	45 sec	53 sec	2 min 5 sec	2 min 31 sec	39 sec	50 sec	37 sec
$\lvert\mathcal{S}_{opt}\rvert$	38	22	35	4	27	24	41
Super-sampling (runtime)	2 h 30 min	3 h 18 min	1 h 19 min	1 h 30 min	1 h 52 min	2 h 9 min	6 h 20 min
Average points per super-sampled surface	9448	9 735	3 483	58 148	25 073	26 320	15 535
Output volume dimension	$700 \times 350 \times 350$	$700 \times 350 \times 350$	$266 \times 266 \times 800$	$500 \times 500 \times 500$			
Solid generation (runtime)	13 min 42 sec	11 min 3 sec	5 min 48 sec	8 min 30 sec			
Hexahedralization (runtime)					1 min 24 sec	23 sec	38 sec
Summed runtime	3 h 04 min	3 h 58 min	1 h 44 min	3 h 32 min	2 h 43 min	3 h 14 min	7 h 20 min
Topology optimization time	7 h 48 min	9 h 54 min	22 h 20 min	40 h 21 min			

when using an integrative method to create a parameterization. As discussed in Groen and Sigmund [2018], Paper-I and Paper-II, alignment of the final structure to the input field needs to be enforced by a constraint when adapting integrative approaches as Bommes et al. [2009], Kälberer et al. [2007], and Nieser et al. [2011]. This is done by enforcing the parameterization's gradient to be orthogonal to the second (and third) normal direction. However, if this alignment is too strict, the gradient of the parameterization may become almost zero in large regions. This, in turn, can then lead to overly thick structural members or to missing structural members especially around singularities as discussed in Paper-II. The new approach creates well-aligned structures before selecting a subset, eradicating the problem since we cannot suffer from vanishing gradients, as we do not integrate the fields. We show an example in Figure 5.12. Note that the same behavior can be observed in three dimensions.

The structure shown in Figure 5.12a has been obtained by de-homogenizing a 320×80 element topology optimization result using an integrative approach proposed by Paper-II. Note how there are missing structural members above and underneath the singularity. The structure has a compliance $C = 26.46$ and a volume fraction of $V = 0.275$. For comparison, we use the compliance-volume value $C \cdot V = 7.30$. In Paper-II we obtained compliance-volume values of 7.05, 7.48, 7.63, and 21.39 for different alignment weights at the same resolution. Here 7.05 is the best performing structure at an intermediate alignment weight,

and 21.39 is a failure case.

Figure 5.12b shows the structure created by the new subselection approach also using a 320×80 element result. Note that the new approach yields a structure with evenly spaced structural members. The structure has a compliance $C = 27.67$ and a volume fraction of $V = 0.269$. The compliance-volume value for this structure is $C \cdot V = 7.44$. Note that this value is only 5.5% worse than the best value from Paper-II. Moreover, with the new approach we do not need to tune an alignment weight, and do not risk a failure case due to bad alignment or zero gradients in a parameterization.

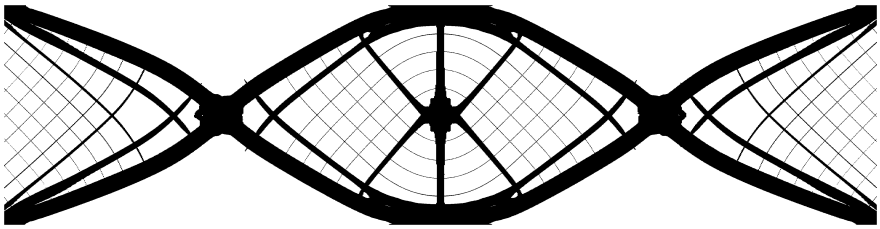

(a) De-homogenization using an integrative approach proposed in Paper-II yielding missing structural members around the singularity, where the gradients have become almost zero. A resolution of 320×80 is used as an input mesh. The shown Figure has a compliance-volume value of $C \cdot V = 7.30$. In Paper-II we obtained compliance-volume values of 7.05, 7.48, 7.63 and 21.39 for different alignment weights, where 7.05 was the best performing structure at an intermediate alignment weight and 21.39 was a failure case.

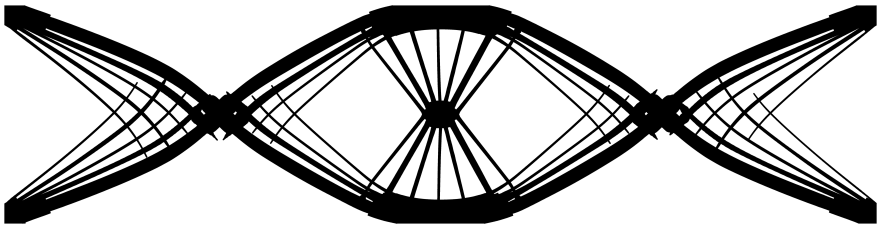

(b) Our new approach yields a structure with evenly spaced structural members for the same 320×80 input field as used above. The compliance-volume value for this structure is $C \cdot V = 7.44$ and is therefore a mere 5.5% worse than the best value from Paper-II. However, with our approach we do not risk a failure case.

Figure 5.12: Comparison between an integrative approach based on Paper-II yielding missing structural members and our new approach which creates evenly spaced structural members.

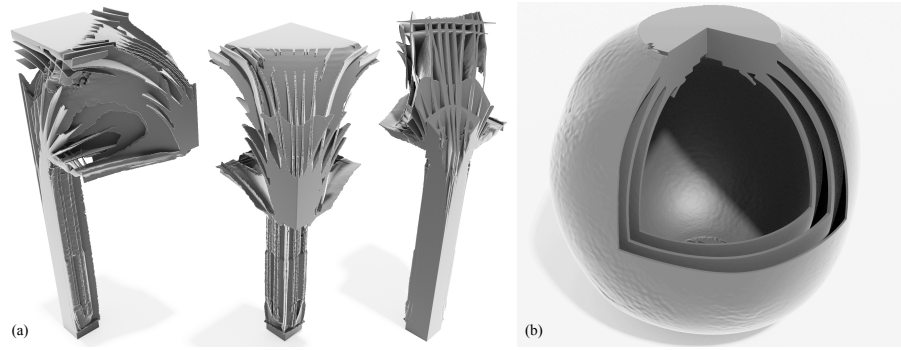

Figure 5.13: This figure show two topology optimization examples created with our method from subsubsection 5.1.4.2. In Figure a we see the electrical mast example introduced in Geoffroy-Donders et al. [2020]. We show here three angles (side, front and back), where in the rightmost image showing the mast from the back, the top has been cut away to reveal the interior of the structure. In Figure b we show the Michell torsion sphere example introduced in Paper-I, where the boundary conditions with torsion applied are located in the top and the botton. Note that we cut out an eigth to reveal the interior laminations of the torsion sphere.

5.1.5.2 Volumetric structures from topology optimized fields

We ran various input fields from topology optimization through our pipeline. The fields were generated by the same method as for Paper-I. The timings of the field generation and the de-homogenization are reported in Table 5.1, where we see that the topology optimization dominates over our de-homogenization approach. In Figure 5.13a we see a quarter of an electrical mast as proposed by Geoffroy-Donders et al. [2020]. The fields generated for the electrical mast example contain spurious singularities in fully solid regions and the void due to the microstructure being isotropic (solid) or non-existent (void). Nevertheless, we produce very smooth surfaces, since our stream surfaces do not need to expand into solid or void regions. In Paper-I we made use of the fact that singularities only arise in fully solid or void regions by combing the fields in intermediate regions first, such that the spurious singularities cannot create seams in the combed field that extend into the intermediate regions. However, we had no control or guarantee over how much singularities influence thee designs since we still relied on the orientations in solid and void for integration, although we recomputed the orientations for such elements.

On the right, in Figure 5.13 we show our version of the torsion sphere example proposed in Paper-I that was based on Michell's famous torsion sphere [M.C.E., 1904]. Note that since we use optimal rank-3 microstructures, we do not obtain

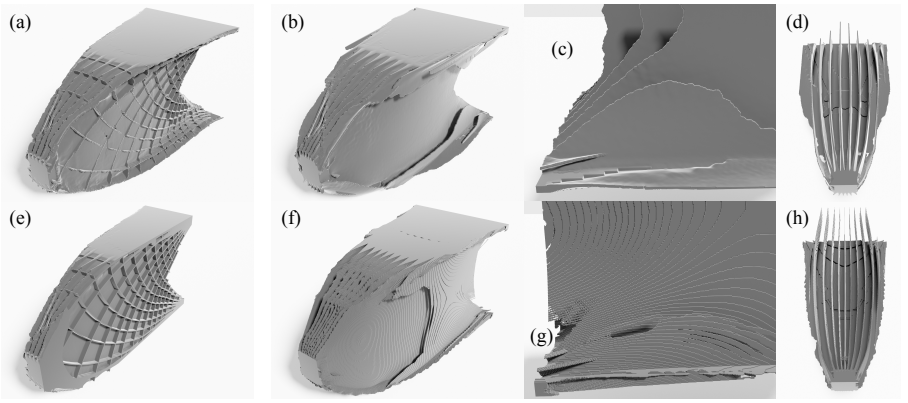

Figure 5.14: On the left, (a,e) show a cantilever produced from a homogenization solution where all three layers have been forced to be active. The images on the right show a comparison of our results for the cantilever (b,c,d) with the results from Paper-I (f,g,h).

a truss structure, but a stiffer layer structure [Sigmund, Aage, et al., 2016].

Figure 5.14 shows the three-dimensional version of Michell's cantilever. We compute de-homogenization results for two versions. In Figure 5.14a, we depict a solution for the cantilever where we enforce that either all three layers have a layer-thickness of more than 5% or that all layer-thicknesses are zero. Such a design is great for resistance against buckling. Note that due to all three layers being enforced to have non-zero layer widths outside of the void, the microstructure orientation becomes unique in this example. Spurious singularities only arise in solid and void regions. A cut section through the structure is given in Figure 5.14e.

In Figure 5.14b, we show the second version of the cantilever that we consider. These input fields have been created without any enforcement on the layer-thicknesses and correspond to the cantilever from Paper-I. A comparison of the results with Paper-I is given, first on a visual level in Figures 5.14b, c, d, f, g and h, and then in terms of compliance and volume in Table 5.2.

In Figures 5.14b and f we see the full de-homogenized structures. The two structures are very alike. Note that in Paper-I we used some additional fine-scale evaluation to remove unused excess material, i.e., low strain energy elements. This puts the structure from Paper-I at a slight advantage over the stream surface-based one, since we do not incorporate such a step for our structure in Figures 5.14b-d. Figures 5.14c and g show a detail and Figures 5.14d and h show horizontal cuts through the structures.

Since our input fields differ from the ones used in Paper-I we cannot compare the values in Table 5.2 with too much emphasis. Note also that in Paper-I we evaluated the designs using a fine scale $960 \times 480 \times 480 = 221\ 184\ 000$ finite element model, whereas in Paper-III we only evaluate our model on $512 \times 256 \times 256 = 33\ 554\ 432$ elements. We therefore also only compare our result to the best performing value from Paper-I. The most meaningful value is certainly $\frac{C_s \cdot V_s}{C_h \cdot V_h}$ which sets the compliance-volume value of the de-homogenized structure to the compliance-volume fraction reported by the topology optimization. We see that we are a mere 5.5% off the best performing structure from Paper-I, although we do not yet treat the tapering structural members. We also have not yet done a parameter study to find the best de-homogenization parameters.

Table 5.2: Comparison of our results for the cantilever example with results obtained in Paper-I. We use the following abbreviations: V_s = volume of the de-homogenized structure, C_s = compliance of de-homogenized structure, V_h = volume of the homogenization-based topology optimization solution, C_h = compliance of the homogenization-based topology optimization solution Note that in Paper-I we evaluate the design on a $960 \times 480 \times 480$ finite elements model, whereas here we only evaluate our model on $512 \times 256 \times 256$ elements.

Cantilever	Paper-I	Paper-III
C_h	226.68	228.45
V_h	0.1000	0.1000
C_s	243.31	223.72
V_s	0.1021	0.1181
$C_s \cdot V_s$	24.845	26.428
$\frac{C_s \cdot V_s}{C_h \cdot V_h}$	1.0960	1.1568

5.1.5.3 Hexahedral meshes from boundary aligned and closed-form fields

We developed the subselection approach with the goal of creating geometric structures from fields arising from the homogenization approach. However, even with our simple approach to hexahedralization we are able to extract hexahedral meshes for certain boundary-aligned and closed form fields. For example, we are able to obtain a highly anisotropic mesh from a cylinder field whose cut section show a index 1 singularity (see Figure 5.16). We are also able to obtain anisotropic hexahedras for a spiraling field, although we again need to cut out the singular region (see Figure 5.16). Note that the need to cut out a rather large area around the singular curve is due to the minimal distance requirement of the hexahedralization and not due to the singular curve itself. In fact, for a simple

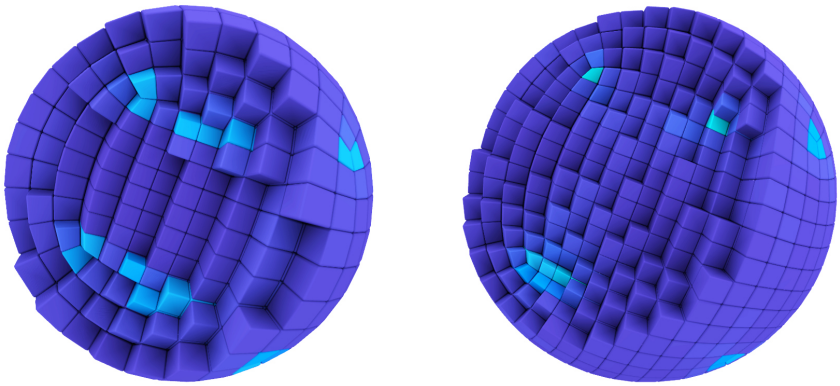

Figure 5.15: Comparison of a hex mesh of a sphere produced by our method based on an octahedral frame field generated using the method of Palmer et al. [2019] and a similar hex mesh produced from a field created with the method of Corman et al. [2019] and hex meshed using CubeCover in an implementation by David Bommes (right). For both visualization we use Bracci et al. [2019]. The hexahedra are colored according to the scaled Jacobian.

boundary aligned mesh, where cut sections only show $^1/_4$ singularities we can extract a reasonable hexahedral mesh without the need to cut out singularities since the frame field has been optimized for smoothness. This can be seen in Figure 5.15.

5.1.6 Conclusion and discussion

In the previous sections, I have presented a novel method for de-homogenization. The so-called subselection approach does, contrary to previous work, not use integration to compute a parameterization. Instead, it finds a set of global structural members (streamlines/stream surfaces) and then creates an evenly spaced subset. In Section 5.1.2.1, I discussed the occurrence and location of singular curves in three dimensions. The obtained knowledge lets us understand three-dimensional singularities in layer-normal fields much better. The finding that traversal singular curves must align with a layer-normal has been crucial since we, therefore, do not need to treat traversal singular curves with the subselection approach. Actually, we do not need to consider singularities at all, as we found traversal singular curves to be the only singular curves outside the void or fully solid regions. This means that, to my knowledge, the subselection approach is the first method to de-homogenize singularity containing three-dimensional single-load problems. Of course, the fields from the homogenization approach

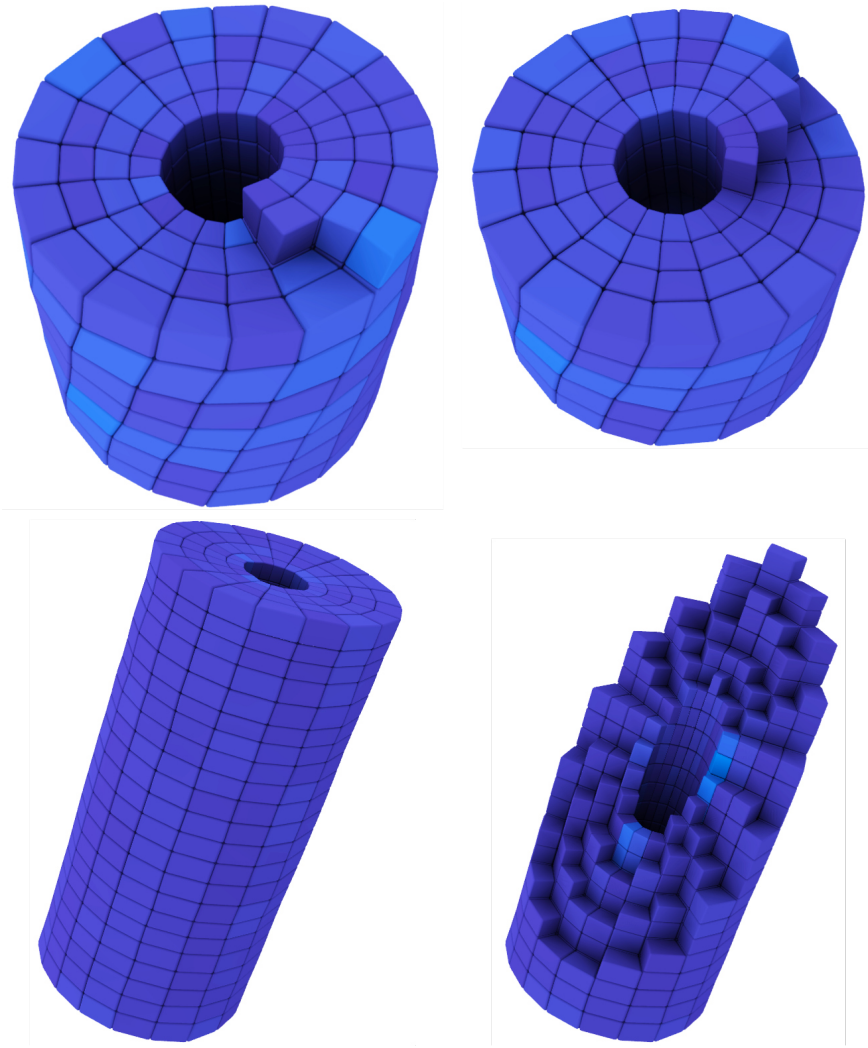

Figure 5.16: In the top row, we see a hex mesh generated using our method on a field describing a helicoid. Note that the underlying field is non-integrable. On the left, we see the entire mesh, whereas on the right, we have removed several layers of hexahedra. In the bottom row, we see a hex mesh generated on a cylindrical field. Note how the shape of the hexahedra changes dramatically from the outside towards the cut out singular curve. On the right, we peel away several layers of hexahedra, which reveals that the minimal edge-length is significantly smaller than the maximal edge-length. Note that we desire this from a field describing an anisotropic mesh.

need to be aligned well enough with the underlying stress fields for active layers. However, since there exists an optimal solution aligned with the principal stress directions [Norris, 2005; Pedersen, 1989], the challenge of obtaining well-aligned layer-normal fields lies in the field of homogenization-based topology optimization and not within de-homogenization. I am convinced that, especially in combination with the observations made in Paper-I and Section 4.3, such fields will be available soon.

In Paper-III, we obtained well-performing structures without treating singularities explicitly. Further, we have shown that the proposed energy can be beneficial for other use cases as, for example, an-isotropic hex-meshing without prescribed edge lengths. In this thesis, I discussed a way to solve the tapering bar problem in two dimensions.

In three dimensions tapering structural members have yet to be addressed. I believe that combining the results from the subselection approach with shape optimization as done in [Nguyen et al., 2020] will decrease the compliance in a similar amount as the 2.7% that I have achieved in two dimensions. Future research on de-homogenization should consider more singularity-containing examples and should create stream surfaces using layer-thickness priority. We also identified the expansion to multi-load as future research in Paper-III. I will, in the next section, present my work on de-homogenizing two-dimensional multi-load designs.

5.2 Using the subselection approach for multi-load designs

In this section, I would like to focus on using the subselection approach for problems with multiple loading cases. Multi-load problems yield far more complex fields than single-load problems. On the one hand, as discussed in Section 2.4.1, the optimal microstructure for multi-load designs consists of a rank-3 material in two dimensions and a rank-6 material in three dimensions. On the other hand, the homogenization-based results for multi-load problems are non-unique, and several orientation and thickness combinations may yield the same optimal stiffness.

For homogenization-based topology optimization to become useful for engineers, the de-homogenization of multi-load problems needs to be addressed. However, the de-homogenization of multi-load examples is far more complex than for single-load problems. So far, there exists, for example, no notion of singularities or seams. It is thus unclear if integrative approaches can be expanded to more complex multi-load examples. For particular layer-normal fields, one can extract three continuous 1-direction fields and parameterize them. However, at the moment, the fields need to be labeled by hand, although a method using combing might be viable.

When I designed the energy for the subselection approach, I realized its applicability to multi-load designs. There is no need to sort the fields by hand or to have a significant understanding of the multi-load design before de-homogenization. Instead, the energy automatically accounts for the presence or absence of the different fields as follows. For each location, we create three probe points in the energy. Then each probe point gets assigned one of the three field directions. If a probe point is assigned to a non-existing layer-normal or if the layer-thickness is zero, we set the target amount of streamlines for this probe point to zero. The optimizer will then not try to position a streamline at that probe point. Note that as for the single-load case problems, we only need local information. An example of an energy for a multi-load example can be seen in Figure 5.20.

Multi-load results are much harder to de-homogenization than single-load results. One of the reasons is that the layers are not orthogonal anymore. Consider the example depicted in Figure 5.17, where the structure is supposed to consists of only one active lamination. In element f_1, the lamination is described by the red normal n_2 and thickness $w_2 = 0.1$. However, at the same time, there exists a second layer with normal n_1 and width $w_1 = 0.01$ in f_1. In the example in Figure 5.17, the widths of the layers are switched in element f_2, i.e., $w_1 = 0.1$ and $w_2 = 0.01$. And in element f_3, we obtain the same widths again as in

element f_1. Note that this interchangeability of layer widths cannot occur for single-load problems due to their orthogonal layers. Both tracing streamlines and combing the fields struggle with the above-described problem. The sudden drop of the layer-thickness to zero produces holes in the de-homogenized structure as shown for a twice loaded cantilever in Figure 5.19a. Figure 5.19b shows the same multi-load results as Figure 5.19a, where both layers were assigned the larger of both layer-thicknesses if their normals enclosed an angle smaller than five degrees. However, one should not do this kind of post-processing normally. The intent here is simply to show one of the difficulties arising when going from single-load to multi-load results. Post-processing of results obtained by the homogenization approach risks to produce structures that were not initially intended by the optimizer and should therefore not be taken lightly.

Luckily researchers of the homogenization method have made it possible to enforce that all layers obtain a minimal width when one of the three layers passes a certain minimum width value. This leads to the very clean fields shown in Figure 5.21a and Figure 5.23a that are much easier to de-homogenize. If we trace streamlines in these fields we obtain the sets of streamlines depicted in Figure 5.21b and Figure 5.23a.

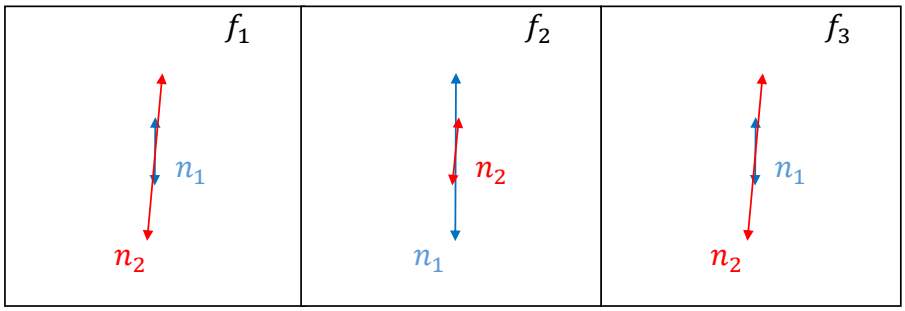

Figure 5.17: Multi-load problems produce layer fields that are much harder to de-homogenize than single-load problems. One example is shown in this figure, where the structure only describes one layer, but where two very similarly orientated layer are assigned alternating widths. Note that this interchangeability of layer widths cannot occur for single-load problems due to their orthogonal layers.

Figure 5.22a and Figure 5.24a show the well-spaced sets of streamlines one obtains from the subselection approach. We can then assign the layer-widths to the streamlines as we did for the single-load case examples to synthesize the geometric structures depicted in Figure 5.22b and Figure 5.24b.

With the subselection approach for multi-load problems, there is no need to sort the fields by hand or to have a significant understanding of the problem

beforehand. Instead, the method can help engineers to get an overview of what the optimizer deems an optimal design very fast. However, we can see tapering structural members in Figure 5.22b and Figure 5.24b. Something that I hope can be solved with a few shape optimization steps. Of course, it will be challenging to prevent surfaces from forking in three dimensions since one suddenly has six directions. Therefore, I believe that it would be advisable to, at first, use the rank-4 microstructures for three-dimensional designs. The fields are likely to be easier to handle, and the designs should only perform around 8% worse than rank-6 microstructures [Wang et al., 2021].

In general, the challenges of creating stream surfaces in multi-load layer-normal fields are similar to combing the fields. Making a mistake while combing or choosing the wrong surface normal will both have global influence. However, one can imagine that the subselection approach should be more robust since a wrongly selected layer-normal only influences the creation of a single stream surface. Further, the subselection is likely to exclude that stream surface if some suitable, non-forking surfaces cover the same area. On the other hand, a wrongly chosen field label for combing approaches will always influence the whole parameterization and the resulting structure. To create surfaces more robustly, one could possibly adopt the idea of using layer-thickness information to stream surface creation. Stream surfaces could be expanded in intermediate regions first using a layer-thickness-based priority queue, and one could choose the surface normals based on the layer-thickness energy described in Section 4.3.6.2.

If we look at the largest examples of density-based compliance optimization [Aage et al., 2017; Baandrup et al., 2020], we see that the obtained designs from the optimization need some human interpretation to create manufacturable structures. However, it is the designs produced by the topology optimization that make it possible to develop those well-performing, interpreted structures. The topology optimization results yield the basis needed for a human designer to identify an optimal solution. For example, tiny features in the airplane wing of Aage et al. [2017] show that new, organic-like features yield an improvement over previous designs. Similarly, Baandrup et al. [2020] identify curved sheets inside the bridge girders to be more optimal than conventional designs. I believe that three-dimensional de-homogenized multi-load structures, at first, will require interpretation as well, even for simple examples. That, however, does not mean that engineers will not profit from an understanding of what the topology optimization believes to be an optimal solution.

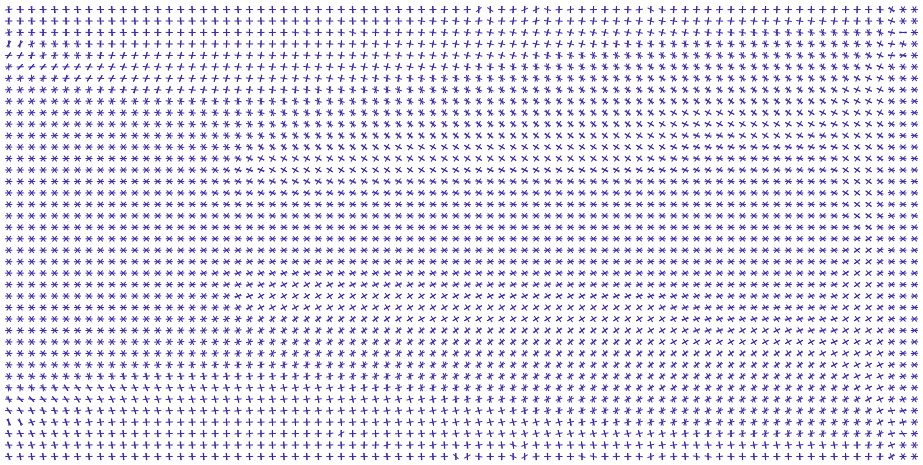

Figure 5.18: Fields obtained for a twice loaded cantilever without any restriction on the layer-thicknesses.

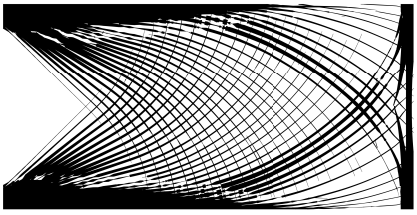

(a) Without any post-processing one can clearly see how certain layers have holes since their width suddenly jumps to zero.

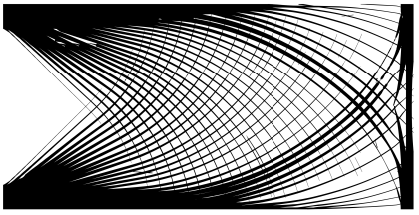

(b) For two layers with normals that enclose an angle of less than five degrees the widths have been post-processed. Per element the larger width was assigned to both layers. Note, that such post-processing is not recommendable, but that the subselection approach allows us to investigate such problems and gain an understanding of what is happening very easily.

Figure 5.19: De-homogenized structures for the twice loaded cantilever without any restriction. The fields for this example are shown in Figure 5.18.

Figure 5.20: An example of thee summed energies for the streamlines chosen by the optimizer for a multi-load examples. The de-homogenized structure of the same example is depicted in Figure 5.19a.

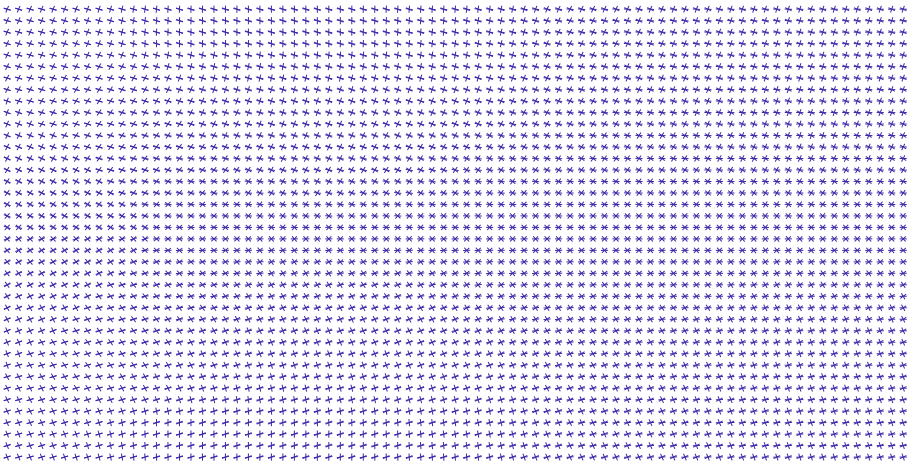

(a) Layer-normal fields obtained from the homogenization approach for a twice loaded cantilever design.

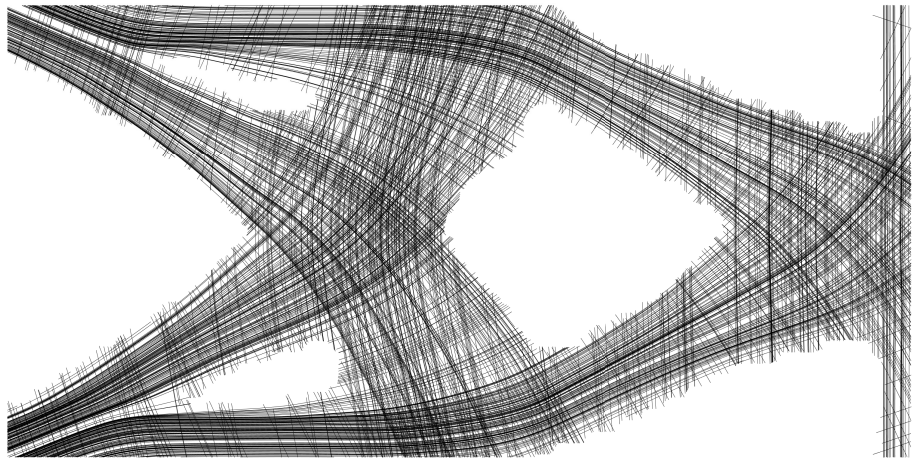

(b) Full set of streamlines created for a twice loaded cantilever design.

Figure 5.21: This figure shows the layer-normal fields and the traced streamlines for a twice loaded cantilever design.

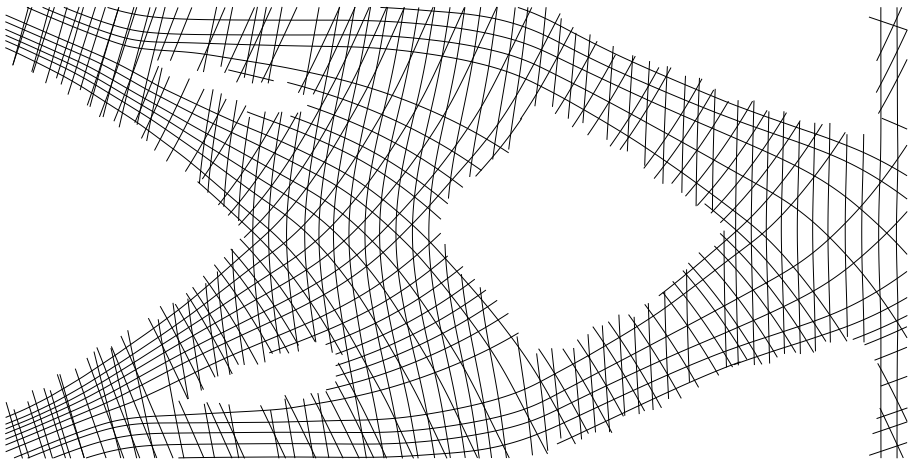

(a) Chosen set of streamlines for a twice loaded cantilever design.

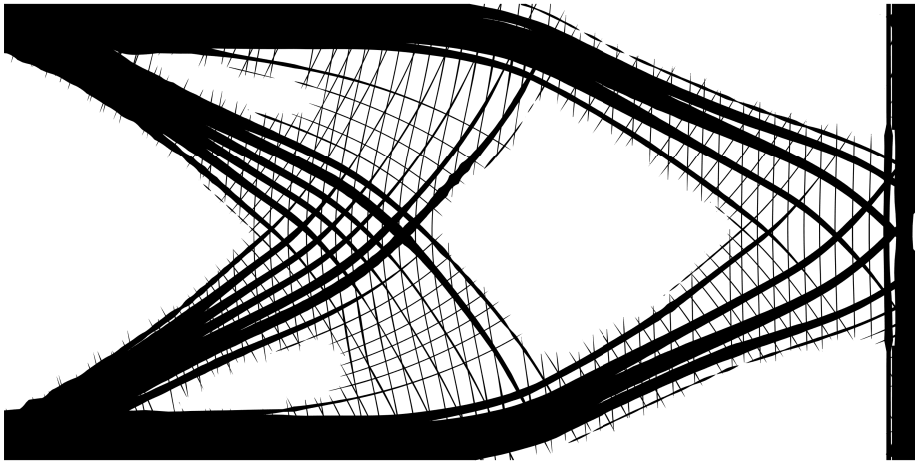

(b) Structure obtained from the subselection approach for a twice loaded cantilever design.

Figure 5.22: This figure shows the selected subset of streamlines and the resulting structure for a twice loaded cantilever design.

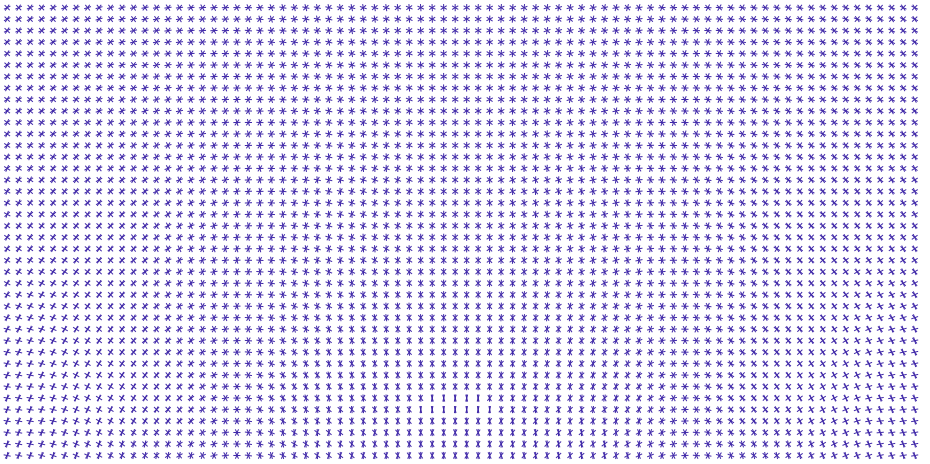

(a) Layer-normal fields obtained from the homogenization approach for a twice loaded bridge design.

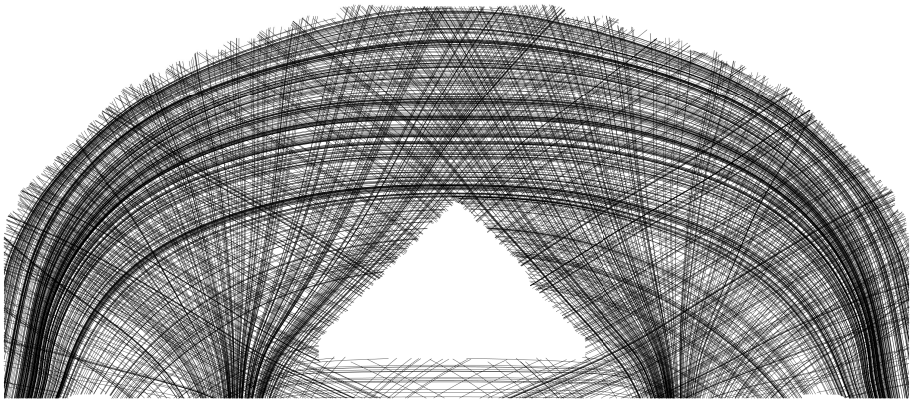

(b) Full set of streamlines created for a twice loaded bridge design.

Figure 5.23: This figure shows the layer-normal fields and the traced streamlines for a twice loaded bridge design.

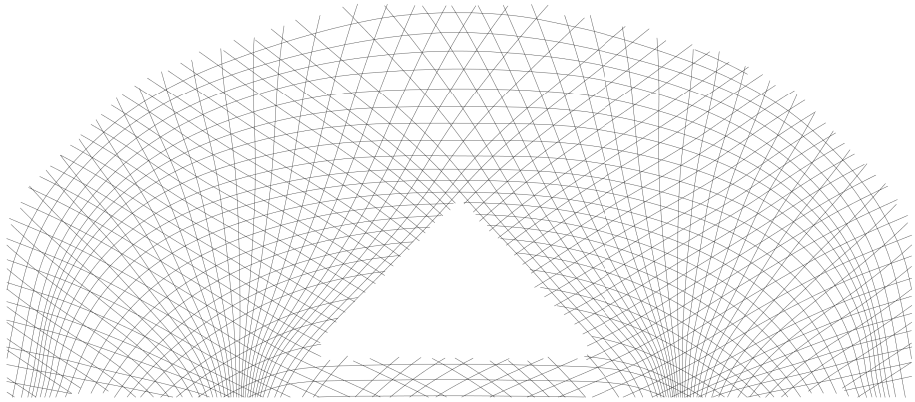

(a) Chosen set of streamlines for a twice loaded bridge design.

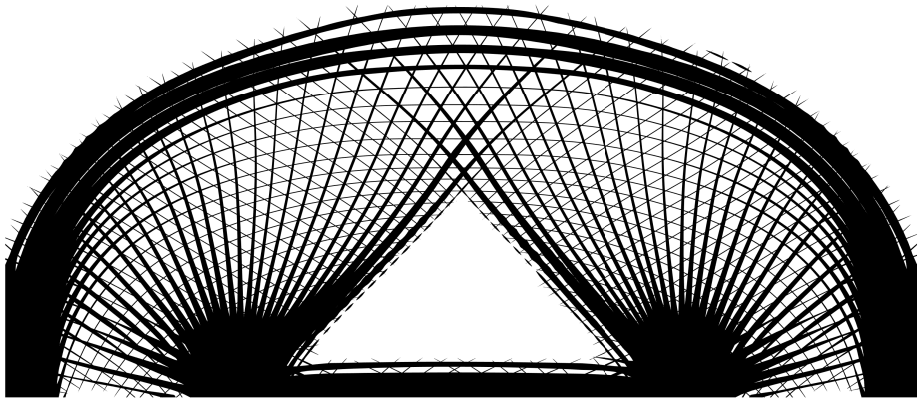

(b) Structure obtained from the subselection approach for a twice loaded bridge design.

Figure 5.24: This figure shows the selected subset of streamlines and the resulting structure for a twice loaded bridge design.

Chapter 6

Concluding remarks

In this thesis, I have presented research in de-homogenization to synthesize geometrical structures from topology optimized multi-scale designs. The main goal was to obtain structures that perform well from a mechanical point of view. Noise, singularities, non-uniqueness, and the lack of global connectivity were the main challenges to achieve this. I would like to revisit the questions from the beginning of my Ph.D. project, as mentioned in Chapter 1.

- Question 1: What kind of singularities arises in homogenization-based topology optimization results, and where are they located?
- Question 2: How can we de-homogenize three-dimensional, singularity-free results obtained by the homogenization approach?
- Question 3: How can we expand de-homogenization to allow the usage of more challenging, singularity-containing problems in two and three dimensions?
- Question 4: Is there a way to expand possible findings to the previous questions to examples with multiple loading cases?

Through this Ph.D. project, we gained a better understanding of the layer-normal fields arising from homogenization-based topology optimization. I have investigated singularities in two and three dimensions and related them to the layer-normal thickness and the principal stress directions [Paper-II, Paper-III]. We can now understand better how de-homogenization methods need to be designed to account for occurring singularities (Question 1).

The research into how regularization and starting orientations influence the final layer-normal fields [Paper-II, Paper-III] yielded much easier fields to de-homogenize, making it easier to create well-performing structures. Here, future research should look into how we can benefit from the gained understanding of singularities to produce layer-normal fields that are easier to de-homogenize. Especially, periodically updating the layer orientations after a certain number of iterations to align to the principal stress directions seems promising to me. This would allow to simultaneously use regularization and profiting from the singularities of principal stress directions.

In two dimensions, we are now able to de-homogenize examples that contain singularities using an integration-based approach, thanks to the usage of preexisting methods from computer graphics (Question 3). The proposed integration-based approach of Paper-I allows to de-homogenize singularity-free examples (Question 2). The understanding of how we can use layer-thicknesses and density for combing yields not only advantages for de-homogenizing current examples in three dimensions but might be expandable to multi-load examples in the future. I believe the performance gain of three orders of magnitude that we saw for single-load three-dimensional problems should motivate further research to bringing de-homogenization to a level where engineers can use it in everyday work.

The novel and first non-integrative de-homogenization approach of selecting stream surfaces has made it possible to address a multitude of problems. The subselection method allows handling layers separately, circumventing the wall problem and paving the path for three-dimensional multi-load problems. The subselection approach is the first method to enable the de-homogenization of three-dimensional singularity-containing examples (Question 3). For multi-load examples, the subselection approach allows extracting structures in two dimensions without sorting the normal fields by hand. Although undoubtedly complex, I am positive that an expansion to three dimensions is possible in the future (Question 4).

Looking back at the questions from the beginning of this Ph.D. project, I think that the state of the art has been progressed for all questions. However, a vast amount of research is left to be done, and the methods proposed in this thesis are not robust enough for everyday usage at the moment. Both integration-based methods and stream surfaces have advantages but also disadvantages. With integration-based methods, one needs to fix the problem of missing structural members and start meshing and combing only active layers. For non-integrative approaches, one needs to deal with the tapering structural members by either computing correction values as shown for two-dimensional problems or, arguably more straightforward, using tetrahedron-based shape optimization to optimize the results. It is important to note that a de-homogenization method

can only profit from smoother layer-normal fields. I believe that research on de-homogenization is inseparable from researching the homogenization approach. Further, the proposed methods might have applications reaching beyond the mere use for de-homogenization since vector fields are a recurring topic throughout physical and mechanical research fields. It is my hope that homogenization-based topology optimization will soon make compliance minimization a widely used tool in everyday engineering.

Bibliography

[Aage et al., 2017] Niels Aage et al. "Giga-voxel computational morphogenesis for structural design". In: *Nature* 550.7674 (2017), pp. 84–86.

[Allaire, Belhachmi, et al., 1996] G. Allaire, Zakaria Belhachmi, and François Jouve. "The homogenization method for topology and shape optimization. Single and multiple loads case". English. In: *Revue Européenne des Éléments Finis* 5.5-6 (1996), pp. 649–672. ISSN: 1250-6559.

[Allaire, Bonnetier, et al., 1997] G. Allaire, Eric Bonnetier, et al. "Shape optimization by the homogenization method". English. In: *Numerische Mathematik* 76.1 (1997), pp. 27–68. ISSN: 0029-599X.

[Allaire and Francfort, 1993] G. Allaire and G. A. Francfort. *A Numerical Algorithm for Topology and Shape Optimization*. 1993. DOI: 10/gjhccq.

[Allaire, Geoffroy-Donders, et al., 2018] G. Allaire, Perle Geoffroy-Donders, and Olivier Pantz. "Topology optimization of modulated and oriented periodic microstructures by the homogenization method". In: *Computers & Mathematics with Applications* (2018).

[Allaire and Kohn, 1993] G. Allaire and Robert V. Kohn. "Optimal design for minimum weight and compliance in plane stress using extremal microstructures". English. In: *European Journal of Mechanics. A. Solids* 12.6 (1993), pp. 839–878. ISSN: 0997-7538.

[Allaire, 2002] Grégoire Allaire. "Shape Optimization by the Homogenization Method". In: (2002). DOI: 10/gjhccs.

[ApS, 2021] M. O. S. E. K. ApS. *MOSEK Fusion API for C++ manual, Version 9.2*. Jan. 2, 2021.

[Arora et al., 2019] Rahul Arora et al. "Volumetric Michell Trusses for Parametric Design & Fabrication". In: *Proceedings of the 3rd ACM Symposium on Computation Fabrication*. SCF '19. Pittsburgh, PA, USA: ACM, 2019.

[Avellaneda, 1987] Marco Avellaneda. "Optimal bounds and microgeometries for elastic two-phase composites". In: *SIAM Journal on Applied Mathematics* 47.6 (1987), pp. 1216–1228.

[Baandrup et al., 2020] Mads Baandrup et al. "Closing the gap towards super-long suspension bridges using computational morphogenesis". In: *Nature Communications* 11.1 (2020), pp. 1–7.

[Bendsøe et al., 1999] M. P. Bendsøe and O. Sigmund. "Material interpolation schemes in topology optimization". In: *Archive of Applied Mechanics* 69.9 (1999), pp. 635–654. ISSN: 1432-0681. DOI: 10/bf42th.

[Bendsøe, 1989] Martin Philip Bendsøe. "Optimal shape design as a material distribution problem". In: *Structural optimization* 1.4 (1989), pp. 193–202.

[Bendsøe and Kikuchi, 1988] Martin Philip Bendsøe and Noboru Kikuchi. "Generating optimal topologies in structural design using a homogenization method". In: *Computer methods in applied mechanics and engineering* 71.2 (1988), pp. 197–224.

[Bendsøe and Sigmund, 2004] Martin Philip Bendsøe and Ole Sigmund. *Topology Optimization*. Springer Berlin Heidelberg, 2004. DOI: 10/gjhccj.

[Bommes et al., 2009] David Bommes, Henrik Zimmer, and Leif Kobbelt. "Mixed-integer quadrangulation". In: *ACM Transactions On Graphics (TOG)* 28.3 (2009), p. 77.

[Bommes et al., 2012] David Bommes, Henrik Zimmer, and Leif Kobbelt. "Practical Mixed-Integer Optimization for Geometry Processing". In: (2012), pp. 193–206. DOI: 10/fzzp66.

[Bourdin, 2001] Blaise Bourdin. "Filters in topology optimization". In: *International Journal for Numerical Methods in Engineering* 50.9 (2001), pp. 2143–2158. DOI: 10/crv452.

[Bracci et al., 2019] Matteo Bracci et al. "HexaLab. net: An online viewer for hexahedral meshes". In: *Computer-Aided Design* 110 (2019), pp. 24–36.

[Bridson, 2007] Robert Bridson. "Fast Poisson disk sampling in arbitrary dimensions". In: *ACM SIGGRAPH* (Aug. 2007). DOI: 10/gf8tsr.

[Bruns et al., 2003] T. E. Bruns and D. A. Tortorelli. "An element removal and reintroduction strategy for the topology optimization of structures and compliant mechanisms". In: *International Journal for Numerical Methods in Engineering* 57.10 (2003), pp. 1413–1430. DOI: 10/fgh24r.

[Bruns et al., 2001] Tyler E. Bruns and Daniel A. Tortorelli. "Topology optimization of non-linear elastic structures and compliant mechanisms". In: *Computer Methods in Applied Mechanics and Engineering* 190.26-27 (Mar. 2001), pp. 3443–3459. DOI: 10/c5ctm4.

[Campen, Bommes, et al., 2012] Marcel Campen, David Bommes, and Leif Kobbelt. "Dual loops meshing. quality quad layouts on manifolds". In: 31 (2012), pp. 1–11. ISSN: 0730-0301. DOI: 10/gjhccn.

[Campen and Kobbelt, 2014] Marcel Campen and Leif Kobbelt. "Dual strip weaving. interactive design of quad layouts using elastica strips". In: 33 (2014), pp. 1–10. ISSN: 0730-0301. DOI: 10/gjhccm.

[Campen, Silva, et al., 2016] Marcel Campen, Cláudio T. Silva, and Denis Zorin. "Bijective maps from simplicial foliations". In: 35 (2016), pp. 1–15. ISSN: 0730-0301. DOI: 10/f89kvs.

[Chapra, 2012] Steven Chapra. *Applied numerical methods with MATLAB for engineers and scientists*. New York: McGraw-Hill, 2012. ISBN: 9780071086189.

[Cherkaev and Palais, 1996] A. Cherkaev and R. Palais. "Optimal design of three-dimensional axisymmetric elastic structures". In: 12 (1996), pp. 35–45. ISSN: 0934-4373. DOI: 10/fbpk4b.

[Cherkaev, 2000] Andrej Cherkaev. *Variational Methods for Structural Optimization*. Springer New York, 2000. DOI: 10/cpqpcr.

[Cherkaev, Krog, et al., 1998] Andrej V. Cherkaev, Lars A. Krog, and Ismail Kucuk. "Stable optimal design of two-dimensional elastic structures". English. In: *Control and Cybernetics* 27.2 (1998), pp. 265–282. ISSN: 0324-8569.

[Christiansen, 2015] Asger Nyman Christiansen. "Combined Shape and Topology Optimization". English. PhD thesis. 2015.

[Corman et al., 2019] Etienne Corman and Keenan Crane. "Symmetric moving frames". In: *ACM Transactions on Graphics* 38.4 (2019), pp. 1–16. DOI: 10/gg55cn.

[Deaton et al., 2014] Joshua D. Deaton and Ramana V. Grandhi. "A survey of structural and multidisciplinary continuum topology optimization: post 2000". In: *Structural and Multidisciplinary Optimization* 49.1 (2014), pp. 1–38. ISSN: 1615-1488. DOI: 10/f5nksp.

[Delmarcelle et al., 1994] Thierry Delmarcelle and Lambertus Hesselink. "The topology of symmetric, second-order tensor fields". In: *Proceedings of the conference on Visualization'94*. IEEE Computer Society Press. 1994, pp. 140–147.

[Díaz and Lipton, 1997] A. Díaz and R. Lipton. "Optimal material layout for 3D elastic structures". In: *Structural optimization* 13.1 (1997), pp. 60–64. ISSN: 1615-1488. DOI: 10/b2vft7.

[Díaz and Sigmund, 1995] A. Díaz and O. Sigmund. "Checkerboard patterns in layout optimization". In: *Structural optimization* 10.1 (1995), pp. 40–45. ISSN: 1615-1488. DOI: 10/bb358v.

[Díaz and Lipton, 2000] Alejandro R. Díaz and Robert Lipton. "Optimal Material Layout in Three-Dimensional Elastic Structures Subjected to Multiple Loads". In: *Mechanics of Structures and Machines* 28.2-3 (Aug. 2000), pp. 219–236. ISSN: 0890-5452. DOI: 10/fvcpsb.

[Díaz, Lipton, and Soto, 1995] Alejandro R. Díaz, Robert Lipton, and Ciro A. Soto. "A new formulation of the problem of optimum reinforcement of Reissner-Mindlin plates". In: *Computer Methods in Applied Mechanics and Engineering* 123.1-4 (June 1995), pp. 121–139. DOI: 10/cnsrvh.

[Francfort and Murat, 1986] G. A. Francfort and F. Murat. "Homogenization and optimal bounds in linear elasticity". In: *Archive for Rational Mechanics and Analysis* 94.4 (1986), pp. 307–334. ISSN: 1432-0673. DOI: 10/fvnbfp.

[Francfort, Murat, and Tartar, 1995] Gilles Francfort, Francois Murat, and Luc Tartar. "Fourth-order moments of nonnegative measures on S2 and applications". In: *Archive for Rational Mechanics and Analysis* 131.4 (1995), pp. 305–333. DOI: 10/d3d4sd.

[Fuhrmann et al., 2014] Simon Fuhrmann and Michael Goesele. "Floating scale surface reconstruction". In: *ACM Transactions on Graphics* 33.4 (July 2014), pp. 1–11. DOI: 10/zck.

[Gao et al., 2017] Xifeng Gao et al. "Robust Hex-Dominant Mesh Generation Using Field-Guided Polyhedral Agglomeration". In: *ACM Trans. Graph.* 36.4 (July 2017). ISSN: 0730-0301. DOI: 10/gbxfzd.

[Geoffrey-Donders, 2018] Perle Geoffrey-Donders. "Homogenization method for topology optmization of struc-tures built with lattice materials." PhD thesis. 2018.

[Geoffroy-Donders et al., 2020] Perle Geoffroy-Donders, Grégoire Allaire, and Olivier Pantz. "3-d topology optimization of modulated and oriented periodic microstructures by the homogenization method". In: *Journal of Computational Physics* 401 (2020), p. 108994.

[Goes et al., 2015] Fernando do Goes, Mathieu Desbrun, and Yiying Tong. "Vector Field Processing on Triangle Meshes". In: *SIGGRAPH Asia 2015 Courses*. SA '15. Kobe, Japan: Association for Computing Machinery, 2015. ISBN: 9781450339247. DOI: 10/gg6423.

[Grant et al., 2008] Michael Grant and Stephen Boyd. "Graph implementations for nonsmooth convex programs". In: *Recent Advances in Learning and Control*. Ed. by V. Blondel, S. Boyd, and H. Kimura. Lecture Notes in Control and Information Sciences. http://stanford.edu/~boyd/graph_dcp.html. Springer-Verlag Limited, 2008, pp. 95–110.

[Grant et al., 2014] Michael Grant and Stephen Boyd. *CVX: Matlab Software for Disciplined Convex Programming, version 2.1*. http://cvxr.com/cvx. Mar. 2014.

[Groen and Sigmund, 2018] J. P. Groen and O. Sigmund. "Homogenization-based topology optimization for high-resolution manufacturable microstructures". In: *International Journal for Numerical Methods in Engineering* 113.8 (2018). (online since April 2017), pp. 1148–1163. DOI: 10/gcw8jx.

[Groen, Stutz, et al., 2020] Jeroen P. Groen, Florian C. Stutz, et al. "De-homogenization of optimal multi-scale 3D topologies". English. In: *Computer Methods in Applied Mechanics and Engineering* 364 (June 2020), pp. 112–979. ISSN: 0045-7825. DOI: 10/gjhccg.

[Groen, Wu, et al., 2019] Jeroen P. Groen, Jun Wu, and Ole Sigmund. "Homogenization based stiffness optimization and projection of 2D coated structures with orthotropic infill". English. In: *Computer Methods in Applied Mechanics and Engineering* 349 (2019), pp. 722–742. ISSN: 0045-7825.

[Guo et al., 2020] Hao-Xiang Guo et al. "Cut-enhanced PolyCube-maps for feature-aware all-hex meshing". In: *ACM Transactions on Graphics (TOG)* 39.4 (2020), pp. 106–1.

[Hammer et al., 1997] V. B. Hammer et al. "Parametrization in laminate design for optimal compliance". In: *International Journal of Solids and Structures* 34.4 (1997), pp. 415–434. ISSN: 0020-7683. DOI: 10/d84jcn.

[Hashin et al., 1963] Z. Hashin and S. Shtrikman. "A variational approach to the theory of the elastic behaviour of multiphase materials". In: *Journal of the Mechanics and Physics of Solids* 11.2 (Mar. 1963), pp. 127–140. DOI: 10/cfhhwm.

[Hotz et al., 2010] Ingrid Hotz et al. "Tensor Field Reconstruction Based on Eigenvector and Eigenvalue Interpolation". In: *Scientific Visualization: Advanced Concepts*. Ed. by Hans Hagen. Vol. 1. Dagstuhl Follow-Ups. Dagstuhl, Germany: Schloss Dagstuhl–Leibniz-Zentrum fuer Informatik, 2010, pp. 110–123. ISBN: 978-3-939897-19-4. DOI: 10/f3rmp7.

[Huang et al., 2011] Jin Huang et al. "Boundary aligned smooth 3D cross-frame field". In: *ACM transactions on graphics (TOG)*. Vol. 30. 6. ACM. 2011, p. 143.

[Hultquist, 1992] J. P. M. Hultquist. "Constructing stream surfaces in steady 3D vector fields". In: *Proceedings Visualization '92*. 1992, pp. 171–178. DOI: 10/brxk9h.

[Jorge Nocedal, 2006] Stephen Wright Jorge Nocedal. *Numerical Optimization*. Springer-Verlag GmbH, Dec. 11, 2006. 664 pp. ISBN: 9780387400655.

[Ju et al., 2002] Tao Ju et al. "Dual contouring of hermite data". In: (2002). DOI: 10/fjvzkr.

[Kälberer et al., 2007] Felix Kälberer, Matthias Nieser, and Konrad Polthier. "QuadCover-Surface Parameterization using Branched Coverings". In: *Computer graphics forum*. Vol. 26. 3. Wiley Online Library. 2007, pp. 375–384.

[Krog et al., 1997] L. A. Krog and N. Olhoff. "Topology and reinforcement layout optimization of disk, plate, and shell structures". English. In: *Topology optimization in structural mechanics*. Wien: Springer, 1997, pp. 237–322. ISBN: 3-211-82907-5.

[Larsen et al., 2018] S. D. Larsen, O. Sigmund, and J. P. Groen. "Optimal truss and frame design from projected homogenization-based topology optimization". In: *Structural and Multidisciplinary Optimization* 57.4 (2018), pp. 1461–1474. ISSN: 1615-1488. DOI: 10/gdfmr2.

[Liu, Hu, et al., 2018] Haixiang Liu, Yuanming Hu, et al. "Narrow-Band Topology Optimization on a Sparsely Populated Grid". In: *ACM Trans. Graph.* 37.6 (Dec. 2018). ISSN: 0730-0301. DOI: 10/gg55hf.

[Liu, Zhang, et al., 2018] Heng Liu, Paul Zhang, et al. "Singularity-constrained octahedral fields for hexahedral meshing". In: *ACM Transactions on Graphics (TOG)* 37.4 (2018), p. 93.

[Livesu et al., 2020] Marco Livesu et al. "LoopyCuts: Practical Feature Preserving Block Decomposition for Strongly Hex-Dominant Meshing". In: *ACM Trans. Graph.* 39.4 (July 2020). ISSN: 0730-0301. DOI: 10/gjhcch.

[Lorensen et al., 1987] William E. Lorensen and Harvey E. Cline. "Marching cubes: A high resolution 3D surface construction algorithm". In: *ACM SIGGRAPH Computer Graphics* 21.4 (Aug. 1987), pp. 163–169. DOI: 10/ft9gsh.

[Lurie et al., 1984] K. A. Lurie and A. V. Cherkaev. "G-closure of some particular sets of admissible material characteristics for the problem of bending

of thin elastic plates". In: *Journal of Optimization Theory and Applications* 42.2 (1984), pp. 305–316. ISSN: 1573-2878. DOI: 10/br3gbr.

[Lyon et al., 2016] Max Lyon, David Bommes, and Leif Kobbelt. "HexEx: Robust Hexahedral Mesh Extraction". In: *ACM Trans. Graph.* 35.4 (July 2016). ISSN: 0730-0301. DOI: 10/gg55hq.

[M.C.E., 1904] A. G. M. Michell M.C.E. "LVIII. The limits of economy of material in frame-structures". In: *The London, Edinburgh, and Dublin Philosophical Magazine and Journal of Science* 8.47 (1904), pp. 589–597. DOI: 10/frd638. eprint: https://doi.org/10.1080/14786440409463229.

[Machado et al., 2014] Gustavo Mello Machado, Filip Sadlo, and Thomas Ertl. "Image-Based Streamsurfaces". eng. In: *Brazilian Symposium of Computer Graphic and Image Processing* (Aug. 2014), p. 6915327. DOI: 10/gjqwpf.

[Milnor, 1970] J. Milnor. "Foliations and foliated vector bundles, mimeographed notes". In: *Institute for Advanced Study, Princeton* (1970).

[Milton, 1986] G. W. Milton. "Modelling the Properties of Composites by Laminates". In: *Homogenization and Effective Moduli of Materials and Media*. Ed. by J. L. Ericksen et al. New York, NY: Springer New York, 1986, pp. 150–174. ISBN: 978-1-4613-8646-9.

[Milton, 2002] Graeme W. Milton. "The Theory of Composites". In: (May 2002). DOI: 10/fpm8r2.

[Misztal et al., 2012] Marek Krzysztof Misztal and Jakob Andreas Bærentzen. "Topology-adaptive interface tracking using the deformable simplicial complex". In: *ACM Transactions on Graphics* 31.3 (May 2012), pp. 1–12. DOI: 10/xbd.

[Murdoch et al., 1997] Peter Murdoch et al. "The spatial twist continuum: A connectivity based method for representing all-hexahedral finite element meshes". In: *Finite Elements in Analysis and Design* 28.2 (Dec. 1997), pp. 137–149. DOI: 10/ftzg54.

[Nguyen et al., 2020] Tuan T. Nguyen et al. "Efficient hybrid topology and shape optimization combining implicit and explicit design representations". English. In: *Structural and Multidisciplinary Optimization* 62 (2020), pp. 1061–1069. ISSN: 1615-147X. DOI: 10/gjhccp.

[Ni et al., 2018] Saifeng Ni et al. "Field-Aligned and Lattice-Guided Tetrahedral Meshing". In: *Computer Graphics Forum* 37.5 (Aug. 2018), pp. 161–172. DOI: 10/gg2mph.

[Nieser et al., 2011] Matthias Nieser, Ulrich Reitebuch, and Konrad Polthier. "Cubecover–parameterization of 3d volumes". In: *Computer graphics forum*. Vol. 30. 5. Wiley Online Library. 2011, pp. 1397–1406.

[Norris, 1985] A. N. Norris. "A differential scheme for the effective moduli of composites". In: *Mechanics of Materials* 4.1 (Mar. 1985), pp. 1–16. DOI: 10/b4f8ss.

[Norris, 2005] Andrew N. Norris. "Optimal orientation of anisotropic solids". In: *The Quarterly Journal of Mechanics and Applied Mathematics* 59.1 (2005), pp. 29–53.

[Olhoff et al., 1998] N. Olhoff, E. Rønholt, and J. Scheel. "Topology optimization of three-dimensional structures using optimum microstructures". In: *Structural optimization* 16.1 (1998), pp. 1–18. ISSN: 1615-1488. DOI: 10/fcwppc.

[Padberg et al., 1991] Manfred Padberg and Giovanni Rinaldi. "A branch-and-cut algorithm for the resolution of large-scale symmetric traveling salesman problems". In: *SIAM review* 33.1 (1991), pp. 60–100.

[Palmer et al., 2019] David Palmer, David Bommes, and Justin Solomon. "Algebraic Representations for Volumetric Frame Fields". In: *arXiv preprint arXiv:1908.05411* (2019).

[Pantz et al., 2008] Olivier Pantz and Karim Trabelsi. "A post-treatment of the homogenization method for shape optimization". In: *SIAM Journal on Control and Optimization* 47.3 (2008), pp. 1380–1398.

[Pantz et al., 2010] Olivier Pantz and Karim Trabelsi. "Construction of minimization sequences for shape optimization". In: *2010 15th International Conference on Methods and Models in Automation and Robotics*. IEEE. 2010, pp. 278–283.

[Pedersen, 1989] Pauli Pedersen. "On optimal orientation of orthotropic materials". In: *Structural optimization* 1.2 (1989), pp. 101–106.

[Petersson, 1999] Joakim Petersson. "A Finite Element Analysis of Optimal Variable Thickness Sheets". In: *SIAM Journal on Numerical Analysis* 36.6 (1999), pp. 1759–1778. ISSN: 0036-1429.

[Ray et al., 2016] Nicolas Ray, Dmitry Sokolov, and Bruno Lévy. "Practical 3d frame field generation". In: *ACM Transactions on Graphics (TOG)* 35.6 (2016), p. 233.

[Reuss, 1929] A. Reuss. "Berechnung der Fließgrenze von Mischkristallen auf Grund der Plastizitätsbedingung für Einkristalle ." In: *Z. angew. Math. Mech.* 9.1 (Jan. 1929), pp. 49–58. ISSN: 0044-2267. DOI: 10/crtqvd.

[Rossow et al., 1973] M. P. Rossow and J. E. Taylor. "A Finite Element Method for the Optimal Design of Variable Thickness Sheets". In: *AIAA Journal* 11.11 (Nov. 1973), pp. 1566–1569. DOI: 10/bpc25r.

[Sigmund and Petersson, 1998] O. Sigmund and J. Petersson. "Numerical instabilities in topology optimization: A survey on procedures dealing with checkerboards, mesh-dependencies and local minima". In: *Structural optimization* 16.1 (1998), pp. 68–75. ISSN: 1615-1488. DOI: 10/bsf5t2.

[Sigmund, 2011] Ole Sigmund. "On the usefulness of non-gradient approaches in topology optimization". In: *Structural and Multidisciplinary Optimization* 43.5 (2011), pp. 589–596.

[Sigmund, Aage, et al., 2016] Ole Sigmund, Niels Aage, and Erik Andreassen. "On the (non-)optimality of Michell structures". In: *Structural and Multidisciplinary Optimization* 54.2 (2016), pp. 361–373. ISSN: 1615-1488. DOI: 10/gftk8d.

[Sigmund and Maute, 2013] Ole Sigmund and Kurt Maute. "Topology optimization approaches". In: *Structural and Multidisciplinary Optimization* 48.6 (Dec. 1, 2013), pp. 1031–1055. ISSN: 1615-1488. DOI: 10/gfsjpn.

[Solomon et al., 2017] Justin Solomon, Amir Vaxman, and David Bommes. "Boundary element octahedral fields in volumes". In: *ACM Transactions on Graphics (TOG)* 36.3 (2017), p. 28.

[Stolpe et al., 2001] M. Stolpe and K. Svanberg. "An alternative interpolation scheme for minimum compliance topology optimization". In: *Structural and Multidisciplinary Optimization* 22.2 (2001), pp. 116–124. ISSN: 1615-1488. DOI: 10/drr58g.

[Stutz, Groen, et al., 2020] F. C. Stutz, J. P. Groen, et al. "Singularity Aware De-Homogenization for High-Resolution Topology Optimized Structures". In: *Structural and Multidisciplinary Optimization* 62 (2020), pp. 2279–2295. DOI: 10/gjhccf.

[Stutz, Olsen, et al., 2021] Florian Cyril Stutz, Tim Felle Olsen, et al. "Synthesis of Frame Field-Aligned Multi-Laminar Structures". In: (Apr. 12, 2021). arXiv: 2104.05550 [cs.CG].

[Svanberg, 1987] Krister Svanberg. "The method of moving asymptotes - A new method for structural optimization". English. In: *International Journal for Numerical Methods in Engineering* 24 (1987), pp. 359–373. ISSN: 0029-5981.

[Szabó et al., 2011] Barna Szabó and Ivo Babuška. *Introduction to Finite Element Analysis*. John Wiley & Sons, Ltd, Mar. 2011. DOI: 10/cznkzc.

[Takayama, 2019] Kenshi Takayama. "Dual Sheet Meshing: An Interactive Approach to Robust Hexahedralization". In: *Computer Graphics Forum* 38.2 (2019), pp. 37–48. ISSN: 0167-7055. DOI: 10/gjhcck.

[Träff et al., 2019] Erik Träff, Ole Sigmund, and J. P. Groen. "Simple single-scale microstructures based on optimal rank-3 laminates". In: *Structural and Multidisciplinary Optimization* 59.4 (2019), pp. 1021–1031.

[Vaxman et al., 2016] Amir Vaxman et al. "Directional field synthesis, design, and processing". In: *Computer Graphics Forum*. Vol. 35. 2. Wiley Online Library. 2016, pp. 545–572.

[Voigt, 1966] Woldemar Voigt. *Lehrbuch der Kristallphysik*. 1966. DOI: 10/gjhccr.

[Wang et al., 2021] Yiqiang Wang, Jeroen P. Groen, and Ole Sigmund. "Plate microstructures with extreme stiffness for arbitrary multi-loadings". In: *Computer Methods in Applied Mechanics and Engineering* 381 (Aug. 2021), pp. 113–778. DOI: 10/gjp45b.

[Wu, Dick, et al., 2016] J. Wu, C. Dick, and R. Westermann. "A System for High-Resolution Topology Optimization". In: *IEEE Transactions on Visualization and Computer Graphics* 22.3 (2016), pp. 1195–1208. ISSN: 1941-0506. DOI: 10/f8bktt.

[Wu, Wang, et al., 2019] J. Wu, W. Wang, and X. Gao. "Design and Optimization of Conforming Lattice Structures". In: *IEEE Transactions on Visualization and Computer Graphics* 27.1 (2019), pp. 43–56. DOI: 10/ggkfmw.

[Zienkiewicz et al., 2013] Olek C. Zienkiewicz, Robert L. Taylor, and J. Z. Zhu. *The Finite Element Method: Its Basis and Fundamentals*. Elsevier LTD, Oxford, Oct. 1, 2013. 768 pp. ISBN: 1856176339.

Appendix A: Paper-I

J. P. Groen, F. C. Stutz, N. Aage, J. A. Bærentzen, and O. Sigmund. **De-Homogenization of Optimal Multi-Scale 3D Topologies**. *Computer Methods in Applied Mechanics and Engineering*, vol. 364, pp. 112–979, 2020. DOI: 10/gjhccg

Available online at www.sciencedirect.com
ScienceDirect
Comput. Methods Appl. Mech. Engrg. 364 (2020) 112979
Computer methods in applied mechanics and engineering
www.elsevier.com/locate/cma

De-homogenization of optimal multi-scale 3D topologies

Jeroen P. Groen[a,*], Florian C. Stutz[b], Niels Aage[a], Jakob A. Bærentzen[b], Ole Sigmund[a]

[a] Department of Mechanical Engineering, Solid Mechanics, Technical University of Denmark, Denmark
[b] Department of Applied Mathematics and Computer Science, Technical University of Denmark, Denmark

Received 28 October 2019; received in revised form 28 February 2020; accepted 1 March 2020
Available online 14 March 2020

Abstract

This paper presents a highly efficient method to obtain high-resolution, near-optimal 3D topologies optimized for minimum compliance on a standard PC. Using an implicit geometry description we derive a single-scale interpretation of optimal multi-scale designs on a very fine mesh (de-homogenization). By performing homogenization-based topology optimization, optimal multi-scale designs are obtained on a relatively coarse mesh resulting in a low computational cost. As microstructure parameterization we use orthogonal rank-3 microstructures, which are known to be optimal for a single loading case. Furthermore, a method to get explicit control of the minimum feature size and complexity of the final shapes will be discussed. Numerical examples show excellent performance of these fine-scale designs resulting in objective values similar to the homogenization-based designs. Comparisons with well-established density-based topology optimization methods show a reduction in computational cost of 3 orders of magnitude, paving the way for giga-scale designs on a standard PC.

Keywords: Optimal microstructures; Giga-scale topology optimization; Numerical efficiency; Length-scale enforcement; De-homogenization

1. Introduction

Topology optimization is an advanced design tool with the power to provide engineers with novel insights about optimal design. Nowadays, availability of high performance computing resources allows for the application of topology optimization on realistic design problems using different types of physics. Examples include, optimization of heat sinks using natural convection [1], optimizing fluid flow systems by modeling turbulence using Reynolds-averaged Navier–Stokes [2], and acoustic horn optimization [3]. However, the most studied (and arguably the most simple) type of optimization problem is compliance minimization (*i.e.* stiffness maximization) of linear elastic structures subject to one or more load-cases and an upper bound on the material usage. Recently, Aage et al. [4] extended the state-of-the-art of solution methods for these type of problems by optimizing an airplane wing using more than 1 billion design variables. To do so, 8000 cores were employed on a high performance computer system up to 5 days. Hence, a significant reduction in computational cost is still required if large-scale topology optimization is to be adapted interactively in engineering practice.

* Correspondence to: Department of Mechanical Engineering, Solid Mechanics, Technical University of Denmark, Nils Koppels Allé, Building 404, 2800 Kgs. Lyngby, Denmark.
E-mail address: jergro@mek.dtu.dk (J.P. Groen).

https://doi.org/10.1016/j.cma.2020.112979
0045-7825/

Theoretically, it is known that the optimal shape for a compliance minimization problem contains periodic details on several length-scales [5,6]. Instead of modeling these microscopic details on an extremely fine mesh, the problem can be decomposed into a multi-scale problem. The theory of homogenization can be used to calculate the effective macroscopic properties of these complex but periodic microstructures [7]. A class of microstructures that is able to reach the bounds on maximum strain energy are the so-called rank-N laminates [8–11]. These composites, which contain several length-scales, have the nice property that their corresponding elasticity tensors can be analytically derived. By using homogenization-based topology optimization the design space can be relaxed to allow for these rank-N laminates [12], such that optimal designs can be obtained at a much lower computational cost compared to density-based topology optimization. The theory for performing homogenization-based topology optimization using optimal microstructures is well-established and described in detail in the books by Allaire [13],Bendsøe and Sigmund [14]. Nevertheless, the interest in this method has faded in the last decade, which can be explained by the fact that the optimal designs are on several length-scales which prohibits their manufacturing.

To avoid the use of multi-scale microstructures, it is possible to use a database of near optimal single-scale microstructures whose properties can be obtained using numerical homogenization [15]. Furthermore, it is possible to perform the optimization procedure in a hierarchical sense, which means that both the material distribution and single-scale microstructures are optimized iteratively by making use of inverse homogenization [16,17]. Unfortunately, such an approach comes at large computational cost [18]. To reduce this cost Liu et al. [19] and Sivapuram et al. [20] restricted the number of different microstructures in the design domain; however, this results in designs far away from the true optimum. Furthermore, the optimized unit-cell designs do not take into account connectivity and load transfer between adjacent microstructures due to the separation of scales. In fact, it is possible to reconstruct near optimal single-scale microstructures based on optimal rank-N laminates [21]. This approach results in simpler microstructures than the ones obtained using inverse homogenization, at a negligible computational cost. Furthermore, Pantz and Trabelsi [22] showed that a multi-scale design can be interpreted on a single-scale using an implicit geometry description. Recent works on this so-called “de-homogenization” approach have shown that high-resolution near-optimal 2D structures subject to a single loading case can be obtained at a fraction of the cost of density-based topology optimization [23–25].

This article presents a natural extension of the de-homogenization approach for elasticity problems in 3D subject to a single loading case. Optimal rank-3 microstructures are used for the homogenization-based topology optimization, and the multi-scale designs are subsequently de-homogenized on fine meshes containing more than 200 million voxels. Using this approach large-scale designs can be efficiently obtained on a modern PC, without the need for a high performance computing system, allowing topology optimization to become a more integrated part of the design process. Finally, it should be noted that simultaneous to this study different research groups have been working on related type of methods. Geoffroy-Donders et al. [26] present an approach in which sub-optimal open-walled microstructures are de-homogenized on a fine grid using a slightly different approach. Wu et al. [27] present an approach to reconstruct a conformal lattice design from a homogenization-based design without creating a global parameterization. Contrary to above studies we use optimal rank-3 microstructures, since these microstructures have much better load carrying capabilities than sub-optimal truss-like microstructures [28]. Nevertheless, the presented approach can be used with other (non-optimal) orthotropic microstructure parameterizations $e.g.$ open-walled. The only condition is that the elastic properties are monotonously increasing for increasing material usage.

The article is organized as follows: the rank-3 parameterization and the methodology to do homogenization-based topology optimization is presented in Section 2. The de-homogenization procedure and a method to control the shape of the final designs is presented in Section 3. A large number of numerical examples to demonstrate the performance of the presented approach as well as extensive comparisons with density-based topology optimization are presented in Section 4. Finally, the most important conclusions of this study will be discussed in Section 5.

2. Homogenization-based topology optimization

2.1. The elasticity tensor of a rank-3 laminate

It is well-known that the optimal design for compliance minimization problems subject to a single loading case can be described by macroscopically varying orthogonal rank-3 laminates [11,29,30]. These multi-scale microstructures consist of two different materials, a stiff isotropic material (+) and a weak/compliant isotropic material (−) mimicking void, using Young’s moduli E^+ and E^-, respectively, and both with identical Poisson’s

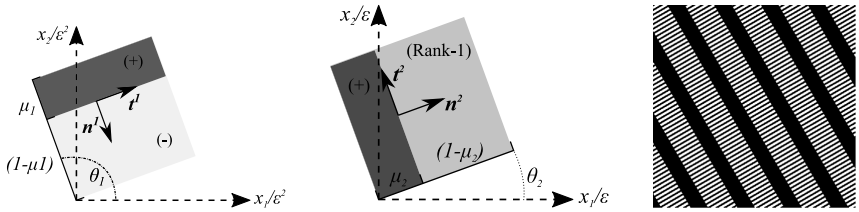

(a) Rank-1 laminate in local frame. (b) Rank-2 laminate in local frame. (c) Periodic rank-2 laminate.

Fig. 1. Visualization of how a rank-2 microstructure is constructed from a stiff isotropic material (+) and a weak/compliant isotropic material (−). Please note the different length-scales.

ratio ν. To visualize such a laminate, we consider the orthogonal rank-2 laminate shown in Fig. 1, which is optimal for a planar problem subject to a single load case. The first layering of this microstructure is a periodic rank-1 laminate, shown in Fig. 1(a). The orientation of the rank-1 laminate is described by the layer normal $\boldsymbol{n}^1$ and layer tangent $\boldsymbol{t}^1$. Furthermore, the relative layer width of the stiff material is described by parameter $\mu_1 \in [0, 1]$, hence the layer width of the compliant material is $(1-\mu_1)$. The elasticity tensor $\boldsymbol{E}^{R1}$ of the rank-1 laminate can be analytically calculated using the theory of homogenization, by assuming a periodic microstructure and perfect bonding between the two material phases, see e.g. [13,14].

The rank-1 microstructure is shown in relation to the global frame of reference (x_1, x_2); however, please note that the depicted length-scale is $\boldsymbol{x}/\varepsilon^2$ with $\varepsilon \to 0$. This means that the microstructure can be assumed uniform at the length-scale $\boldsymbol{x}/\varepsilon$. The rank-2 microstructure is then constructed on this length-scale, (*i.e.* $\boldsymbol{x}/\varepsilon$) by combining the stiff material phase and the rank-1 microstructure as is shown in Fig. 1(b). By setting $\boldsymbol{n}^2 = \boldsymbol{t}^1$ and $\boldsymbol{t}^2 = \boldsymbol{n}^1$ orthogonality of the layers is enforced. In a similar fashion as before the elasticity tensor $\boldsymbol{E}^{R2}$ of the rank-2 laminate can be analytically derived as a function of orientation angle θ_2 and relative layer widths μ_1 and μ_2.

The procedure for constructing a rank-3 laminate in 3D is exactly the same; however, now each layer i has two tangents $\boldsymbol{t}^{i,1}$ and $\boldsymbol{t}^{i,2}$ to describe the plane spanned by the stiff material. The elasticity tensor for a rank-3 laminate $\boldsymbol{E}^{R3}$ can be described by,

$$\boldsymbol{E}^{R3} = \boldsymbol{E}^{+} - (1-\mu_1)(1-\mu_2)(1-\mu_3)\Big((\boldsymbol{E}^{+} - \boldsymbol{E}^{-})^{-1} - (1+\nu)(1-2\nu)\frac{\mu_1 \boldsymbol{\Lambda}(\boldsymbol{n}^1, \boldsymbol{t}^{1,1}, \boldsymbol{t}^{1,2}) + (1-\mu_1)(\mu_2 \boldsymbol{\Lambda}(\boldsymbol{n}^2, \boldsymbol{t}^{2,1}, \boldsymbol{t}^{2,2}) + (1-\mu_2)\mu_3 \boldsymbol{\Lambda}(\boldsymbol{n}^3, \boldsymbol{t}^{3,1}, \boldsymbol{t}^{3,2}))}{E^{+}} \Big)^{-1}. \tag{1}$$

The elasticity tensor is thus described by the layer normals $\boldsymbol{n}^i$ and tangents $\boldsymbol{t}^{i,1}, \boldsymbol{t}^{i,2}$ as well as the relative layer widths μ_i, for $i = 1, 2, 3$. The influence of the orientation of each layer is captured by the fourth-order tensor $\boldsymbol{\Lambda}$,

$$\begin{aligned}\boldsymbol{\Lambda}(\boldsymbol{n}^i, \boldsymbol{t}^{i,1}, \boldsymbol{t}^{i,2}) = \frac{1}{(1-\nu)}\boldsymbol{n}^i \otimes \boldsymbol{n}^i \otimes \boldsymbol{n}^i \otimes \boldsymbol{n}^i + \frac{1}{2(1-2\nu)} \\ \Big(\boldsymbol{t}^{i,1} \otimes \boldsymbol{n}^i \otimes \boldsymbol{t}^{i,1} \otimes \boldsymbol{n}^i + \boldsymbol{n}^i \otimes \boldsymbol{t}^{i,1} \otimes \boldsymbol{t}^{i,1} \otimes \boldsymbol{n}^i + \boldsymbol{t}^{i,1} \otimes \boldsymbol{n}^i \otimes \boldsymbol{n}^i \otimes \boldsymbol{t}^{i,1} + \boldsymbol{n}^i \otimes \boldsymbol{t}^{i,1} \otimes \boldsymbol{n}^i \otimes \boldsymbol{t}^{i,1} + \\ \boldsymbol{t}^{i,2} \otimes \boldsymbol{n}^i \otimes \boldsymbol{t}^{i,2} \otimes \boldsymbol{n}^i + \boldsymbol{n}^i \otimes \boldsymbol{t}^{i,2} \otimes \boldsymbol{t}^{i,2} \otimes \boldsymbol{n}^i + \boldsymbol{t}^{i,2} \otimes \boldsymbol{n}^i \otimes \boldsymbol{n}^i \otimes \boldsymbol{t}^{i,2} + \boldsymbol{n}^i \otimes \boldsymbol{t}^{i,2} \otimes \boldsymbol{n}^i \otimes \boldsymbol{t}^{i,2} \Big),\end{aligned} \tag{2}$$

where $\otimes$ indicates the dyadic product. The normal and tangent vectors of the three layers are linked since we use an orthogonal rank-3 microstructure. It is well-known that three Euler angles are required to represent an orthogonal frame in 3D. Hence, we use angles θ_1, θ_2 and θ_3 to define the different layer normals and tangents,

$$\boldsymbol{n}^1 = \boldsymbol{t}^{2,1} = \boldsymbol{t}^{3,1} = \begin{Bmatrix} \cos(\theta_1)\cos(\theta_3)\sin(\theta_2) + \sin(\theta_1)\sin(\theta_3) \\ \cos(\theta_1)\sin(\theta_2)\sin(\theta_3) - \cos(\theta_3)\sin(\theta_1) \\ \cos(\theta_1)\cos(\theta_2) \end{Bmatrix},$$

$$\boldsymbol{n}^2 = \boldsymbol{t}^{1,1} = \boldsymbol{t}^{3,2} = \begin{Bmatrix} \cos(\theta_3)\sin(\theta_1)\sin(\theta_2) - \cos(\theta_1)\sin(\theta_3) \\ \sin(\theta_1)\sin(\theta_2)\sin(\theta_3) + \cos(\theta_1)\cos(\theta_3) \\ \sin(\theta_1)\cos(\theta_2) \end{Bmatrix},$$
$$\boldsymbol{n}^3 = \boldsymbol{t}^{1,2} = \boldsymbol{t}^{2,2} = \begin{Bmatrix} \cos(\theta_2)\cos(\theta_3) \\ \cos(\theta_2)\sin(\theta_3) \\ -\sin(\theta_2) \end{Bmatrix}. \tag{3}$$

This means that the elasticity tensor of a rank-3 laminate can be described by six parameters $\mu_1, \mu_2, \mu_3, \theta_1, \theta_2$ and θ_3. And it is possible to find the derivatives of $\boldsymbol{E}^{R3}$ w.r.t to these variables to perform gradient-based optimization. These expressions for the gradients are long but not necessarily difficult to derive; furthermore, the material volume fraction ρ of a rank-3 microstructure is defined as,

$$\rho = \mu_1 + \mu_2 + \mu_3 - \mu_1\mu_2 - \mu_1\mu_3 - \mu_2\mu_3 + \mu_1\mu_2\mu_3. \tag{4}$$

2.2. Regularization of layer widths and avoiding thin features

The homogenization-based topology optimization problem will be solved on a finite element mesh discretized using tri-linear finite elements, which each hold a uniform microstructure. As is shown by Díaz and Sigmund [31] a checkerboard-like pattern analyzed using linear finite elements can be stiffer than an optimal microstructure with the same average density. To avoid these artificially stiff patterns, a classical density filter is used to obtain filtered relative layer widths $\tilde{\mu}_i$ from μ_i [32,33]. As filter radius we use $R = 1.5\ h^c$, with h^c the length of an element.

Additionally, we want to avoid very thin and very thick layers. Instead we want the layers to be either void, completely solid or in the interval $[\eta, (1-\eta)]$, with $\eta = 0.05$ used in this study. To do so, we use the same interpolation scheme as proposed in [23] that links the filtered relative layer widths $\tilde{\mu}_i$ to the physical relative layer widths $\bar{\tilde{\mu}}_i$,

$$\bar{\tilde{\mu}}_i = \tilde{\mu}_i\big(1 - \bar{H}(\beta, (1-\eta), \tilde{\mu}_i)\big)\bar{H}(\beta, \eta, \tilde{\mu}_i) + \left(\frac{\beta - 1}{\beta} + \frac{\tilde{\mu}_i}{\beta}\right)\bar{H}(\beta, (1-\eta), \tilde{\mu}_i). \tag{5}$$

Where $\bar{H}$ is the smoothed Heaviside function [34],

$$\bar{H}(\beta, \eta, \tilde{\mu}_i) = \frac{\tanh(\beta\eta) + \tanh(\beta(\tilde{\mu}_i - \eta))}{\tanh(\beta\eta) + \tanh(\beta(1-\eta))}, \tag{6}$$

with parameter β controlling the sharpness of the projection and η the threshold parameter. The interpolation curves for different values of β and η are shown in Fig. 2. The order of lines in the legend shows the continuation approach that is taken, with 50 iterations per step. This means that the material interpolation scheme begins close to a linear function, gradually η is increased to enforce a length-scale on the relative layer widths. Finally, β is increased to a high value to ensure that $\bar{\tilde{\mu}}_i$ is either 0, 1 or in the region $[0.05, 0.95]$.

2.3. Optimization and regularization of the microstructure orientation

It is known that a microstructure with an elasticity tensor having orthotropic symmetry conditions is optimally aligned using the principal stress directions when a single load case problem is considered [35–37]. It is therefore appealing to align the microstructure normals $\boldsymbol{n}^1, \boldsymbol{n}^2, \boldsymbol{n}^3$ with the eigenvectors $\boldsymbol{v}^I, \boldsymbol{v}^I, \boldsymbol{v}^{III}$ corresponding to the principal stresses. Unfortunately, solving the cubic equation for the 3D eigenvalue problem leads to an arbitrary order of the principal stresses as $\sigma_I \geq \sigma_{II} \geq \sigma_{III}$. This means that eigenvectors can swap 90 degrees when there is multiplicity in eigenvalues, in turn leading to instability in the optimization when the layer normals interchange. To circumvent these instabilities we update the orientation vectors based on the gradients w.r.t. θ_1, θ_2 and θ_3.

For the de-homogenization approach to work it is very important that $\boldsymbol{n}^1, \boldsymbol{n}^2, \boldsymbol{n}^3$ are smooth and continuous throughout the design domain Ω. This is unfortunately neither possible using the principal stress directions, nor using gradient-based optimization of the Euler angles. As possible solution one can regularize the orientation field using the approach by Geoffroy-Donders et al. [26]; however, in our experience this may lead to misaligned members w.r.t. the load path. To have a de-homogenized design that performs well, we propose a computational approach in which the smooth and continuous vector fields $\tilde{\boldsymbol{n}}^1, \tilde{\boldsymbol{n}}^2, \tilde{\boldsymbol{n}}^3$ are reconstructed from $\boldsymbol{n}^1, \boldsymbol{n}^2, \boldsymbol{n}^3$. This approach, that will

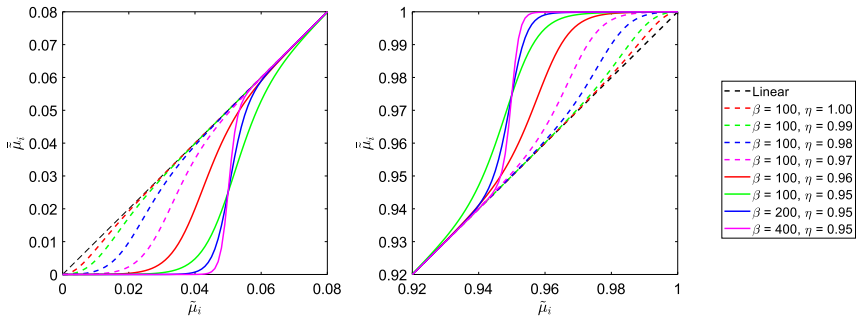

Fig. 2. Interpolation scheme plotted for the intervals where the behavior is non-linear, for different values of η and β, that follow the order of the continuation approach.

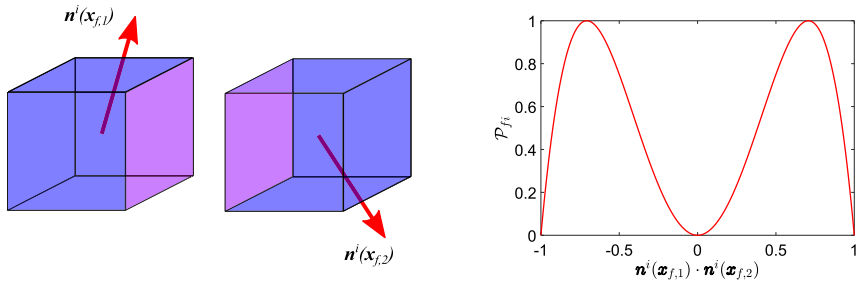

(a) Orientation vectors n^i corresponding to face f. (b) $\mathcal{P}_{fi}$ as a function of the inner product.

Fig. 3. Visualization of the penalization of difference in orientation vectors in two elements connected by face f.

be described in detail in the next Section, requires that n^1, n^2, n^3 are smoothly varying through Ω with a rotational symmetry of $\pi/2$. Hence interchanging vectors are allowed; however, large changes in frame orientation should be avoided.

We perform a regularization step on the discretized mesh and consider all faces n_f connecting two elements. A penalization function $\mathcal{P}_{fi} \in [0, 1]$ is introduced that penalizes the difference between two vectors $n^i(x_{f,1})$ and $n^i(x_{f,2})$ that are connected by face f,

$$\mathcal{P}_{fi} = 4\big(n^i(x_{f,1}) \cdot n^i(x_{f,2})\big)^2 - 4\big(n^i(x_{f,1}) \cdot n^i(x_{f,2})\big)^4. \tag{7}$$

This function has a minimum value if the vectors have the same orientation or an angle difference of $k\pi/2$, for an integer k, and a maximum value for a relative angle difference of $\pi/4 + k\pi/2$. To demonstrate this, consider face f and corresponding normal vectors $n^i(x_{f,1})$ and $n^i(x_{f,2})$ shown in Fig. 3(a). The value of penalization function $\mathcal{P}_{fi}$ plotted against the inner product of the two corresponding vectors is shown in Fig. 3(b).

By looping over the three normal vector directions, and all faces n_f connecting two elements, we can obtain a single regularization objective $\mathcal{F}_\theta$,

$$\mathcal{F}_\theta = \Big(\sum_{f=1}^{n_f}\sum_{i=1}^{3}\mathcal{P}_{fi}^q\Big)^{1/q}. \tag{8}$$

Numerical experiments have shown that a norm aggregation of $q = 1$ yields the best results. Finally, it should be noted that regularization objective $\mathcal{F}_\theta$ can be used to augment the optimization objective or can be imposed as a

constraint. The sensitivities w.r.t. Euler angles $\boldsymbol{\theta}_1, \boldsymbol{\theta}_2$ and $\boldsymbol{\theta}_3$ can be derived analytically to allow for gradient-based optimization.

2.4. Topology optimization problem

The goal of the homogenization-based topology optimization problem is to minimize objective functional $\mathcal{F}$, which is a combination of the compliance $\mathcal{J}$ (*i.e.* the external work), and regularization objective $\mathcal{F}_\theta$. The domain is discretized using $n_x \times n_y \times n_z$ tri-linear finite elements, and hence the design variables can be discretized in design vectors $\boldsymbol{\mu}_1, \boldsymbol{\mu}_2, \boldsymbol{\mu}_3, \boldsymbol{\theta}_1, \boldsymbol{\theta}_2$ and $\boldsymbol{\theta}_3$. The optimization problem is solved in a nested form, which means that for each design iteration we solve the state equation after which the design vectors are updated. Hence, the discretized optimization problem can be written as,

$$\begin{aligned} \min_{\boldsymbol{\mu}_1,\boldsymbol{\mu}_2,\boldsymbol{\mu}_3,\boldsymbol{\theta}_1,\boldsymbol{\theta}_2,\boldsymbol{\theta}_3} &: \mathcal{F}(\boldsymbol{\mu}_1, \boldsymbol{\mu}_2, \boldsymbol{\mu}_3, \boldsymbol{\theta}_1, \boldsymbol{\theta}_2, \boldsymbol{\theta}_3, \mathbf{U}) = \gamma_c \mathcal{J}(\boldsymbol{\mu}_1, \boldsymbol{\mu}_2, \boldsymbol{\mu}_3, \boldsymbol{\theta}_1, \boldsymbol{\theta}_2, \boldsymbol{\theta}_3, \mathbf{U}) + \gamma_\theta \mathcal{F}_\theta(\boldsymbol{\theta}_1, \boldsymbol{\theta}_2, \boldsymbol{\theta}_3), \\ \text{s.t.} &: \mathbf{K}(\boldsymbol{\mu}_1, \boldsymbol{\mu}_2, \boldsymbol{\mu}_3, \boldsymbol{\theta}_1, \boldsymbol{\theta}_2, \boldsymbol{\theta}_3)\mathbf{U} = \mathbf{F}, \\ &: \mathbf{v}^T \boldsymbol{\rho}(\boldsymbol{\mu}_1, \boldsymbol{\mu}_2, \boldsymbol{\mu}_3) - V_f^{max} V \leq 0, \\ &: \mathbf{0} \leq \boldsymbol{\mu}_1, \boldsymbol{\mu}_2, \boldsymbol{\mu}_3 \leq \mathbf{1}, \\ &: -\mathbf{4\pi} \leq \boldsymbol{\theta}_1, \boldsymbol{\theta}_2, \boldsymbol{\theta}_3 \leq \mathbf{4\pi}, \end{aligned} \tag{9}$$

here $\mathbf{v}$ is the vector containing the element volumes and V_f^{max} is the maximum allowed fraction of the material in Ω, with V the volume of Ω. $\mathbf{K}$ is the stiffness matrix and vector $\mathbf{F}$ describes the loads acting on the domain. We solve for the displacement vector $\mathbf{U}$ using a conjugate gradient method in combination with a geometrical multigrid pre-conditioner [38]. For the design update the MATLAB implementation of the Method of Moving Asymptotes (MMA) introduced by Svanberg [39] is used.

As a starting guess for the layer widths we use $\boldsymbol{\mu}_1 = \boldsymbol{\mu}_2 = \boldsymbol{\mu}_3$, such that the volume constraint is exactly satisfied. The starting guess for the orientation is based on a pre-analysis using isotropic microstructures, the corresponding principal stress directions are used to determine $\boldsymbol{\theta}_1, \boldsymbol{\theta}_2$ and $\boldsymbol{\theta}_3$.

Finally it should be mentioned that the scaling parameters γ_c and γ_θ have a large influence on the optimization procedure. γ_c is based on compliance of the first analysis step $\mathcal{J}^{(1)}$, while γ_θ is based on the regularization objective for the starting guess $\mathcal{F}_\theta^{(1)}$, such that,

$$\gamma_c = \frac{1}{\mathcal{J}^{(1)}}, \quad \gamma_\theta = \frac{1}{2\mathcal{F}_\theta^{(1)}}. \tag{10}$$

2.5. Numerical examples

In this paper we will use four different examples, comprising the Michell cantilever, Michell's torsion sphere, an electrical mast example and the L-shaped beam all shown in Fig. 4.

For the Michell cantilever the load is applied in a distributed sense over a patch of $L/6 \times L/6$ with a magnitude of $36/L^2$. Furthermore, this patch of elements is set to solid with a depth of $L/24$ into the domain. For the torsion sphere both the load and the Dirichlet boundary condition are applied on a square with dimensions $L/12 \times L/12$. The load is applied as a line load along the boundary of this square using a magnitude of 3/L. Finally, there are solid elements at both boundary conditions. The electrical mast example is inspired by Geoffroy-Donders et al. [26]. Like them, we only model a fourth of the full structure, hence the red shaded boundaries represent symmetry conditions. The load is applied in a distributed sense over a patch of $L/8 \times L/8$ with a magnitude of $64/L^2$. The L-shaped design domain, consists of passive elements to show a torsion bending coupling. The load is applied in a distributed sense over a square patch of solid materials of $L/6 \times L/6$ with a magnitude of $36/L^2$. Finally, it has to be mentioned that all examples are obtained using a Young's modulus for the stiff material $E^+ = 1$, and $E^- = 10^-3$ to represent the weak material in the rank-3 microstructures, since lower values result in a much slower convergence. Furthermore, we use a length $L = 1$ and a maximum allowed volume fraction $V_f^{max} = 0.1$.

To demonstrate the effect between the angle optimization and regularization methods we consider the electrical mast example. The structure is optimized on two different mesh sizes, and corresponding compliance values on the coarse optimization mesh $\mathcal{J}^c$ are shown in Table 1. We demonstrate the difference between gradient-based alignment

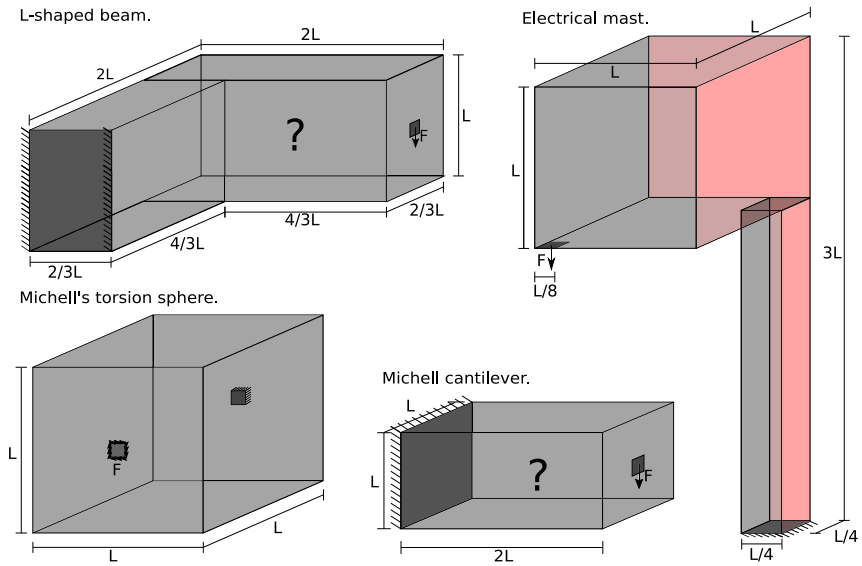

Fig. 4. Dimensions and boundary conditions for the four numerical examples used in this work.

Table 1
Compliance values $\mathcal{J}^c$ for the electrical mast example, optimized using different discretizations, alignment methods, starting guesses and regularization schemes. The method used in this work is denoted in boldface.

Mesh size	Alignment method	Starting orientation	**Regularization method**	$\mathcal{J}^c$
24 × 24 × 72	**gradient-based**	**principal directions**	**Both widths and angles**	**98.23**
24 × 24 × 72	Gradient-based	Principal directions	Only on widths	97.12
24 × 24 × 72	Gradient-based	Principal directions	Only on angles	99.17
24 × 24 × 72	Gradient-based	Principal directions	No regularization	97.17
24 × 24 × 72	Gradient-based	$\boldsymbol{\theta}_1 = \boldsymbol{\theta}_2 = \boldsymbol{\theta}_3 = \mathbf{0}$	Both widths and angles	100.10
24 × 24 × 72	Gradient-based	$\boldsymbol{\theta}_1 = \boldsymbol{\theta}_2 = \boldsymbol{\theta}_3 = \mathbf{0}$	Only on widths	97.39
24 × 24 × 72	Stress-based	Principal directions	Only on widths	97.69
48 × 48 × 144	**gradient-based**	**principal directions**	**Both widths and angles**	**98.03**
48 × 48 × 144	Gradient-based	Principal directions	Only on widths	97.44
48 × 48 × 144	Gradient-based	Principal directions	Only on angles	99.63
48 × 48 × 144	Gradient-based	Principal directions	No regularization	98.43
48 × 48 × 144	Gradient-based	$\boldsymbol{\theta}_1 = \boldsymbol{\theta}_2 = \boldsymbol{\theta}_3 = \mathbf{0}$	Both widths and angles	102.13
48 × 48 × 144	Gradient-based	$\boldsymbol{\theta}_1 = \boldsymbol{\theta}_2 = \boldsymbol{\theta}_3 = \mathbf{0}$	Only on angles	98.43
48 × 48 × 144	stress-based	Principal directions	Only on widths	97.57

of the microstructure and the use of a stress-based alignment procedure. Furthermore, we show the effect of the starting guess for the microstructure orientation, which can be either based on stress directions in a pre-analysis or by setting the Euler angles to zero. Finally, we show the effect of regularization on the angles and the regularization scheme that avoids thin features in the relative widths of the layers. The method used in this work is denoted in boldface.

As can be seen, the best results are obtained using gradient-based optimization of the orientation angles in combination with the principal directions as starting guess. In general the effect of adding the projection scheme

(see Fig. 2) to avoid thin relative widths does not increase the compliance, in fact it improves the performance. Furthermore, the regularization of the angles only reduces the performance by $1-2\%$; however, it ensures structures that can be de-homogenized as will be discussed in the next Section.

3. De-homogenization method

A design with rank-3 microstructures can be approximated on single scale using an approach similar to the one presented in [23,25]. However, some extra steps need to be taken, since the vector fields that describe the layer normals should be smooth and continuous. First of all, it is not directly possible to interchange the layer normals $\boldsymbol{n}^i$, $\boldsymbol{n}^j$ and the physical relative layer widths $\tilde{\bar{\mu}}_i$ and $\tilde{\bar{\mu}}_j$ for $i \neq j$, due to the hierarchy contained in $\tilde{\bar{\mu}}_i$ Hence, before the three layers are sorted to be smooth and continuous throughout domain Ω it is important that this hierarchy is taken into account. Afterwards, we have three orthogonal vector fields that are aligned up to $\pi/2$. However, we should note that the normal vectors $\boldsymbol{n}^1, \boldsymbol{n}^2, \boldsymbol{n}^3$ describing the microstructure orientation are rotationally symmetric up to π, *i.e.* using $-\boldsymbol{n}^1$ instead of $\boldsymbol{n}^1$ results in the same microstructures. Hence, we have a 3-dimensional 6-direction field, *i.e.* 3 orthogonal 2-direction fields, which are rotationally symmetric vector fields with no assigned magnitude [40]. From this 6-direction field we extract 3 orthogonal, smooth and continuous 1-direction fields $\tilde{\boldsymbol{n}}^1, \tilde{\boldsymbol{n}}^2, \tilde{\boldsymbol{n}}^3$.

3.1. Single scale interpretation of a rank-3 microstructure

As discussed in [21] for the 2D case, it is possible to approximate a multi-scale rank-3 laminate with small loss in performance on a single scale. Here, we extend the idea to orthogonal rank-3 microstructures in 3D. To do so we make use of the relative layer contributions p_i. These layer contributions are linked to the physical relative layer width $\tilde{\bar{\mu}}_i$ using,

$$\begin{aligned} p_1 &= \frac{\tilde{\bar{\mu}}_1}{\rho}, \\ p_2 &= \frac{(1-\tilde{\bar{\mu}}_1)\tilde{\bar{\mu}}_2}{\rho}, \\ p_3 &= \frac{(1-\tilde{\bar{\mu}}_1)(1-\tilde{\bar{\mu}}_2)\tilde{\bar{\mu}}_3}{\rho}. \end{aligned} \tag{11}$$

In a subsequent step we can obtain the single scale layer widths $w_i = \alpha p_i$, with $\alpha > 0$ a scaling factor such that the following equation holds,

$$\rho = \alpha(p_1 + p_2 + p_3) - \alpha^2(p_1p_2 + p_1p_3 + p_2p_3) + \alpha^3 p_1p_2p_3. \tag{12}$$

3.2. Obtaining smooth and continuous vector fields

Consider the 6-direction vector field consisting of layer normals $\pm\boldsymbol{n}^1, \pm\boldsymbol{n}^2, \pm\boldsymbol{n}^3$ and layer widths w_1, w_2, w_3. From this we want to extract three smooth and continuous 1-direction fields $\tilde{\boldsymbol{n}}^1, \tilde{\boldsymbol{n}}^2, \tilde{\boldsymbol{n}}^3$ with sorted widths $\tilde{w}_1$, $\tilde{w}_2$, and $\tilde{w}_3$. Where the normal vectors $\tilde{\boldsymbol{n}}^i$ are smooth and continuous throughout the domain.

Similar to the method described by Geoffroy-Donders et al. [26] we require that the vector fields used for the de-homogenization are free from singularities. The effect of singularities is that if you trace a curve around them and follow a given vector as you move along this curve, then the vector will be rotated when you come full circle. A more detailed explanation about vector fields, direction fields, singularities and possible treatments can be found in [40–42].

Fortunately, we observe that singularities tend to occur in (nearly) void regions outside of the mechanical structure, and this points to an effective way of computing the 1-direction fields such that the singularities do not affect our results. We observe that in the absence of singularities, we can simply propagate a consistent choice of vectors for our 1-direction fields from an initial element. If we propagate in such a way that we visit elements which might have singularities (*i.e.* nearly void elements) only *after* we have visited all of the elements pertinent to the mechanical structure, then we could stop once all significantly non-void elements have been visited and it will not be possible to draw a loop containing a singularity in this region. Clearly, this does not protect us from singularities

inside the mechanical structure (regardless of density) but these seem to occur only for specific boundary conditions. Actually, Michell's torsion sphere contains an internal singularity. The layer normals $\boldsymbol{n}^i$ that describe the sphere all point towards the center. However, since there is no material in the center we do not have a problem obtaining smooth and continuous vector fields.

Informed by the observations above, we have designed a front propagation approach that visits all elements in density sorted order. Initially, we take a starting element with all layers widths $w_i \in [0.05, 0.95]$ and we set $\tilde{\boldsymbol{n}}^1 = \boldsymbol{n}^1, \tilde{\boldsymbol{n}}^2 = \boldsymbol{n}^2, \tilde{\boldsymbol{n}}^3 = \boldsymbol{n}^3$, hence the widths follow such that $\tilde{w}_1 = w_1$, $\tilde{w}_2 = w_2$, and $\tilde{w}_3 = w_3$. Then we add its neighbors to a priority queue, $\boldsymbol{Q}$. The priority is given by $|0.5 - \boldsymbol{\rho}|$ where smaller values correspond to higher priority. Subsequently, when we take an element out of the queue, we fix its 1-direction fields in a way discussed below, and add its non-visited neighbors to $\boldsymbol{Q}$. Finally, we mark this element as visited in a vector $\boldsymbol{V}$. This procedure leads to a traversal of all elements in order of density closest to 0.5, but in a spatially contiguous fashion. If there is a singularity in the void domain outside the mechanical structure, it will not influence the direction fields computed by this approach.

If we take an element e out of $\boldsymbol{Q}$, we find the right handed frame $\tilde{\boldsymbol{F}}_e$ that describes the layer widths,

$$\tilde{\boldsymbol{F}}_e = \left[\tilde{\boldsymbol{n}}^1(\boldsymbol{x}_e) \quad \tilde{\boldsymbol{n}}^2(\boldsymbol{x}_e) \quad \tilde{\boldsymbol{n}}^3(\boldsymbol{x}_e)\right]. \tag{13}$$

There are $j = 24$ possible frame orientations $\boldsymbol{F}_e^j$ that have to be tested to find the best $\tilde{\boldsymbol{F}}_e$. To do this, we identify the set of neighbors of element e that already have been visited $\mathcal{N}_e$. For each of these neighbor elements $i \in \mathcal{N}_e$ we identify the rotation matrix $\boldsymbol{R}_{e,i}^j$ between possible orientation $\boldsymbol{F}_e^j$ and the already defined frame $\tilde{\boldsymbol{F}}_i$,

$$\boldsymbol{R}_{e,i}^j = \tilde{\boldsymbol{F}}_i^T \boldsymbol{F}_e^j. \tag{14}$$

The corresponding orientation angle $\psi_{e,i,j}$ that defines the frame orientation can be calculated as,

$$|\psi_{e,i,j}| = \arccos\left(\frac{\text{trace}(\boldsymbol{R}_{e,i}^j) - 1}{2}\right), \tag{15}$$

Hence, $\psi_{e,i,j} = 0$ would mean that the frame in e coincides with the frame in i for a given possibility j. The best orientation follows as,

$$\tilde{\boldsymbol{F}}_e = \boldsymbol{F}_e^k, \quad \text{for} \quad k = \arg\min_{j=1,\dots,24} \sum_i |\psi_{e,i,j}|. \tag{16}$$

Once, we have the sorted vectors for element e, $\tilde{\boldsymbol{n}}^1, \tilde{\boldsymbol{n}}^2, \tilde{\boldsymbol{n}}^3$ that describe frame $\tilde{\boldsymbol{F}}_e$ we store the corresponding widths $\tilde{w}_i$. Subsequently we remove element e from the queue and mark it as visited; furthermore, we add the unvisited neighbors of element e to the queue and sort again based on density. Subsequently, we take the element with the highest priority out of the queue and perform the same procedure again. This process is repeated until we have three smooth 1-direction fields.

3.3. De-homogenization of multi-scale designs

Similar to the work presented in [23] we need to calculate a mapping field ϕ_i for each of the three layers. Using this mapping function we can create an implicit geometry description $\tilde{\rho}_i(\boldsymbol{x})$ of the $i\text{-}th$ layer,

$$\tilde{\rho}_i(\boldsymbol{x}) = H\left(\left(\frac{1}{2} + \frac{1}{2}\mathcal{S}\left\{P_i\phi_i(\boldsymbol{x})\right\}\right) - \tilde{w}_i(\boldsymbol{x})\right). \tag{17}$$

Here H is the Heaviside function and $\mathcal{S} \in [-1, 1]$ corresponds to a triangle wave. Furthermore, P_i is a periodicity scaling, which as will be discussed later, depends on mapping function ϕ_i. The three implicit geometry functions for each layer can be combined to create an implicit geometry description of the de-homogenized structure,

$$\tilde{\rho}(\boldsymbol{x}) = \min\left\{1, \sum_{i=1}^{3} \tilde{\rho}_i(\boldsymbol{x})\right\}. \tag{18}$$

Since small widths are avoided using the continuation scheme presented in Fig. 2 we only need an accurate description of ϕ_i in $\tilde{\Omega}_i$,

$$\boldsymbol{x} \in \tilde{\Omega}_i \quad \text{if} \quad \tilde{w}_i(\boldsymbol{x}) > 0.01 \text{ and } \rho(\boldsymbol{x}) < 0.99. \tag{19}$$

To solve for ϕ_i we solve the following least-squares problem,

$$\begin{aligned} &\min_{\phi_i(\boldsymbol{x})} : \mathcal{I}(\phi_i(\boldsymbol{x})) = \frac{1}{2}\int_{\Omega} \alpha_1^i(\boldsymbol{x}) \left\| \nabla\phi_i(\boldsymbol{x}) - \tilde{\boldsymbol{n}}^i(\boldsymbol{x}) \right\|^2 \mathrm{d}\Omega, \\ &\text{s.t.} : \alpha_2^i(\boldsymbol{x}) \nabla\phi_i(\boldsymbol{x}) \cdot \tilde{\boldsymbol{t}}^{i,1}(\boldsymbol{x}) = 0, \\ &\text{s.t.} : \alpha_2^i(\boldsymbol{x}) \nabla\phi_i(\boldsymbol{x}) \cdot \tilde{\boldsymbol{t}}^{i,2}(\boldsymbol{x}) = 0. \end{aligned} \tag{20}$$

The domain is split into three parts, which dictate the weights on the objective α_1^i and the weights on the constraints α_2^i,

$$\alpha_1^i(\boldsymbol{x}) = \begin{cases} 0.01 & \text{if} \quad \tilde{w}_i(\boldsymbol{x}) < 0.01, \\ 0.1 & \text{if} \quad \rho(\boldsymbol{x}) > 0.99, \\ 1 & \text{if} \quad \boldsymbol{x} \in \tilde{\Omega}_i. \end{cases}, \quad \alpha_2^i(\boldsymbol{x}) = \begin{cases} 0 & \text{if} \quad \tilde{w}_i(\boldsymbol{x}) < 0.01, \\ 0 & \text{if} \quad \rho(\boldsymbol{x}) > 0.99, \\ 1 & \text{if} \quad \boldsymbol{x} \in \tilde{\Omega}_i. \end{cases} \tag{21}$$

The term α_1^i is introduced to relax the requirements for ϕ_i in regions that are either solid or void, where the low values still ensure some regularization to the lattice spacing. Furthermore, the term α_2^i is used to turn off exact angular enforcement in these regions. Numerically, we solve the above mentioned problem using a finite element approach, where the constraints are enforced in an augmented setting using a penalty parameter γ_ϕ. Furthermore, the complete sequence of topology optimization, creating mapping fields, and creating an implicit geometry description can be solved in a multi-scale manner. It is known that homogenization-based topology optimization can be performed on a relatively coarse mesh $\mathcal{T}^c$, while it can still contain a lot of details. The implicit geometry function $\tilde{\rho}$ is a continuous description of the de-homogenized shape as long as the mapping functions ϕ_i and widths $\tilde{w}_i$ have a continuous description. For practical purposes $\tilde{\rho}$ is evaluated using a discrete number of points; however, on a fine mesh $\mathcal{T}^f$, such that $h^f \leq h^c/20$.

Finally, it should be mentioned that we can impose an average layer spacing ε, which can be interpreted as the unit-cell size. To do so, we define the periodicity scaling parameter P_i based on the average lattice spacing in the domain of interest $\tilde{\Omega}_i$,

$$P_i = \frac{2\pi}{\epsilon} \frac{\int_{\tilde{\Omega}_i} \mathrm{d}\tilde{\Omega}_i}{\int_{\tilde{\Omega}_i} \|\nabla\phi_i(\boldsymbol{x})\| \mathrm{d}\tilde{\Omega}_i}. \tag{22}$$

3.4. Verification and clean up of de-homogenized designs

The de-homogenized designs can be interpolated on a very fine voxel grid, since an interpolation basis can be made for mapping functions ϕ_i and widths $\tilde{w}_i$. Similar to the 2D case (see [23]) we can identify: (1) de-homogenized layers that consist of thin widths, (2) regions that do not carry load and (3) disconnected patches of material.

De-homogenized layers consisting of thin widths can be identified by evaluating the local spacing λ_i, corresponding to layer i,

$$\lambda_i(\boldsymbol{x}) = \frac{2\pi}{P_i \|\nabla\phi_i(\boldsymbol{x})\|}. \tag{23}$$

This local spacing can be used to get a description of the actual feature size on the solid f_i for layer i.

$$f_i(\boldsymbol{x}) = \tilde{w}_i(\boldsymbol{x}) \lambda_i(\boldsymbol{x}). \tag{24}$$

Similar to Groen and Sigmund [23], we add a minimum feature size f_{min} to the solid at places where this feature size was violated. To do so we obtain a modified local width $\tilde{w}_i^*$ in cases where the feature size on the solid is violated, such that

$$\tilde{w}_i^*(\boldsymbol{x}) = \begin{cases} \tilde{w}_i(\boldsymbol{x}), & \text{if} \quad f_i(\boldsymbol{x}) \geq f_{min} \quad \text{and} \quad \boldsymbol{x} \in \tilde{\Omega}_i, \\ \frac{f_{min}}{\lambda_i(\boldsymbol{x})}, & \text{if} \quad f_i(\boldsymbol{x}) < f_{min} \quad \text{and} \quad \boldsymbol{x} \in \tilde{\Omega}_i. \end{cases} \tag{25}$$

This new width $\tilde{w}_i^*$ is then used in Eq. (18). However, this means that the volume of the de-homogenized shape is slightly increased. This can be alleviated by proportionally removing material in the rest of the domain; however, this option is not considered in this study.

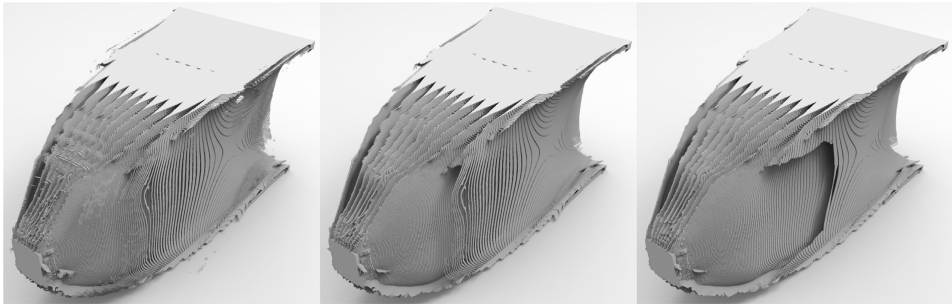

(a) With floating material. (b) De-homogenized design. (c) After post-processing.

Fig. 5. A Michell cantilever de-homogenized on a fine mesh of 960 × 480 × 480 using $\varepsilon = 30\ h^f$ and $f_{min} = 0$.

An example of the Michell cantilever evaluated on a mesh of 960 × 480 × 480 elements is shown in Fig. 5(a) where it can be seen that there are disconnected patches of material. These patches of material can be identified using the in-built connected component labeling algorithm in MATLAB (*i.e.* `bwconncomp`), which can identify the separate components of solid material. By only keeping the component with the largest number of solid voxels, the disconnected patches are removed as can be seen in Fig. 5(b). Unfortunately, this scheme cannot take care of solid regions at the boundary that do not carry any load. These artifacts arise due to the fact that the modified local widths $\tilde{w}_i^*$ jump from a finite width to zero at the boundary of $\tilde{\Omega}_i$. To address this problem, we can either apply a coated structure approach where boundary and infill are optimized simultaneously (see [25] and [43]) or ensure that triangle wave $\mathcal{S}$ is at a minimum at the boundary of $\tilde{\Omega}_i$. Both remedies will be investigated in more detail in a future study. For now, we make use of the simple iterative update scheme as proposed in [23].

First, we perform a fine-scale finite element analysis using a slightly modified version of the publicly available topology optimization code using the PETSc framework [44]. Second, the solid elements that have a strain energy density $\mathcal{E}$ lower than $10^{-2.5}$ of the mean strain energy density $\bar{\mathcal{E}}$ are set to void. Third, to make sure that the length-scale f_{min} is still satisfied after each iteration, an open–close filter operation [45] is applied. These steps are then repeated until no changes are made. The final design for the Michell cantilever can be seen in Fig. 5(c).

The combination of removal of solid elements with a low strain energy density, followed by the open–close filter operation, generally convergences within 5–10 iterations. Besides a clean and well-connected design, the performance of the design on the fine-scale $\mathcal{J}^f$ is immediately known. Furthermore, it has to be noted that for the fine-scale analysis void is modeled using a Young's modulus $E^- = 10^{-9}E^+$.

4. Numerical examples

To demonstrate that our approach requires moderate computational resources, we perform both the homogenization-based topology optimization step and the de-homogenization step on a modern workstation PC using a single core MATLAB code. To be more specific, the PC uses Ubuntu 16.04.6 as operating system, contains an Intel Xeon Platinum 8160 processor, with 64 GB RAM memory. Although the homogenization-based designs can be evaluated on an infinitely fine voxel grid, we have been restricted by memory size to examples in the range of 200 million voxels. These large-scale designs have been verified on the DTU Sophia cluster using 100 nodes each containing 2 AMD EPYC 7351 processors and 128 GB RAM memory. Hence, a total of 3200 cores was used.

4.1. Homogenization-based topology optimization

The first step in the procedure is the homogenization-based topology optimization. All examples shown in Fig. 4 are optimized on differently discretized coarse meshes $\mathcal{T}^c$. The corresponding compliance values on the coarse optimization meshes $\mathcal{J}^c$, the volume fraction V_f^c, number of iterations n_{iter} and the total time used for the optimization T^c are shown in Table 2.

Table 2
Compliance $\mathcal{J}^c$, volume fraction V_f^c, the number of iterations n_{iter}, and run time T^c for different optimization examples optimized using homogenization-based topology optimization. Reference compliance values $\mathcal{J}^{ref}$ obtained using density-based topology optimization are shown as well.

Example	$\mathcal{T}^c$	$\mathcal{J}^c$	$\mathcal{J}^{ref}$	V_f^c	n_{iter}	T^c $[hh:mm:ss]$
Michell cantilever	$48 \times 24 \times 24$	227.89	269.763	0.100	400	01:23:51
Michell cantilever	$96 \times 48 \times 48$	226.68	265.52	0.100	400	09:45:35
Michell's torsion sphere	$48 \times 48 \times 48$	12.33	12.51	0.100	400	04:28:35
Michell's torsion sphere	$72 \times 72 \times 72$	14.00	14.14	0.100	400	15:14:11
Electrical mast	$24 \times 24 \times 72$	98.23	107.53	0.100	400	01:14:20
Electrical mast	$48 \times 48 \times 144$	98.09	104.28	0.100	400	07:16:38
L-beam	$48 \times 48 \times 24$	590.56	668.37	0.100	400	02:02:02
L-beam	$96 \times 96 \times 48$	567.62	608.56	0.100	400	13:32:11

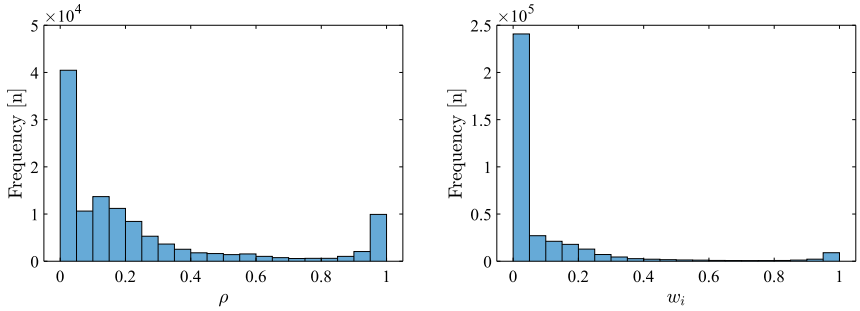

(a) Histogram plot of ρ.

(b) Histogram plot of w_i.

Fig. 6. Histograms demonstrating the frequency of intermediate density ρ and widths w_i corresponding to the active elements in the Electrical mast example optimized on a mesh of $48 \times 48 \times 144$ elements.

It can be seen that even the example with the finest discretization (using approximately 1.2 million degrees of freedom) does not require more than 16 CPU hours on the workstation, making the computational cost manageable. All optimization examples took 400 design iterations due to the continuation scheme to avoid very thin or thick lamination widths. After the last update of η and β at iteration 350, the design has to be updated for at least 50 more iterations. Furthermore, it should be mentioned that there is great potential for a speed up if the code is run in parallel or in a lower-level programming language (e.g. C++) compared to MATLAB.

Contrary to many multi-scale approaches using non-optimal ($e.g.$ isotropic and/or open-walled) microstructures, our optimized designs have a large number of microstructures with intermediate density instead of being solid or void. This can be seen in Fig. 6(a) which contains a histogram plot of the element densities ρ corresponding to the active elements in the Electrical mast example optimized on a mesh of $48 \times 48 \times 144$ elements. It is also interesting to note that in most parts of the design domain, only one or two layers have a finite width as can be seen in Fig. 6(b). This observation is in agreement with the work of Gibiansky and Cherkaev [30], where it is shown that not all loading situations result in laminates of third rank.

Finally, reference compliance values $\mathcal{J}^{ref}$ for designs obtained using the well-known Solid Isotropic Microstructure with Penalty (SIMP) method obtained on the same mesh sizes are shown in Table 2 as well. These reference values have been obtained using a continuation scheme on the penalization factor (p). We start with $p = 1$ and slowly increase this to $p = 4$ such that the design converges within 450 iterations. Furthermore, it should be noted that the density filter is used in these examples with a filter radius of $R = 2h^c$, where the filter is turned off in the final iterations to allow for black and white designs. Furthermore, it has to be noted that the void material is modeled using a Young's modulus $E^- = 10^{-9}E^+$.

Table 3
Different mesh sizes $\mathcal{T}^c$, and $\mathcal{T}^i$, $\mathcal{T}^f$, and computational cost for the de-homogenization step T^ϕ.

Example	$\mathcal{T}^c$	$\mathcal{T}^i$	$\mathcal{T}^f$	T^ϕ $[hh:mm:ss]$
Michell cantilever	$48 \times 24 \times 24$	$192 \times 96 \times 96$	$960 \times 480 \times 480$	00:15:36
Michell cantilever	$96 \times 48 \times 48$	$192 \times 96 \times 96$	$960 \times 480 \times 480$	00:45:39
Michell's torsion sphere	$48 \times 48 \times 48$	$144 \times 144 \times 144$	$576 \times 576 \times 576$	00:36:28
Michell's torsion sphere	$72 \times 72 \times 72$	$144 \times 144 \times 144$	$576 \times 576 \times 576$	01:19:44
Electrical mast	$24 \times 24 \times 72$	$96 \times 96 \times 288$	$384 \times 384 \times 1152$	00:21:43
Electrical mast	$48 \times 48 \times 144$	$96 \times 96 \times 288$	$384 \times 384 \times 1152$	00:54:49
L-beam	$48 \times 48 \times 24$	192×96	$768 \times 768 \times 384$	00:23:32
L-beam	$96 \times 96 \times 48$	192×96	$768 \times 768 \times 384$	01:08:06

As expected the homogenization-based designs perform much better than the single-scale density-based designs. The reason is obvious, for the multi-scale designs optimal rank-3 microstructures are used, which contain much more information on this coarse mesh than the isotropic material using the SIMP method. Only for Michell's torsion sphere the values are close, this is expected since it is well-known that the optimal solution is a closed sphere of solid material [28].

4.2. De-homogenization

As discussed before, the de-homogenization consists of two parts. The first part is the sorting of the vector fields. The second part is calculating mapping functions ϕ_i, applying an average unit-cell spacing ε and a length-scale f_{min}. The de-homogenization is performed in a multi-scale fashion, where the vector fields are sorted on coarse optimization mesh $\mathcal{T}^c$, the mapping functions are calculated on $\mathcal{T}^i$, while the design is projected on fine mesh $\mathcal{T}^f$. The total computational cost to de-homogenize each of the above-mentioned examples to a fine mesh of approximately 200 million elements is shown in Table 3. For each example an average unit-cell spacing $\varepsilon = 40\ h^f$ is chosen, with $f_{min} = 2\ h^f$; however, it is noted that changing these values does not affect the computational cost.

As can be seen all examples can be de-homogenized into very fine designs in less than one and a half hours, rendering the total computational cost for obtaining very fine designs in the range of approximately 2–17 hours, utilizing only a single core on the workstation PC.

4.3. Performance of the de-homogenized designs

The next step is to demonstrate the performance of the presented approach. First, we show the effect of changing minimum length-scale f_{min} and average unit-cell spacing ε on the volume fraction of the de-homogenized design V_f^ϕ. To do so, we use the Electrical mast example projected on a fine mesh of $384 \times 384 \times 1152$ elements. The results for both optimization meshes $\mathcal{T}^c$ are shown in Table 4.

As can be seen, adding a minimum length-scale adds a significant amount of material, hence the volume constraint can be violated up to 0.20 V_{max}. Nevertheless, this effect can be minimized if reasonable values for ε and f_{min} are chosen. When f_{min} is large compared to ε, a large amount of material will be added to satisfy the minimum length-scale, which results in a large violation of the volume constraint. Generally, a good rule of thumb is that $\frac{\varepsilon}{f_{min}} > 10$, such that the violation of the volume constraint stays below 10% of V_{max}. Furthermore, it is obvious that ε has to be small compared to the domain size, otherwise the de-homogenized design cannot represent the homogenization-based design. Ideally, we would thus like to de-homogenize the multi-scale design to a finer mesh, see *e.g.* Groen and Sigmund [23], since this would allow finer details and smaller or no violations of the volume constraint, while a minimum length-scale can still be guaranteed, ideally related to η used in the homogenization-based topology optimization procedure.

Furthermore, all the de-homogenized designs perform close to the homogenization-based solutions. This can be verified by analyzing the compliance of the de-homogenized designs on the fine mesh $\mathcal{J}^\phi$, which is also shown in Table 4. As expected the designs which have a higher volume have a lower compliance. Nevertheless, it can be seen that all values are close to the homogenization-based compliance $\mathcal{J}^c$. It can be seen that a smaller ε results in a better performance, which is expected, since the de-homogenized designs better resemble the multi-scale designs. Hence,

Table 4
The volume fraction V_f^{ϕ}, compliance $\mathcal{J}^{\phi}$, stiffness per weight measure $\mathcal{S}^{\phi}$ and total computation time T^{tot} of the de-homogenized electrical mast on a fine mesh of $384 \times 384 \times 1152$ elements. Furthermore, the volume fraction V_f^{post} and compliance $\mathcal{J}^{post}$ and stiffness per weight $\mathcal{S}^{post}$ after the post-processing step are shown. Results are shown for different $\mathcal{T}^c$, f_{min} and ε.

$\mathcal{T}^c$	ε	f_{min}	V_f^{ϕ}	$\mathcal{J}^{\phi}$	$\mathcal{S}^{\phi}$	T^{tot} [$hh:mm:ss$]	V_f^{post}	$\mathcal{J}^{post}$	$\mathcal{S}^{post}$
$24 \times 24 \times 72$	$24\ h^f$	$0\ h^f$	0.0993	106.17	10.544	01:36:03	0.0992	106.17	10.528
$24 \times 24 \times 72$	$24\ h^f$	$2\ h^f$	0.1046	101.83	10.650		0.1041	101.83	10.598
$24 \times 24 \times 72$	$24\ h^f$	$3\ h^f$	0.1093	98.96	10.814		0.1086	98.42	10.692
$24 \times 24 \times 72$	$24\ h^f$	$4\ h^f$	0.1156	95.19	11.003		0.1151	93.83	10.796
$24 \times 24 \times 72$	$32\ h^f$	$0\ h^f$	0.0990	107.87	10.678		0.0987	107.86	10.650
$24 \times 24 \times 72$	$32\ h^f$	$2\ h^f$	0.1020	105.08	10.720		0.1015	105.06	10.669
$24 \times 24 \times 72$	$32\ h^f$	$3\ h^f$	0.1050	102.81	10.799		0.1043	102.40	10.680
$24 \times 24 \times 72$	$32\ h^f$	$4\ h^f$	0.1088	100.42	10.923		0.1077	99.44	10.713
$24 \times 24 \times 72$	$40\ h^f$	$0\ h^f$	0.0979	110.80	10.843		0.0976	110.78	10.812
$24 \times 24 \times 72$	$40\ h^f$	$2\ h^f$	0.0996	109.11	10.870		0.0993	109.11	10.837
$24 \times 24 \times 72$	$40\ h^f$	$3\ h^f$	0.1016	107.64	10.933		0.1008	107.36	10.824
$24 \times 24 \times 72$	$40\ h^f$	$4\ h^f$	0.1040	105.78	10.996		0.1028	105.27	10.822
$48 \times 48 \times 144$	$24\ h^f$	$0\ h^f$	0.0994	108.14	10.755	08:11:27	0.0993	108.14	10.737
$48 \times 48 \times 144$	$24\ h^f$	$2\ h^f$	0.1059	102.52	10.858		0.1054	102.50	10.805
$48 \times 48 \times 144$	$24\ h^f$	$3\ h^f$	0.1121	98.21	11.008		0.1115	97.37	10.853
$48 \times 48 \times 144$	$24\ h^f$	$4\ h^f$	0.1195	93.64	11.194		0.1198	91.70	10.984
$48 \times 48 \times 144$	$32\ h^f$	$0\ h^f$	0.0974	114.03	11.109		0.0972	114.03	11.080
$48 \times 48 \times 144$	$32\ h^f$	$2\ h^f$	0.1013	109.98	11.145		0.1007	109.99	11.083
$48 \times 48 \times 144$	$32\ h^f$	$3\ h^f$	0.1054	106.69	11.240		0.1042	106.38	11.088
$48 \times 48 \times 144$	$32\ h^f$	$4\ h^f$	0.1105	102.75	11.350		0.1088	102.00	11.097
$48 \times 48 \times 144$	$40\ h^f$	$0\ h^f$	0.0979	113.90	11.153		0.0976	113.90	11.119
$48 \times 48 \times 144$	$40\ h^f$	$2\ h^f$	0.1006	111.26	11.189		0.1001	111.26	11.139
$48 \times 48 \times 144$	$40\ h^f$	$3\ h^f$	0.1035	108.89	11.272		0.1026	108.15	11.098
$48 \times 48 \times 144$	$40\ h^f$	$4\ h^f$	0.1071	106.08	11.364		0.1058	104.76	11.086

this again shows the need for an even finer resolution of the de-homogenized designs. Furthermore, we introduce an additional measure $\mathcal{S}^{\phi}$, which is the compliance multiplied by the volume and can be seen as a measure of stiffness per volume. The lower this value, the better the material usage and hence performance. The use of $\mathcal{S}^{\phi}$ allows us to quantitatively compare the different de-homogenized designs with each other to show that an almost constant performance is achieved for the different values of ε and f_{min}. However, with a slight advantage for the designs without length-scale enforcement. The values for the stiffness per volume of the homogenization-based structures are $\mathcal{S}^c = 9.823$ and $\mathcal{S}^c = 9.809$ for the coarse and slightly finer mesh respectively.

It is also interesting to see that the mesh on which the homogenization-based designs are achieved can be very coarse. This demonstrates how much information is captured by using a rank-3 parameterization. Furthermore, this shows that the total time T^{tot} to obtain the de-homogenized designs without evaluating the fine-scale compliance can be as low as one and a half hour on a single PC. The times are only shown once per optimization mesh, since the choice of ε and f_{min} does not affect the calculation of mapping functions ϕ_i. Section views of the de-homogenized designs for different values of ε and f_{min} are shown in Figs. 7(a),(b) and (c).

From these Figures it can also be seen that the average unit-cell spacing ε has to be small enough to allow for the de-homogenized design to represent the homogenization-based design. Furthermore, it can be seen that the de-homogenized design obtained using $\mathcal{T}^c = 48 \times 48 \times 144$ contains more microstructural details. Finally, the post-processing method described in the previous section can be used to get rid of some members that do not carry any load. An example of a de-homogenized design including this post-processing step can be seen in Figs. 7(d) and 8(a) and (b). The corresponding values for the volume fraction V_f^{post}, compliance $\mathcal{J}^{post}$ and measure for stiffness per weight $\mathcal{S}^{post}$ can be seen in Table 4 as well. Here it should be noted that in general the post-processing step not only removes material but also improves the stiffness per weight measure. Unfortunately however, this requires several fine-scale analyses that come at a large computational cost, *i.e.* using 3200 cores on the DTU Sophia cluster.

The performance of the de-homogenized designs of the Michell cantilever, Michell's torsion sphere and the L-shaped beam are shown in Tables 5–7. The values for the stiffness per volume of the homogenization-based structures are $\mathcal{S}^c = 22.79$ and $\mathcal{S}^c = 22.67$ for the coarse and slightly finer mesh respectively for the Michell

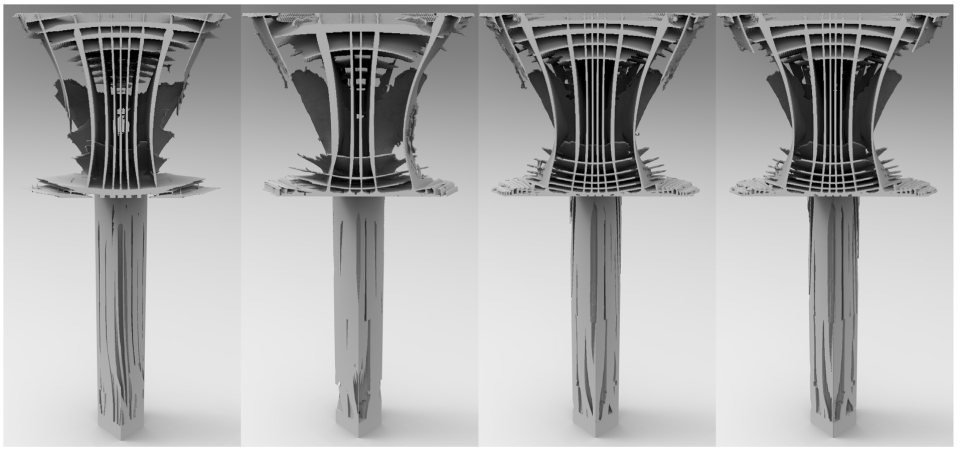

(a) $\varepsilon = 24\ h^f$, $f_{min} = 0\ h^f$. (b) $\varepsilon = 40\ h^f$, $f_{min} = 2\ h^f$. (c) $\varepsilon = 24\ h^f$, $f_{min} = 3\ h^f$. (d) $\varepsilon = 24\ h^f$, $f_{min} = 3\ h^f$, after post-processing.

Fig. 7. Cut-outs of the de-homogenized designs of the electrical mast example de-homogenized on a fine mesh of 1152 × 384 × 384 voxels for different values of ε and f_{min}. Example (a) is optimized on $\mathcal{T}^c = 24 \times 24 \times 72$, while the other examples are obtained using $\mathcal{T}^c = 48 \times 48 \times 144$. For other views of the design in Fig. 7(d), see Figs. 8(a) and (b).

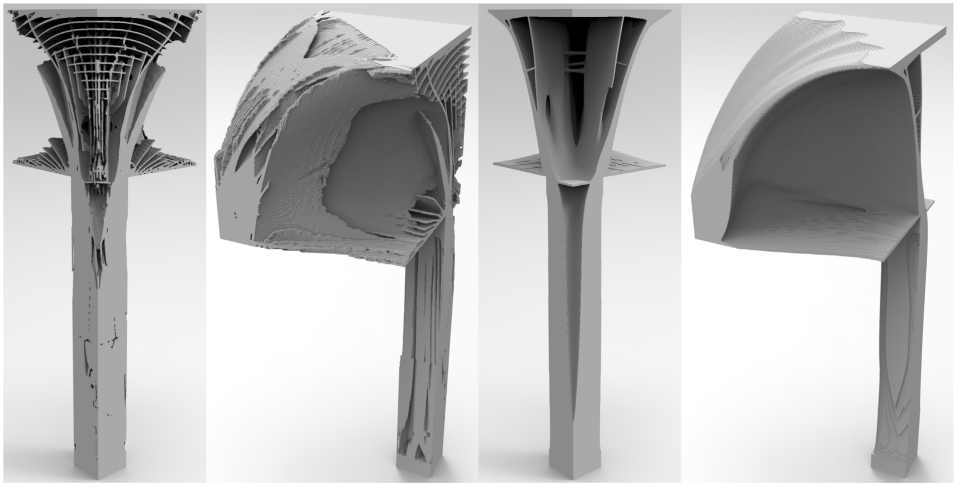

(a) De-homogenized. (b) De-homogenized. (c) Density-based. (d) Density-based.

Fig. 8. The de-homogenized design of the electrical mast on a fine mesh of 1152 × 384 × 384 voxels for $\varepsilon = 24\ h^f$ and $f_{min} = 3\ h^f$, after post-processing. Furthermore, a reference design using density-based topology optimization is shown.

Table 5
The volume fraction V_f^{ϕ}, compliance $\mathcal{J}^{\phi}$, stiffness per weight measure $\mathcal{S}^{\phi}$ and total computation time T^{tot} of the de-homogenized Michell cantilever on a fine mesh of $960 \times 960 \times 480$ elements. Furthermore, the volume fraction V_f^{post} and compliance $\mathcal{J}^{post}$ and stiffness per weight $\mathcal{S}^{post}$ after the post-processing step are shown. Results are shown for different $\mathcal{T}^c$, f_{min} and ε.

$\mathcal{T}^c$	ε	f_{min}	V_f^{ϕ}	$\mathcal{J}^{\phi}$	$\mathcal{S}^{\phi}$	T^{tot} [$hh:mm:ss$]	V_f^{post}	$\mathcal{J}^{post}$	$\mathcal{S}^{post}$
$48 \times 24 \times 24$	24 h^f	0 h^f	0.1004	253.37	25.427	01:39:27	0.0993	253.39	25.171
$48 \times 24 \times 24$	24 h^f	2 h^f	0.1109	232.91	25.825		0.1099	232.92	25.591
$48 \times 24 \times 24$	24 h^f	3 h^f	0.1228	214.72	26.367		0.1202	215.45	25.888
$48 \times 24 \times 24$	24 h^f	4 h^f	0.1378	195.72	26.978		0.1343	195.50	26.258
$48 \times 24 \times 24$	32 h^f	0 h^f	0.1018	245.15	24.947		0.1012	245.15	24.801
$48 \times 24 \times 24$	32 h^f	2 h^f	0.1081	234.41	25.345		0.1076	234.56	25.241
$48 \times 24 \times 24$	32 h^f	3 h^f	0.1153	222.83	25.697		0.1137	1152.2	130.98
$48 \times 24 \times 24$	32 h^f	4 h^f	0.1250	209.35	26.171		0.1229	209.79	25.784
$48 \times 24 \times 24$	40 h^f	0 h^f	0.1017	247.14	25.143		0.1010	247.15	24.952
$48 \times 24 \times 24$	40 h^f	2 h^f	0.1058	240.84	25.480		0.1051	240.86	25.321
$48 \times 24 \times 24$	40 h^f	3 h^f	0.1102	234.62	25.848		0.1082	235,31	25.449
$48 \times 24 \times 24$	40 h^f	4 h^f	0.1165	224.94	26.214		0.1140	225.64	25.712
$96 \times 48 \times 48$	24 h^f	0 h^f	0.1008	251.43	25.344	10:31:14	0.1004	251.43	25.231
$96 \times 48 \times 48$	24 h^f	2 h^f	0.1073	235.96	25.322		0.1069	236.55	25.281
$96 \times 48 \times 48$	24 h^f	3 h^f	0.1162	220.87	25.670		0.1149	222.73	25.598
$96 \times 48 \times 48$	24 h^f	4 h^f	0.1306	200.48	26.184		0.1287	201.98	25.988
$96 \times 48 \times 48$	32 h^f	0 h^f	0.1024	245.40	25.136		0.1019	245.42	25.010
$96 \times 48 \times 48$	32 h^f	2 h^f	0.1061	237.64	25.219		0.1055	237.86	25.104
$96 \times 48 \times 48$	32 h^f	3 h^f	0.1105	230.28	25.437		0.1089	231.80	25.236
$96 \times 48 \times 48$	32 h^f	4 h^f	0.1179	218.49	25.759		0.1156	220.10	25.447
$96 \times 48 \times 48$	40 h^f	0 h^f	0.1026	243.29	24.966		0.1021	243.31	24.845
$96 \times 48 \times 48$	40 h^f	2 h^f	0.1052	237.14	24.942		0.1049	238.70	25.034
$96 \times 48 \times 48$	40 h^f	3 h^f	0.1087	232.77	25.292		0.1076	234.29	25.202
$96 \times 48 \times 48$	40 h^f	4 h^f	0.1131	227.19	25.706		0.1117	228.36	25.508

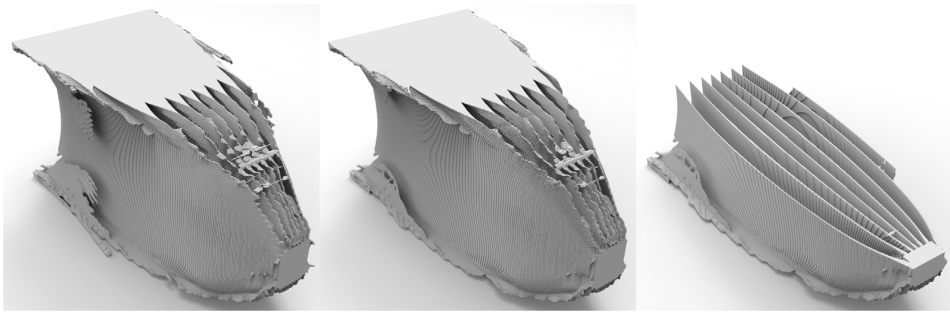

(a) De-homogenized design. (b) After post-processing. (c) After post-processing.

Fig. 9. A Michell cantilever optimized on $\mathcal{T}^c = 96 \times 48 \times 48$ elements and de-homogenized on a fine mesh of $960 \times 480 \times 480$ using $\varepsilon = 40\ h^f$ and $f_{min} = 2\ h^f$.

cantilever, $\mathcal{S}^c = 1.233$ and $\mathcal{S}^c = 1.400$ for Michell's torsion sphere and $\mathcal{S}^c = 59.06$ and $\mathcal{S}^c = 56.76$ for the L-shaped beam.

As can be seen the Michell cantilever, is very sensitive to the enforcement of a minimum feature size. This is because there are many vertical thin plates just a few voxels wide as can be seen in Figs. 9(a),(b) and (c). Hence, the layer widths corresponding to that direction are around 0.1. This means that for a small unit-cell spacing, the minimum width can be violated and a lot of material is added. Hence, for this example a slightly larger value of ε is actually better. Furthermore, it can be seen that there is no noticeable difference between the two mesh sizes on

Table 6
The volume fraction V_f^{ϕ}, compliance $\mathcal{J}^{\phi}$, stiffness per weight measure $\mathcal{S}^{\phi}$ and total computation time T^{tot} of Michell's torsion sphere de-homogenized on a fine mesh of $576 \times 576 \times 576$ elements. Furthermore, the volume fraction V_f^{post} and compliance $\mathcal{J}^{post}$ and stiffness per weight $\mathcal{S}^{post}$ after the post-processing step are shown. Results are shown for different $\mathcal{T}^c$, f_{min} and ε.

$\mathcal{T}^c$	ε	f_{min}	V_f^{ϕ}	$\mathcal{J}^{\phi}$	$\mathcal{S}^{\phi}$	T^{tot} $[hh:mm:ss]$	V_f^{post}	$\mathcal{J}^{post}$	$\mathcal{S}^{post}$
$48 \times 48 \times 48$	24 h^f	0 h^f	0.0955	20.77	1.983	05:05:03	0.0953	20.77	1.979
$48 \times 48 \times 48$	24 h^f	2 h^f	0.0969	20.46	1.981		0.0959	20.55	1.971
$48 \times 48 \times 48$	24 h^f	3 h^f	0.0988	20.53	2.029		0.0976	20.54	2.005
$48 \times 48 \times 48$	24 h^f	4 h^f	0.1051	20.59	2.164		0.1040	20.57	2.139
$48 \times 48 \times 48$	32 h^f	0 h^f	0.0989	20.16	1.995		0.0854	20.87	1.783
$48 \times 48 \times 48$	32 h^f	2 h^f	0.1023	20.44	2.090		0.1003	20.60	2.065
$48 \times 48 \times 48$	32 h^f	3 h^f	0.1082	20.55	2.225		0.0886	20.75	1.839
$48 \times 48 \times 48$	32 h^f	4 h^f	0.1152	19.82	2.284		0.0911	20.63	1.879
$48 \times 48 \times 48$	40 h^f	0 h^f	0.0976	20.20	1.972		0.0943	20.66	1.949
$48 \times 48 \times 48$	40 h^f	2 h^f	0.1012	19.84	2.007		0.0976	20.72	2.021
$48 \times 48 \times 48$	40 h^f	3 h^f	0.1034	20.70	2.140		0.0947	20.73	1.963
$48 \times 48 \times 48$	40 h^f	4 h^f	0.1055	20.58	2.170		0.0951	20.65	1.964
$72 \times 72 \times 72$	24 h^f	0 h^f	0.0968	20.71	2.005	16:33:55	0.0953	20.71	1.974
$72 \times 72 \times 72$	24 h^f	2 h^f	0.1018	20.60	2.097		0.1012	20.61	2.087
$72 \times 72 \times 72$	24 h^f	3 h^f	0.1068	20.69	2.210		0.1062	20.69	2.197
$72 \times 72 \times 72$	24 h^f	4 h^f	0.1156	20.37	2.355		0.1128	20.58	2.321
$72 \times 72 \times 72$	32 h^f	0 h^f	0.0898	20.91	1.878		0.0826	20.93	1.729
$72 \times 72 \times 72$	32 h^f	2 h^f	0.0964	17.54	1.690		0.0833	20.84	1.736
$72 \times 72 \times 72$	32 h^f	3 h^f	0.1027	20.43	2.098		0.0853	20.73	1.768
$72 \times 72 \times 72$	32 h^f	4 h^f	0.1100	16.19	1.781		0.0884	20.71	1.831
$72 \times 72 \times 72$	40 h^f	0 h^f	0.0984	20.70	2.036		0.0983	20.70	2.034
$72 \times 72 \times 72$	40 h^f	2 h^f	0.0992	20.57	2.040		0.0988	20.58	2.034
$72 \times 72 \times 72$	40 h^f	3 h^f	0.1011	19.58	1.980		0.1006	20.61	2.074
$72 \times 72 \times 72$	40 h^f	4 h^f	0.1035	20.67	2.139		0.1030	20.67	2.130

which the homogenization-based designs are obtained. Finally, it can be seen that for one case the post-processing scheme resulted in a significantly worse compliance, which is caused by the open–close filter step in which also load carrying material has been removed.

Moving on to Michell's torsion sphere example, we observe a large difference in compliance between the homogenization-based designs and the de-homogenized designs. This is mainly caused by the fact that the load is applied along a line for simplicity, which results in a different loading condition depending on the mesh size. Nevertheless, the goal of this example was to show that the optimized solution visually represents the analytical solution of Michell's torsion sphere which is a close-walled sphere [28]. Interestingly, this is the case; however, the de-homogenized solution contains several closed spheres of different radii as can be seen in Fig. 10. The reason for the multiple spheres is the relatively high volume fraction, the rank-3 material model and the fact that a relatively coarse mesh is used for the homogenization-based topology optimization. Finally, it should be mentioned that using the post-processing procedure a large number of passive solid elements at the boundary condition have been removed, making the comparison with the homogenization-based design unfair.

The orientation field for the L-shaped beam actually contains a singularity at the corner with the passive void domain. However, since this singularity is at the boundary of the domain, the sorting algorithm managed to return smooth and continuous vector fields, although we have to note that this cannot be guaranteed for other cases including singularities. In this example the microstructures and layer orientations are rapidly changing and hence the design obtained on a very coarse optimization mesh resulted in worse performing de-homogenized designs than the ones obtained on $\mathcal{T}^c = 96 \times 96 \times 48$. As can be seen in Fig. 11(a) and (b), the optimized solution is a combination of a cantilever optimized for bending stiffness and a hollow box optimized for torsion.

Table 7
The volume fraction V_f^{ϕ}, compliance $\mathcal{J}^{\phi}$, stiffness per weight measure $\mathcal{S}^{\phi}$ and total computation time T^{tot} de-homogenized L-shaped beam on a fine mesh of $768 \times 768 \times 384$ elements. Furthermore, the volume fraction V_f^{post} and compliance $\mathcal{J}^{post}$ and stiffness per weight $\mathcal{S}^{post}$ after the post-processing step are shown. Results are shown for different $\mathcal{T}^c$, f_{min} and ε.

$\mathcal{T}^c$	ε	f_{min}	V_f^{ϕ}	$\mathcal{J}^{\phi}$	$\mathcal{S}^{\phi}$	T^{tot} [$hh:mm:ss$]	V_f^{post}	$\mathcal{J}^{post}$	$\mathcal{S}^{post}$
$48 \times 48 \times 24$	24 h^f	0 h^f	0.0945	764.85	72.309	02:26:04	0.0934	764.93	71.476
$48 \times 48 \times 24$	24 h^f	2 h^f	0.1033	716.24	74.013		0.1004	716.32	71.947
$48 \times 48 \times 24$	24 h^f	3 h^f	0.1097	689.16	75.587		0.1039	2484.8	258.22
$48 \times 48 \times 24$	24 h^f	4 h^f	0.1164	663.32	77.220		0.1093	657.80	71.881
$48 \times 48 \times 24$	32 h^f	0 h^f	0.0951	833.78	79.321		0.0943	834.47	78.728
$48 \times 48 \times 24$	32 h^f	2 h^f	0.1050	765.99	80.425		0.1014	766.04	77.666
$48 \times 48 \times 24$	32 h^f	3 h^f	0.1004	795.00	79.812		0.0939	831.00	78.006
$48 \times 48 \times 24$	32 h^f	4 h^f	0.1098	736.13	80.859		0.1036	741.82	76.851
$48 \times 48 \times 24$	40 h^f	0 h^f	0.0991	682.37	67.589		0.0971	682.39	66.274
$48 \times 48 \times 24$	40 h^f	2 h^f	0.1031	669.78	69.083		0.0997	669.87	66.756
$48 \times 48 \times 24$	40 h^f	3 h^f	0.1064	659.90	70.249		0.1010	4193.0	423.55
$48 \times 48 \times 24$	40 h^f	4 h^f	0.1100	651.10	71.615		0.1030	643.14	66.140
$96 \times 96 \times 48$	24 h^f	0 h^f	0.1034	593.08	61.337	14:31:17	0.1031	593.08	61.122
$96 \times 96 \times 48$	24 h^f	2 h^f	0.1073	582.47	62.479		0.1066	582.56	62.083
$96 \times 96 \times 48$	24 h^f	3 h^f	0.1107	574.35	63.599		0.1087	4170.3	453.17
$96 \times 96 \times 48$	24 h^f	4 h^f	0.1143	564.24	64.486		0.1117	559.72	62.542
$96 \times 96 \times 48$	32 h^f	0 h^f	0.1051	599.99	63.037		0.1048	600.10	62.906
$96 \times 96 \times 48$	32 h^f	2 h^f	0.1075	590.90	63.546		0.1070	590.94	63.212
$96 \times 96 \times 48$	32 h^f	3 h^f	0.1100	581.51	63.986		0.1090	578.38	63.038
$96 \times 96 \times 48$	32 h^f	4 h^f	0.1128	571.21	64.433		0.1113	567.38	63.179
$96 \times 96 \times 48$	40 h^f	0 h^f	0.0985	645.21	63.569		0.0982	645.25	63.371
$96 \times 96 \times 48$	40 h^f	2 h^f	0.1002	638.44	63.974		0.0998	638.46	63.728
$96 \times 96 \times 48$	40 h^f	3 h^f	0.1018	633.05	64.490		0.1008	29504	2974.7
$96 \times 96 \times 48$	40 h^f	4 h^f	0.1038	625.70	64.924		0.1024	619.13	63.377

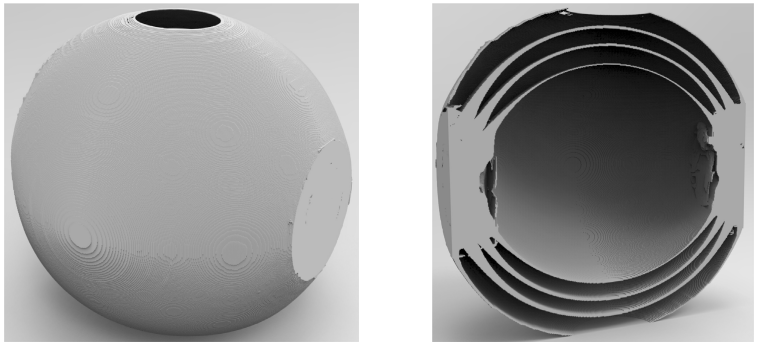

(a) Full view. (b) Section view.

Fig. 10. Michell's torsion sphere optimized on $\mathcal{T}^c = 48 \times 48 \times 48$ and de-homogenized on a fine mesh of $576 \times 576 \times 576$ using $\varepsilon = 32\ h^f$ and $f_{min} = 2\ h^f$.

4.4. Comparison with large-scale topology optimization

Besides verifying that the de-homogenized designs perform similar to the homogenization-based designs, it is interesting to compare the results with a well-established density-based topology optimization method. To do so, we make use of the publicly available topology optimization code using the PETSc framework [44]. The code has been slightly modified to allow for different boundary conditions, passive elements and a continuation scheme on the

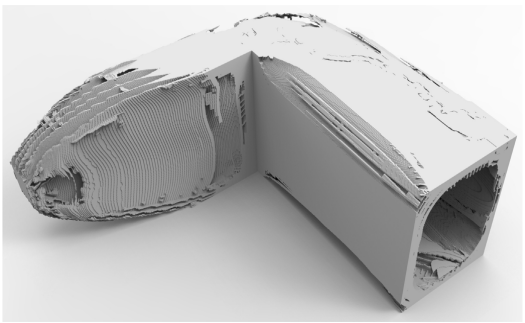

(a) Side view.

(b) Section view from the top.

Fig. 11. The L-shaped beam example optimized on $\mathcal{T}^c = 96 \times 96 \times 48$ and de-homogenized on a fine mesh of $768 \times 768 \times 384$ using $\varepsilon = 24\ h^f$ and $f_{min} = 2\ h^f$.

Table 8
Compliance $\mathcal{J}_f$, volume fraction V_f^f, the number of iterations n_{iter}, and run time T_f for different optimization examples optimized using a density-based optimization procedure.

Example	Mesh size	$\mathcal{J}^f$	$\mathcal{S}^f$	V_f^f	n_{iter}	T^f
Michell cantilever	$960 \times 480 \times 480$	236.262	23.626	0.100	450	08:13:28
Michell's torsion sphere	$576 \times 576 \times 576$	20.916	2.0916	0.100	450	01:03:06
Electrical mast	$384 \times 384 \times 1152$	99.961	9.9961	0.100	450	02:16:28
L-beam	$768 \times 768 \times 384$	585.114	58.511	0.100	450	04:38:50

penalization factor (p). We start with $p = 1$ and slowly increase this to $p = 4$, and stop the optimization procedure after 450 iterations when the change in design is negligible. Furthermore, it should be noted that the density filter is used in these examples with a filter radius of $R = 3h^f$, where the filter is turned off in the final iterations to allow for black and white designs.

All four examples shown in Fig. 4 are optimized on the same resolution as the de-homogenized designs discussed above. The corresponding fine-scale compliance $\mathcal{J}^f$, measure of stiffness per weight $\mathcal{S}^f$, volume fraction V_f^f, the number of iterations n_{iter}, and run time T^f are shown in Table 8. Furthermore, the design for the cantilever, and the electrical mast example are shown in Figs. 8(c) and (d) respectively. Finally it is mentioned that the same high-performance computing cluster is used as for the fine scale validations. Hence, for each optimization example 100 nodes each with 32 cores are used.

It can be seen that the compliance values of the density-based designs are close and in general even 5–10% better than the de-homogenized designs. This is more or less similar when we compare the stiffness per weight measure. The main reason is that the de-homogenized designs represent a multi-scale structure, which ideally should be de-homogenized on a finer mesh, to accurately capture all these multi-scale features. But more importantly, the well-performing de-homogenized designs can be obtained using a modern PC, while for the density-based designs an expensive high-performance computing cluster is required. The de-homogenization procedure can therefore reduce the threshold for using topology optimization for generating large-scale designs. By looking at the run time and number of cores we can conclude that the total computational cost can be reduced by at least 3 orders of magnitude compared to standard density-based topology optimization!

Finally, it should be mentioned that another improvement in compliance can be obtained by creating a conformal mesh from the implicit geometry description $\tilde{\rho}$. This approach, which will be pursued in future work, allows for more details and a better boundary description compared to the use of a voxel mesh.

5. Concluding remarks

We have presented a highly efficient approach to obtain manufacturable and ultra-high resolution designs from homogenization-based topology optimization. By doing homogenization-based topology optimization using optimal microstructures, an optimal design can be represented on a relatively coarse mesh. A good rule of thumb would be that at least 48 elements in each direction of the mesh are required. The subsequently de-homogenized designs perform in general 5–10% worse than the designs obtained using well-established density-based topology optimization. Hence, there is still room for improvement, for example by addressing the artifacts at the boundary that do not carry any load. However, instead of using high performance computing facilities with more than 3000 cores the presented designs have been obtained using a single core MATLAB process on a modern workstation PC. Hence, the presented procedure is a first step on the way to achieve giga-scale interactive topology optimization.

Besides obtaining near-optimal designs, we have presented a method to control the shape and minimum feature size of these de-homogenized designs ensuring manufacturability. From the results it can also be seen that even better performing designs can be obtained when de-homogenizing on a finer mesh. This paves the way for future studies into different methods to represent the de-homogenized designs, other than the voxel grid that has been used now. Note however that the presented procedure only works for examples where the homogenization-based designs are free of singularities. Hence, a natural extension would be to better understand the occurrence of singularities and extend the de-homogenization procedure such that it takes these singularities into account. We are confident that this can be done to make topology optimization an integrated part of the design process for large-scale problems.

It is noted that the current formulation is only applicable to a single loading case. For multiple independent loading cases, the optimal solution space consists of rank-6 laminates, where multiple different microstructures can reach the same bounds on strain energy, see e.g. [21] regarding non-uniqueness. This type of optimization problems consist of several new challenges, including the non-uniqueness, which will be addressed in future work. Finally, it is important that more complex problems than compliance minimization are considered. Possible formulations can be optimization of fundamental frequency for free vibration problems [46] or multi-physics design problems. Although challenging, we believe that addressing these types of problems also can be solved in a multi-scale sense allowing for efficient high-resolution designs.

Acknowledgments

The authors acknowledge the financial support from the Villum Foundation, Denmark (InnoTop VILLUM investigator project). Furthermore, the authors would like to express their gratitude to the members of the TopOpt group at DTU for valuable discussions during the preparation of this work. Finally, the authors wish to thank Krister Svanberg for the Matlab MMA code.

References

[1] J. Alexandersen, O. Sigmund, N. Aage, Large scale three-dimensional topology optimisation of heat sinks cooled by natural convection, Int. J. Heat Mass Transfer 100 (2016) 876–891, http://dx.doi.org/10.1016/j.ijheatmasstransfer.2016.05.013.

[2] C.B. Dilgen, S.B. Dilgen, D.R. Fuhrman, O. Sigmund, B.S. Lazarov, Topology optimization of turbulent flows, Comput. Methods Appl. Mech. Engrg. 331 (2018) 363–393, http://dx.doi.org/10.1016/j.cma.2017.11.029.

[3] S. Schmidt, E. Wadbro, M. Berggren, Large-scale three-dimensional acoustic horn optimization, SIAM J. Sci. Comput. 38 (6) (2016) B917–B940, http://dx.doi.org/10.1137/15M1021131.

[4] N. Aage, E. Andreassen, B.S. Lazarov, O. Sigmund, Giga-voxel computational morphogenesis for structural design, Nature 550 (7674) (2017) 84–86, http://dx.doi.org/10.1038/nature23911.

[5] R.V. Kohn, G. Strang, Optimal design and relaxation of variational problems, I, Comm. Pure Appl. Math. 39 (1) (1986) 113–137, http://dx.doi.org/10.1002/cpa.3160390107.

[6] G. Allaire, S. Aubry, On optimal microstructures for a plane shape optimization problem, Struct. Optim. 17 (2) (1999) 86–94, http://dx.doi.org/10.1007/BF01195933.

[7] A. Bensoussan, J.-L. Lions, G. Papanicolaou, Asymptotic Analysis for Periodic Structures (Studies in Mathematics and Its Applications), Elsevier Science Ltd., 1978.

[8] K.A. Lurie, A.V. Cherkaev, G-closure of some particular sets of admissible material characteristics for the problem of bending of thin elastic plates, J. Optim. Theory Appl. 42 (2) (1984) 305–316, http://dx.doi.org/10.1007/bf00934301.

[9] A. Norris, A differential scheme for the effective moduli of composites, Mech. Mater. 4 (1) (1985) 1–16, http://dx.doi.org/10.1016/0167-6636(85)90002-x.

[10] G.W. Milton, Modelling the properties of composites by laminates, in: J.L. Ericksen, D. Kinderlehrer, R. Kohn, J.-L. Lions (Eds.), Homogenization and Effective Moduli of Materials and Media, Springer New York, New York, NY, 1986, pp. 150–174.

[11] G.A. Francfort, F. Murat, Homogenization and optimal bounds in linear elasticity, Arch. Ration. Mech. Anal. 94 (4) (1986) 307–334, http://dx.doi.org/10.1007/BF00280908.
[12] M.P. Bendsøe, Optimal shape design as a material distribution problem, Struct. Optim. 1 (4) (1989) 193–202, http://dx.doi.org/10.1007/bf01650949.
[13] G. Allaire, Shape Optimization By the Homogenization Method, Springer-Verlag, New York, 2002.
[14] M.P. Bendsøe, O. Sigmund, Topology Optimization-Theory, Methods, and Applications, Springer, Berlin, 2004.
[15] M.P. Bendsøe, N. Kikuchi, Generating optimal topologies in structural design using a homogenization method, Comput. Methods Appl. Mech. Engrg. 71 (2) (1988) 197–224, http://dx.doi.org/10.1016/0045-7825(88)90086-2.
[16] O. Sigmund, Materials with prescribed constitutive parameters: An inverse homogenization problem, Int. J. Solids Struct. 31 (17) (1994) 2313–2329, http://dx.doi.org/10.1016/0020-7683(94)90154-6.
[17] H. Rodrigues, J. Guedes, M. Bendsøe, Hierarchical optimization of material and structure, Struct. Multidiscip. Optim. 24 (1) (2002) 1–10, http://dx.doi.org/10.1007/s00158-002-0209-z.
[18] P. Coelho, J. Cardoso, P. Fernandes, H. Rodrigues, Parallel computing techniques applied to the simultaneous design of structure and material, Adv. Eng. Softw. 42 (5) (2011) 219–227, http://dx.doi.org/10.1016/j.advengsoft.2010.10.003.
[19] L. Liu, J. Yan, G. Cheng, Optimum structure with homogeneous optimum truss-like material, Comput. Struct. 86 (13) (2008) 1417–1425, http://dx.doi.org/10.1016/j.compstruc.2007.04.030, Structural Optimization.
[20] R. Sivapuram, P.D. Dunning, H.A. Kim, Simultaneous material and structural optimization by multiscale topology optimization, Struct. Multidiscip. Optim. 54 (5) (2016) 1267–1281, http://dx.doi.org/10.1007/s00158-016-1519-x.
[21] E. Träff, O. Sigmund, J.P. Groen, Simple single-scale microstructures based on optimal rank-3 laminates, Struct. Multidiscip. Optim. 59 (4) (2019) 1021–1031, http://dx.doi.org/10.1007/s00158-018-2180-3.
[22] O. Pantz, K. Trabelsi, A post-treatment of the homogenization method for shape optimization, SIAM J. Control Optim. 47 (3) (2008) 1380–1398, http://dx.doi.org/10.1137/070688900.
[23] J.P. Groen, O. Sigmund, Homogenization-based topology optimization for high-resolution manufacturable microstructures, Internat. J. Numer. Methods Engrg. 113 (8) (2018) 1148–1163, http://dx.doi.org/10.1002/nme.5575.
[24] G. Allaire, P. Geoffroy-Donders, O. Pantz, Topology optimization of modulated and oriented periodic microstructures by the homogenization method, Comput. Math. Appl. 78 (7) (2019) 2197–2229, http://dx.doi.org/10.1016/j.camwa.2018.08.007, Simulation for Additive Manufacturing.
[25] J.P. Groen, J. Wu, O. Sigmund, Homogenization-based stiffness optimization and projection of 2D coated structures with orthotropic infill, Comput. Methods Appl. Mech. Engrg. 349 (2019) 722–742, http://dx.doi.org/10.1016/j.cma.2019.02.031.
[26] P. Geoffroy-Donders, G. Allaire, O. Pantz, 3-D topology optimization of modulated and oriented periodic microstructures by the homogenization method, J. Comput. Phys. 401 (2020) 108994, http://dx.doi.org/10.1016/j.jcp.2019.108994.
[27] J. Wu, W. Wang, X. Gao, Design and optimization of conforming lattice structures, IEEE Trans. Vis. Comput. Graphics (2019) 1, http://dx.doi.org/10.1109/TVCG.2019.2938946.
[28] O. Sigmund, N. Aage, E. Andreassen, On the (non-)optimality of Michell structures, Struct. Multidiscip. Optim. 54 (2) (2016) 361–373, http://dx.doi.org/10.1007/s00158-016-1420-7.
[29] M. Avellaneda, Optimal bounds and microgeometries for elastic two-phase composites, SIAM J. Appl. Math. 47 (6) (1987) 1216–1228, http://dx.doi.org/10.1137/0147082.
[30] L.V. Gibiansky, A.V. Cherkaev, Microstructures of Composites of Extremal Rigidity and Exact Estimates of the Associated Energy Density, Report 1115, Ioffe Physico-Technical Institute, Acad of Sc, USSR, Leningrad, USSR, 1987, English translation in: Cherkaev, A.V., Kohn, R.V. (Eds), 1997. Topics in the mathematical modelling of composite materials. Birkhäuser Boston, MA..
[31] A. Díaz, O. Sigmund, Checkerboard patterns in layout optimization, Struct. Optim. 10 (1) (1995) 40–45, http://dx.doi.org/10.1007/bf01743693.
[32] B. Bourdin, Filters in topology optimization, Internat. J. Numer. Methods Engrg. 50 (9) (2001) 2143–2158, http://dx.doi.org/10.1002/nme.116.
[33] T. Bruns, D. Tortorelli, Topology optimization of non-linear elastic structures and compliant mechanisms, Comput. Methods Appl. Mech. Engrg. 190 (26–27) (2001) 3443–3459, http://dx.doi.org/10.1016/S0045-7825(00)00278-4.
[34] F. Wang, B.S. Lazarov, O. Sigmund, On projection methods, convergence and robust formulations in topology optimization, Struct. Multidiscip. Optim. 43 (6) (2010) 767–784, http://dx.doi.org/10.1007/s00158-010-0602-y.
[35] P. Pedersen, Bounds on elastic energy in solids of orthotropic materials, Struct. Optim. 2 (1) (1990) 55–63, http://dx.doi.org/10.1007/BF01743521.
[36] S.C. Cowin, Optimization of the strain energy density in linear anisotropic elasticity, J. Elasticity 34 (1) (1994) 45–68, http://dx.doi.org/10.1007/bf00042425.
[37] A.N. Norris, Optimal orientation of anisotropic solids, Quart. J. Mech. Appl. Math. 59 (1) (2005) 29–53, http://dx.doi.org/10.1093/qjmam/hbi030.
[38] O. Amir, N. Aage, B.S. Lazarov, On multigrid-CG for efficient topology optimization, Struct. Multidiscip. Optim. 49 (5) (2013) 815–829, http://dx.doi.org/10.1007/s00158-013-1015-5.
[39] K. Svanberg, The method of moving asymptotes–a new method for structural optimization, Internat. J. Numer. Methods Engrg. 24 (2) (1987) 359–373, http://dx.doi.org/10.1002/nme.1620240207.
[40] A. Vaxman, M. Campen, O. Diamanti, D. Panozzo, D. Bommes, K. Hildebrandt, M. Ben-Chen, Directional field synthesis, design, and processing, in: Computer Graphics Forum, Vol. 35, Wiley Online Library, 2016, pp. 545–572, http://dx.doi.org/10.1111/cgf.12864.
[41] F. Kälberer, M. Nieser, K. Polthier, QuadCover - Surface parameterization using branched coverings, Comput. Graph. Forum 26 (3) (2007) 375–384, http://dx.doi.org/10.1111/j.1467-8659.2007.01060.x.

[42] M. Nieser, U. Reitebuch, K. Polthier, CubeCover- Parameterization of 3D volumes, Comput. Graph. Forum 30 (5) (2011) 1397–1406, http://dx.doi.org/10.1111/j.1467-8659.2011.02014.x.

[43] P. Geoffroy-Donders, G. Allaire, G. Michailidis, O. Pantz, Coupled optimization of macroscopic structures and lattice infill, 2020, URL https://hal.archives-ouvertes.fr/hal-02429166, working paper or preprint.

[44] N. Aage, E. Andreassen, B.S. Lazarov, Topology optimization using PETSc: An easy-to-use, fully parallel, open source topology optimization framework, Struct. Multidiscip. Optim. 51 (3) (2014) 565–572, http://dx.doi.org/10.1007/s00158-014-1157-0.

[45] O. Sigmund, Morphology-based black and white filters for topology optimization, Struct. Multidiscip. Optim. 33 (4–5) (2007) 401–424, http://dx.doi.org/10.1007/s00158-006-0087-x.

[46] L.A. Krog, N. Olhoff, Optimum topology and reinforcement design of disk and plate structures with multiple stiffness and eigenfrequency objectives, Comput. Struct. 72 (4–5) (1999) 535–563, http://dx.doi.org/10.1016/s0045-7949(98)00326-5.

Appendix B: Paper-II

F. C. Stutz, J. P. Groen, O. Sigmund, and J. A. Bærentzen. **Singularity Aware De-Homogenization for High-Resolution Topology Optimized Structures**. *Structural and Multidisciplinary Optimization*, vol. 62, pp. 2279–2295, 2020. DOI: 10/gjhccf

Structural and Multidisciplinary Optimization (2020) 62:2279–2295
https://doi.org/10.1007/s00158-020-02681-6

RESEARCH PAPER

Singularity aware de-homogenization for high-resolution topology optimized structures

F. C. Stutz[1] · J. P. Groen[2] · O. Sigmund[2] · J. A. Bærentzen[1]

Received: 10 April 2020 / Revised: 2 July 2020 / Accepted: 6 July 2020 / Published online: 20 August 2020

Abstract
Homogenization-based topology optimization has been shown to be effective but does not directly create mechanical structures. Instead, the method gives a multi-scale description of the optimized design, e.g., lamination thicknesses and directions. To obtain a realizable single-scale design, one can perform a subsequent de-homogenization step. This is done by converting the lamination directions to integrable vector fields from which it is possible to compute a parameterization of the domain. Unfortunately, however, singularities often make it impossible to find integrable vector fields that align with lamination directions. We present a short introduction to homogenization-based topology optimization followed by an overview of different types of singularities and how they impinge on the problem. Based on this, we propose a singularity aware de-homogenization pipeline, where we use a method for vector field combing which produces consistent labeling of the lamination directions but also introduces necessary seams in the domain. We demonstrate how methods from computer graphics can subsequently be used to compute the final parameterization from which the mechanical structure can easily be extracted. We demonstrate the method on several test cases.

Keywords De-homogenization · Singularities · Topology optimization · High-resolution structures

1 Introduction

Topology optimization, a numerical tool for determining optimal mechanical layouts, has a broad spectrum of possible industrial applications. Over the last decades, the development and accessibility of computational power have made it an interesting design tool for the industry. However, further developments are still needed before large-scale, real-time topology optimization is possible on desktop computers.

Homogenization-based topology optimization, as proposed by Bendsøe and Kikuchi (1988), allows for composite material properties, which contain much more information compared to the isotropic material used in the SIMP (Solid Isotropic Material with Penalisation) approach (Bendsøe 1989). Hence, performing homogenization-based topology optimization allows us to solve the problem on a coarse grid while still enabling near-optimal, high-resolution results as shown in Groen and Sigmund (2018). In homogenization-based topology optimization, we can describe the composite material as infinitesimally small periodic unit cells on a microscopic level. On a macroscopic level, we can assume the material properties to be homogeneous. Hence, we can analyze the performance of a design where these composite properties are spatially varying in a multi-scale sense.

A subset of problems of interest in topology optimization is the compliance minimization of a plane structure subject to a single-load case, which is considered in this paper. For these types of problems, it is known that hierarchical rank-2 laminates are the optimal material parameterization (Allaire and Kohn 1993). Nevertheless, we use the square unit cell with a rectangular hole as proposed by Bendsøe and Kikuchi (1988) since these microstructures consist of a single length-scale and have only a small difference in performance (Bendsøe and Sigmund 1999; Träff et al. 2019).

The output from the single-load homogenization-based optimization method can be interpreted as a cross-field: at

Responsible Editor: Hyunsun Alicia Kim

✉ F. C. Stutz
fstu@dtu.dk

[1] Department of Applied Mathematics and Computer Science, Technical University of Denmark, 2800 Kgs. Lyngby, Denmark

[2] Department of Mechanical Engineering, Technical University of Denmark, 2800 Kgs. Lyngby, Denmark

each point of the optimized domain (in 2D), we have a pair of directions (as well as lamination thicknesses). Ultimately, our goal is to create a mechanical design whose structural members are well aligned with these frame directions. A particular approach to this problem involves creating a parametrization of the domain such that the gradients of the coordinate functions in the parametric domain are aligned with the cross-field obtained from the optimization procedure. If we are able to do that, it is possible to create a regular structure in the parametric domain and map it via the inverse parametrization back into the domain of the optimization. This procedure is known as the de-homogenization method (Pantz and Trabelsi 2008; Groen and Sigmund 2018; Donders 2018; Groen et al. 2020).

There are different ways to optimize the unit cell orientation of spatially varying designs. For instance, it is well-known that for 2- and 3-dimensional single-load case examples a unit cell is optimally aligned using the principal stress directions (Pedersen 1989; Norris 2005). However, the principal stress directions are not consistently labeled. Only in 2D can the stress directions be sorted to be smooth up to 180 degrees (see, e.g., Groen and Sigmund 2018). Similarly, when the unit cell orientations are optimized using gradient-based optimization, jumps of 90 degrees can occur. In other words, the first lamination direction at one point might correspond to the second lamination direction at a nearby point.

Recently, Groen and Sigmund (2018) simplified and further developed the projection approach by Pantz and Trabelsi (2008). However, this approach relied on two smooth vector fields (see Definition 2; 1-vector fields). They showed that these can be obtained by using orientations based on the principal stress direction. Similar to these directions, the orientation of the microstructure is rotationally symmetric by 180 degrees, i.e., the 1-vector fields often contain jumps of angle π. Groen and Sigmund (2018) showed that this problem can be solved by using connected component labeling in case there is no singularity present.

1.1 Contributions

In this paper, we would like to investigate how integration approaches can be extended for usage in fields containing singularities. This has been researched in Pantz and Trabelsi (2010) and Donders (2018). The main contribution of this paper is a pipeline for the de-homogenization of structures containing singularities as they occur, for example, not only due to loads inside the domain, but also due to numerically unstable results in low-density areas and regularization. Here, we use the word de-homogenization for the process of extracting a mechanically well-performing structure from the solution of the homogenization method. The pipeline allows us to investigate the location and type of singularities that appear in fields arising from the homogenization-based topology optimization method, and their relation to the density distribution. We compare different starting guesses for the homogenization-based topology optimization and their influence on the resulting structure. Furthermore, we will investigate how to extract two as smooth as possible vector fields in the presence of singularities. This extraction of two vectors per element is called combing in computer graphics and is normally done by using a breadth-first search: Starting from a root element, all elements in the domain are visited in order of growing distance to the root element (see further in Section 5.2, Skiena 2008). We will use a density-based approach, which allows for simpler seams (see Definition 5, seams) than in the case of using a breadth-first search. We then relate the parametrization step to a computer graphics method for quadrilateral meshing (Bommes et al. 2009), by introducing seams in the parameterization domain in order to allow for mismatches caused by the singularities, while still getting smooth de-homogenized designs.

In general, we specify parameters, running times, and compliance values in order to allow the reader to observe the influence of these parameters to the de-homogenized structure and motivate further research areas. It is not our primary goal in this work to tune the parameters of the pipeline for mechanical performance.

2 Related work

Pantz and Trabelsi (2008) proposed a method to project the unit square microstructure macroscopically. Their de-homogenization approach minimizes alignment energy to find a parametrization aligned with the orientation of the microstructure. The approach assumes two separate vector fields, whose orientation is not of importance. Groen and Sigmund (2018) simplified the approach by Pantz and Trabelsi, still using two separate vector fields, however, with the challenge of having consistently aligned vector fields as the approach is not invariant to angle jumps of angle π. This was solved by using a connected component analysis on the vector fields. Both approaches do not explicitly deal with jumps of angle $\pi/2$. Pantz and Trabelsi (2010) investigated the challenge of singularities for the first time. The singularities, located in void regions, are nucleated, i.e., the areas containing singularities are excluded from the parametrization step and onwards. Donders (2018) proposed a method of spotting singularities of index $\pm 1/2$ using a technique explained in more detail in Hotz et al. (2010). This only allows for jumps of angle π. In order

to deal with the singularities, correction functions are computed to prevent mismatches at seams.

The work of Kälberer et al. (2007) proposed the "QuadCover" algorithm for field-guided quad meshing using multiple coverings. Multiple coverings in the sense that the parametrization domain is duplicated multiple times. This means that the rotationally symmetric field simplifies to vector fields on every single covering and thus becomes integrable. In practice, only a single parametrization domain is used and operators to account for the different coverings are introduced. Bommes et al. (2009) proposed a refinement of QuadCover, solving the resulting system in an iterative approach yielding better results.

3 Homogenization-based topology optimization

The methodology to perform homogenization-based topology optimization used here is very similar to the method in Groen and Sigmund (2018), and therefore, this section will be kept brief, with an emphasis on the differences.

3.1 Microstructure parameterization

As a microstructure parameterization, we use the square unit cell with a rectangular hole proposed by Bendsøe and Kikuchi (1988) and shown in Fig. 1. The constitutive properties of this microstructure, consisting of void and isotropic material using $E = 1$ and $\nu = 0.3$, can be obtained using numerical homogenization on a conformal mesh. A database of the constitutive properties in the local frame can be pre-computed for various physical heights $\bar{\tilde{a}}_1$ and physical widths $\bar{\tilde{a}}_2$ of the hole. Afterwards, we can interpolate the effective properties $\boldsymbol{E}^H$ and corresponding sensitivities for any combination of $\bar{\tilde{a}}_1$ and $\bar{\tilde{a}}_2$. The elasticity tensor in the global frame of reference $\boldsymbol{E}$ can then be obtained as

$$\boldsymbol{E}(\theta, \bar{\tilde{a}}_1, \bar{\tilde{a}}_2) = \boldsymbol{R}(\theta)\boldsymbol{E}^H(\bar{\tilde{a}}_1, \bar{\tilde{a}}_2)\boldsymbol{R}(\theta)^{\mathrm{T}}, \tag{1}$$

with $\boldsymbol{R}$ being the rotation matrix. The volume fraction of the microstructure ρ is given as

$$\rho = 1 - \bar{\tilde{a}}_1 \bar{\tilde{a}}_2. \tag{2}$$

3.2 Optimization and regularization of the microstructure orientation

Contrary to the approach presented in Groen and Sigmund (2018) we update the angles based on their gradients instead of the principal stress directions. There are two reasons for this. First, updating the angles based on the gradients is slightly more stable than updating the orientation based on the principal stress directions (Pedersen 1989), since first-order finite elements are used. Second, and more importantly, we can introduce regularization energy, similar to the one in Groen et al. (2020) such that the 4-direction field is slowly varying over the domain.

To perform the regularization, we loop over all n_e edges, each connecting two elements. We introduce a penalization function $\mathcal{P}_e \in [0, 1]$. This penalization function is based on the orientation angles of the microstructure in the two adjacent elements f_1 and f_2 connected by edge e. We denote these two angles with θ_{f_1} and θ_{f_2} and calculate

$$\mathcal{P}_e = \frac{1}{2} - \frac{1}{2}\cos(4\theta_{f_1} - 4\theta_{f_2}). \tag{3}$$

It can be seen that $\mathcal{P}_e$ has minimum values at angle differences of 0 or $k\pi/2$ with k an integer and returns a small penalty value for small angle differences. By looping over all edges e, we obtain a single regularization objective $\mathcal{F}_\theta$,

$$\mathcal{F}_\theta = \sum_{f=1}^{n_e} \mathcal{P}_e, \tag{4}$$

which is normalized in the optimization problem using the regularization objective $\mathcal{F}_\theta^{(1)}$ for the starting guess of the layer normals.

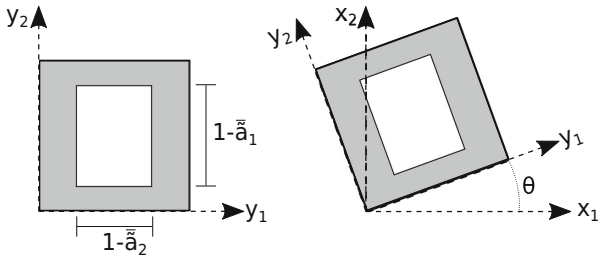

Fig. 1 Layout of the unit cell with a rectangular hole, in local (y_1,y_2), and global (x_1,x_2) coordinate system

3.3 Problem formulation

We focus on minimizing the objective functional $\mathcal{F}$, which is a combination of the compliance $\mathcal{J}$ and regularization objective $\mathcal{F}_\theta$. The domain is discretized using bi-linear finite elements and the material properties are assumed to be element-wise constant. We want to avoid checkerboard-like instabilities that can occur due to the use of bi-linear finite elements (Díaz and Sigmund 1995). Therefore, we use a standard density filter to obtain the filtered hole height $\tilde{\boldsymbol{a}}_1$ and width $\tilde{\boldsymbol{a}}_2$ from design vectors $\boldsymbol{a}_1$ and $\boldsymbol{a}_2$ (Bourdin 2001; Bruns and Tortorelli 2001).

Furthermore, we want the microstructure widths to be either void, completely solid or in the interval $[\eta, 1-\eta]$, with $\eta = 0.05$ used in this study. To do so, we use the same interpolation scheme as in (Groen and Sigmund 2018; Groen et al. 2020), which modifies the variables $\tilde{\boldsymbol{a}}_1$ and $\tilde{\boldsymbol{a}}_2$ into the physical hole height $\tilde{\tilde{\boldsymbol{a}}}_1$ and width $\tilde{\tilde{\boldsymbol{a}}}_2$. The optimization problem is solved in nested form, which means that for each design iteration we solve the state equation after which the design vectors are updated. Hence, the discretized optimization problem can be written as,

$$\begin{aligned}
\min_{\boldsymbol{a}_1,\boldsymbol{a}_2,\boldsymbol{\theta}} &: \mathcal{F}(\boldsymbol{a}_1,\boldsymbol{a}_2,\boldsymbol{\theta},\mathbf{U}) = \\
&\qquad \frac{\mathcal{J}(\boldsymbol{a}_1,\boldsymbol{a}_2,\boldsymbol{\theta},\mathbf{U})}{\mathcal{J}^{(1)}} + \gamma_\theta \frac{\mathcal{F}_\theta(\boldsymbol{\theta})}{\mathcal{F}_\theta^{(1)}}, \\
\text{s.t.} &: \mathbf{K}(\boldsymbol{a}_1,\boldsymbol{a}_2,\boldsymbol{\theta})\mathbf{U} = \mathbf{F}, \\
&: \mathbf{v}^T \boldsymbol{\rho}(\boldsymbol{a}_1,\boldsymbol{a}_2) - V_f^{max} A \le 0, \\
&: \mathbf{0} \le \boldsymbol{a}_1, \boldsymbol{a}_2 \le \mathbf{1}, \\
&: \mathbf{-4\pi} \le \boldsymbol{\theta} \le \mathbf{4\pi},
\end{aligned} \tag{5}$$

where $\mathbf{v}$ is the vector containing the element areas and V_f^{max} is the maximum allowed fraction of the material in Ω, with A the area of Ω. $\mathbf{K}$ is the stiffness matrix and vector $\mathbf{F}$ describes the loads acting on the domain. $\mathcal{J}^{(1)}$ is the compliance of the first analysis step and $\mathcal{F}_\theta^{(1)}$ the regularization objective for the starting guess. For the design update, we use the MATLAB implementation of the method of moving asymptotes (MMA) introduced by Svanberg (1987). Finally, it should be mentioned that the compliance minimization problem is self-adjoint, meaning that we only require the solution of one linear system to obtain both compliance and corresponding sensitivities.

As a starting guess for the microstructure, we use $\boldsymbol{a}_1 = \boldsymbol{a}_2$, such that the volume constraint is exactly satisfied. The starting guess for the orientation is based on a pre-analysis using isotropic microstructures, the corresponding principal stress directions are used to determine $\boldsymbol{\theta}$ unless otherwise noted. Finally, it should be mentioned that the scaling parameter γ_θ has a large influence on the optimization procedure and is in general chosen to be $\gamma_\theta = 1/20$.

4 Singularities

In order to study the vector fields generated by the homogenization method, it is important to have a general understanding of vector fields, direction fields, and the eigenvectors and eigenvalues of the stress tensors. This allows us to precisely define singularities and their indices and use this knowledge to study stress tensor and layer-normal fields. Vaxman et al. (2016) introduced a notation that is tailored for this purpose. We will in the following section describe relevant definitions from Vaxman et al. (2016) related to the homogenization method and introduce their notation. We start with the definition of a directional field and N-directional fields.

Definition 1 (Directional field, vector field, and direction field) A directional field denotes a function $\mathbf{v}$ that assigns directional information to almost every point in a given domain. If a directional field $\mathbf{v}$ provides a magnitude of importance for every point p, for which $\mathbf{v}$ is defined, then $\mathbf{v}$ is called a vector field (see Fig. 2a). If the directional field does not provide any magnitude (e.g. all assigned vectors are normalized) it is called a direction field (see Fig. 2b).

Definition 2 (N-directional field) A directional field can assign multiple directions to the same point in a domain Ω. Let us assign N vectors to almost every point in Ω. Then, the use-cases of $N = 1, 2, 4$ are of importance to the application of the homogenization method. We write **N-vector** or **N-direction** field to indicate the number of directional information given at every point.

Figure 3 shows direction fields and vector fields important to the homogenization method, where we indicate a given magnitude with arrows. The 1-vector fields are what we usually refer to when talking about vector fields. If $N = 2$, the vector is invariant under a rotation of angle π and we call such a field a 2-vector field. For $N = 4$ follows the 4-vector field with rotational symmetry of $\pi/2$.

4.1 Index of a singularity

Singularities often arise in the presence of internal loads, multiple loads, or a designated passive domain. The following definitions describe singularities and their indices.

Definition 3 (Singular point, singularity) A point $\mathbf{p}$ in a 1-vector field $\mathbf{v}$ for which $\mathbf{v}$ is not defined or zero is called a singular point or singularity (see Fig. 4).

Definition 4 (Index of a singularity) A singular point $\mathbf{p}$ can be assigned an index by the following procedure. We consider the vector field $\mathbf{v}$ on a closed, simple curve $\mathbf{c}(t)$,

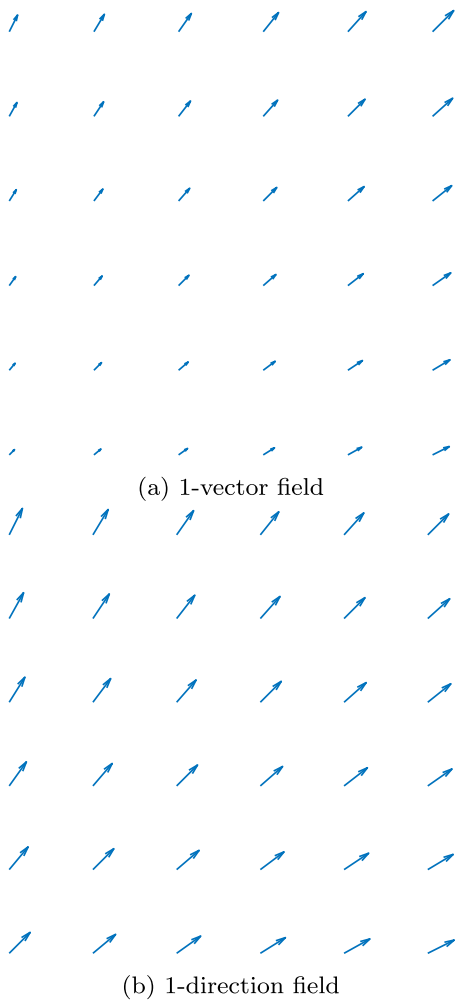

Fig. 2 Comparison of 1-vector and 1-direction field

$t \in [0, 1]$, around $\mathbf{p}$, which does not contain a second singular point. We obtain $\mathbf{v}$ limited to $\mathbf{c}(\mathbf{t})$, by

$$\mathbf{v}(\mathbf{c}(t)) = \|\mathbf{v}(\mathbf{c}(t))\| \begin{pmatrix} \cos(\alpha(t)) \\ \sin(\alpha(t)) \end{pmatrix}.$$

Here, $\mathbf{c} : [0, 1] \to \mathbb{R}^2$ denotes the counterclockwise parametrization of the curve and $\alpha : [0, 1] \to \mathbb{R}$ the enclosed angle between the x-axis and $\mathbf{v}(\mathbf{c}(t))$. The index of

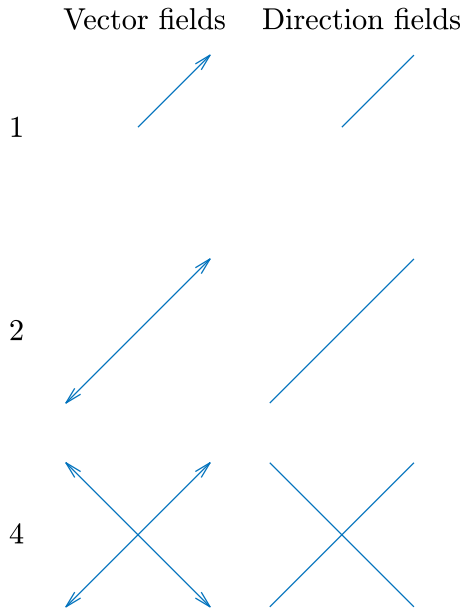

Fig. 3 Vector and direction fields for $N \in \{1, 2, 4\}$. A given magnitude is indicated by arrows

$\mathbf{p}$ is then defined as $\text{idx}_p = \frac{1}{2\pi}(\alpha(1) - \alpha(0))$ measuring the rotation of the vector field around the singular point.

In Fig. 4, we consider a singularity in $(0, 0)$ and depict the curve c with $c(0) = c(1) = (1, 0)$ as a red circle. Further, we see that the enclosed angles α, depicted as black circle arcs, grow from $\alpha(0) = 0$ to $\alpha(1) = 2\pi$. Thus, we have a singularity (depicted in green) with index $\text{idx}_p = \frac{1}{2\pi}(2\pi - 0) = 1$. Note that singularities exist for all types of N-directional fields, where the index must always be a multiple of $1/N$. In order to identify the index of a singularity in a N-directional field, one proceeds similar to singularities in 1-directional fields. Following a closed curve around the singular point, one measures the change of the angle of the N-directional field. In a discrete example, as in Fig. 7d for example, one chooses one of the directions and follows that one along the curve.

4.2 Singularities in smooth tensor fields

The singularities of smooth tensor fields have been studied exhaustively in order to visualize tensor fields. Delmarcelle and Hesselink (1994) show that singularities in tensor fields

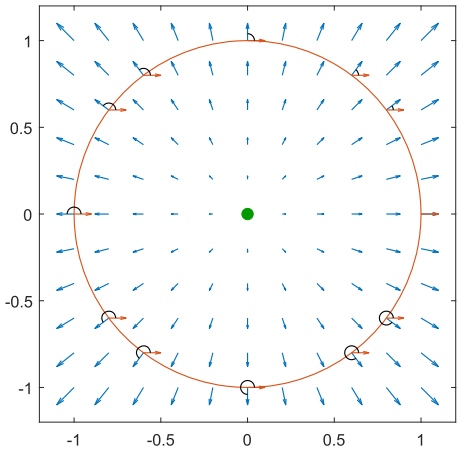

Fig. 4 Vector field containing a singularity of index 1 (in green), showing the tracked curve (in red) and the angle arcs (in black)

can only have indices that are multiples of $\pm 1/2$. We try to present a descriptive version in the following theorem.

Theorem 1 *A smooth tensor field can only incorporate singularities of index* $\pm 1/2$ *or multiples thereof.*

(Sketch) If we follow a closed, simple curve around a singularity **p**, not containing a second singularity, with index $\pm 1/4$ as depicted in Fig. 5, we see that red and blue vectors trade places. That would not be a problem for a 4-direction field where all four directions are equivalent, but if we have a tensor, we can distinguish the red and blue direction from each other by the magnitude of the eigenvalue. So, say blue is the direction of maximum eigenvalue that we follow, but coming back to the initial point it then must be red. The tensor has changed smoothly along the black curve, so there must have been a point along the black curve at which the eigenvalues were the same. However, if the eigenvalues are the same, any plane vector is an eigenvector, and we have a singular point. This contradicts the way the black curve was chosen and concludes the proof. □

In homogenization-based topology optimization, the layer normals are aligned with the stress tensors either by demanding it through the implementation or in a gradient descent algorithm since layers aligned to the load-path are optimal (Pedersen 1989). Therefore, the following singularity types are found regularly in the output fields of the homogenization method.

For example, if all corners of a triangle are pulled apart (see Fig. 6a) a singularity of index $-1/2$ occurs (see Fig. 7a). Figure 7b shows a singularity of type -1. This can be seen as two singularities of type $-1/2$ pushed together. This type of singularity occurs in a corner loaded square (see Fig. 6b). Figure 7c shows a singularity of index $1/2$ as occurs for example in a center loaded clamped beam (see Fig. 6c).

4.3 Singularities in 4-direction fields

It is important to differentiate between the 4-vector field described by a stress tensor field and the 4-direction field described by the layer normals output by the homogenization method. The latter can also incorporate singularities of index $\pm 1/4$ due to numerical errors or regularization of the layer normals or simply due to the optimizer being stuck in a local minimum.

Figure 7 d and e show 4-direction fields incorporating each a singularity of index $\pm 1/4$. It is not possible to separate these 4-direction fields into two 1-direction fields, which are shown in Fig. 7f. Especially regularization seems to result in singularities of index $\pm 1/4$. Increasing the regularization value γ_θ limits the angular changes. In Fig. 8a–f, we depict how a singularity of index $\pm 1/2$ is spatially ripped apart more and more with increasing regularization. In this example, the singularity of index $\pm 1/2$ is split into two singularities of index $\pm 1/4$ that are located in the center of the domain at the end of the red lines.

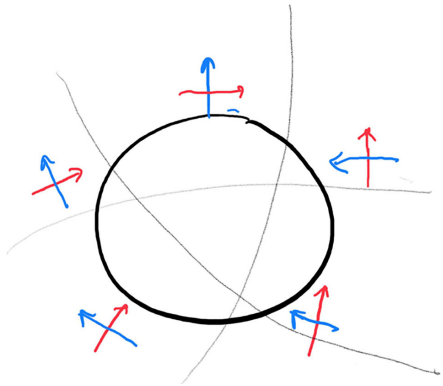

Fig. 5 Sketch of a singularity with index 1/4

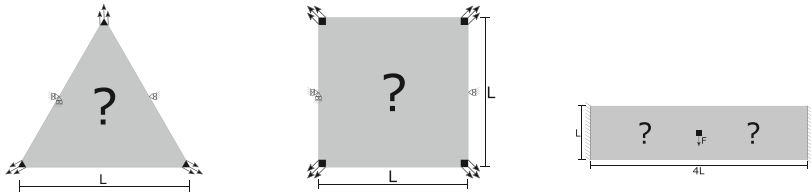

(a) Corner-loaded triangle (b) Corner-loaded square (c) Center-loaded clamped beam

Fig. 6 Examples of load cases leading to singularities

The red lines indicate where the vector fields jump by 90 or 180 degrees.

4.4 Occurrence of singularities in the homogenization results

For the de-homogenization, it is of importance to have an understanding of where singularities occur in the layer-fields output by the homogenization method. We are not aware of a theoretical solution to this, but we observe that, in general, singularities occur in regions with very high or very low density.

Let us assume that in the output of the homogenization method, the layer normals are well aligned with the stress directions everywhere, such that singularities in the stress field correspond to singularities in the layer field. We investigate a singularity **p**, where the stress field is non-zero. At such a singular point, the stress field rotates with an index $\mathrm{idx}_p \neq 0$. Thus, in the immediate surrounding, we see all directions in the interval $I = [0, 2\pi\,\mathrm{idx}_p]$. If we measure the angular velocity on several curves around **p**, we realize that the shorter the curve, i.e., the closer to **p**, the higher the angular velocity becomes, as the field always needs to rotate by $2\pi\mathrm{idx}_p$. Or in other words, at **p**, the stress field rotates infinitely fast. The homogenization method outputs two-layer normals $\boldsymbol{n}^{1,2}$ and widths $w_{1,2}$ and thus a density $\rho = w_1 + w_2 - w_1 w_2$ for the element containing **p**. Now, if $0 \leq \rho < 1$, only the directions $\boldsymbol{n}^{1,2}$ in I are well aligned with the unit cell. Thus, for all other directions in I, a shearing force will arise. The optimizer can improve compliance by making the element containing **p** isotropic, which means that we can observe a density peak $\rho \to 1$ in

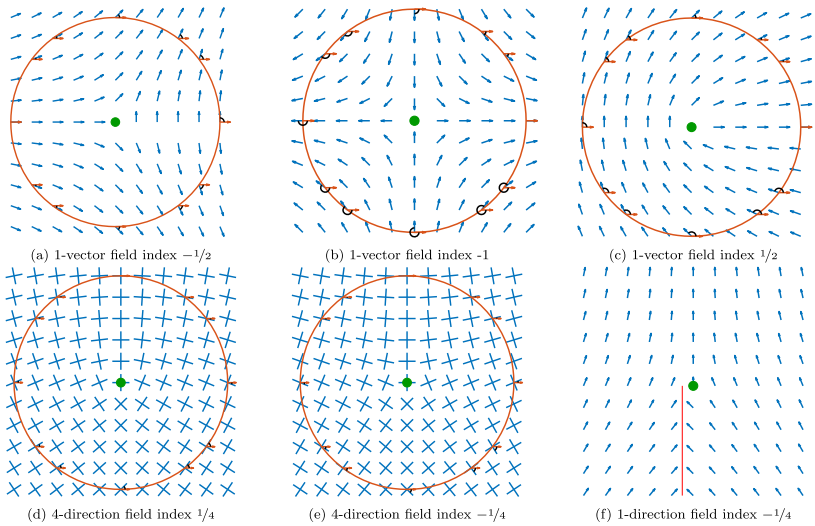

(a) 1-vector field index $-1/2$ (b) 1-vector field index -1 (c) 1-vector field index $1/2$

(d) 4-direction field index $1/4$ (e) 4-direction field index $-1/4$ (f) 1-direction field index $-1/4$

Fig. 7 Vector and direction fields for different singularities

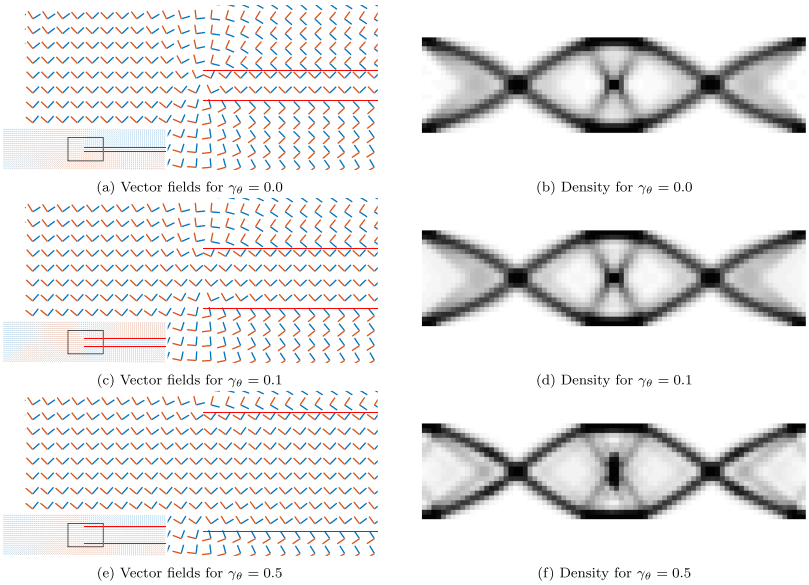

(a) Vector fields for $\gamma_\theta = 0.0$ (b) Density for $\gamma_\theta = 0.0$

(c) Vector fields for $\gamma_\theta = 0.1$ (d) Density for $\gamma_\theta = 0.1$

(e) Vector fields for $\gamma_\theta = 0.5$ (f) Density for $\gamma_\theta = 0.5$

Fig. 8 Vector fields and densities for different degrees of regularization

the vicinity of the singularity **p**. The same effect can be seen in Fig. 8, where the material is distributed differently due to the layer directions differing from the stress direction due to smoothing. It is important to note that singularities also may occur in void regions. Following the above thought of using the material to create isotropic elements, it is intuitively understandable that the optimizer mostly tries to stay clear of regions with fast turning stress fields and hence creates singularities in elements with $\rho = 0$ as well.

The above observation does not allow a prediction of where singularities occur in the layer field. It does however allow to reason, why regions containing singularities can often be filled completely with the material in the post-processing without an excessive amount of additional material needed as we already see a density peak. One needs to be careful as the above observation assumes layer fields that are well aligned to the principal stress directions.

5 De-homogenization for singularity containing 4-direction fields

With the knowledge accrued about singularities in the last section, we are now able to study examples that contain singularities. In this section, we revisit approaches for the de-homogenization in singularity free problems (see Section 5.1), propagate consistent labeling of the direction fields in the case of singularities (see Section 5.2), and show the connection to quad meshing (see Section 5.3).

5.1 De-homogenization for smooth, continuous, and singularity free 4-direction fields

Similar to Pantz and Trabelsi (2008), Groen and Sigmund (2018), and Allaire et al. (2018), we de-homogenize the square unit cell with a rectangular hole using two periodic layers superimposed onto each other. Provided that vector fields are smooth, we can use the procedure as presented in Groen et al. (2019) which will be repeated here for convenience.

Based on the two smooth 1-direction fields $\boldsymbol{n}^i$, $i \in \{1, 2\}$, we create two mapping functions ϕ_1 and ϕ_2 that preserve the orientation of the microstructures. Nevertheless, it should be noted that the map is not strictly conformal. The values of ϕ_i do not need to be accurate when there is no material in the layer (i.e., $w_i < 0.01$) or when the domain is completely solid (i.e., $\rho > 0.99$). Hence, the problem only needs to be solved accurately in the intermediate material part of the

domain of the $i-th$ layer $\tilde{\Omega}_i$. This leads to the following spatially weighted partial differential equations (PDE),

$$\begin{aligned} &\alpha_1^i(\boldsymbol{x})\nabla\phi_i(\boldsymbol{x}) = \alpha_1^i(\boldsymbol{x})\boldsymbol{n}^i(\boldsymbol{x}), \quad \boldsymbol{x}\in\Omega \\ \text{s.t.} \quad &\alpha_2^i(\boldsymbol{x})\nabla\phi_i(\boldsymbol{x})\cdot\boldsymbol{t}^i(\boldsymbol{x}) = 0, \quad \boldsymbol{x}\in\Omega \end{aligned} \tag{6}$$

where $\boldsymbol{t}^i$ denotes the orthogonal vector to $\boldsymbol{n}^i$. The domain is split up into three parts, which dictate the weights on the objective α_1^i and the weights on the constraints α_2^i,

$$\begin{aligned} \alpha_1^i(\boldsymbol{x}) &= \begin{cases} 0.01 & \text{if} \quad w_i(\boldsymbol{x}) < 0.01, \\ 0.1 & \text{if} \quad \rho(\boldsymbol{x}) > 0.99, \\ 1 & \text{if} \quad \boldsymbol{x}\in\tilde{\Omega}_i. \end{cases} \\ \alpha_2^i(\boldsymbol{x}) &= \begin{cases} 0 & \text{if} \quad w_i(\boldsymbol{x}) < 0.01, \\ 0 & \text{if} \quad \rho(\boldsymbol{x}) > 0.99, \\ 1 & \text{if} \quad \boldsymbol{x}\in\tilde{\Omega}_i. \end{cases} \end{aligned} \tag{7}$$

Numerically, we solve the above-mentioned problem as a linear system using the finite element approach, where the constraint is enforced in an augmented setting using penalty parameter γ_ϕ, called the alignment weight. With both mapping fields known, we can create an implicit geometry description $\tilde{\rho}_i$ for each of the layers:

$$\tilde{\rho}_i(\boldsymbol{x}) = H\left(\left(\frac{1}{2}+\frac{1}{2}\mathcal{S}\left\{P_i\phi_i(\boldsymbol{x})\right\}\right) - \tilde{w}_i(\boldsymbol{x})\right). \tag{8}$$

Here, H is the Heaviside function and $\mathcal{S}\in[-1,1]$ corresponds to a triangle wave. Furthermore, P_i is a periodicity scaling. Hence, the design can be de-homogenized by an implicit geometry function $\tilde{\rho}$ as

$$\tilde{\rho}(\boldsymbol{x}) = \min\left\{1, \sum_{i=1}^{2}\tilde{\rho}_i(\boldsymbol{x})\right\}. \tag{9}$$

Finally, we can impose an average layer spacing ε, which can be interpreted as the unit cell size. To do so, we define the periodicity scaling parameter P_i based on the average lattice spacing in the domain of interest $\tilde{\Omega}_i$

$$P_i = \frac{2\pi}{\varepsilon}\frac{\int_{\tilde{\Omega}_i}\mathrm{d}\tilde{\Omega}_i}{\int_{\tilde{\Omega}_i}||\nabla\phi_i(\boldsymbol{x})||\mathrm{d}\tilde{\Omega}_i}, \tag{10}$$

where the average layer spacing ε allows to steer the average spacing between the structural members.

We depict the main steps in Fig. 9. From a 4-direction field (Fig. 9a), two 1-direction fields are extracted (Fig. 9b) for a standard cantilever beam. The corresponding parametrization ϕ_i is depicted in Fig. 9c, where contour lines have been added for a better understanding. Figure 9 d shows the cosine of the parametrization indicating all isocontours and the periodic structure. Figure 9e shows $\tilde{\rho}_i$ and ultimately $\tilde{\rho}$ is depicted in Fig. 9f. For further examples of de-homogenization using smooth 1-direction fields in 2- and 3D, the reader is referred to Groen and Sigmund (2018), Groen et al. (2019, 2020).

5.2 De-homogenization in the presence of singularities

In the presence of singularities, the above-described methods can fail for several reasons. Depending on the index of the singularity, different issues can arise:

- If a singularity of index ±1 is contained in the 4-direction layer-normal field, the separation into two integrable 1-direction fields is still possible (see Fig. 7b). As locally neighboring vectors need to be pointing in the same direction, the extraction of vector fields does not arise trivially. This extraction is called combing. In practice, a breadth-first search has shown to fail with this task as depicted in Fig. 10b because the singular point is hit. More robust results can be reached by expanding the search through intermediate densities first, before expanding into void and solid. This algorithm has been used in 3D in Groen et al. (2020) and is explained in Section 5.2.1 and depicted in Fig. 11 and the result for the corner loaded square in Fig. 10c.
- In the case of a singularity of index $\pm1/2$, the 4-direction field can still be combed, such that two separate 1-direction fields arise (see Fig. 7a and c). However, the combing of these 1-direction fields cannot be done consistently anymore. Any combing strategy will inevitably create mismatches, i.e., some neighboring elements will contain vectors that are rotated by π (see further Section 5.2.2). A promising approach to extract a high-resolution structure for such fields has been proposed in Donders (2018).
- In case of a singularity with index $\pm1/4$, the whole procedure gets even more challenging. Recall that following a curve c around a singularity of index $1/4$ in a 4-direction field means that we return to the start of our curve misaligned by $\pi/2$ (see Fig. 7d–f). Therefore, we cannot find two 1-direction fields to which we can assign the directions of our 4-direction field. Instead, one needs to cut open the field in such a way that one can integrate the 1-direction fields using multiple coverings as introduced in Kälberer et al. (2007). We will discuss this topic extensively in Section 5.3.

5.2.1 Combing the 4-direction field

As a first step, we have to comb our 4-direction field. This means we want to choose two orthogonal 1-directions for every element. In quad meshing, this is normally done with a breadth-first search as shown in Kälberer et al. (2007). As the homogenization method results are noisy and unreliable in normals of layers with very low or very high width, it makes sense to prioritize combing in medium-density

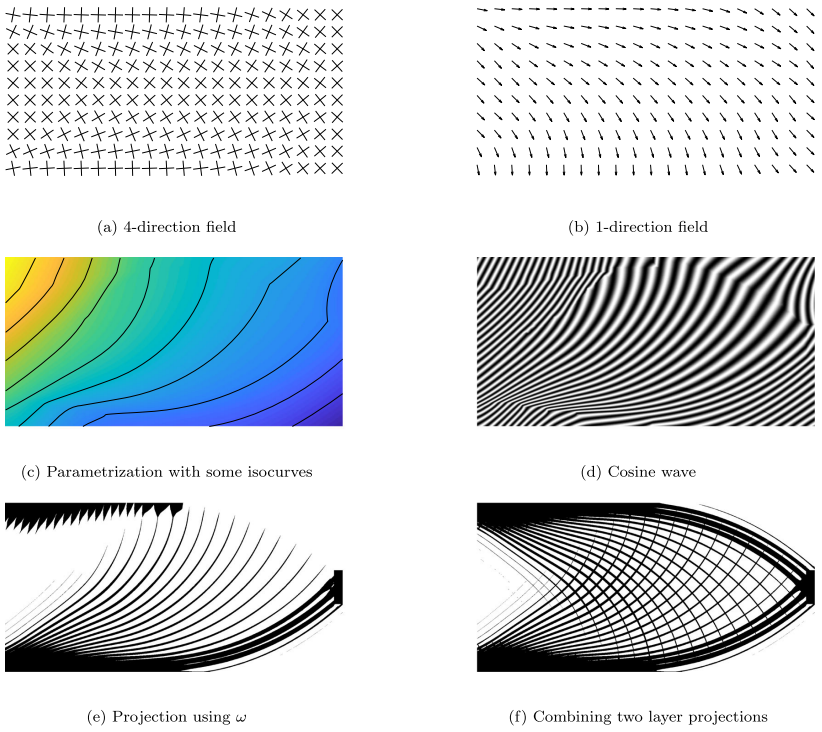

(a) 4-direction field

(b) 1-direction field

(c) Parametrization with some isocurves

(d) Cosine wave

(e) Projection using ω

(f) Combining two layer projections

Fig. 9 Projection pipeline—from a 4-direction field to de-homogenized mechanical structure

regions. This has recently been proposed in Groen et al. (2020) and we depict an example of our implementation in Fig. 11, where the chosen directions are given as black arrows and seam edges are depicted in bright red. We color the elements according to the time where they are visited by the combing algorithm. For readability, we bundle 50 elements to one step and color them with the same color. Unlike Groen et al. (2020), we only use the direction of a single neighboring element to compute the direction to be fixed in element f. This allows for a much faster algorithm and is possible due to the angular information being more robust in 2D. The density priority is obtained by $\rho_{priority} = |\rho_{start} - \rho_f|$, where normally $\rho_{start} = 0.5$ is chosen. We therefore comb the field first in areas with a density close to 0.5 and then spread out into the remaining domain. The numerical implementation of the combing only selects one direction per element. The second direction is implicitly given as the rotation of the extracted 1-direction field by $\pi/2$.

5.2.2 Finding the seams

For every 4-direction field containing a singularity with index $1/4$ or $1/2$, we receive a combed 1-direction field that has jumps of angle $\pi/2$ and/or π. Such fields are not integrable and to be able to parameterize our domain, we need to cut open our mesh as done in Kälberer et al. (2007).

Definition 5 (Seams, mismatch, seam edge) Two directions whose enclosed angle exceeds $\pi/4$ are said to mismatch by $\pi/2$. Accordingly, two directions whose enclosed angle exceeds $3\pi/4$ are said to mismatch by π. An edge e is called

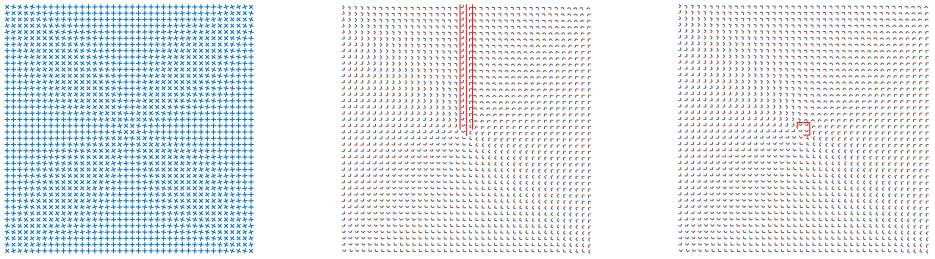

(a) 4-direction field before combing (b) Breadth-first combing (c) Density-based combing

Fig. 10 Example of two different combing strategies for a given 4-direction field resulting in different seams. The breadth-first combing only uses information about the neighborhood of elements, whereas the density-based combing uses density values to prioritize the combing of elements

seam edge if the directions in the two adjacent elements f_1, f_2 mismatch. A seam is any series of connected seam edges.

5.3 Constrained mixed-integer solver

In quad meshing, multiple coverings and thus resulting seams were introduced in Kälberer et al. (2007). An expansion introducing an iterative scheme to enforce integers is given in Bommes et al. (2009). We want to exploit the underlying mechanisms to create a topology on which we can integrate the combed fields, combining them with the integration scheme introduced in Groen and Sigmund (2018). Therefore, we give a short simplified introduction to Bommes et al. (2009) in Sections 5.3.1–5.3.3.

5.3.1 Cutting the mesh open

As a first step, one cuts open the mesh along the seams created in Section 5.2.2. Let $e = (v_1, v_2)$ be a seam edge, connecting the vertices v_1 and v_2 as in Fig. 12. The edge e separates the two elements f_1 and f_2. Auxiliary vertices $\tilde{v}_1$ and $\tilde{v}_2$ are introduced and the connectivity of f_2 is changed from $[v_1, v_2, v_t, v_s]$ to $[\tilde{v}_1, \tilde{v}_2, v_t, v_s]$.

5.3.2 Gluing the mesh together

If one would solve the resulting linear system in (6) on this cut open mesh, disconnected structural members would arise at the seam locations, since the integer isolines on the left and the right side of the seam would not meet up. Therefore, one needs to make sure that the parametrizations ϕ_1 and ϕ_2 in vertex v differ by integers i, j from the parametrizations in $\tilde{v}$. This ensures connected bars and also the same spacing between bars on both sides of the seam. In case of a singularity of $1/4$, the parametrization ϕ_1 can corresponds to the parametrization ϕ_2 on the other side. These rotations Rot^e_{90} are given implicitly by the combed field. Kälberer et al. (2007) formulate the rotational and integer condition with the following equations

$$\begin{aligned}(\phi_1(\tilde{v_1}), \phi_2(\tilde{v_1})) &= Rot^e_{90}((\phi_1(v_1), \phi_2(v_1))) + (i, j),\\ (\phi_1(\tilde{v_2}), \phi_2(\tilde{v_2})) &= Rot^e_{90}((\phi_1(v_2), \phi_2(v_2))) + (i, j),\end{aligned} \tag{11}$$

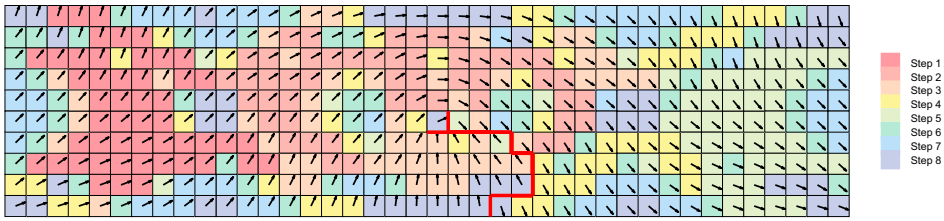

Fig. 11 Extraction of a 1-direction field using a density-based combing strategy. The combing is started at a root element and follows intermediate densities first. The colors show steps of 50 elements at a time, whose 1-direction has been fixed. The colors show steps of 50 elements at a time, whose 1-direction has been fixed

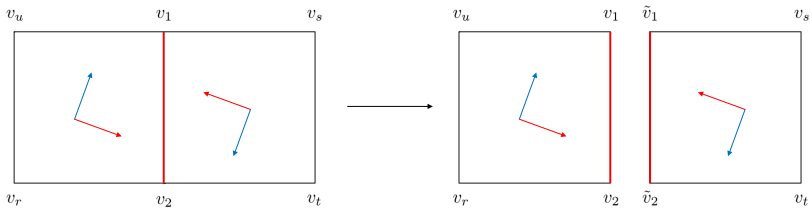

Fig. 12 Sketch of cutting a grid open between two neighboring elements at a seam edge

where $i, j \in \mathbb{Z}$ enforces that the integer isolines meet up. The operator Rot^e_{90} accounts for the mismatch of the rotations on both sides of the seam. It can be seen as a multiplication with the imaginary number i in the complex plane, where we regard the parameterizations $(\phi_1(v_1), \phi_2(v_1))$ as a complex number. Maybe most intuitively is the rotation with angle π. When we look at Fig. 12 and think of the vectors as gradients of the parameterizations ϕ_1 and ϕ_2, we see, that if the value of a parameterizations ϕ increases on one element, then it must be decreasing on the other element. Thus, the signs of the parameterizations need to change, which corresponds to a multiplication with i^2. For rotations of angle $\pi/2$ or $3\pi/2$, the two parameterizations ϕ_1 and ϕ_2 need to switch position, since the "blue" field becomes the "red" field. This corresponds to a multiplication with i or i^3 in the complex plane. If we define the angle as the rotation in counterclockwise direction, we get

$$Rot^e_{90}((\phi_1(v_1), \phi_2(v_1))) = i^{l(e)}(\phi_1(v_1), \phi_2(v_1)),$$

where $l(e) \in \{1, 2, 3\}$ is given by the mismatch of the angles at edge e. Further details about the operator Rot^e_{90} and this procedure can be found in Kälberer et al. (2007) and Bommes et al. (2009).

5.3.3 Solving for the parametrization

Once the system is assembled, it is solved in the continuous case, i.e., no integer restrictions are applied at first. This yields an approximation to the desired solution solving the problem up to disconnected bars at the seams. The mismatch variables (i, j) can now be seen as slack variables $j \in J$, where J is the set of all slack variables. For every iteration, the slack variable closest to an integer

$$k = \underset{j \in J}{argmin} \mid j - \text{round}(j) \mid,$$

is enforced to round(k) and the new system is solved. In an iterative fashion, this procedure is continued until no more slack variables are left.

6 Parameter choice for homogenization and de-homogenization

The homogenization and the de-homogenization are both influenced by some key parameters. The pipeline introduced in Section 5 allows us to study different examples of start orientations for the layer normal and regularization values (see Section 6.1). Further, we also outline the important de-homogenization parameters (see Section 6.2).

6.1 Influence of the start point choice and the regularization of the homogenization method

It is known for the corner loaded square (see Figs. 6b, 13, 14, 15, and 16) that there does not exist a unique optimal solution. The shown examples were all achieved using a resolution of 120×120 elements for the topology optimization as well as for the parameterization step. To visualize the resulting structures, we choose for the de-homogenization an average layer spacing $\varepsilon = 5h_f$, where $h_f = 15$ is the number of fine-scale elements used, and an alignment weight $\gamma_\phi = 50$. For the examples in Figs. 14 and 16, the value $\gamma_\theta = \frac{1}{5}$ is applied. In this example, we see that the start guess dictates the resulting structure. If the start point for the homogenization method consists of a grid aligned 4-direction field, we receive the structures depicted in Figs. 15 and 16 that are fairly grid aligned. However, if we solve one finite element step, assuming that in all elements we have a density $\rho = 1$, we receive a stress tensor field, whose eigenvectors can be used as a start guess for the homogenization method, as shown in Groen et al. (2020). The results differ from the grid aligned start guess and are shown in Figs. 13 and 14. Note that even if we impose regularization, the start guess still dictates the outcoming structure as shown in the Figs. 14 and 16. With the principal stress directions as starting guess, we receive spatially ripped apart singularities, when imposing regularization. With the uniform grid as starting guess, we stay completely clear of getting a singularity in the center of the domain. Note that despite the large

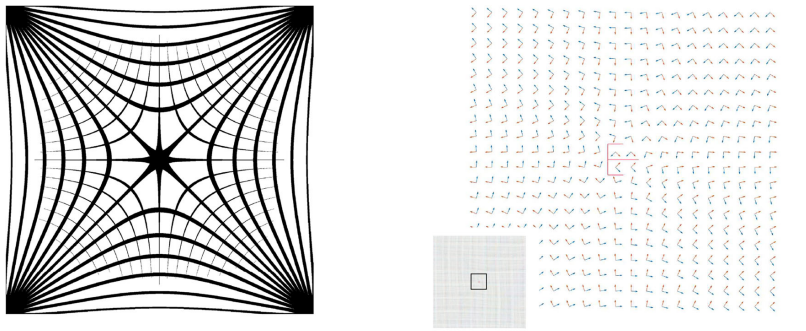

(a) Structure (b) Enlargement of the centre of the combed vector fields

Fig. 13 Example of a corner loaded square using principal stresses as a start guess for the layer-orientation, no regularization applied

geometric variations in these solutions, compliance values C_h for obtained homogenization results are extremely close demonstrating the non-uniqueness of this problem.

6.2 Alignment weight γ_ϕ and structural member thickness ε

There are two main parameter choices influencing the result during the de-homogenization: the alignment weight γ_ϕ and the average layer spacing ε. We refer to Groen and Sigmund (2018) for the choice of the layer spacing ε. For comparison reasons, we use in this subsection an $\varepsilon = 10/L$, where L is the resolution in vertical direction. Further, topology optimization and de-homogenization are done on the same resolution. If no singularity is present, then the alignment weight γ_ϕ should be chosen in a range of 100–1000 as shown in Groen et al. (2019). It holds that the lower the maximal absolute divergence of a vector field, the bigger ε can be chosen, as it simply enforces a very strict alignment to the second vector field. However, in case of a singular point, the field spins with a certain index around that point. If we now enforce a big alignment weight on a low-resolution (80×20 elements) example, we receive stretched isocontours as shown in Fig. 17a. The gradient of the parametrization becomes almost zero in a large region. The constraint of (6) is implemented as a penalization term multiplied with the alignment weight γ_ϕ. Note that this term can be minimized by the gradient becoming zero due to the usage of the dot product. However, this leads to an increase in the first term of (6) and an

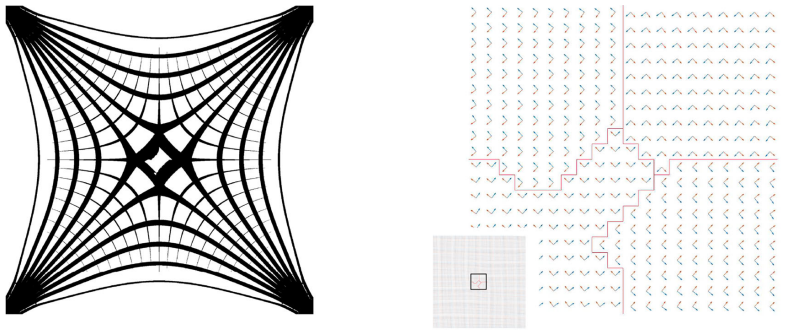

(a) Structure (b) Enlargement of the centre of the combed vector fields

Fig. 14 Example of a corner loaded square using principal stresses as a start guess for the layer-orientation, regularization $\gamma_\theta = \frac{1}{5}$ applied

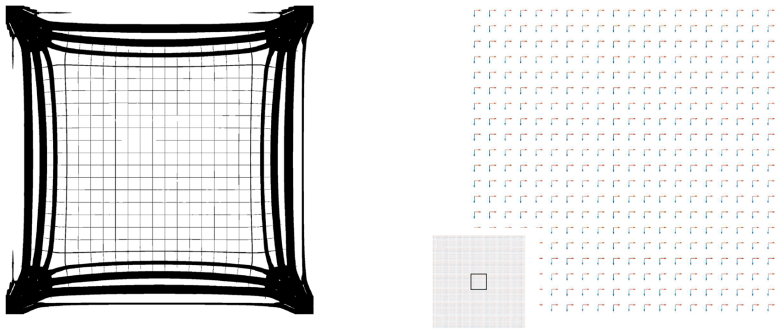

(a) Structure (b) Enlargement of the centre of the combed vector fields

Fig. 15 Example of a corner loaded square using grid aligned directions as a start guess for the layer-orientation, no regularization applied

unwanted stretching of the isocontours. For a low-resolution example, the space of bi-linear basis-functions is limited and thus the parametrization is limited in adapting to the rotation around a singularity. This leads to smearing out of the rotational influence from the singularity to neighboring elements. If the element size is large, this influences a higher relative area of the optimization domain. Thus, if the alignment weight is chosen very high, the gradient becomes zero in these elements due to the first term of (6) being suboptimal already. This often results in a violation of the volume constraint as can be extracted from Table 1. In order to allow for a better comparison, we provide the value $V_s C_s$, which should however not be considered as the sole objective, since the compliance does not depend linearly on the volume. By using a higher resolution (160 $\times$ 40, 320 $\times$ 80, 640 $\times$ 160) (see Fig. 17b, c and Table 1) most of this problem is resolved. We can see that a tradeoff in the alignment weight is still desirable for these high-resolutions. On the one hand, a low alignment weight can lead to non-load-bearing bars, as isocurves might lead to an area with zero layer width due to bad alignment. On the other hand, a too large alignment weight can lead to an overvaluing of the constraint and thus to stretched isocontours. For the examples in Table 1, we observe that the optimal alignment weight can depend on the resolution γ_ϕ between 50 and 5000 dependent on the de-homogenization grid.

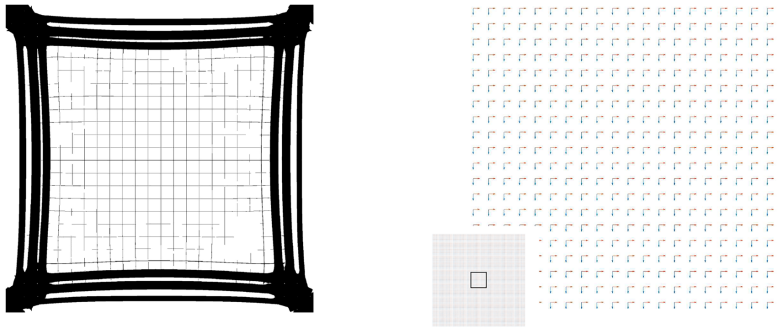

(a) Structure (b) Enlargement of the centre of the combed vector fields

Fig. 16 Example of a corner loaded square using grid aligned directions as a start guess for the layer-orientation, regularization $\gamma_\theta = \frac{1}{5}$ applied

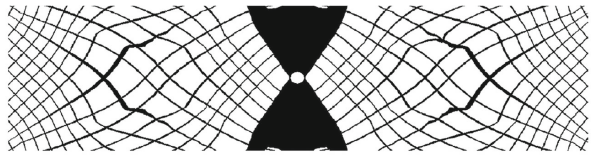

(a) Isocontours with resolution 80×20 and alignment weight $\gamma_\phi = 500$

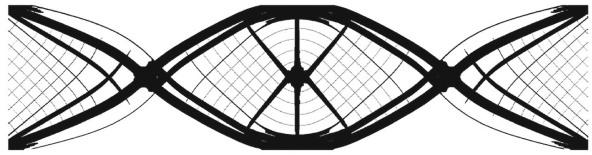

(b) Structure with resolution 320×80 and alignment weight $\gamma_\phi = 5000$

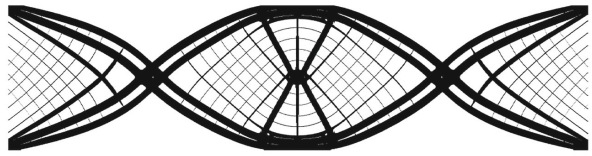

(c) Structure with resolution 640×160 and alignment weight $\gamma_\phi = 5000$

Fig. 17 Examples of center loaded clamped beam for different resolutions and alignment weights

Table 1 Performance for different alignment weights γ_ϕ and resolutions res

res	γ_ϕ	C_h	V_s	C_s	$V_s C_s$	t_h	t_s	t
80×20	0	21.89	0.298	61.79	18.42	44.8	5.4	50.2
	50	21.89	0.316	32.60	10.30	44.8	6.2	51.0
	500	21.89	0.349	24.26	8.45	44.8	5.2	50.0
	5000	21.89	0.351	24.50	8.60	44.8	4.0	48.7
160×40	0	21.82	0.295	337.74	99.52	135.4	11.2	146.6
	50	21.82	0.334	24.69	8.25	135.4	10.2	145.6
	500	21.82	0.343	22.76	7.81	135.4	10.2	145.7
	5000	21.82	0.338	23.46	7.93	135.4	10.8	146.2
320×80	0	21.84	0.297	71.95	21.39	402.9	34.3	437.2
	50	21.84	0.313	22.52	7.05	402.9	30.8	433.8
	500	21.84	0.300	24.89	7.48	402.9	30.7	433.7
	5000	21.84	0.285	26.75	7.63	402.9	30.8	433.7
640×160	0	22.02	0.298	73.51	21.90	1824.5	112.8	1937.3
	50	22.02	0.293	25.57	7.48	1824.5	109.9	1934.3
	500	22.02	0.288	25.91	7.46	1824.5	147.1	1971.6
	5000	22.02	0.313	22.07	6.91	1824.5	111.5	1936.0

C_h compliance of homogenization method, V_s, C_s volume and compliance of de-homogenized structure, t_h, t_s, t time for homogenization-based topology optimization, the de-homogenization and the overall time in seconds. Since the compliance does not depend linearly on the volume, $V_s C_s$ should not be considered as the sole objective

6.3 Island removal via connected component

To get rid of elements that are neither connected to the boundary condition nor to the load, we do a simple connected component analysis, where we only retain the largest component. This immediately leads to the desired removal of islands. However, this still leaves some unloaded bars, these can be removed by a couple of FE analysis and removal of unloaded elements as proposed in Groen and Sigmund (2018).

7 Conclusion and future work

We have identified the singularities occurring most often in 4-direction fields arising from homogenization-based topology optimization. Further, we investigated the location and reasons for singularities to occur. We have shown the influence of the start guess of the layer-orientations on the outcome of the optimization. The proposed parametrization approach using QuadfCover allows parametrizing fields containing singularities of index $\pm 1/4$. The proposed parametrization approach also allows us to cut out areas completely filled with void or solid material from the parametrization step. These contributions increase the number of designs for which the de-homogenization method can generate high-resolution near-optimal structures at a low computational cost. In order for the aforementioned points to come to carry the next step for further research is the adaptation of the projection step outlined in Groen and Sigmund (2018) to allow for singularities with index $1/4$. As an alternative, it might be of interest to extract an explicit quad mesh from the parametrizations produced in this paper. Such an explicit structure would allow the use of graph-based algorithms, which in turn enable the investigation of several challenges, like disconnected or badly aligned structural members, but also stretched isocontours. Finally, we identify the expansion of the presented approach to 3D as another, highly interesting research area. Besides an increase in computational cost, most of the ideas introduced in this paper can be reused, but we envision challenges such as non-uniqueness of 6-direction fields when only 1 layer has a finite width and challenges with the smoothness of the layer fields as has been discussed in Groen et al. (2020).

8 Replication of results

Our work relies on several programming languages (Python, Matlab, C++) and also several other codes. Specifically, we use the described homogenization-based topology optimization based on the 88 line MATLAB code by Andreassen et al. (2011). The resulting 4-direction fields are combed using the described density-based search method, and in order to compute the final structures, we use the QuadCover implementation in libigl.

Rather than providing a source code package which would only work under very strict platform requirements, we instead opt to aid the reader in reproducing our results by providing three types of materials:

- An example 4-direction field with associated densities of the type produced for example by the code from Groen and Sigmund (2018)
- A Python script that demonstrates the density-based combing
- A document outlining the necessary changes that have to be made to the libigl library to make QuadCover work on our type of problems. In particular, this supplementary document explains the implementation of the constraint in (6).

Acknowledgments The authors would like to thank professor Niels Aage for discussions and valuable inputs to the project. The authors acknowledge the support of the Villum Fonden through the Villum investigator project InnoTop. The authors would also like to thank Krister Svanberg for providing the MATLAB MMA code.

Compliance with ethical standards

Conflict of interests The authors declare that they have no conflict of interest.

References

Allaire G, Geoffroy-Donders P, Pantz O (2018) Topology optimization of modulated and oriented periodic microstructures by the homogenization method. Computers & Mathematics with Applications

Allaire G, Kohn R (1993) Optimal-design for minimum weight and compliance in plane-stress using extremal microstructures. Eur J Mech A-Solids 12(6):839–878

Andreassen E, Clausen A, Schevenels M, Lazarov BS, Sigmund O (2011) Efficient topology optimization in matlab using 88 lines of code. Struct Multidiscip Optim 43(1):1–16. https://doi.org/10.1007/s00158-010-0594-7

Bendsøe MP (1989) Optimal shape design as a material distribution problem. Structural Optim 1(4):193–202

Bendsøe MP, Kikuchi N (1988) Generating optimal topologies in structural design using a homogenization method. Comput Methods Appl Mech Eng 71(2):197–224

Bendsøe MP, Sigmund O (1999) Material interpolation schemes in topology optimization. Arch Appl Mech 69(9-10):635–654

Bommes D, Zimmer H, Kobbelt L (2009) Mixed-integer quadrangulation. ACM Trans Graph (TOG) 28(3):77

Bourdin B (2001) Filters in topology optimization. Int J Numer Methods Eng 50(9):2143–2158

Bruns T, Tortorelli D (2001) Topology optimization of non-linear elastic structures and compliant mechanisms. Comput Methods Appl Mech Eng 190(26–27):3443–3459

Delmarcelle T, Hesselink L (1994) The topology of symmetric, second-order tensor fields. In: Proceedings of the conference on visualization'94. IEEE Computer Society Press, pp 140–147

Díaz A, Sigmund O (1995) Checkerboard patterns in layout optimization. Structural Optim 10(1):40–45

Donders PG (2018) Homogenization method for topology optmization of struc-tures built with lattice materials. Ph.D. Thesis

Groen JP, Sigmund O (2018) Homogenization-based topology optimization for high-resolution manufacturable microstructures. Int J Numer Methods Eng 113(8):1148–1163

Groen JP, Stutz FC, Aage N, Bærentzen JA, Sigmund O (2020) De-homogenization of optimal multi-scale 3d topologies. Comput Methods Appl Mech Eng 364:112979

Groen JP, Wu J, Sigmund O (2019) Homogenization-based stiffness optimization and projection of 2d coated structures with orthotropic infill. Comput Methods Appl Mech Eng 349:722–742. http://www.sciencedirect.com/science/article/pii/S0045782519301021

Hotz I, Sreevalsan-Nair J, Hagen H, Hamann B (2010) Tensor field reconstruction based on eigenvector and eigenvalue interpolation. In: Hagen H (ed) Scientific visualization: advanced concepts. Vol 1 of dagstuhl follow-ups. Schloss dagstuhl–leibniz-zentrum fuer informatik. Dagstuhl, Germany, pp 110–123. http://drops.dagstuhl.de/opus/volltexte/2010/2700

Kälberer F, Nieser M, Polthier K (2007) Quadcover-surface parameterization using branched coverings. In: Computer Graphics Forum, vol 26. Wiley Online Library, pp 375–384

Norris AN (2005) Optimal orientation of anisotropic solids. Q J Mech Appl Math 59(1):29–53

Pantz O, Trabelsi K (2008) A post-treatment of the homogenization method for shape optimization. SIAM J Control Optim 47(3):1380–1398

Pantz O, Trabelsi K (2010) Construction of minimization sequences for shape optimization. In: 2010 15th international conference on methods and models in automation and robotics. IEEE, pp 278–283

Pedersen P (1989) On optimal orientation of orthotropic materials. Structural Optim 1(2):101–106

Skiena SS (2008) Sorting and searching. Springer, London, pp 103–144. https://doi.org/10.1007/978-1-84800-070-4_4

Svanberg K (1987) The method of moving asymptotes–a new method for structural optimization. Int J Numer Methods Eng 24(2):359–373

Träff E, Sigmund O, Groen J (2019) Simple single-scale microstructures based on optimal rank-3 laminates. Struct Multidiscip Optim 59(4):1021–1031

Vaxman A, Campen M, Diamanti O, Panozzo D, Bommes D, Hildebrandt K, Ben-Chen M (2016) Directional field synthesis, design, and processing. In: Computer graphics forum, vol 35. Wiley Online Library, pp 545–572

Appendix C: Paper-III

F. C. Stutz, T. F. Olsen, J. P. Groen, N. Aage, O. Sigmund, J. Solomon, and J. A. Bærentzen. **Synthesis of Frame Field-Aligned Multi-Laminar Structures**. *arXiv preprint*, 2021. arXiv: 2104.05550

Synthesis of Frame Field-Aligned Multi-Laminar Structures

Florian Cyril Stutz*,[1], Tim Felle Olsen[1], Jeroen Peter Groen[1], Niels Aage[1], Ole Sigmund[1], Jakob Andreas Bærentzen[1], and Justin Solomon[2]

*Corresponding author: fstu@dtu.dk

[1] Technical University of Denmark, Anker Engelunds Vej 1, 2800, Kgs. Lyngby, Denmark

[2] Massachusetts Institute of Technology, 77 Massachusetts Ave, 02139, Cambridge, MA, United States of America

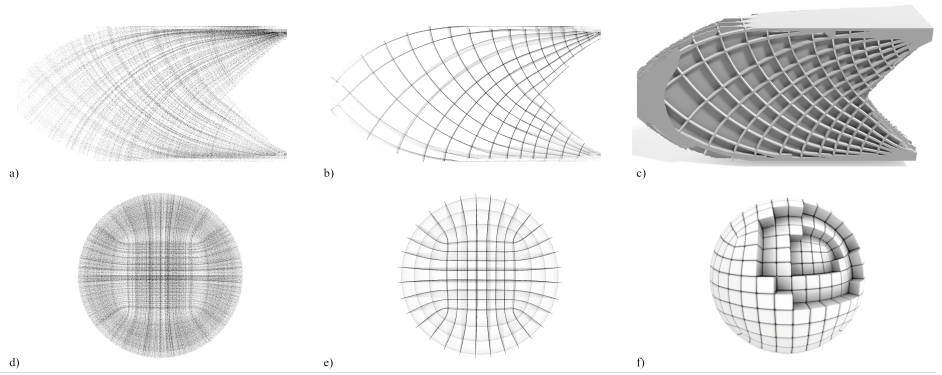

Fig. 1: Given a frame field as an input we can generate a set of optimal laminations aligning exactly with the field orientations (Subfigures a and d). Using a novel optimization energy that only needs local orientation awareness, we can create a well-spaced subset of these laminations (Subfigures b and e). We then proceed to create near optimal, highly stiff multi-laminar structure as a volumetric solid (Subfigure c) or in some cases output a hexahedral mesh (Subfigure f).

Abstract

In the field of topology optimization, the homogenization approach has been revived as an important alternative to the established, density-based methods because it can represent the microstructural design at a much finer length-scale than the computational grid. The optimal microstructure for a single load case is an orthogonal rank-3 laminate. A rank-3 laminate can be described in terms of frame fields, which are also an important tool for mesh generation in both 2D and 3D.

We propose a method for generating multi-laminar structures from frame fields. Rather than relying on integrative approaches that find a parametrization based on the frame field, we find stream surfaces, represented as point clouds aligned with frame vectors, and we solve an optimization problem to find well-spaced collections of such stream surfaces. The stream surface tracing is unaffected by the presence of singularities outside the region of interest. Neither stream surface tracing nor selecting well-spaced surface rely on combed frame fields.

In addition to stream surface tracing and selection, we provide two methods for generating structures from stream surface collections. One of these methods produces volumetric solids by summing basis functions associated with each point of the stream surface collection. The other method reinterprets point sampled stream surfaces as a spatial twist continuum and produces a hexahedralization by dualizing a graph representing the structure.

We demonstrate our methods on several frame fields produced using the homogenization approach for topology optimization, boundary-aligned, algebraic frame fields, and frame fields computed from closed-form expressions.

1 Introduction

In recent years, *topology optimization* [Bendsøe and Sigmund, 2004] has emerged as an important tool in digital modeling and fabrication. By minimizing compliance, for example, topology optimization can produce mechanical structures that are stiffer than what a human designer would usually be able to achieve, using only a specified amount of material. More generally, topology optimization algorithms can directly optimize for structures, extremizing assorted quality measures of fabricated objects.

Density-based approaches for topology optimization employ a straightforward minimization over parameters that represent element-wise material density and, as such, operate directly on a volumetric shape representation. Unfortunately, large-scale topology optimization problems are very computationally demanding with this type of approach, albeit feasible in many contexts [Aage et al., 2017; Baandrup et al., 2020].

The *homogenization-based* approach to topology optimization offers an alternative wherein the material is represented in terms of homogenized microstructures [Bendsøe and Kikuchi, 1988]. The optimal microstructure for single-load case stiffness optimization, which we also employ, is the rank-3 microstructure, a lamination system with three orthogonal lamination directions. Using the orientation and lamination thicknesses obtained during topology optimization, we can realize a physical structure from the homogenization solution at a finite length scale in a process called *dehomogenization*. In practice, this two-step procedure yields finely resolved structures at a much lower computational cost than density-based methods [Bendsøe and Sigmund, 2004; Pantz and Trabelsi, 2008; Geoffrey-Donders, 2018; Geoffroy-Donders et al., 2020; Groen and Sigmund, 2018; Groen et al., 2020].

Clearly, one could also choose truss-based microstructures for homogenization-based topology optimization, resulting in a final structure consisting of trusses as done in Wu et al. [2019]. However, a truss carries load only in the direction of the truss itself, while a sheet can carry load along two directions. In practice, this means that closed wall structures are up to three times stiffer than Michell structures [Sigmund et al., 2016]. Consequently, our goal is to construct closed wall structures.

The specific problem we address is the following. Assuming the lamination orientations are given by a frame field, we seek a set of surfaces such that each surface aligns everywhere with one of the frame orientations. The surfaces should be approximately evenly-spaced, and the spacing corresponding to a choice of length scale; up to three surfaces might intersect at any point.

If we can find a 3D parametrization of the domain such that the gradients of the coordinate functions are everywhere aligned with the frame field, the surfaces are simply constant coordinate surfaces pulled back from the parametrization domain. Unfortunately, the frame field might be far from integrable, and there are few if any robust approaches that can handle such cases. While recent work modifies the frame field at the cost of structural performance to promote integrability [Arora et al., 2019], we take a different route which does not require a parametrization of the domain.

We seek a set of surfaces whose local tangent planes are aligned to a frame field. We find these surfaces individually using an approach that amounts to stream surface tracing. Given a large superset of such surfaces, it is then possible to find an evenly-spaced subset by solving a binary optimization problem, which we solve efficiently through relaxation.

Our first contribution is a method that solves the aforementioned problem by tracing and selecting stream surfaces that locally align with frame fields. The tracing is discussed in Section 4.1 and the selection procedure in Section 4.3.

Given a set of stream surfaces, we further provide two methods for the synthesis of output shapes. In topology optimization, we usually need a manufacturable solid as the output. This volumetric solid can be extracted by compositing samples of each stream surface onto a voxel grid—a procedure sometimes known as *splatting*, described in Section 5.2. For frame fields that lead to reasonably isotropic families of surfaces, we also can compute a graph of the intersection points and output a combinatorial structure from which a hexahedral mesh can be obtained, as described in Section 5.3.

2 Related Work

Frame fields resulting from topology optimization impose particular requirements on hexahedral mesh generation schemes. For example, the frame fields might exhibit anisotropy to an extent where one edge length deteriorates. Moreover, the rotation of the frame fields might be higher than is usual in the case of fields designed for hexahedral meshing, and this could make the fields non-integrable. These challenges suggest that existing hex-meshing or hex-dominant meshing algorithms are not suitable for such problems.

In recent years, density-based topology optimization has been used to find optimal mechanical structures in various fields. In the area of compliance minimization, giga-scale finite element models have been applied [Aage et al., 2017; Baandrup et al., 2020]. While such large-scale topology optimization makes the benefits of topology optimized structures very apparent, it also relies on supercomputing hardware and is not applicable in real time, which is one of the key steps towards the goal of incorporating topology optimization in the everyday engineering design process.

Density-based topology optimization methods such as SIMP or RAMP [Sigmund and Maute, 2013] were designed to directly produce single-scale mechanical structures. However, earlier work, specifically the groundbreaking work by Bendsøe and Kikuchi [1988], modelled material as having an infinitesimal microstructure—as opposed to being locally characterized only by density. Materials consisting of mi-

crostructures have been shown to be computationally optimal, while circumventing the problem that density-based topology optimized structures depend on the size of the chosen finite element mesh [Avellaneda, 1987; Francfort et al., 1995; Sigmund and Maute, 2013].

The process of going from the results of homogenization based topology optimization to high-resolution structures is called *de-homogenization*. It was introduced by Pantz and Trabelsi [2008], who combined homogenization-based topology optimization with field integration, as done in quad-meshing, to de-homogenize 2D examples whose orientation fields do not contain singularities. They expanded their approach in Pantz and Trabelsi [2010] to structures with singularities of index $\pm 1/2$ lying in void regions by punching out holes around these singularities. Groen and Sigmund [2018] revisited this method and simplified the approach, while introducing additional parameters for more control of the de-homogenized structure. Their approach was limited to singularity-free fields and has since been ported to 3D in Groen et al. [2020]. Geoffrey-Donders [2018] proposed a method for de-homogenizing structures in 2D with singularities of index $\pm 1/2$ without the need of punching holes based on Hotz et al. [2010]. Stutz et al. [2020] expanded the approach by Groen and Sigmund [2018] to incorporate examples with singularities of index $\pm 1/4$.

All of the above papers indicate a strong relationship to quad-dominant meshing in 2D and hex-dominant meshing in 3D. Depending on the examples, a deterioration of the hexahedra is desirable as is the anisotropy resulting thereof. However, as shown in [Groen and Sigmund, 2018; Stutz et al., 2020], spurious singularities can occur. In 3D, orientations of the microstructures are not unique, a problem for the de-homogenization that can to a certain degree be circumvented by regularization [Groen et al., 2020].

Approaches for truss-structures have been presented for singularity-free fields in Larsen et al. [2018]; Arora et al. [2019] and in Wu et al. [2019] for fields containing singularities.

Field-based quad-meshing and hex-meshing is most often done by combing fields and integrating to find scalar functions with integer-jump conditions, where the combed field are differently labelled [Kälberer et al., 2007; Bommes et al., 2009; Nieser et al., 2011]. A lot of research for field-based hex-meshing focuses on achieving pure-hex meshes [Huang et al., 2011; Ray et al., 2016; Solomon et al., 2017; Palmer et al., 2019]. These methods focus on the field design part of the hex-meshing pipeline with the main goal to achieve as many hexahedral elements as possible. Thus, these methods minimize a smoothness energy while ensuring that at the surface one direction of the octahedral frame is well-aligned with the surface normal [Huang et al., 2011]. As a natural effect, hex-meshes extracted from such a model tend to have minimized anisotropy and minimized deterioration of the hexahedral elements.

For de-homogenization and hex-dominant meshing of homogenization-based topology optimization results, it is of importance to note that the fields are typically *prescribed* (rather than optimized during the meshing procedure) and cannot be changed to obtain more smoothness without reducing the mechanical performance of the obtained structure [Stutz et al., 2020]. Approaches like Kälberer et al. [2007] and Nieser et al. [2011] are promising for de-homogenization but contain a major pitfall since fields arising from the homogenization method often have singularities of higher indices ($\pm 1/2$ in 2D) or have significant divergence at mechanical boundary conditions. Such higher indices imply a greater rotational speed and typically integration based methods for de-homogenization must enforce alignment to the fields with a penalization approach [Groen and Sigmund, 2018; Groen et al., 2020; Stutz et al., 2020]. This penalization weight trades off structural alignment with spacing of the structural members and implicitly introduces anisotropy. If the alignment weight is chosen too small, the resulting parametrization will not align well with the underlying field as it tries to create unit-length gradients. If the alignment weight is chosen too large, the gradient of the parametrization will become zero and result in stretched out iso-contours [Stutz et al., 2020]. These problems might be mitigated by introduction of additional optimization terms, which has so far not been deeply investigated. It is important to note that anisotropy is desired and of the utmost importance for the mechanical performance.

In field-based hex-dominant meshing as done by Gao et al. [2017], the isotropy of the desired hexahedra is a key ingredient of the algorithm. This is due to the optimization, which trades off the regularity of the hexahedra and their alignment to the underlying field. An expansion to anisotropic hex-dominant meshing might be achieved, if the desired hex-edge length was known beforehand and not only given implicitly.

Ni et al. [2018] have a promising approach to solve for vertex position of a tetrahedral mesh, which is similar to Gao et al. [2017]. The nature of the approach is aimed at producing vertices of a hex-mesh with a prescribed isotropic edge-length. Note that Gao et al. [2017] and Ni et al. [2018] create tetrahedra where the hexahedra do not align with the field, which could cost dearly in terms of mechanical performance, when used for de-homogenization, since the resulting structure would not align with the load path at all in these regions. Recently, polycube methods have advanced the hex-meshing field, but since methods like Guo et al. [2020] and Livesu et al. [2020] do not rely on fields they are not applicable to de-homogenization.

The work of Takayama [2019] expanding the 2D work of Campen et al. [2012] and [Campen and Kobbelt, 2014] relies on user-defined (as opposed to frame field aligned) implicit surfaces as an input to guide the creation of hex-meshes. Moreover, several authors, including us, draw inspiration from the notion of the spatial twist continuum which is, essentially, the dual of a hexahedralization and was introduced by Murdoch et al. [1997].

Campen et al. [2016] create a foliation as a means of finding

a bijective parametrization of a 3D shape. While there is a clear similarity between the notion of a stream surface and a transversal section of a leaf of a foliation of a 3-manifold [Milnor, 1970], their aim is to create a bijective map entailing strong conditions on the direction field whereas we take the frame field as is.

It should be mentioned that stream surfaces are often used as a visualization tool seen in fluid dynamics [Hultquist, 1992; Machado et al., 2014].

We strive for global surfaces or layers, which are locally well-aligned with the results from the homogenization-based topology optimization, while incorporating implicitly the anisotropy dictated by these fields and circumventing the issue of missing structural parts due to enforcing field alignment and resulting zero-gradient regions.

3 Sources of Frame Fields

We are mainly motivated by fields arising from topology optimization, but one can also think of fields that would not permit generating laminations or even hexahedral meshes obtained from an integration based method. In the following, we will shortly discuss these fields and their origins. As we will demonstrate in Section 6, our algorithm can take fields from *any* of these sources as input; it is designed to extract field-aligned structures while being agnostic to the source of the field.

3.1 Topology Optimization

Homogenization-based topology optimization uses microstructures that vary their shape and orientation at an infinitesimal scale. The optimization aligns microstructures with the principal stresses implicitly [Pedersen, 1989; Norris, 2005]. Two examples of microstructures are depicted in Figures 2a and 2b, the rectangular hole microstructure considered for topology optimization by Bendsøe and Kikuchi [1988] and a rank-2 material with orthogonal layers considered by Bendsøe [1989]. The rectangular hole microstructure can be rotated, and the size of the hole can be changed for both directions independently. The rectangular hole microstructure is a single-scale approximation of the multiscale rank-2 material in Figure 2b. These multiscale rank-2 materials have been shown to be optimal for two-dimensional problems with a single strain tensor by Avellaneda [1987]. The rank-2 microstructure can also be orientated and the relative thickness of its layers can vary independently. Note that the three dimensional equivalent to the rank-2 microstructure is called a rank-3 microstructure with orthogonal layers and is optimal for three-dimensional problems with a single strain tensor.

These infinitesimal microstructures are used in topology optimization using the theory of homogenization. By assuming periodicity at the infinitesimal microscale we can obtain effective (homogenized) properties at the macroscale. By assuming only variation of the microstructures at the macro-scale we can model a complex structure using relatively few finite elements compared to the mesh-dependent density-based topology optimization [Bendsøe and Sigmund, 2004]. Now the optimizer can optimize the orientations of the microstructure and the layer-widths. We obtain a coarse representation of the locally optimal microstructure orientation and layer thicknesses as a result of the topology optimization. The orientations are described as 4-direction fields in two dimensions and as octahedral fields in three dimensions.

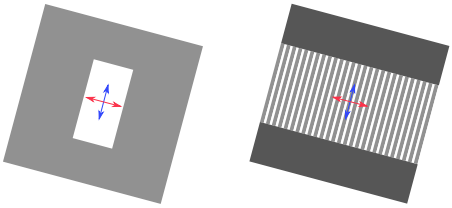

(a) Rectangular hole microstructure.

(b) Rank-2 microstructure with orthogonal layers.

Fig. 2: Most commonly used microstructures in two dimensions. On the left the rectangular hole microstructure introduced for topology optimization in Bendsøe and Kikuchi [1988]. On the right the rank-2 microstructure with orthogonal layers first used for topology optimization in Bendsøe [1989]. This rank-2 microstructure with orthogonal layers at two different length scales is known to be optimal for single strain tensor problems [Avellaneda, 1987].

A crucial part of the homogenization-based topology optimization is to find the optimal rotations of the microstructures, since microstructures have a high stiffness in their principal directions but low shear. Thus regularization of the orientations during the topology optimization will influence the resulting performance of the mechanical structure since more material needs to be allocated to strongly regularized regions [Stutz et al., 2020]. If regularization of the orientation fields is done after the topology optimization, either actively as discussed in Arora et al. [2019] or by not enforcing high enough penalization weights for an integrative method as discussed in Groen and Sigmund [2018] and Stutz et al. [2020], the resulting structure will not align well to the optimal microstructure orientation. Such non-optimally aligned regions may cause a dramatic loss of performance of the structure [Groen and Sigmund, 2018; Stutz et al., 2020]. Therefore the motivation of this paper is to find structures that adhere to the local orientation of the microstructure as closely as possible outside of void or fully solid regions. This in turn introduces anisotropy between the global members of the structures. Note, however, that this anisotropy is not negatively influencing the structure from a mechanical point of view.

Singularities arise in homogenization-based topology optimization for three reasons in two dimensions [Stutz et al., 2020];

- Singularities in the underlying stress field will lead to singularities in the layer-normal fields since the microstructure aligns to the principal stress directions.
- Regularization inflicted on the layer-normal fields during the topology optimization will break up singularities with a higher index in the stress fields into multiple singularities of lower index in the layer-normal fields.
- In regions where the microstructure is completely solid or void, singularities can be introduced by noise. In solid regions the microstructure becomes isotropic and the optimal orientation of it becomes non-unique. In void regions the microstructure is not present and an optimal orientation of the microstructure is therefore non-existing.

Stutz et al. [2020] show that in two dimensions singularities in topology optimized layer-normal fields must occur in completely solid or void regions.

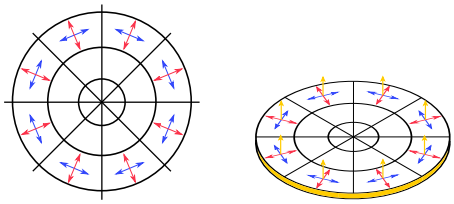

(a) Two dimensional example of a singularity with index 1.

(b) The same singularity as in Figure 3a but now embedded in an orthogonal layer (in yellow) in three dimensions.

Fig. 3: On the left we see an example of a singularity with index 1 in two dimensions. It is clear that the rotational speed increases the closer we get to the singular point. Stutz et al. [2020] have shown, that the optimizer has an incentive to put such singularities in an either fully void or fully solid region, since there would always be shear forces acting on any non-solid microstructure at the singular point. On the right we see the same field and singularity embedded into an orthogonal layer (in yellow) in three dimensions. Note how the optimizer now can choose to fill the yellow layer with material and completely ignore the red and blue field, while still creating a stiff structure. Moreover, this singularity does not have to be in a completely solid region since the relative layer thickness of the yellow layer can be lower than 100 percent. In this case we refer to the microstructure as *transversely isotropic* since the the microstructure is isotropic in one plane (the yellow one) but anisotropic perpendicular to this plane.

Unfortunately, this observation does not hold in three dimensions. Firstly, microstructure orientations in three dimensions are non-unique due to in-plane stress; this can cause spurious singularities to appear. These singularities can be tackled with a low amount of regularization, as shown by Groen et al. [2020]. Secondly, as seen in Figure 3 that singularities in stress fields can occur, even when the microstructures are not completely solid. If we consider Figure 3a we see a field describing a singularity with index 1. Stutz et al. [2020] observed that because the rotational velocity of the field increases towards infinity at the singularity, the topology optimization process fills the region around the singularity with material to account for the spinning stress-field at the singularity. On the other hand, when we embed the fields from Figure 3a in three dimensions, as shown in Figure 3b, the optimizer can choose to fill the newly introduced orthogonal layer with material and not assign any material to the two existing layers. Furthermore, we observe that this third layer does not have to be completely solid but can have any arbitrary layer-thickness, e.g. 50%. In this case we refer to the microstructure as being *transversely isotropic* since the the microstructure is isotropic in one plane (the yellow one) but anisotropic perpendicular to this plane. The option to cut out singularities and later on fill them with material, will inevitably lead to excessive use of material in three dimensions. The example described in Figure 3 is, to the best of the author's knowledge, the only singularity in three dimensions that occurs outside of fully solid or entirely void regions.

The following thoughts can explain this. First, if all layer normals change direction at a location outside the void, for example, around a source, then the region would need to be filled with material by the optimizer to be made isotropic. Second, non-zero stress directions will always be perpendicular to a layer normal, with non-zero layer thickness, meaning that stresses must always be transferred within a solid slab or plate. This will always align a stress field's singular curve with a layer normal outside of fully solid or entirely void regions. This leaves us only with fields as shown in Figure 3b, where of course, the indices of the singularities can be different. Third, consider for a moment that the red or blue layer would be non-zero. Then their layer-normal would rotate infinitely fast at the singular curve, and thus the optimizer would fill the region completely with material to make the microstructure isotropic at the singular curve. Hence we conclude that the only singular curve not embedded into complete solid or void can be seen in Figure 3b, where the red and blue layer thicknesses are zero.

Our stream surfaces generation method can differentiate the expansion of stream surfaces near a singular region. Note how in Figure 3b the field with the yellow normal is aligned with the singular curve while having a constant normal. We can use this observation to identify which layer is traversing the singular region orthogonal to the singular curve in a computationally cheap manner and expand the corresponding stream surface through the singular region. However, in practice, we do not need to do this for topology optimized fields since we stop the expansion of stream surfaces in zero-material layers. This means that only the stream surface following the traversing layer is created.

3.2 Boundary-Aligned Frame Fields

Topology optimization yields frame fields as a by-product of a mechanical problem; the fields are not designed with me-

shability or integrability in mind. In contrast, a number of techniques in geometry processing optimize for frame fields with the specific goal of extracting a quadrilateral or hexahedral mesh. Since our work focuses primarily on the volumetric case, we refer the reader to Vaxman et al. [2016] for discussion of the many methods available for two-dimensional field computation, and briefly highlight representative three-dimensional methods below.

The basic goal of volumetric frame field computation is to optimize for a field of three orthogonal directions at each point in a region enclosed by a surface, with the constraint that one of the three directions aligns to the surface normal along the boundary. This field is then used as input to methods like Lyon et al. [2016] and Nieser et al. [2011] to extract a mesh through parametrization.

Huang et al. [2011] originally propose a representation of orthogonal frames—later dubbed "octahedral" frames by Solomon et al. [2017]—that is agnostic to their labeling. Their work extracts smooth fields by optimizing Euler angle variables, with additional constraints at the boundary; their approach was refined by Ray et al. [2016] with improved boundary constraints and optimization. Solomon et al. [2017] propose a relaxation of [Ray et al., 2016], allowing for use of the boundary element method (BEM). Palmer et al. [2019] provide a more complete description of the space of octahedral frames, leveraging the structure they identify to propose manifold-based optimization schemes; they also propose a related orthogonally decomposable ("odeco") frame representation in which the directions remain orthogonal but can scale independently.

Many open questions remain regarding the singular topology of octahedral/odeco fields and its relationship to hexahedral meshing; see Liu et al. [2018] for initial results and some relevant discussion. Corman and Crane [2019] and Liu et al. [2018] propose algorithms that compute frame fields with prescribed singular structures.

3.3 Closed-Form Frame Fields

A closed-form frame field is a field where the orientations of the frames can be found using a closed-form mathematical expression instead of being found using optimization or by solving a system of equations. In this paper, we consider a field describing a cylinder, much like the field illustrated in Figure 3, where there is a single singular curve in the center of the cylinder. Suppose one tries to extract well-aligned hexahedra from such a field using integrative methods. In that case, one will be challenged due to the high anisotropy of the hexahedral elements, which can not be treated by methods, that were designed to create isotropic hexahedra [Stutz et al., 2020]. Note that the edge length of hexahedra will ultimately deteriorate towards the singular curve with such a cylinder field. A stream surface based approach can be designed to expand through singular curves for the cylinder's near-constant field (as discussed earlier in Section 3.1), while creating highly anisotropic hexahedra in the remaining domain. Extending this example, we also run our algorithm on a non-integrable field describing a helicoid. Again, this produces highly anisotropic hexahedra matching the spiral shape of the input field.

4 Computing Collections of Stream Surfaces

The overarching idea of our method is to compute a large set of surfaces, $\mathcal{S}$, which align with the frame field and then find a well-spaced selection of these, $\mathcal{S}_{opt}$, to get a representation of the multi-laminar structure that we seek. In this section, we discuss how we find and select these aligned surfaces using stream surface tracing. In the next section, Section 5, we will discuss how the final output is computed from this representation.

In engineering, a *streamline* is simply a curve that is everywhere tangential to a vector field [Hultquist, 1992]. A stream surface is simply the generalization to 3D, i.e. a surface whose normal is everywhere aligned with one of the vectors of the input frame field.

We cannot rely on the frame field being combed, and hence, we do not have consistent labeling of the vectors in the frame. This is handled by simply finding the frame vector best aligned with the estimated normal of the next point that we compute when expanding a stream surface. It is also worth noting that we generally wish to stop stream surface tracing when the stream surface would otherwise exit a given bounding shape. Thus, we assume a known mask or layer thickness in the following.

4.1 Tracing Stream Surfaces

We start by tracing stream surfaces to create the set $\mathcal{S}$. The stream surfaces are traced independently, starting from random seed points in the domain. Rather than constructing a surface connectivity, we compute a point cloud for each stream surface. The points are placed using a method similar to the technique for *Poisson Disk Sampling* (PDS) sampling introduced by Bridson [2007], except that our points are placed on a surface in 3D and are not filling the entire 3D domain.

We initialize each surface with a single seed point $\mathbf{p}_0$ and with two of the three frame vectors at $\mathbf{p}_0$. The first vector is our desired surface normal $\mathbf{N}$ at the seed point, and the second vector is perpendicular to $\mathbf{N}$ and describes our rotational origin $\mathbf{D}$. New points are now generated in an annulus centered on the seed point and perpendicular to the surface normal. Uniformly distributed random variables control the rotation angle from $\mathbf{D}$ and distance from $\mathbf{p}_0$. The annulus has an inner radius of r, which is the minimum distance allowed between points. The outer radius is set to $2r$ in accordance with Bridson's algorithm [Bridson, 2007]. Each time we generate a new point, we check if it is too close to any previously generated points of the stream surface, using a lookup grid

for efficiency. This generation process is visualized in Figure 4. When a new point is accepted, it is added to a queue of points used to further expand the surface.

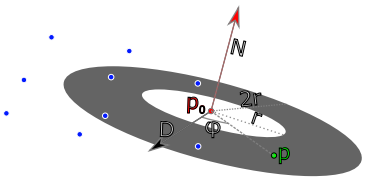

Fig. 4: Outline of how a new point $\mathbf{p}$ is generated at a random position inside the annulus around $\mathbf{p}_0$ oriented perpendicularly to the desired surface normal $\mathbf{N}$.

To mitigate drift, we employ the fourth order Runge-Kutta method [Chapra, 2012]. Starting from a previously determined point, $\mathbf{p}_0$, with normal $\mathbf{N}$, we search in direction $\mathbf{d}_0$ with step length Δ. We need a parallel transform operator $\mathcal{P} : \mathbb{R}^3 \to \mathbb{R}^3$ to transform the initial direction $\mathbf{d}_0$ onto the tangent plane estimated at a given point $\mathbf{x}$ with a normal defined by the field. The RK4 method combines partial steps through a weighted sum, to estimate the new point. The full update can be described by,

$$\mathbf{k}_1 = \Delta \cdot \mathcal{P}(\mathbf{p}_0) \ ,$$
$$\mathbf{k}_2 = \Delta \cdot \mathcal{P}(\mathbf{p}_0 + \frac{\mathbf{k}_1}{2}) \ ,$$
$$\mathbf{k}_3 = \Delta \cdot \mathcal{P}(\mathbf{p}_0 + \frac{\mathbf{k}_2}{2}) \ ,$$
$$\mathbf{k}_4 = \Delta \cdot \mathcal{P}(\mathbf{p}_0 + \mathbf{k}_3) \ ,$$
$$\mathbf{p}_n = \mathbf{p}_0 + \frac{1}{6}(\mathbf{k}_1 + 2\mathbf{k}_2 + 2\mathbf{k}_3 + \mathbf{k}_4) \ .$$

While this method is relatively precise, some drift is still unavoidable. To improve precision, we compute the position of p_n had p_0 instead been any point inside the sphere with radius $2r$ centered at p_n. These new estimates are aveараged to produce the new point p.

We discard a point if it is too close to a neighbor, distance $< r$. This could still allow for spiralling surfaces, therefore we also look at all neighbours within $3r$. If any of these neighbours, when projected onto the tangent plane defined by p and the associated normal, are closer to p than r we also discard the point. We also do not expand stream surfaces into regions where the corresponding layer has a layer-thickness of zero. No material would be assigned in these regions by the splatting method described in subsection 5.2. We also do not expand into fully solid regions, since these areas will be filled with material anyways by the splatting procedure. Note that these two last cases are why we do not need to actively handle singular curves in fully solid or entirely void regions.

Unfortunately, the computed stream surfaces are not entirely independent of the starting point. The drifting can be problematic when the front of the stream surface meets itself having traced around a round object (see the torsion sphere example in subsection 6.2 and closeup in Figure 5). This can lead to seams in the surface where it does not entirely close up. To mitigate this problem, we post-process the surface by recomputing the positions of all points from their neighbors using the scheme described above. This will strengthen alignment to the field, since we use the field information from all directions instead of only behind the expanding front. Pseudocode for the above algorithm is given in Algorithm 1.

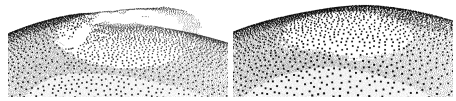

Fig. 5: Here we see the effect of drifting. Small deviations in point position and interpolation of the field over long distances lead to a crack in the surface. To the right, we show the resulting surface after smoothing.

We now have a method that allows us to trace stream surfaces in our input fields.

Algorithm 1 Stream surface creation

Inputs: Frame field, lamination thicknesses, list of seed points, list of probe points.

```
for each seed point p_s, do
    Initialize queue Q with p_s and PDS grid with desired radius.
    while Q is not empty, do
        Set p_0 to front of Q.
        Compute 30 new points p_i using weighted RK4.
        if p_i is a valid point, then
            Save p_i to point-cloud S_s, PDS grid and Q.
        end if
    end while
    for every point p in S_s, do
        Re-estimate p using weighted RK4.
    end for
    Save S_s to the set of surfaces S.
end for
```

4.2 Singularities

When tracing stream surfaces, we will inevitably expand into regions containing singularities. In 3D, singularities are curves along which the frame field is not defined. For a more complete discussion of the notion, we refer the reader to the comprehensive overview by Vaxman et al. [2016]. In this context, singularities are challenging because the frame field

rotates quickly in their vicinity. In particular, singularities of index ± 1 are challenging since the frame makes a complete turn around these. These rapid rotations mean that we cannot reliably continue tracing the stream surface when it is close to a singularity. It would often lead to the stream surface effectively splitting into two or more parts (which we call "forking") due to local variations in the amount of rotation. We illustrate a forking stream surface in Figure 6.

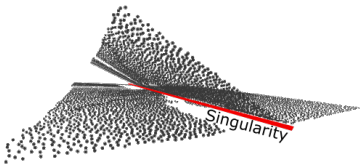

Fig. 6: Here we see a stream surface that has hit a singularity during the expansion through the domain. We see the surface fork into several sheets, which is highly undesirable and is caused by numerical imperfections when generating the stream surface and rapid changes in the frame field.

Forking surfaces can be detrimental to the quality of our results. If a surface forks, it is challenging to obtain a uniform spacing between surfaces in the selection part of our approach in subsection 4.6. Therefore, it is essential to have a way to handle these problematic regions. We choose to stop tracing surfaces in areas close to singularities. This approach will produce holes in our models (see for example Figure 18). However, we preserve the overall quality of the output. As explained in Section 3.1 cutting out the singular curve in topology optimized fields does not cause problems. Recall that for singularities outside of complete solid or void only the case in Figure 3b occurs, where we can track the layer traversing the singular curve perpendicular by its nearly constant layer normal.

Identifying singularities is a common problem in meshing and a wide range of other fields. We are using an approach adapted from the combing approach in Groen et al. [2020]. The rotational energy at a voxel is computed by examining the rotation needed to align the frame in a voxel to the frames in the neighboring voxels. The average rotation is saved since we are looking for spikes in the energy. Once we have computed the energy value at every voxel, we compute some simple statistics to identify singular curves.

We then prevent stream surfaces from entering regions close to these singular curves and now have everything that we need to create the set of stream surfaces $\mathcal{S}$

4.3 Energy for an Optimization-Based Subselection Approach

We will now take the set of surfaces $\mathcal{S}$ that we have created in the previous sections and continue with finding a well-spaced subset $\mathcal{S}_{opt}$. We will compute $\mathcal{S}_{opt}$ by optimizing over binary variables w that will be assigned to the stream surfaces. However, before we can define our optimization problem, we need to define the contribution of each stream surfaces to the optimization energy. For simplicity and consistency with the figures, we will describe this procedure in two dimensions. The algorithm works the same in three dimensions, and we will explain essential details for the implementation inline on an ongoing basis.

First let γ denote the desired average spacing in the set $\mathcal{S}_{opt}$. As an aid, we define the projection of a point $\mathbf{x} \in \mathbb{R}^2$ onto a streamline $S \in \mathbb{R}^2$ as $\mathbf{x}_p = \arg\min_{x_s \in S} ||\mathbf{x} - \mathbf{x_s}||$. We can then define an energy for the streamline S by

$$\begin{aligned} &\bar{E}_S : \mathbb{R}^2 \to \{0,1\} \ , \\ &\bar{E}_S(\mathbf{x}) = \begin{cases} 1, & \text{if } ||\mathbf{x} - \mathbf{x_p}|| \leq \gamma, \\ 0, & \text{else.} \end{cases} \end{aligned} \tag{1}$$

This energy is shown in Figure 7b for the two streamlines following orthogonal field directions in Figure 7a. For our application to 4-direction fields, we need to distinguish between the two orthogonal field directions locally. Therefore, we choose for every $\mathbf{x} \in \Omega$, two orthogonal directions from the 4-direction field at random and assign them to 2-direction fields f_1 and f_2. This assignment of the orthogonal directions to f_1 and f_2 allows us to define a function $S_{dir}(\mathbf{x}_s) = \{1, 2\}$ that indicates for every point $\mathbf{x}_s \in S$ if the streamline follows the local label of field f_1 or field f_2. In three dimensions, we use the normal of the stream surface as a field identifier. We now split the energy for every streamline into two parts:

$$\begin{aligned} &E_S : \mathbb{R}^2 \to \{0,1\} \times \{0,1\} \ , \\ &E_S = (E_{S_1}, E_{S_2}) \ , \end{aligned} \tag{2}$$

where the split energies E_{S_1} and E_{S_2} are defined as,

$$\begin{aligned} E_{S_1}(\mathbf{x}) &= \begin{cases} 1, & \text{if } S_{dir}(\mathbf{x}_p) = 1 \wedge ||\mathbf{x} - \mathbf{x}_p|| \leq \gamma \ , \\ 0, & \text{else,} \end{cases} \\ E_{S_2}(\mathbf{x}) &= \begin{cases} 1, & \text{if } S_{dir}(\mathbf{x}_p) = 2 \wedge ||\mathbf{x} - \mathbf{x}_p|| \leq \gamma \ , \\ 0, & \text{else.} \end{cases} \end{aligned} \tag{3}$$

Note that there is no need for consistency of the field labels f_1 or f_2 in a neighborhood, i.e. no combing is needed, as shown in Figure 8. This makes the energies very simple to implement and the approach very robust. The split energies from Equation 3 can be seen in Figure 12. Having defined the energy we can now formulate a binary optimization problem,

$$\underset{\mathbf{w} \in \{0,1\}^{n_S}}{\text{minimize}} \int_\Omega \left| \sum_{i=1}^{n_S} w(i) E_S(\mathbf{x}) - (1,1) \right| \ \mathrm{d}\Omega \ , \tag{4}$$

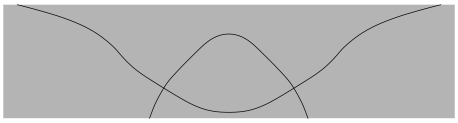

(a) Two streamlines following two different orthogonal fields.

(b) Sum of energies $\bar{E}_S$ for the streamlines in Figure 7a. Green and blue elements have an energy value of one, orange elements have a value of two.

Fig. 7: On the left, we see two streamlines following orthogonal field directions. On the right, we see the sum of the energies $\bar{E}_S$ from Equation 1 for the two streamlines. Here the contributions of the streamlines are colored in blue and green in regions with value one. The orange highlighted regions are elements where both streamlines create an energy response and subsequently the summed value equals two. An optimizer would try to minimize the amount of these orange elements since it tries to minimize overlapping streamline-energies. This version of the energy is blind for the fact that the two streamlines follow different fields. In order to be able to space out both family of streamlines correctly, we need to split the energy as shown in Equations 2 and Figures 8 and 12.

where we refer to the optimization variables w_i as weights and $n_S = |\mathcal{S}|$. If we were to use the energies from Equation 1 the selected streamlines would all follow the same lamination direction, since the optimizer would penalize crossing streamlines. This can be seen in Figure 9. If we use the same set of streamlines but use the energies defined in Equation 2 for the optimization we obtain both lamination as can be seen in Figure 10

Note that defining the problem in Equation 4 as a least-squares problem instead of a least absolute deviations problem would overly punish multiple covered regions of the energy and lead to missing streamlines. The L^1 norm in Equation 4 on the other hand, penalizes double covered probe points equally as hard as non-covered probe points. The difference of using an L1-norm or an L2-norm can be seen in Figures 11. Details on the solution of the minimization problem in Equation 4 are discussed in Section 4.6. We now continue to find the variable $n_{\mathcal{S}}$.

4.4 Number of Streamlines $n_{\mathcal{S}}$ in the Covering Set of Streamlines $\mathcal{S}$

To solve the minimization problem in Equation 4 we need to know how large the number of streamlines $n_S = |\mathcal{S}|$ provided to the optimizer needs to be.

First, we need to define the desired average spacing γ of the streamlines in $\mathcal{S}_{opt}$. Then the cardinality of $\mathcal{S}_{opt}$ can be approximated by,

$$|\mathcal{S}_{opt}| = \frac{n_x}{\gamma} + \frac{n_y}{\gamma} \ , \tag{5}$$

where n_x and n_y are the dimensions of the design space in $\mathbf{x}$, respectively y direction. Note that the cardinality of $\mathcal{S}_{opt}$ grows in linear dependence to the dimensions of the design space, since streamlines are one dimensional objects. This means that doubling all dimensions of the design space will only lead to a doubling of the cardinality of $\mathcal{S}_{opt}$. This also holds true in three dimensions, here due to the two-dimensionality of stream surfaces. We further need to define the error ε by which a streamline should deviate on average from its optimal position. We denote this in fraction of the optimal average spacing γ, e.g. $\varepsilon = 0.1$ would allow a streamline to be placed in a band of 0.2γ width around its optimal location. We can then derive the cardinality of $\mathcal{S}$ by:

$$n_{\mathcal{S}} = |\mathcal{S}| = \frac{1}{\varepsilon}|\mathcal{S}_{opt}| = \frac{1}{\varepsilon}\left(\frac{n_x}{\gamma} + \frac{n_y}{\gamma}\right) \ . \tag{6}$$

As with $\mathcal{S}_{opt}$, we note that the cardinality of $\mathcal{S}$ grows linear with the dimensions of the design space. We also note that the cardinality of $\mathcal{S}$ grows linear in dependence to the desired error ε, meaning that reducing ε by a factor k will increase the cardinality of $\mathcal{S}$ only by a factor k. Both these observations are again valid in two dimensions as well as in three dimensions.

We have now computed how many stream surfaces we need to provide to the minimization problem in Equation 4 to obtain good results.

4.5 Resolution of the Energy

To solve the minimization problem in Equation 4 the only thing that remains is to discretize the energy E_S on a pixel grid, where we refer to a single pixel as a probe point. To efficiently subselect streamlines, we need to know the resolutions of the discretized energies, i.e. the number of probe points needed to differentiate streamlines in the set $\mathcal{S}$. This number depends on the desired error ε and the desired average spacing γ. Each streamline should activate the probe points lying in a band of width γ around the streamline. Two streamlines that are more than $\varepsilon \cdot \gamma$ apart should activate a different set of probe points. This implies that the number of probe points needed can be computed by,

$$n_p = \frac{n_x}{\varepsilon \cdot \gamma} \cdot \frac{n_y}{\varepsilon \cdot \gamma} = \frac{1}{\varepsilon^2}\left(\frac{n_x}{\gamma} \cdot \frac{n_y}{\gamma}\right) \ . \tag{7}$$

Here we note that the number of probe points grows quadratically in two dimensions, meaning doubling both dimensions of the design space will increase the number of probe points needed by a factor of four. Respectively, the number of probe points grows cubically in three dimensions. Note, however,

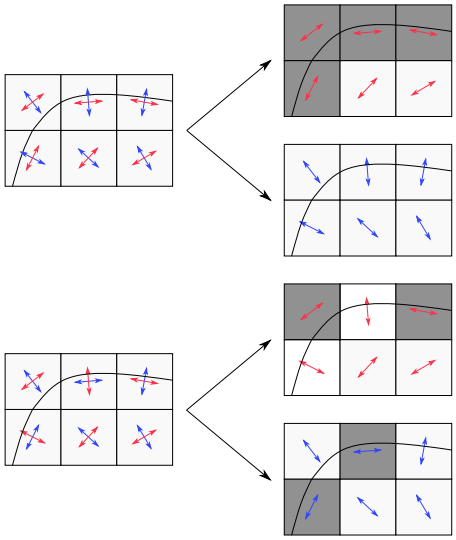

Fig. 8: Example of the energies created from a streamline traced in the same field but differently labeled. On the left, we see a streamline traced in a combed (above) and uncombed (below) version of a 4-direction field. On the right, we see the corresponding energies for label "red" and label "blue", which are local labels. Note how the streamline activates only one of the two energies for each element, as indicated by the gray coloring.

that the subselection is only a fraction of the time spent on the whole approach as can be extracted from Table 1.

We have now discretized the energy E_S in the minimization problem in Equation 4 and are now ready to solve it.

4.6 Subselection using a Relaxed Approach to Binary Programming

Solving the minimization problem in Equation 4 can be done by using integer linear programming. However, the underlying problem is likely NP-hard due to the binary constraints. This makes a direct solve of the problem formulated in Equation 4 infeasible. To solve the least absolute deviations problem, we relax the optimization variables w_i to be in the interval $[0, 1]$ instead of $\{0, 1\}$. This leads to the following convex linear program, which can be solved in polynomial time:

$$\underset{\mathbf{w}\in[0,1]^{n_S}}{\text{minimize}} \int_\Omega \left| \sum_{i=1}^{n_S} w(i) E_S(\mathbf{x}) - (1,1) \right| \quad \mathrm{d}\Omega \ . \tag{8}$$

We solve the relaxed problem in Equation 8 with an interior point method and then fix weights that have been set to either 0 or 1. Subsequently, we solve a binary program with the remaining weights (typically ¡ 5% of the original weights) using a branch and cut algorithm. A branch and cut algorithm splits the original problem into sub-problems and uses cutting planes to cut away parts of the possible solution space until an optimal integer solution is found for a sub-problem. If that solution is better than a relaxed solution of a second sub-problem, the second sub-problem does not need to be solved. This is done iteratively until the algorithm converges. For details, we refer to Padberg and Rinaldi [1991]. We use the implementation provided in CVX [Grant and Boyd, 2014].

Note that the high number of binary weights chosen in the relaxed problem is due to the energy having binary values. If we were to base the energy on a signed distance function instead, we would almost exclusively receive non-binary weights as a result from the relaxed problem in Equation 8 since the optimizer would try to trade off contributions of different streamlines.

The observation in subsection 4.4 that the computational burden of the problem in Equation 4 grows linear in the amount of stream surfaces has an important practical use. Forking stream surfaces, which can occur due to heavy noise in the topology optimized fields and are described in subsection 4.2, will cover more space than non-splitting surfaces. They are therefore chosen less by the optimizer when the number of surfaces in $\mathcal{S}$ increases.

We have now found a well-spaced set of laminar surfaces $\mathcal{S}_{opt}$ and can now continue with the generation of output structures.

5 Output Generation

The stream surface tracing and selection procedure described above produces a set of stream surfaces, $\mathcal{S}_{opt}$, each represented as a point cloud. In itself, this representation is useful for visualization. However, our end goal is to provide methods for synthesizing output structures. Here we present a method that produces a volumetric solid from the stream surfaces by compositing a small implicit primitive into a voxel grid for each point in the point cloud representing the stream surfaces. As an additional output modality, we also describe a mesh generator that converts stream surfaces to hexahedral meshes. While imposing restrictions on the proximity of the stream surfaces, the mesh generator can mesh certain non-integrable frame fields.

5.1 Post-Processing the Surfaces

When constructing the initial set of surfaces, we do not need a particularly high density of points in each surface. We only need enough to be able to compute the activation of probe points. However, a high density of points will provide a smoother and more precise volumetric solid and will make it easier to tell surfaces apart when computing a hex mesh.

(a) The sum of the energies E_S of all streamlines provided to the optimizer.

(b) The sum of the energies E_S of the streamlines selected by the optimizer.

(c) The curves selected by the optimizer.

Fig. 9: Optimization results using the energies defined in Equation 1.

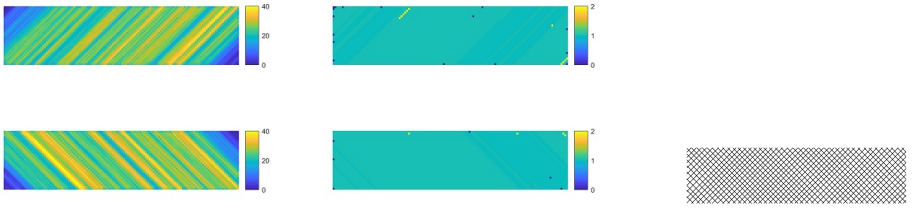

(a) The sum of the energies E_{S_1} and E_{S_2} of all streamlines provided to the optimizer.

(b) The sum of the energies E_{S_1} and E_{S_2} of the streamlines selected by the optimizer.

(c) The curves selected by the optimizer.

Fig. 10: Optimization results using the energies defined in Equation 2.

It is crucial that our post-processing still adheres to the field and follows the initial surface. Therefore, our upsampling is a continuation of the generation procedure. We initialize a new grid for our Poisson Disk Sampling procedure with a much smaller allowed point distance. We then add all of the original points of a selected stream surface to the grid. Subsequently, we add all original points to a queue and restart the point generation. This way, we fill in additional points between the original points since we have chosen a smaller distance for the Poisson Disk Sampling. Any new position is generated as the average of estimates from neighboring points, hence the super-sampled surface will still be following the field closely.

5.2 Volumetric Solids

A volume representation is convenient for shapes of complex topology, and we can efficiently synthesize a volumetric representation from a stream surface collection.

We compute the volume representation of each stream surface as a sum of basis functions. This is very similar to methods used for volumetric reconstruction of surfaces from point clouds, e.g. [Fuhrmann and Goesele, 2014], except that we design the basis functions to attain their maximum value at the origin. In contrast, in point cloud reconstruction, the basis function's zero level contour typically passes through the origin. The specific basis function that we employ is,

$$\phi_i(\mathbf{x}) = \mathrm{ss}(-\tau_i, 0, -|\mathbf{n}_i \cdot (\mathbf{x} - \mathbf{p}_i)|) \ , \tag{9}$$

where $\mathbf{p}_i$ is the position of point i which is orientated according to the normal, $\mathbf{n}_i$, and has thickness τ_i. Finally, ss is the *smoothstep* function,

$$\begin{aligned} &\mathrm{ss}(a, b, x) = 3t^2 - 2t^3, \\ &\text{where,} \quad t = \min\left(1, \max\left(0, \frac{x-a}{b-a}\right)\right) \ . \end{aligned} \tag{10}$$

For each stream surface, s, we compute the volumetric representation as a sum for each voxel,

$$V_s[\mathbf{x}] = \frac{\sum_i w_i(\mathbf{x})\phi_i(\mathbf{x})}{\sum_i w_i(\mathbf{x})} \ , \tag{11}$$

where V_s is the voxel grid, $\mathbf{x}$ ranges over the positions of all voxels, s indexes the stream surface, and the weight, w_i, is given by

$$w_i(\mathbf{x}) = \mathrm{ss}(-r, 0, -\|\mathbf{x} - \mathbf{p}_i - \mathbf{n}(\mathbf{n}_i \cdot (\mathbf{x} - \mathbf{p}_i))\|) \ . \tag{12}$$

The product of w_i and ϕ_i is non-zero only in a cylindrical region of radius r centered in point i. We only need to consider this region when adding the contribution to Equation 11. The weights are summed to a separate grid, and then normalization is performed in a second step.

Having computed a volumetric representation of each stream surface, the volumetric solid corresponding to stream surface collection is simply the union of the solids for each of the stream surfaces. The union is computed as the maximum over all stream surfaces,

$$V[\mathbf{x}] = \max_s(V_s[\mathbf{x}]) \ . \tag{13}$$

Finally, we compute a triangle mesh of the boundary of the volumetric solid using dual contouring with the iso-value 0.5 [Ju et al., 2002].

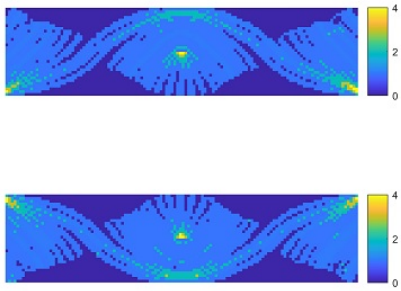

(a) The sum of the energies E_{S_1} and E_{S_2} when using an L1 norm for selecting streamlines.

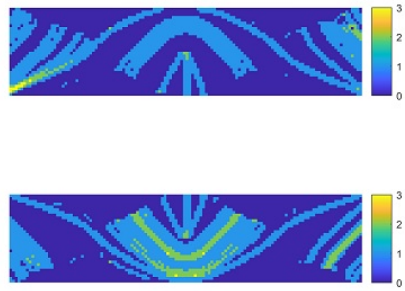

(b) The sum of the energies E_{S_1} and E_{S_2} when using an L2 norm for selecting streamlines.

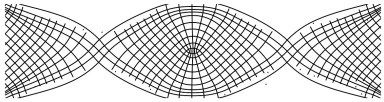

(c) The curves selected by the optimizer when using an L1 norm.

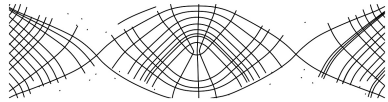

(d) The curves selected by the optimizer when using an L2 norm.

Fig. 11: Streamline selection results obtained when providing an L1 norm or an L2 norm to the optimizer. Note the missing streamlines that occur for the L2 norm results due to multiply covered regions being penalized too harsh.

5.3 Hexahedral Meshes

For certain frame fields, we are also able to produce hexahedral meshes. For reasons explained in subsubsection 5.3.1, we require a minimum separation between stream surfaces of $4r$ where r is the minimum distance between samples on a single stream surface. In practice, this requirement is not possible to fulfill for our topology optimization examples, but with this approach, we can, in fact, handle certain non-integrable fields.

The hex meshing approach is based on the following observation. Given a collection of surfaces in 3D, we can form a curve network by finding all the intersecting curves between pairs of surfaces. It has been observed by Murdoch et al. [1997] that such a system of interlocking surfaces, called the *spatial twist continuum* (STC), is the dual of a hexahedral mesh. It is relatively easy to see that this is true if we assume that surfaces only intersect along a curve and that no more than three surfaces meet at a single point. Since in that case, all the vertices formed as triple intersections must have valence six and thus correspond to a hexahedral cell in the dual. A very simple example with two hexahedra formed by dualizing an STC consisting of four surfaces is shown in Figure 13.

5.3.1 Constructing the STC Graph

Since our stream surfaces are represented as point clouds, we cannot directly compute the intersections. Instead, we formulate the problem as a graph problem. We form a graph, $G = \langle P, E \rangle$, whose vertices, P, are the union of the points in all stream surfaces, i.e. $P = \bigcup_j S_j \in \mathcal{S}_{opt}$. Two vertices are connected by an edge in E if their distance is smaller than $2r$, where r is the distance used in the stream surface super-sampling. Assuming that the stream surfaces corresponding to the same lamination direction are always further away than $4r$, no vertex should have neighbors belonging to more than three stream surfaces. In fact, the vertices of P belong to three classes: *surface vertices* all of whose neighbors belong to a single stream surface, *intersection vertices* whose neighbors belong to two stream surface, and *triple intersection vertices* whose neighbors belong to three stream surfaces.

Forming connected components of vertices which satisfy the equivalence relation, we can now create a model of the STC as a new graph $G_{\text{STC}} = \langle P_{\text{STC}}, E_{\text{STC}} \rangle$ from G based on the vertex classification. Initially, we discard all surface vertices and form the vertex set, P_{STC}, by creating a vertex for each connected component of triple intersection vertices of P. The vertex connectivity is found using a simple run of Dijkstra's algorithm on G. We initialize all triple intersection vertices with distance 0 and compute the graph distance to all intersection vertices. Each such vertex is also assigned

(a) Sum of energies E_{S_1} for a combed field.

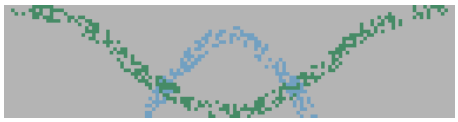

(b) Sum of energies E_{S_1} for an uncombed field.

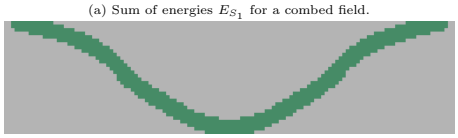

(c) Sum of energies E_{S_2} for a combed field.

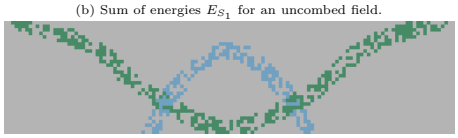

(d) Sum of energies E_{S_2} for an uncombed field.

Fig. 12: Sum of split energies from Equation 2 for the streamlines depicted in Figure 7a. The sums of the energies are shown once when a combed version of the underlying field is used and once when an uncombed version is used. Note how in a combed field the streamlines are separated into the energy that follows the same field label as the streamlines. In an uncombed field, the contributions of the streamlines split to both energies. However, it is clear that the contributions of a streamline to the two energies form a disjoint union. Regions with value two (highlighted in orange in Figure 7) do no longer exist.

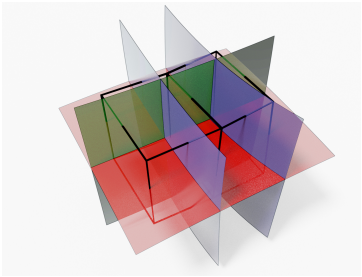

Fig. 13: The two hexahedra (dark wireframe) are dual to the structure formed by intersecting the four surfaces.

the index of its predecessor, allowing us to recursively trace back to the originating cluster. Once all intersection vertices have been visited, we visit all edges in G. If the two incident vertices were reached from different clusters, then the vertices in P_{STC} that correspond to these clusters are connected by an edge in E_{STC}.

5.3.2 Hexahedralization

From G_{STC} we compute a hexhedral mesh by computing the dual. A hexahedron is created for each vertex in P_{STC}. The hexahedron is scaled to the average length of edges incident on the vertex and rotated to align with the same edges. Finally, we assign the best-aligned quadrilateral face with each outgoing edge of the vertex.

To construct the connectivity of the hexahedral mesh, we now visit all edges in E_{STC} and cluster the vertices of the associated quads. Since every vertex is associated with up to eight hexahedra, these clusters may be of size up to eight. We compute each cluster's barycenter and assign this as the position of the vertex in the final hex mesh.

This method can only produce hexahedra. Hence, the frame field singularities do not result in irregular cells but gaps in the mesh or irregular vertices. The former is shown in Figure 18 where a field that spirals around a central axis has been hexahedralized. Since stream surface tracing stops at the central singularity, it leaves a gap in the mesh. The latter effect is shown in Figure 17 where the hexahedra can be observed to have slightly worse quality near the network of singular curves inside the sphere.

6 Implementation and Results

Our implementations are in C++ and Matlab. Codes related to the creation and manipulation of surfaces are primarily written in C++. Codes for selecting surfaces are running in Matlab by use of the CVX package [Grant and Boyd, 2014, 2008] and the Mosek solvers [MOSEK ApS, 2021].

The generation of stream surfaces and the synthesis of volumetric solids are parallel processes and have been parallelized using MPI and native threading facilities of C++, respectively. The stream surface tracing and the subselection were executed on a node equipped with two Intel Xeon E5-2650 v4 processors. The volumetric solid and hex meshing was executed on a single Intel Core i7. An overview of the statistics, including computation time, is shown in Table 1.

6.1 Missing Structural Members and Field Alignment – a Comparison

As discussed in section 2 our method aims to circumvent the problem of missing structural members due to enforcement of alignment to the input field when using an integra-

Table 1: Here we show the statistics for the different steps in our pipeline. The first three blocks of rows show relevant statistics for the initial point sampling of stream surfaces, the selection of optimal stream surfaces, and the super-sampling of the selected stream surfaces. The fourth block reports statistics for generating the volumetric solids and the fifth block shows the time to run the hexahedralization algorithm. We then report in the sixth block the overall runtime of our approach. We include the times for the homogenization-based topology optimization and report them in the last block for completeness. Note how our algorithm is only a fraction of the topology optimization runtime.

	Cantilever (3 layers)	Cantilever (1 layer)	Electrical Mast	Torsion Sphere	Sphere	Helix	Cylinder
$\|\mathcal{S}\|$ (Number of stream surfaces)	480	478	450	374	480	170	400
Generating $\mathcal{S}$ (runtime)	20 min	28 min	17 min	1h 51 min	49 min	1 h 4 min	1 h 1 min
Average points per surface	961	1 351	667	5 043	2 019	5 082	1 906
Subselection (runtime)	45 sec	53 sec	2 min 5 sec	2 min 31 sec	39 sec	50 sec	37 sec
$\|\mathcal{S}_{opt}\|$	38	22	35	4	27	24	41
Super-sampling (runtime)	2 h 30 min	3 h 18 min	1 h 19 min	1 h 30 min	1 h 52 min	2 h 9 min	6 h 20 min
Average points per super-sampled surface	9448	9 735	3 483	58 148	25 073	26 320	15 535
Output volume dimension	$700 \times 350 \times 350$	$700 \times 350 \times 350$	$266 \times 266 \times 800$	$500 \times 500 \times 500$			
Solid generation (runtime)	13 min 42 sec	11 min 3 sec	5 min 48 sec	8 min 30 sec			
Hexahedralization (runtime)					1 min 24 sec	23 sec	38 sec
Summed runtime	3 h 04 min	3 h 58 min	1 h 44 min	3 h 32 min	2 h 43 min	3 h 14 min	7 h 20 min
Topology optimization time	7 h 48 min	9 h 54 min	22 h 20 min	40 h 21 min			

tive method to create a parametrization. As discussed in Groen and Sigmund [2018]; Groen et al. [2020]; Stutz et al. [2020], alignment of the final structure to the input field needs to be enforced by a constraint when adapting integrative approaches as Kälberer et al. [2007]; Bommes et al. [2009]; Nieser et al. [2011]. This is done by enforcing the parametrization to be orthogonal to the second (and third) normal direction. However, if this alignment is too strict, the gradient of the parametrization may become almost zero in large regions. This, in turn, can then lead to overly thick structural members or to missing structural members especially around singularities as discussed by Stutz et al. [2020]. Our approach creates well-aligned structures before selecting a subset, eradicating the problem since we cannot suffer from vanishing gradients, as we do not integrate the fields. We show an example in Figure 14. Note that the same behavior can be observed in three dimensions.

The structure shown in Figure 14a has been obtained dehomogenizing a 320×80 layer-normal field by an integrative approach proposed by Stutz et al. [2020]. Note how there are missing structural members above and underneath the singularity. The structure has a compliance $C = 26.46$ and a volume fraction of $V = 0.275$. For comparison we use the compliance-volume value $C \cdot V = 7.30$. Stutz et al. [2020] report compliance-volume values of 7.05, 7.48, 7.63, and 21.39 for different alignment weights at the same resolution. Here 7.05 is their best performing structure at an intermediate alignment weight, and 21.39 is a failure case.

Figure 14b shows the structure created by our approach using also a 320×80 layer-normal field as was used by Stutz et al. [2020] in Figure 14a. Note that our approach yields a structure with evenly spaced structural members. The structure has a compliance $C = 27.67$ and a volume fraction of $V = 0.269$. The compliance-volume value for this structure is $C \cdot V = 7.44$. Note that this value is only 5.5% worse than Stutz et al. [2020] best value. Moreover, with our approach we do not risk a failure case due to bad alignment or zero gradients in a parametrization.

6.2 Volumetric Structures from Topology Optimized Fields

We ran various input fields from topology optimization through our pipeline. The fields were generated by the method proposed by Groen et al. [2020]. For problem formulations of the homogenization-based topology optimization and a description of the load cases, we refer to Geoffroy-Donders et al. [2020]; Groen et al. [2020]. The timings of the field generation and the de-homogenization are reported in Table 1, where we see that the topology optimization dominates over our de-homogenization approach. In Figure 15a we see a quarter of an electrical mast as proposed in [Geoffroy-Donders et al., 2020]. The fields generated for the electrical mast example contain spurious singularities in fully solid regions and the void due to the microstructure being isotropic (solid) or non-existent (void). Nevertheless, we produce very smooth surfaces, since our streamsurfaces do not need to expand into solid or void regions. Groen et al. [2020] make use of the fact that singularities only arise in fully solid or void regions by combing the fields in intermediate regions first, such that the spurious singularities cannot create seams in the combed field that extend into the intermediate regions. However, their approach yields no control or guarantee over how much singularities influence their designs

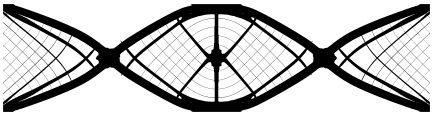

(a) De-homogenization using an integrative approach proposed in Stutz et al. [2020] yielding missing structural members around the singularity, where the gradients have become almost zero. A resolution of 320×80 is used as an input mesh. The shown Figure has a compliance-volume value of $C \cdot V = 7.30$. Stutz et al. [2020] report Compliance-Volume values of 7.05, 7.48, 7.63 and 21.39 for different alignment weights, where 7.05 is their best performing structure at an intermediate alignment weight and 21.39 is a failure case.

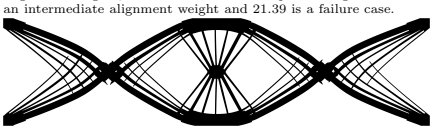

(b) Our approach yields a structure with evenly spaced structural members for the same 320×80 input field as used above. The compliance-volume value for this structure is $C \cdot V = 7.44$ and is therefore a mere 5.5% worse than Stutz et al. [2020] best value. However, with our approach we do not risk a failure case.

Fig. 14: Comparison between an integrative approach based on Stutz et al. [2020] yielding missing structural members and our approach which creates evenly spaced structural members.

since they still rely on the orientations in solid and void for integration, although they use relaxation for such elements.

On the right, in Figure 15 we show our version of the torsion sphere example proposed in Groen et al. [2020] that was based on Michell's famous torsion sphere [Michell, 1904]. Note that since we use optimal rank-3 microstructures, we do not get a truss structure, but a stiffer layer structure [Sigmund et al., 2016]. The torsion sphere has a singularity that connects the two boundary conditions, similar to a towel being wrung out. This singular curve passes through the solid region at one boundary condition, then through the void and the solid region at the opposite boundary condition. Note that this is again not a problem for our algorithm since we neither need to expand into void nor solid regions. Groen and Sigmund [2018] include the singular curve in their integration of the field without any special measurement, since they are relaxing the parametrization in the void and fully solid regions. Our method produces three high-quality shells that align well with the input field.

Figure 16 shows the three dimensional version of Michell's cantilever. For loading cases and problem formulation we refer to Geoffroy-Donders et al. [2020]; Groen et al. [2020]. We compute de-homogenization results for two versions. In Figure 16a, we depict a solution for the cantilever where we enforce that either all three layers have a layer thickness of more than 5% or that all layer thicknesses are zero. Such a design is great for resistance against buckling. Note that due to all three layers being enforced to have non-zero layer widths outside of the void, the microstructure orientation becomes unique in this example. Spurious singularities only arise in solid and void regions; therefore, we have no problems with forking stream surfaces in this example neither. A cut section through the structure is given in Figure 16e.

In Figure 16b, we show the second version of the cantilever that we consider. These input fields have been created without any enforcement on the layer-thicknesses and correspond to the cantilever Groen et al. [2020] propose. We compare our results with theirs, first on a visual level in Figures 16b, c, d, f, g and h and then in terms of compliance and volume in Table 2.

In Figures 16b and f we see the full de-homogenized structures. The two structures are very alike. Note that Groen et al. [2020] use some additional fine-scale evaluation to remove unused excess material, i.e. low strain energy elements. This puts their structure at a slight advantage over ours, since we do not incorporate such a step for our structure in Figures 16b-d. Figures 16c and g show a detail and Figures 16d and h show horizontal cuts through the structures.

Since our input fields differ from Groen et al. [2020] we cannot compare the values in Table 2 with too much emphasis. Note also that Groen et al. [2020] evaluated their design using a fine scale $960 \times 480 \times 480 = 221\,184\,000$ finite elements model, where as we only evaluate our model on $512 \times 256 \times 256 = 33\,554\,432$ elements. We therefore also only compare our result to the best performing values that Groen et al. [2020] report for a $96 \times 48 \times 48$ frame field as we use. The most meaningful value is certainly $\frac{C_s \cdot V_s}{C_h \cdot V_h}$ which sets the compliance-volume value of the de-homogenized structure to the compliance-volume fraction reported by the topology optimization. We see that we are a mere 5.5% off the Groen et al. [2020] best performing structure, even though we do no parameter study to find the best performing structure for the de-homogenization parameters since this would be outside of the scope of this paper.

Table 2: Comparison of our results for the cantilever example with results obtained by Groen et al. [2020]. We use the following abbreviations: V_s = volume of the de-homogenized structure, C_s = compliance of de-homogenized structure, V_h = volume of the homogenization-based topology optimization solution, C_h = compliance of the homogenization-based topology optimization solution Note that Groen et al. [2020] evaluated their design on a $960 \times 480 \times 480$ finite elements model, where as we only evaluate our model on $512 \times 256 \times 256$ elements.

Cantilever	Groen et al. [2020]	Our approach
C_h	226.68	228.45
V_h	0.1000	0.1000
C_s	243.31	223.72
V_s	0.1021	0.1181
$C_s \cdot V_s$	24.845	26.428
$\frac{C_s \cdot V_s}{C_h \cdot V_h}$	1.0960	1.1568

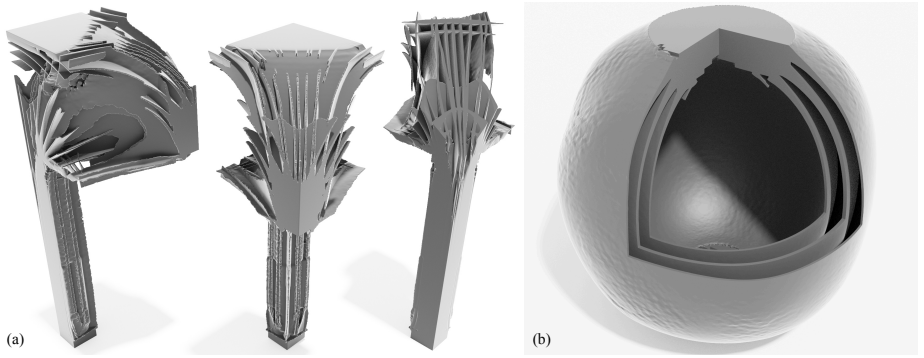

Fig. 15: This figure show two topology optimization examples created with our method from subsection 5.2. In (a) we see the electrical mast example introduced in Geoffroy-Donders et al. [2020]. We show here three angles (side, front and back), where in the rightmost image showing the mast from the back, the top has been cut away to reveal the interior of the structure. In (b) we show the Michell torsion sphere example introduced in Groen et al. [2020], where the boundary conditions with torsion applied are located in the top and the botton. Note that we cut out an eigth to reveal the interior laminations of the torsion sphere.

6.3 Hexahedral Meshes from Boundary Aligned and Closed-Form Fields

Our main goal was to synthesis volumetric structures from frame fields, but it is also possible to generate hex meshes from a collection of stream surfaces. However, it should be noted that while the volumetric synthesis method does not impose demanding requirements on the stream surfaces, hex mesh generation requires a minimum distance between the stream surfaces. Moreover, our topology optimization examples (in particular, the torsion sphere and the cantilever with one active layer) are clearly ill-suited to hex meshing. For this reason, our hex meshing examples are very different from the examples above.

Figure 17 illustrates the hex meshing of a sphere (3328 hexahedra) based on a boundary aligned frame field created using the method of Palmer et al. [2019]. We compared this mesh to one created by Corman and Crane [2019] with assistance from David Bommes containing 4032 hexahedra. The meshes are structurally similar, and the min/average scaled Jacobian [Bracci et al., 2019] for our mesh are 0.425/0.956 vs Corman et al.: 0.474/0.964. Note that since the boundary aligned frame field inside the sphere has been optimized for smoothness, it only contains singularities of index 1/4. In this specific example our stream surface tracing can be used without cutting out the singular curves, since the field is smooth enough.

Figure 18 shows hex meshes of a spiral and a cylinder generated based on frame fields from closed-form expressions. In both cases we have an index 1 singularity in the center, and the spiraling frame field is non-integrable making it challenging for many other strategies. The min/average scaled Jacobian are 0.474/0.964 (spiraling frame field) and 0.870/0.977 (cylinder).

7 Discussion and Future Work

In this paper, we have introduced a novel method for creating multi-laminar structures that align to frame fields. The main challenge lies in the fact that even though we can easily make a local structure that aligns with the frame field, we cannot easily assemble these into a global structure. One way to approach this is through the introduction of a parametrization of the domain. Indeed, the previous methods of which we are aware require a parametrization of the domain. This is however *only* straightforward to compute in the absence of singularities in the frame field.

While singularities do need to be taken into account with our method, their presence does not fundamentally change the algorithms we use to create and select stream surfaces. In that sense, our approach is (almost) oblivious to singularities. In contrast, a parametrization based approach needs to explicitly deal with singularities by introducing seams and clearly cannot align perfectly to a non-integrable field. For the application of de-homogenization this translates into the pitfall that the parametrization modifies the resulting mechanical structures negatively. Moreover, a practical challenge when computing a parametrization is that the frame field must be combed – i.e. there must be a consistent labeling of the frame vectors.

Stream surface tracing and selection sidestep both of these issues, and we have demonstrated that our approach can provide robust output for various types of fields and cre-

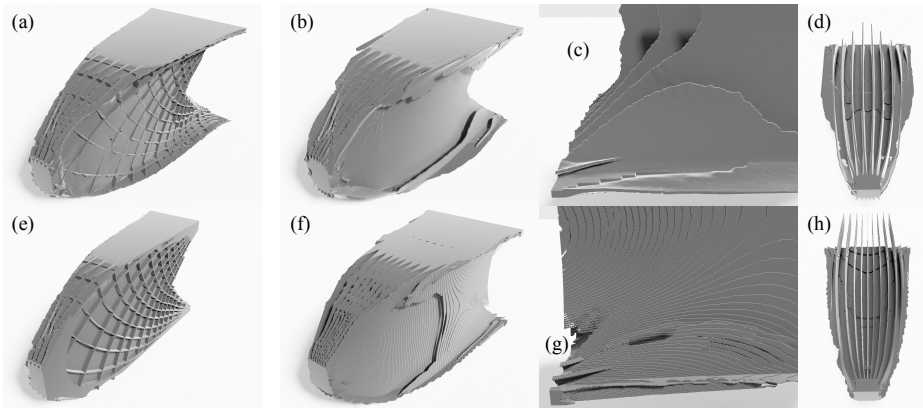

Fig. 16: On the left, (a,e) show a cantilever produced from a homogenization solution where all three layers have been forced to be active. The images on the right show a comparison of our results for the cantilever (b,c,d) with the results produced using the method of Groen et al. [2020] (f,g,h).

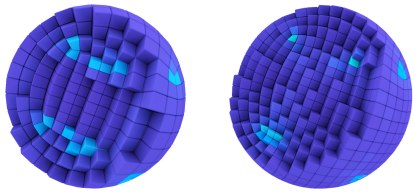

Fig. 17: Comparison of a hex mesh of a sphere produced by our method based on an octahedral frame field generated using the method of Palmer et al. [2019] and a similar hexmesh produced from a field created with the method of Corman and Crane [2019] and hex meshed using CubeCover in an implementation by David Bommes (right). For both visualization we use Bracci et al. [2019]. The hexahedra are colored according to the scaled Jacobian.

ate highly anisotropic structures and hex meshes outside of the singular region. We do not require any prescribed edge-lengths; the implicit description of anisotropy by the input fields suffices.

Admittedly, there are also several limitations to our approach. Stream surface tracing in highly rotating fields is difficult. We need to stop tracing stream surfaces that cross the singular regions at an angle not perpendicular to the singular curve. However, for topology optimized fields this is no major concern as discussed in Section 3.1. We are further able to keep the hole size minimal, such that these regions can mostly be filled with hexahedra for a boundary optimized field if a hexahedral mesh is output. However, our hex meshing scheme is admittedly simplistic. The limit on the proximity of stream surfaces means that we can only reliably generate hexahedral meshes for relatively simple frame fields, whereas there is no restriction on the frame fields for which we can synthesize volumetric solids. As a further limitation, we have realized that an excess amount of stream surfaces can overload the optimizer. This situation occurs if one field is activated by a large amount of stream surfaces, which are all equally good, such as in the case of the helicoid example (Figure 18). Here, it is possible to end up with hundreds of helicoidal surfaces each of which activates almost all probe points. Consequently, an important next step is to avoid oversampling by monitoring which regions (i.e. probe points) are already well-covered.

Finally, we have focused on applying the method to fields arising from compliance minimization in this paper, but topology optimization is replete with problems where the proposed method might be applicable, hinting at future application areas.

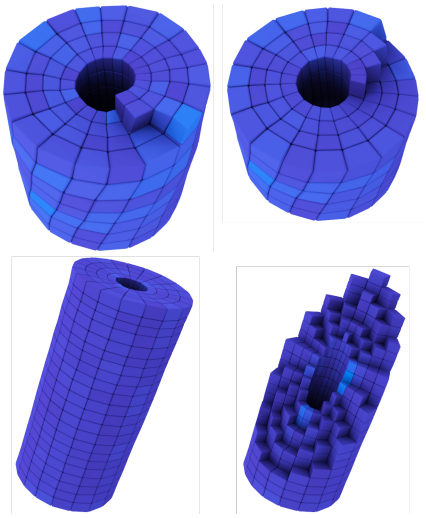

Fig. 18: In the top row, we see a hex mesh generated using our method on a field describing a helicoid. Note that the underlying field is non-integrable. On the left, we see the entire mesh, whereas on the right, we have removed several layers of hexahedra. In the bottom row, we see a hex mesh generated on a cylindrical field. Note how the shape of the hexahedra changes dramatically from the outside towards the cut out singular curve. On the right, we peel away several layers of hexahedra, which reveals that the minimal edge-length is significantly smaller than the maximal edge-length. Note that we desire this from a field describing an anisotropic mesh.

References

Aage, N., Andreassen, E., Lazarov, B. S., and Sigmund, O. (2017). Giga-voxel computational morphogenesis for structural design. *Nature*, 550(7674):84–86.

Arora, R., Jacobson, A., Langlois, T. R., Huang, Y., Mueller, C., Matusik, W., Shamir, A., Singh, K., and Levin, D. I. (2019). Volumetric michell trusses for parametric design & fabrication. In *Proceedings of the 3rd ACM Symposium on Computation Fabrication*, SCF '19, New York, NY, USA. ACM.

Avellaneda, M. (1987). Optimal bounds and microgeometries for elastic two-phase composites. *SIAM Journal on Applied Mathematics*, 47(6):1216–1228.

Baandrup, M., Sigmund, O., Polk, H., and Aage, N. (2020). Closing the gap towards super-long suspension bridges using computational morphogenesis. *Nature Communications*, 11(1):1–7.

Bendsøe, M. P. (1989). Optimal shape design as a material distribution problem. *Structural optimization*, 1(4):193–202.

Bendsøe, M. P. and Kikuchi, N. (1988). Generating optimal topologies in structural design using a homogenization method. *Computer methods in applied mechanics and engineering*, 71(2):197–224.

Bendsøe, M. P. and Sigmund, O. (2004). *Topology Optimization*. Springer Berlin Heidelberg.

Bommes, D., Zimmer, H., and Kobbelt, L. (2009). Mixed-integer quadrangulation. *ACM Transactions On Graphics (TOG)*, 28(3):77.

Bracci, M., Tarini, M., Pietroni, N., Livesu, M., and Cignoni, P. (2019). Hexalab. net: An online viewer for hexahedral meshes. *Computer-Aided Design*, 110:24–36.

Bridson, R. (2007). Fast poisson disk sampling in arbitrary dimensions. *ACM SIGGRAPH*.

Campen, M., Bommes, D., and Kobbelt, L. (2012). Dual loops meshing. 31:1–11.

Campen, M. and Kobbelt, L. (2014). Dual strip weaving. 33:1–10.

Campen, M., Silva, C. T., and Zorin, D. (2016). Bijective maps from simplicial foliations. 35:1–15.

Chapra, S. (2012). *Applied numerical methods with MATLAB for engineers and scientists*. McGraw-Hill, New York.

Corman, E. and Crane, K. (2019). Symmetric moving frames. *ACM Transactions on Graphics (TOG)*, 38(4):1–16.

Francfort, G., Murat, F., and Tartar, L. (1995). Fourth-order moments of nonnegative measures on s2 and applications. *Archive for Rational Mechanics and Analysis*, 131(4):305–333.

Fuhrmann, S. and Goesele, M. (2014). Floating scale surface reconstruction. *ACM Transactions on Graphics (ToG)*, 33(4):1–11.

Gao, X., Jakob, W., Tarini, M., and Panozzo, D. (2017). Robust hex-dominant mesh generation using field-guided polyhedral agglomeration. *ACM Trans. Graph.*, 36(4).

Geoffrey-Donders, P. (2018). *Homogenization method for topology optmization of struc-tures built with lattice materials*. PhD thesis.

Geoffroy-Donders, P., Allaire, G., and Pantz, O. (2020). 3-d topology optimization of modulated and oriented periodic microstructures by the homogenization method. *Journal of Computational Physics*, 401:108994.

Grant, M. and Boyd, S. (2008). Graph implementations for nonsmooth convex programs. In Blondel, V., Boyd, S., and Kimura, H., editors, *Recent Advances in Learning and Control*, Lecture Notes in Control and Information Sciences, pages 95–110. Springer-Verlag Limited. `http://stanford.edu/~boyd/graph_dcp.html`.

Grant, M. and Boyd, S. (2014). CVX: Matlab software for disciplined convex programming, version 2.1. `http://cvxr.com/cvx`.

Groen, J. and Sigmund, O. (2018). Homogenization-based topology optimization for high-resolution manufacturable microstructures. *International Journal for Numerical Methods in Engineering*, 113(8):1148–1163. (online since April 2017).

Groen, J., Stutz, F., Aage, N., Bærentzen, J., and Sigmund, O. (2020). De-homogenization of optimal multi-scale 3d topologies. *Computer Methods in Applied Mechanics and Engineering*, 364.

Guo, H.-X., Liu, X., Yan, D.-M., and Liu, Y. (2020). Cut-enhanced polycube-maps for feature-aware all-hex meshing. *ACM Transactions on Graphics (TOG)*, 39(4):106–1.

Hotz, I., Sreevalsan-Nair, J., Hagen, H., and Hamann, B. (2010). Tensor Field Reconstruction Based on Eigenvector and Eigenvalue Interpolation. In Hagen, H., editor, *Scientific Visualization: Advanced Concepts*, volume 1 of *Dagstuhl Follow-Ups*, pages 110–123. Schloss Dagstuhl–Leibniz-Zentrum fuer Informatik, Dagstuhl, Germany.

Huang, J., Tong, Y., Wei, H., and Bao, H. (2011). Boundary aligned smooth 3d cross-frame field. In *ACM transactions on graphics (TOG)*, volume 30, page 143. ACM.

Hultquist, J. P. M. (1992). *Constructing stream surfaces in steady 3D vector fields*.

Ju, T., Losasso, F., Schaefer, S., and Warren, J. (2002). Dual contouring of hermite data. In *Proceedings of the 29th Annual Conference on Computer Graphics and Interactive Techniques*, SIGGRAPH '02, page 339–346, New York, NY, USA. Association for Computing Machinery.

Kälberer, F., Nieser, M., and Polthier, K. (2007). Quadcover-surface parameterization using branched coverings. In *Computer graphics forum*, volume 26, pages 375–384. Wiley Online Library.

Larsen, S. D., Sigmund, O., and Groen, J. P. (2018). Optimal truss and frame design from projected homogenization-based topology optimization. *Structural and Multidisciplinary Optimization*, 57(4):1461–1474.

Liu, H., Zhang, P., Chien, E., Solomon, J., and Bommes, D. (2018). Singularity-constrained octahedral fields for hexahedral meshing. *ACM Transactions on Graphics (TOG)*, 37(4):93.

Livesu, M., Pietroni, N., Puppo, E., Sheffer, A., and Cignoni, P. (2020). ¡i¿loopycuts¡/i¿: Practical feature-preserving block decomposition for strongly hex-dominant meshing. *ACM Trans. Graph.*, 39(4).

Lyon, M., Bommes, D., and Kobbelt, L. (2016). HexEx: Robust hexahedral mesh extraction. *ACM Transactions on Graphics (TOG)*, 35(4):1–11.

Machado, G. M., Sadlo, F., and Ertl, T. (2014). Image-based streamsurfaces. *Brazilian Symposium of Computer Graphic and Image Processing*, page 6915327.

Michell, A. G. M. (1904). Lviii. the limits of economy of material in frame-structures. *The London, Edinburgh, and Dublin Philosophical Magazine and Journal of Science*, 8(47):589–597.

Milnor, J. (1970). Foliations and foliated vector bundles, mimeographed notes. *Institute for Advanced Study, Princeton*.

MOSEK ApS (2021). *MOSEK Fusion API for C++ manual, Version 9.2*.

Murdoch, P., Benzley, S., Blacker, T., and Mitchell, S. A. (1997). The spatial twist continuum: A connectivity based method for representing all-hexahedral finite element meshes. *Finite elements in analysis and design*, 28(2):137–149.

Ni, S., Zhong, Z., Huang, J., Wang, W., and Guo, X. (2018). Field-aligned and lattice-guided tetrahedral meshing. *Computer Graphics Forum*, 37(5):161–172.

Nieser, M., Reitebuch, U., and Polthier, K. (2011). Cubecover–parameterization of 3d volumes. In *Computer graphics forum*, volume 30, pages 1397–1406. Wiley Online Library.

Norris, A. N. (2005). Optimal orientation of anisotropic solids. *The Quarterly Journal of Mechanics and Applied Mathematics*, 59(1):29–53.

Padberg, M. and Rinaldi, G. (1991). A branch-and-cut algorithm for the resolution of large-scale symmetric traveling salesman problems. *SIAM review*, 33(1):60–100.

Palmer, D., Bommes, D., and Solomon, J. (2019). Algebraic representations for volumetric frame fields. *arXiv preprint arXiv:1908.05411*.

Pantz, O. and Trabelsi, K. (2008). A post-treatment of the homogenization method for shape optimization. *SIAM Journal on Control and Optimization*, 47(3):1380–1398.

Pantz, O. and Trabelsi, K. (2010). Construction of minimization sequences for shape optimization. In *2010 15th International Conference on Methods and Models in Automation and Robotics*, pages 278–283. IEEE.

Pedersen, P. (1989). On optimal orientation of orthotropic materials. *Structural optimization*, 1(2):101–106.

Ray, N., Sokolov, D., and Lévy, B. (2016). Practical 3d frame field generation. *ACM Transactions on Graphics (TOG)*, 35(6):233.

Sigmund, O., Aage, N., and Andreassen, E. (2016). On the (non-)optimality of michell structures. *Structural and Multidisciplinary Optimization*, 54(2):361–373.

Sigmund, O. and Maute, K. (2013). Topology optimization approaches. *Structural and Multidisciplinary Optimization*, 48(6):1031–1055.

Solomon, J., Vaxman, A., and Bommes, D. (2017). Boundary element octahedral fields in volumes. *ACM Transactions on Graphics (TOG)*, 36(3):28.

Stutz, F., Groen, J., Sigmund, O., and Bærentzen, J. (2020). Singularity aware de-homogenization for high-resolution topology optimized structures. *Structural and Multidisciplinary Optimization*, 62:2279–2295.

Takayama, K. (2019). Dual sheet meshing: An interactive approach to robust hexahedralization. In *Computer Graphics Forum*, volume 38, pages 37–48. Wiley Online Library.

Vaxman, A., Campen, M., Diamanti, O., Panozzo, D., Bommes, D., Hildebrandt, K., and Ben-Chen, M. (2016). Directional field synthesis, design, and processing. In *Computer Graphics Forum*, volume 35, pages 545–572. Wiley Online Library.

Wu, J., Wang, W., and Gao, X. (2019). Design and optimization of conforming lattice structures. *IEEE transactions on visualization and computer graphics*, 27(1):43–56.